Dipl.-Ing. Max E. Sorantin, Msc Bsc

Developments and applications of the auxiliary master equation approach

DISSERTATION

zur Erlangung des akademischen Grades

Doktor der Naturwissenschaften

eingereicht an der

Technischen Universität Graz

Betreuer

Univ.-Prof. Dr.rer.nat. Enrico Arrigoni

Institut für Theoretische Physik - Computational Physics

Graz, Juli 2019

EIDESSTATTLICHE ERKLÄRUNG

Ich erkläre an Eides statt, dass ich die vorliegende Arbeit selbstständig verfasst, andere als die angegebenen Quellen/Hilfsmittel nicht benutzt, und die den benutzten Quellen wörtlich und inhaltlich entnommenen Stellen als solche kenntlich gemacht habe. Das in TUGRAZonline hochgeladene Textdokument ist mit der vorliegenden Dissertation identisch.

Datum

Unterschrift

Abstract

The topic of this thesis is the auxiliary master equation approach (AMEA), which is further developed and applied to study nonequilibrium many-body effects in the interacting resonant level model (IRLM) and the Hubbard model. AMEA is a numerical approach to simulate quantum impurity problems out of equilibrium in a non-perturbative and systematically improvable manner. The main idea is to embed the interacting region of the original problem into an auxiliary open quantum system of Lindblad form with additional bath sites, which mimics the physical situation as close as possible. This mapping to an auxiliary system is most effective when the free parameters of the bath sites are optimized with respect to some suitable cost-function measuring the deviation between the auxiliary and physical situation. After the mapping is performed, the resulting many-body Lindblad system has to be solved. Since the latter explicitly describes only the dynamics of a finite number of degrees of freedom, the auxiliary system can be solved by numerical many-body techniques. One of the main strengths of AMEA is that it allows to numerically simulate the auxiliary system for arbitrarily long times. This allows not only to reliably reach the steady state but also to disturb it and measure the response, which yields accurate nonequilibrium steady state Green's functions (NEGF's). This property makes AMEA a suitable impurity solver to be used in nonequilibrium steady state dynamical mean-field theory (DMFT), which is a self-consistent approximation scheme to investigate interacting lattice systems. Employing AMEA as such, we study the effect of impact ionization on the photo-current across a Mott insulating layer modeled by a periodically driven Hubbard model and discuss its relation to the idea of Mott photovoltaics. Outside DMFT, we apply AMEA to the self-dual IRLM, where an analytic solution of the I/V-characteristic is known, to investigate the relation of its negative differential conductance to the NEGF's of the model and benchmark technical developments. In particular, we test an alternative solution strategy for the auxiliary open quantum system, namely stochastic wave-functions (SWF's). In contrast to the previously used technique of superfermions, where the density matrix is "purified" by doubling the degrees of freedom, the density matrix is unraveled in a stochastic manner, thereby circumventing the need to introduce additional degrees of freedom.

This dissertation is conducted in a cumulative manner and therefore build around a series of publications. As is customary for this style of thesis, we first provide a comprehensive introductory part providing background on the physical applications that were studied and discussing the main findings. In this first chapter, we also review AMEA presenting technical details of the developments and complementing them with material and considerations not included in the respective publications. After this all-encompassing first chapter, the individual publications are presented, summarized and discussed with respect to contributions of the different authors.

Key words: Nonequilibrium Green's functions, nonequilibrium impurity solver, Floquet dynamical mean-field theory (DMFT), stochastic wave-functions, Mott photovoltaics, negative differential conductance, steady state transport.

Acknowledgements

I want to express my sincere gratitude to my supervisor Enrico Arrigoni for his kind supervision and support over the years as well as all the time he spared for discussions. Especially, I am grateful for his sympathy in personal issues related to my young family. I also want to thank Wolfgang von der Linden, for co-supervising most of the work in this thesis and his input in many discussions, as well as Karsten Held for his kind co-supervision on the first publication. Also, I am thankful to Yuta Murakami and Phillip Werner for the pleasant collaboration.
I want to say thank-you to my group members Antonius Dorda, Irakli Tidvinitze and Delia Fugger for the collaborations and numerous discussions as well as the great atmosphere within the group. Also, I want to thank my colleagues Markus Aichorn, Manuel Zingl, Robert Triebl, Gernot Kraberger, Florian Maislinger, Daniel Bauernfeind, Mathias Gruber, Gerhard Dorn, Michael Rumetshofer and all other members at the institute for the commitment towards an open door policy - always sparing time for discussions - and also for all the great time outside the university on hiking trips, ski tours and conferences.
Last but not least, I want to thank my family for their support during the years, in particular my parents Erich & Silvia and my wife Johanna for being there for me and the encouragements. A special mention goes to my little son Nils for making a good Job in taking my head off work.

Contents

1 Introduction **1**
1.1 Physical applications 4
1.1.1 Photovoltaic effect and impact ionization in Mott insulators 4
1.1.2 Charge transport in quantum impurity models 6
1.1.2.1 The NDC in the IRLM 7
1.2 Method development 9
1.2.1 Summary of nonequilibrium steady state GF's 9
1.2.1.1 Floquet GF 13
1.2.2 Auxiliary master equation approach 13
1.2.3 Mapping 16
1.2.3.1 Auxiliary geometries and parameterization 16
1.2.3.2 Optimization algorithm 17
1.2.4 Extrapolation to zero cost-function 19
1.2.4.1 Error estimation 19
1.2.5 Stochastic wave-functions 22
1.2.5.1 Fixed time-stepping in the SWF algorithm within ED . . 22
1.2.6 AMEA as impurity solver in Floquet DMFT 24
1.2.6.1 AMEA in Floquet DMFT 25
1.2.6.2 FDSA in the Mott regime: AMEA, IPT and NCA 26

2 Publications **34**
2.1 Publication 1: Geometries of the auxiliary Lindblad system 36
2.2 Publication 2: Floquet DMFT 58
2.3 Publication 3: Stochastic Wavefunctions 69
2.4 Publication 4: Steady state NEGF in the IRLM 82
2.5 Contributions to further publications 91

3 Summary and Outlook **92**

A Details on the Floquet transformation **96**

List of Figures

1.1 Sketch of a quantum dot setup for transport calculations. 6
1.2 Sketch of the transport schemes. 7
1.3 The Keldysh contour 11
1.4 Sketch of the AMEA mapping 14
1.5 The steady state current in the IRLM 21
1.6 Sketch of the norm within SWF 23
1.7 The FDSA compared to full Floquet DMFT within IPT 28
1.8 Floquet sidebands within IPT 29
1.9 AMEA+FDSA versus NCA 32
1.10 The AMEA fits for the AMEA+FDSA versus NCA results in Fig.1.9 . . . 33

List of Abbreviations

GF - Green's function

NEGF - nonequilibrium Green's functions

DMFT - dynamical mean-field theory

IPT - iterated perturbation Theory

NCA - non-crossing Approximation

AMEA - auxiliary master equation approach

ED - exact diagonalization

SWF - stochastic wave-functions

SF - superfermions

DFT - density functional theory

UHB - upper Hubbard band

LHB - lower Hubbard band

NDC - negative differential conductance

IRLM - interacting resonant level model

SIAM - single impurity anderson model

PT - parallel tempering

MPS - matrix product states

FDSA - Floquet diagonal selfenergy approximation

PSD - positive semi-definite

Chapter 1

Introduction

Many complex phenomena arising in condensed matter systems are driven by interactions present between the constituents, such as electrons, phonons and other quasi-particles. Examples are (high T_c-) superconductivity and the related Josephson effect, magnetism, ferroelectricity, the Kondo effect[7] and Mott insulators[8] to name a few. To understand these phenomena, theoreticians have devised approximate models which often capture the relevant physics. Representatives are the famous Hubbard model and variants thereof, like the Hubbard-Holstein, Bose-Hubbard and extended Hubbard model as well as spin systems like the Kondo, Heisenberg and Ising model. Technical applications of such many-body effects, like the Superconducting Quantum Interference Device (SQUID), which is based on the Josephson effect, for instance, are naturally operated in nonequilibrium situations. Further, studying these systems beyond the linear response opens the way to even richer physics featuring genuine nonequilibrium effects like dynamical phase transitions where the system undergoes a phase transition as some parameter inducing the nonequilibrium situation is changed. While the theoretical foundations for the description of nonequilibrium quantum systems were already laid in the sixties[9, 10], the growing field of nonequilibrium many-body physics has developed mainly over the last two decades. On the theoretical side, this is because, in contrast to equilibrium, one cannot rely on thermodynamics principles for simplification but one has to resolve the full quantum dynamics instead. Since the analytic treatment of the latter is very limited, except for integrable models, one has to rely on computer simulations, which became feasible only with the development of modern computers and cluster facilities. On the experimental side, the realization of these theoretical models under clean and controlled conditions became possible around the same time with the aid of ultracold atomic gases. For instance, the realization of the Hubbard model in the Mott regime was reported in 2008[11, 12].

In nonequilibrium one can distinguish two cases. In the first, one is interested in the correlations between some time-evolving state and the initial condition, which is referred to as initial correlations. For example, this could be transient dynamics or the long time behavior after a quantum quench, which is of great interest for the fundamental question of thermalization in closed many-body quantum systems. This thesis is concerned with the second case, where one is not interested in initial correlations, but the nonequilibrium

steady state forming in the presence of dissipation. The simplest and one of the most intensively studied class of many-body systems that can give rise to such steady states are so-called quantum impurity problems, where a single interacting site is in contact with some non-interacting environment. These systems, for example, allow to study the Kondo effect in a nonequilibrium setting[13–17] or fundamental principles of information theory, like the entropy production in nonequilibrium steady states[18]. Apart from being interesting by themselves, they constitute the backbone of nonequilibrium DMFT[19] which allows to treat local correlations in extended systems in a non-perturbative manner. While originally developed for the equilibrium case[20], DMFT has been extended to nonequilibrium[19] and applied to study especially the Hubbard model out of equilibrium[21–33].

In recent years, the area of nonequilibrium steady states of many-body systems has developed a new branch with increasing attention in periodically driven systems, so-called (interacting) Floquet systems. The field is driven by the idea of Floquet engineering, where the additional band structure induced by the periodic drive is exploited to control material properties or create new states of matter by realizing effective Hamiltonians not accessible in static systems. The adaptation of nonequilibrium DMFT to Floquet systems[34] opened the way to theoretically simulate the interplay of strong correlations and periodic driving in extended systems[21, 27, 28, 31, 35–39], revealing for instance enhanced high harmonic generation in Mott insulators[38].

This thesis: The success of nonequilibrium DMFT on the model level, recently experimentally verified also for the periodically driven Hubbard model[40], motivates the endeavor to treat more realistic systems as in equilibrium. In equilibrium the DFT+DMFT[41] approach , where a DMFT calculation is carried out on top of DFT, is well established to treat strongly correlated materials on an ab-initio basis. The key point is, that multiple orbitals have to be considered in order to reliably treat such realistic materials which on the technical side demands efficient and accurate impurity solvers applicable to the multi-orbital case.

As mentioned above, this thesis concentrates on nonequilibrium steady states. Besides various approaches to address a nonequilibrium impurity problem, see Sec.2.3 for a list of references, a systematically improvable and non-perturbative method which directly targets the steady state is AMEA[16, 42, 43]. In this thesis, we further develop AMEA[1, 2], paving the way to be used as multi-band steady state impurity solver in the future. We apply AMEA as impurity solver within nonequilibrium steady state [3, 4] and Floquet DMFT, where we study the effect of impact ionization on the photo-current across a periodically driven Mott insulator[5]. Further, we apply AMEA to a multi-site impurity model, namely the IRLM, to benchmark the new developments[2] and complement studies on the NDC in the IRLM by calculating the NEGF in depence of the bias voltage[6].

Outline: The present thesis is written in a cumulative manner and is organized in three chapters. The first chapter introduces the two physical applications that were studied (Sec.1.1) and presents the technical developments within AMEA (Sec.1.2). The second

chapter constitutes the main part of this thesis and is devoted to the conducted publications. A summary and outlook of the results and advances is presented in the final chapter.

1.1 Physical applications

During the course of this thesis we studied two physical situations. Here, we present background on the corresponding fields together with an overview of the previous literature and highlight the contributions within this thesis. We note that naturally, and for the sake of readability and self-containment of this section, there is a substantial overlap with the introductory parts of the corresponding publications[5, 6], attached in Sec.2.2 and Sec.2.4.

1.1.1 Photovoltaic effect and impact ionization in Mott insulators

The photovoltaic effect is the conversion from radiative to electrical energy. It is based on the principle of the photoelectric effect where a photon is absorbed and some electronic system excited. Its break through in applications was achieved by the use of semiconductors and corresponding devices are nowadays referred to as "conventional" in contrast to other devices based on organic materials[44] for instance.

Let us consider a direct bandgap semiconductor with some bandgap Δ and conduction(valence) bandwidth $W_c(W_v)$. To excite an electron from the filled valence band into the conduction band, the photon energy, ε_γ, must fulfill $\Delta \leq \varepsilon_\gamma \leq \Delta + W_c + W_v$. Since the time scale for the separation of the excited electron-hole pair in some (internal or external) electric field, is much larger than the scattering time with other degrees of freedom, mostly phonons, the excited electron(hole) has typically relaxed to the bottom(top) of the conduction(valence) band before contributing to the photo current. Thus, only the gap energy is converted into electrical energy and the excess energy, $\varepsilon_\gamma - \Delta$, is dissipated as heat thereby limiting the efficiency in applications. For instance, this wasting of the excess energy, together with other factors, leads to the famous Shockley-Queiser limit for the efficiency of conventional solar cells[45].

A spectral gap is also present in a so-called Mott insulator. Such a state exists in the strongly correlated regime of the Hubbard model and is realized in transition metal oxides. In contrast to semiconductors, the gap is not a conventional bandgap, but it is induced by the strong electronic correlations which split a single band into the so-called LHB and UHB, that, in the present context, can be seen in analogy to the valence and conduction band in a semiconductor. Thus, the same scenario for energy conversion, as described above, holds true with one key difference. Due to the strong electronic correlations the electron-phonon coupling in such systems is usually much weaker than the electron-electron interactions. This means, that an excited electron, referred to as doublon in a Mott insulator, relaxing to the bottom of the UHB is likely to undergo electronic scattering, if possible, keeping the excess energy in the electronic system, thereby increasing the efficiency of the photovoltaic effect in comparison to semiconductors. For instance, an excited high energy electron with an energy[1] ε_e, higher than twice the gap energy[2], $\varepsilon_e \geq 2\Delta$, is expected to "impact

[1] measured with respect to the top of the LHB.

[2] For this, the bandwidth of the UHB must fulfill $W_{\mathrm{UHB}} \geq 2\Delta$.

ionize" an electron from the LHB turning into two low energy doublons near the bottom of the UHB[3]. This basic process is called impact ionization, see Fig.1 in Ref.[5] attached in Sec.2.2, and constitutes the leading order inter band electronic scattering process for the decay of a high energy doublon or hole.

At this point, we want to note that the idea of enhancing the photovoltaic efficiency by increasing the effect of impact ionization is an old concept[47] and it is pursued also in other classes of materials[48, 49].

Previous works on Mott photovoltaics: The photovoltaic effect in a Mott insulator, observed experimentally in Refs.[50, 51], was first discussed theoretically by considering the strong coupling limit of the Hubbard model in a pn-junction setup. It was found that the energy conversion efficiency in narrow gap Mott insulators can be significantly enhanced by impact ionization acting on time scales shorter than alternative decay mechanisms[52]. This work was followed by ab initio based studies of transition metal oxides reporting a direct bandgap in the optical range and an internal electric field gradient forming in a *pn*-junction setup of $LaVO_3$ transition metal oxides heterostructures[53] as well as a greatly enhanced impact ionization rate in the M_1-phase of VaO_2[4] compared to silicium within the solar spectrum[54]. Later on, the carrier multiplication via impact ionization in the M_1-phase of VaO_2 was verified experimentally[55] and several experiments where conducted to investigate the photovoltaic efficiency and photoresponse of $LaVO_3$ thin films[56–58]. The latter overall find a poor photovoltaic efficiency due to low carrier mobility, mainly hindered by defects, in $LaVO_3$ thin films[56, 58] and a high sensitivity of electronic and optical properties on the growth conditions[57, 58]. Especially, stoichiometry was found to be key to high quality samples, with respect to defect concentration, and greatly enhanced photoresponsivity[57]. Further, numerical simulations based on nonequilibrium DMFT investigated the Mott insulating phase of the Hubbard model after a photo excitation[24–26, 28, 46, 59–62]. In particular, impact ionization was found to be the dominant channel on short time scales in the consequent thermalization process after an initial photo excitation[46] and high mobility of photo excited carriers in heterostructures from Mott antiferromagnets was reported[62].

Contribution of this thesis: We saw, that the theoretical considerations regarding Mott photovoltaics and impact ionization have been focused on either equilibrium properties of realistic materials or the time evolution after a photo excitation in model calculations. However, in a photovoltaic application a corresponding device will typically[5] operate in a periodic steady state. Despite the promising theoretical results, experiments have measured poor photovoltaic efficiencies and demonstrated that sample quality is of major importance. Since the samples in experiments are inevitably plagued by imperfec-

[3]If the initial hole is also highly energetic, forming at the bottom of the LHB, it can undergo the particle-hole symmetric analog process, thereby creating an additional low-energy doublon-hole pair[46].

[4]a prototypical example for a Mott insulator

[5]An exception would be, for example, a highly sensitive photo detector in the single photon regime.

Figure 1.1: Sketch of a quantum dot setup for transport calculations.

tions, it is very interesting to complement the previous theoretical studies and consider an idealized Mott photovoltaic model setup allowing to investigate the role of impact ionization in the periodic steady state under clean conditions.

Within this thesis[5], we devised a simplistic toy model tailored to study the effect of impact ionization on the continuous energy harvesting across a periodically driven Mott insulating layer by investigating the photo current as a function of the external driving frequency. We find that impact ionization plays a dominant role also in the periodic steady state dynamics and leads to a significant increase of the photo current, if the external driving frequency is consistent with impact ionization.

1.1.2 Charge transport in quantum impurity models

Transport through nanostructures has been intensively studied over the last decades, due to its relevance in electronic devices. In particular, quantum dot setups have been studied due to their rich physics, experimental versatility and theoretical simplicity. In a typical quantum dot setup one considers a central region, where many-body interactions are present, connected to a left and a right lead, as sketched in Fig.1.1.2.

To study the nonequilibrium charge transfer across the central region induced by a symmetrically applied bias voltage, one usually considers two physically distinct scenarios, which can be realized in time-dependent simulations of finite systems[63, 64]. In the first[65], denoted by (I) in the following, the three subsystems are assumed to be initially decoupled and in grand canonical equilibrium with different chemical potentials[6], $\mu_{L/R} = \pm V/2$. Upon turning on the coupling between the leads and the central region a steady state is reached. In the second scheme[66], denoted by (II), the system is initially assumed to be coupled and thus characterized by a single chemical potential, μ. To induce the nonequilibrium situation, the leads are energetically quenched by the application of potentials $\pm V/2$ and the steady state is reached after time evolution with the voltage bias present.

When targeting the time invariant steady state directly, the two different scenarios and initial conditions are translated into boundary conditions for a static problem by using the fact that far enough away from the central region, the leads are always in their respective

[6]The steady state is independent of the initial conditions in the central region. This is why the initial choice of μ_c is arbitrary.

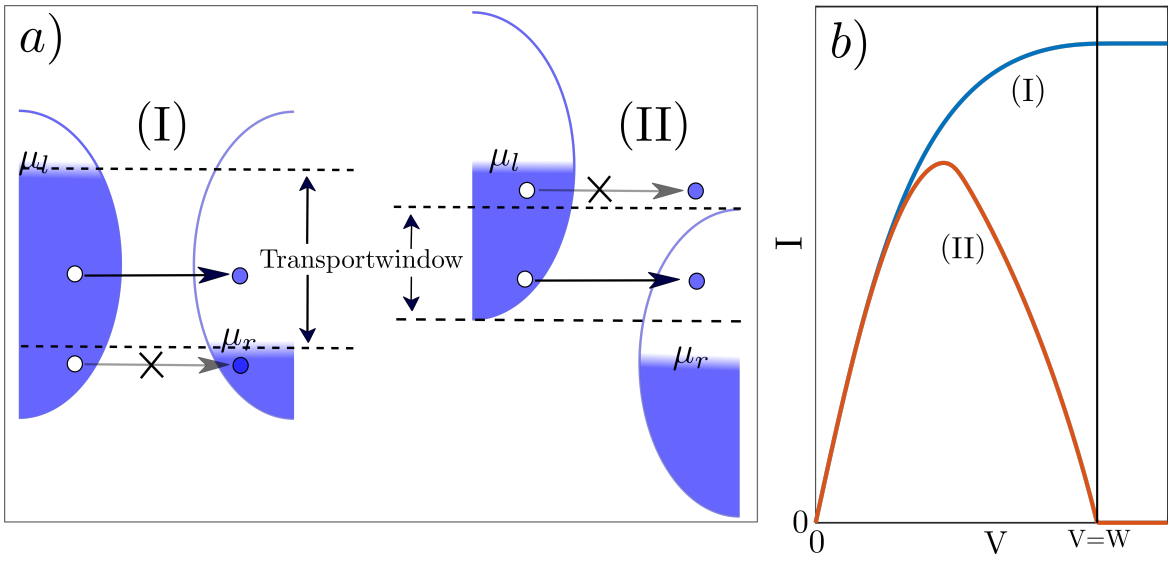

Figure 1.2: Panel a): Sketch of the two transport schemes described in the main text. The indicated transport window refers to independent particles. Panel b): Sketch of a typical I/V-characteristic for the two transport schemes.

equilibrium state. Thus, (I) is characterized by leads which asymptotically differ only in the chemical potentials while (II) is obtained by considering them energetically shifted as well. As a consequence, the leads asymptotically maintain half filling in (II), while their filling in (I) depends on the specific bias voltage. Fig.1.1.2a shows a sketch of the two different situations.

While the two scenarios have the same linear response and agree well, for voltages V which are small compared to the lead bandwidth W, they lead to drastically different behaviors for large voltages. In particular, for $V > W$, the steady state current settles on a finite value in (I) and vanishes for (II), see Fig. 1.1.2b. Consequently, (II) naturally features a regime of NDC when the voltage becomes comparable to the bandwidth due to the decreasing spectral overlap of the leads. In contrast, even in the presence of interactions, one generally does not expect such a regime in (I) since the density of lead states available for transport is increasing with the bias voltage.

1.1.2.1 The NDC in the IRLM

The IRLM is a quantum impurity model of spinless fermions consisting of a single impurity site connected to two semi-infinite tight-binding chains and a density-density interaction term between the impurity site and its nearest neighbors. In the following, we will denote the interaction strength by U, the hopping inside the tight-binding chains by J, resulting in a bandwidth $W = 4J$, and the hopping at the contact links to the impurity by J'.

In the context of nonequilibrium transport, the IRLM has gained considerable attention over the last decade due to the seminar work by Boulat et al.[67], who derived an analytic

expression for the steady state current, when a voltage bias is applied by (I), which is in excellent agreement with numerical tDMRG simulations. The solution is based on a mapping to a continuum model and valid at the so-called self-dual point, where $U = 2J$, and at zero temperature. The mapping to a continuum model is a priori valid in the scaling regime, where the bandwidth is the dominant energy scale in the system. More fundamentally, the defining property of the scaling regime is that the physics becomes universal depending only on a single energy scale, $\propto J'^{4/3}$ within the IRLM. Since numerical simulations[67, 68] have obtained scaling at the sef-dual point up to values $J' \lesssim J/2$ and $V \lesssim 2J$, the scaling regime is parametrically extended up to these values.

Most notably, the solution for the steady state current features a regime of NDC and the numerical simulations further revealed that the NDC prevails also for other values of U. This rose the question of the physical mechanism in the lattice model responsible for the observed NDC. This was addressed by RG approaches[69–71] showing that J' is renormalized to lower values by large voltages resulting in the NDC. These studies were complemented by a perturbative analysis within NEGF[72] which agree with the RG results up to leading order in the interaction. Further, the NDC in the IRLM is already captured within Hartree-Fock[73] where it is technically encoded into the renormalization of J' as well.

Contribution of this thesis: While the RG results are arguably applicable within the full realm of the scaling regime and especially reliable for $J' \ll J$ and small values of the interactions, the first order perturbative NEGF approach is valid for $U \ll J$ and arbitrary J'. To extend the confirmation of the RG results up to the (parametric-) boundaries of the scaling regime, i.e. the sef-dual point with $J' \lesssim J/2$, the NEGF's need to be evaluated with an approach which, treats the interaction and the hybridization to the leads in a non-perturbative manner and on equal footing.

Within this thesis, we have calculated the NEGF's in the corresponding parameter regime by employing AMEA. Investigating the numerical results of the nonequilibrium spectralfunction and effective local distribution functions on the sites next to the impurity, we found that the NDC is carried by the change in the effective local distribution functions, which resemble the equilibrium form of their corresponding leads for high voltages. Since this can be interpreted as consequence of an effective decoupling of the leads from the impurity, we were able to confirm this mechanism within a non-perturbative approach.

1.2 Method development

In this section, we review AMEA and present details of the new developments, with respect to the works[42, 1], summarized in the dissertation of Antonius Dorda[43]. To lighten the notation, we use the convention $\hbar = c = e = k_B = 1$.
We start with a brief summary of steady state NEGF's (Sec.1.2.1) and discuss details of AMEA as well as its developments (Sec.1.2.2-1.2.4). We close this section with the discussion of AMEA as impurity solver in Floquet DMFT, presenting a method comparison with the NCA and IPT (Sec.1.2.6).

1.2.1 Summary of nonequilibrium steady state GF's

In this thesis, we use the framework of NEGF's to study many-body systems out of equilibrium. For a concise introduction see for example the reviews[21, 74] while a more thorough treatment can be found in the textbooks[75, 76].

In this work, we are interested in nonequilibrium steady states that form in the presence of dissipation where initial correlations[7] can be neglected[8]. We consider a closed but infinite quantum system and denote an expectation value in the steady state limit by $\langle ... \rangle_{ss}$ which is defined as the long time limit when the expectation value becomes time-translation invariant. For instance, for a single time expectation value, we have

$$\langle A(t) \rangle_{ss} \equiv \lim_{\tau\to\infty} \lim_{L\to\infty} \langle A(\tau + t) \rangle_L \equiv \lim_{\tau\to\infty} \langle A(\tau + t) \rangle_{L\to\infty} , \tag{1.1}$$

where L denotes the system size. Of course, in the steady state, this is just a constant since

$$\lim_{\tau\to\infty} \langle A(\tau + t) \rangle_{L\to\infty} = \lim_{\tilde{\tau}=(\tau+t)\to\infty} \langle A(\tilde{\tau}) \rangle_{L\to\infty} = \langle A \rangle_{ss} . \tag{1.2}$$

Also multi-time correlation functions are given by the usual form

$$\begin{aligned} G^{(n)}_{A_n A_{n-1}...A_1}(t_n, t_{n-1}, ..., t_1)_{ss} &= \langle A_n(t_n) A_{n-1}(t_{n-1}) ... A_1(t_1) \rangle_{ss} \\ &= \lim_{\tau\to\infty} \langle A_n(\tau + t_n) A_{n-1}(\tau + t_{n-1}) ... A_1(\tau + t_1) \rangle_{L\to\infty} \\ &= \lim_{\tau\to\infty} \left\langle e^{iH\tau} A_n(t_n) A_{n-1}(t_{n-1}) ... A_1(t_1) e^{-iH\tau} \right\rangle_{L\to\infty} , \end{aligned} \tag{1.3}$$

and also depends only on the time differences. For the $n = 2$ case, we have

$$\begin{aligned} \langle A(t) B(t') \rangle_{ss} &= \lim_{\tau\to\infty} \langle A(\tau + t) B(\tau + t') \rangle_{L\to\infty} = \lim_{\tilde{\tau}=(\tau+t')\to\infty} \langle A(\tilde{\tau} + t - t') B(\tilde{\tau}) \rangle_{L\to\infty} \\ &= \langle A(t - t') B \rangle_{ss} = \langle AB(-(t - t') \rangle_{ss} . \end{aligned} \tag{1.4}$$

In the following, we consider the single particle GF and explicit expressions will refer to the fermionic case. For instance, the retarded and advanced GF's are defined, in equivalence

[7] Correlations between some initial state and the steady state.
[8] This is equivalent to the statement that the steady state is unique and independent of the initial state.

to equilibrium, as

$$G^R(t-t') = -i\Theta(t-t')\left\langle\{c(t-t'),c^\dagger\}\right\rangle_{ss}\,,$$
$$G^A(t-t') = i\Theta(-(t-t'))\left\langle\{c,c^\dagger(-(t-t'))\}\right\rangle_{ss} = G^R(-(t-t'))^*\,,$$

where $c/c^\dagger$ denote creation/annihilation operators[9] in the Heisenberg picture and curly brackets are used for the anti-commutator. While in equilibrium, the knowledge of the retarded GF is enough to completely specify the state of the system because the occupation is prescribed by thermodynamics principles, the nonequilibrium situation requires to consider also an additional correlation function that keeps track of this information. It turns out that this information is encoded in the so called keldysh GF

$$G^K(t-t') = -i\left\langle\left[c(t-t'),c^\dagger\right]\right\rangle_{ss}\,. \tag{1.5}$$

It is further convenient to define also a lesser and greater GF as

$$G^<(t-t') = i\left\langle c^\dagger c(t-t')\right\rangle_{ss}\,,$$
$$G^>(t-t') = -i\left\langle c(t-t')c^\dagger\right\rangle_{ss}\,, \tag{1.6}$$

which are related to the retarded, advanced and keldysh GF's by

$$G^< = \frac{1}{2}(G^K - G^R + G^A)\,,$$
$$G^> = \frac{1}{2}(G^K + G^R - G^A)\,. \tag{1.7}$$

The family of GF's considered in the steady state situation is completed by the definition of the causal (or time-ordered) and anti-causal (or anti-time-ordered) GF

$$G^c(t-t') = -i\left\langle\mathcal{T}c(t-t')c^\dagger\right\rangle_{ss}\,,$$
$$G^{\tilde{c}}(t-t') = -i\left\langle\tilde{\mathcal{T}}c(t-t')c^\dagger\right\rangle_{ss}\,, \tag{1.8}$$

where $\tilde{\mathcal{T}}/\mathcal{T}$ denotes the time/anti-time-ordering operator. In the NEGF theory, essentially different GF's are then viewed as real time components of a contour-ordered GF, see below.

The reason why we consider GF's is of course the machinery of many-body perturbation theory which is formulated in terms of them. The corresponding perturbation expansion relies on Wick's theorem, which requires that expectation values are calculated with respect to a non-interacting state. In the standard (groundstate) theory, this is achieved by considering a reference state in the infinite past which is time-evolved into the targeted interacting state by adiabatic switching of interactions. Due to the "Gell-Mann and Low" theorem [77, 78], which is a statement about eigenstates, the standard theory allows to

[9]We suppress any label on the c-operators, such as a spin, site or band index, for clarity. The latter would just result in a matrix structure of the GF

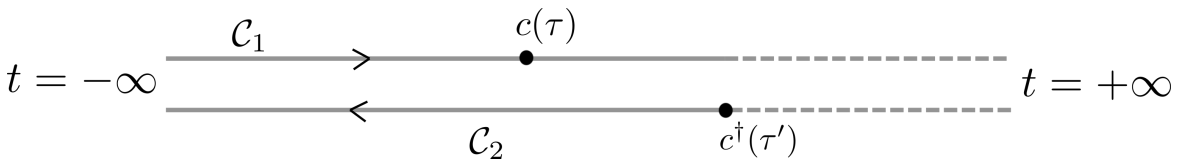

Figure 1.3: The Keldysh contour as two copies of a real time axis. For the single particle GF, operators $c^{(\dagger)}$ are then inserted at times τ and τ' on the upper and/or lower branch of the contour. The dashed parts in the contour indicate redundant time evolutions.

control also the infinite future where the initial state[10] is recovered when the interactions are adiabatically switched off again. The crucial difference to the present case is that the steady state is *not* an eigenstate. Thus the "Gell-Mann and Low" theorem and its corresponding protocol of adiabatic switching of interactions can not be used to have certainty about the infinite future. More fundamentally, while the nonequilibrium situation can be generated according to a suitable protocol starting from a non-interacting initial state in the infinite past, there does not exist a general protocol to return back to this initial state in the infinite future. This is the reason why in the nonequilibrium theory one has to unwind the initial protocol and time-evolve the system back to the non-interacting initial reference state. This gives rise to the so-called Keldysh contour, see Fig.1.2.1, which comprises two branches, a forward branch $\mathcal{C}_1$ and a backward branch $\mathcal{C}_2$.

To obtain a systematic perturbation expansion, the time-ordered GF from the standard theory is generalized to a contour-ordered GF, where time is viewed along the Keldysh contour. This yields a GF with 2x2=4 real time components, stemming from the two operators being inserted along the two branches, $G_{ij}(t,t')$, with $t \in \mathcal{C}_i, t' \in \mathcal{C}_j$. The four components are not independent and related by[11]

$$G_{11} + G_{22} = G_{12} + G_{21}\,. \tag{1.9}$$

If the two operators lie on the forward branch, the corresponding component is nothing else than the causal GF, $G_{11} = G^c$ and one can further identify $G_{22} = G^{\tilde{c}}$, $G_{12} = G^<$ and $G_{21} = G^>$. The matrix build from these real time components,

$$\hat{G}(t,t') = \begin{pmatrix} G^c & G^< \\ G^> & G^{\tilde{c}} \end{pmatrix}, \tag{1.10}$$

is then referred to as the NEGF. Due to the relation between the components, Eq.(1.9), it is convenient to transform into a basis where this redundancy is accounted for, which is achieved by the so called Keldysh rotation given by

$$\underline{G} = L\tau_3\hat{G}L^\dagger = \begin{pmatrix} G^R & G^K \\ 0 & G^A \end{pmatrix}, \tag{1.11}$$

[10] apart from a phase

[11] This is because the time evolution after $t_{\max} = \max(t,t')$ cancels among the two branches which means the operator at $t_{\max}$ can be thought of as belonging to both the forward and backward branch.

with

$$L = \frac{1}{\sqrt{2}}\begin{pmatrix} 1 & -1 \\ 1 & 1 \end{pmatrix}, \quad \tau_3 = \begin{pmatrix} 1 & 0 \\ 0 & -1 \end{pmatrix}. \tag{1.12}$$

Hereby the retarded, advanced and keldysh GF appear. Explicitly, they are related to the original components by

$$\begin{aligned} G^R &= \frac{1}{2}(G_{11} - G_{12} + G_{21} - G_{22}), \\ G^A &= \frac{1}{2}(G_{11} + G_{12} - G_{21} - G_{22}), \\ G^K &= \frac{1}{2}(G_{11} + G_{12} + G_{21} + G_{22}). \end{aligned} \tag{1.13}$$

The advantage of the matrix representation is that a convolution in contour variables, $[G_1 \star G_2](\tau, \tau') = \int_{\mathcal{C}} d\tau'' G_1(\tau, \tau'')G_2(\tau'', \tau')$, is translated to a single real-time integral $\underline{G_1 \star G_2}(t, t') = \int_{-\infty}^{+\infty} dt'' \underline{G}_1(t, t'')\underline{G}_2(t'', t')$. In this form, the theory is structurally equivalent to the equilibrium case and the existing equations, such as the Dyson equation, can be reused when respecting the additional matrix structure.

Connections to physical quantities: Here, we want to exemplify the relation of the different GF's defined above to physical quantities. Since the GF's in the steady state only depend on a single real time argument, it is expedient to work with their Fourier transform, $G(\omega) = \int dt e^{i\omega(t-t')}G(t - t')$.

The retarded and advanced components hold the information about the density of states of our system, while the keldysh GF keeps track of how these states are occupied. More explicitly, the retarded and advanced GF are related to the spectralfunction $A(\omega)$ by

$$A(\omega) = -\frac{1}{2\pi}(G^R(\omega) - G^A(\omega)) = -\frac{1}{\pi}\operatorname{Im} G^R(\omega). \tag{1.14}$$

The particle density can be expressed as

$$n = \frac{1}{2}\left(1 - \int \frac{d\omega}{2\pi} G^K(\omega)\right) = -i \int \frac{d\omega}{2\pi} G^<(\omega). \tag{1.15}$$

Redundancies when applied to Equilibrium: In equilibrium, the occupation is predetermined by thermodynamics principles which leads to the fact that here the keldysh GF is related to the retarded/advanced GF by the so called fluctuation-dissipation theorem,

$$G^K(\omega) = (1 - 2f(\omega)(G^R(\omega) - G^A(\omega)), \tag{1.16}$$

where $f(\omega)$ is the thermodynamic distribution function, i.e. the Fermi-function for fermions. Equivalently, we can write Eq.(1.16) in the alternative forms

$$\begin{aligned} G^<(\omega) &= if(\omega)A(\omega), \\ G^>(\omega) &= -i[1 - f(\omega)]A(\omega). \end{aligned} \tag{1.17}$$

This motivates the interpretation of the lesser(greater) GF as the spectral density of (un-) occupied states and the keldysh GF as the difference between them. This interpretations can be carried over to the nonequilibrium case, although the density of states and corresponding filling may be well defined only locally.

Dyson's equation and the selfenergy A central equation in the GF formalism is the so-called Dyson equation, which is a formal result of the diagrammatic perturbation expansion originally developed by Feynman in the context of quantum field theory. Historically, it expresses the GF G of a system in the presence of many-body interactions, in terms of a reference GF, G_0 of a non-interacting system, and a term which is called the selfenergy, Σ. The selfenergy contains all the information about the many-body interactions, when added to the non-interacting system, at the level of the single-particle GF. The nonequilibrium steady state Dyson equation in frequency is given by

$$\underline{G}^{-1}(\omega) = \underline{G}_0^{-1}(\omega) - \underline{\Sigma}(\omega)\,. \tag{1.18}$$

1.2.1.1 Floquet GF

The method of steady state NEGF's can be conveniently generalized to the case of periodically driven systems, where the system is assumed to synchronize with the driving resulting in a periodic steady state. In this state all expectation values of the system, and thus also the GF, are periodic in time

$$\langle A(t)\rangle = \langle A(t+T)\rangle\ , \tag{1.19}$$
$$G(t,t') = G(t+T,t'+T)\,, \tag{1.20}$$

with some period T. By exploiting this, one can arrive at a formulation where the periodicity is encoded in an additional matrix structure for the Fourier transformed GF, the so-called Floquet GF[79–83],

$$\underline{G}_{mn}(\omega) = \int d(t-t')\frac{1}{T}\int_{-\frac{T}{2}}^{\frac{T}{2}} dt(\frac{t+t'}{2})e^{i(\omega+m\Omega)t-i(\omega+n\Omega)t'}\underline{G}(t,t')\,, \tag{1.21}$$

where Ω denotes the frequency corresponding to the period T. For more details, we refer to Appendix A. The important point is that the targeted periodic steady state is independent of the initial conditions such that the Keldysh formalism is applicable, with only an additional matrix structure, resulting in the Floquet-Keldysh GF $\underline{G}_{mn}(\omega)$.

1.2.2 Auxiliary master equation approach

AMEA is a numerical approach to solve nonequilibrium many-body quantum impurity problems with special emphasis on the steady state. To demonstrate the idea, we consider a Hamiltonian

$$H = H_S + H_E = H_0 + H_{\text{int}} + H_E \tag{1.22}$$

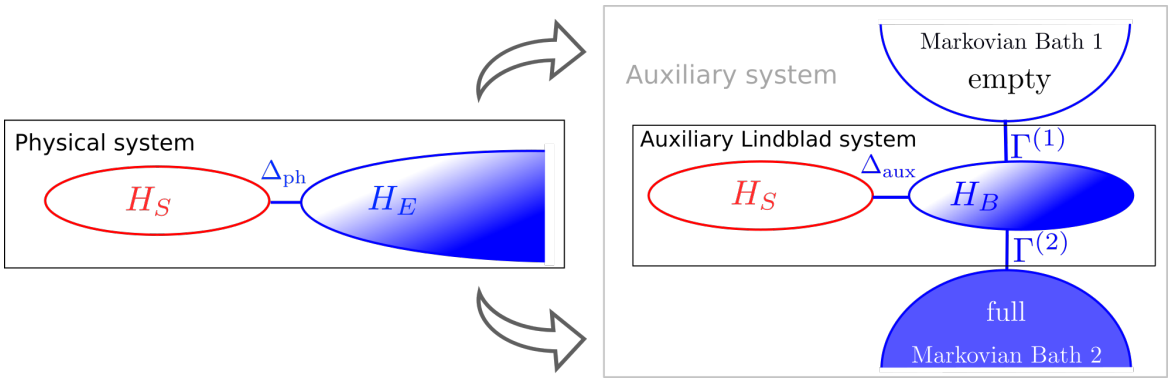

Figure 1.4: Sketch of the AMEA mapping from the infitnie physical system to the auxiliary finite open quantum system. Finite parts are sketched as closed objects and infinite parts are indicated by open ones. In the auxiliary system the two infinite Markovian baths are traced out leading to the finite auxiliary Lindblad system described by Eq.1.24-1.28.

that consists of a system part H_S, hosting possible many-body interactions, and a non-interacting and infinite environment H_E, which allows the system part to reach a nonequilibrium steady state situation. The Dyson equation for the system GF reads,

$$\underline{G}^{-1}_{\mathrm{ph}}(\omega) = \underline{g}^{-1}_{H_0}(\omega) - \underline{\Delta}_{\mathrm{ph}}(\omega) - \underline{\Sigma}_{\mathrm{ph}}(\omega) = \underline{G}^{-1}_{0,\mathrm{ph}}(\omega) - \underline{\Sigma}_{\mathrm{ph}}(\omega)\,. \tag{1.23}$$

Here, the so-called hybridization function, $\underline{\Delta}_{\mathrm{ph}}$, describes the effect of H_E on H_0 resulting in the GF $\underline{G}_{0,\mathrm{ph}}$, while $\underline{\Sigma}_{\mathrm{ph}}$ holds all information about the action of H_{int} on H_0 when the system is already coupled to the environment. Since $H_0 + H_E$ describes a non-interacting system, the corresponding GF, $\underline{G}_{0,\mathrm{ph}}$, and therefore also the hybridization function, can be solved for exactly. In contrast to the hybridization function, the determination of the selfenergy is a many-body problem and one usually has to resort to approximations.

One such approach to obtain an approximation to the selfenergy is AMEA. It relies on the fact, that the influence of H_E on H_S is uniquely determined by the hybridization function, $\underline{\Delta}_{\mathrm{ph}}$, and does not depend on the details of H_E[84]. Especially, this means that the selfenergy in Eq.(1.23) only depends on H_S and $\underline{\Delta}_{\mathrm{ph}}$. The idea of AMEA is now to replace the infinite, and thus numerically intractable, but formally closed quantum system of Eq.(1.22) with a finite but open one. In more detail, instead of coupling the system part to H_E, H_S is considered as part of a finite sized open quantum system such that it is immersed into an auxiliary bath[12] which approximates the original one, see also Fig.1.2.2.

More technically, we consider an open quantum system of Lindblad form[85] consisting of H_S plus N_B additional sites that are coupled to Markovian baths. The resulting equation of motion for the density matrix of the open quantum system, the so-called Lindblad equation, reads

$$\frac{\mathrm{d}\rho}{\mathrm{d}t} = \mathcal{L}\rho\,. \tag{1.24}$$

[12]Generically not an equilibrium one.

The Liouvillian,

$$\mathcal{L} = \mathcal{L}_{H_S} + \mathcal{L}_B = \mathcal{L}_{H_S} + \mathcal{L}_{H_B} + \mathcal{L}_{D_B}\,, \tag{1.25}$$

comprises two parts. The first is the unitary evolution, due to the system Hamiltonian H_S, which, according to the von Neumann equation, acts as

$$\mathcal{L}_{H_S}\rho = -i[H_S, \rho]\,. \tag{1.26}$$

The second term, $\mathcal{L}_B$, describes the additional N_B sites and can further be decomposed into a unitary part

$$\begin{aligned} \mathcal{L}_{H_B}\rho &= -i[H_B, \rho]\,, \\ H_B &= \sum_{i=1}^{N_B} E_{ij} c_i^\dagger c_j\,, \end{aligned} \tag{1.27}$$

and the dissipative term

$$\mathcal{L}_{D_B}\rho = 2\sum_{ij=1}^{N_B} \Gamma_{ij}^{(1)} \left(c_j \rho c_i^\dagger + \frac{1}{2}\Big\{\rho, c_i^\dagger c_j\Big\}\right) + \tag{1.28}$$

$$2\sum_{ij=1}^{N_B} \Gamma_{ij}^{(2)} \left(c_i^\dagger \rho c_j + \frac{1}{2}\Big\{\rho, c_j c_i^\dagger\Big\}\right)\,, \tag{1.29}$$

stemming from the couplings to the Markovian baths that are traced out. For the GF of H_S in the Lindblad system, we can write in analog to Eq.(1.23)

$$\underline{G}_{\text{aux}}^{-1}(\omega) = \underline{g}_{H_0}^{-1}(\omega) - \underline{\Delta}_{\text{aux}}(\omega) - \underline{\Sigma}_{\text{aux}}(\omega) = \underline{G}_{0,\text{aux}}^{-1}(\omega) - \underline{\Sigma_{\text{aux}}}(\omega)\,. \tag{1.30}$$

The free parameters in the three matrices $E, \Gamma^{(1),(2)}$, Eq.(1.27) and Eq.(1.28), are then optimized such that $\underline{\Delta}_{\text{aux}}(\omega) \approx \underline{\Delta}_{\text{ph}}(\omega)$.
Once the mapping has been performed, any quantity of H_S calculated in the auxiliary Lindblad system serves as an approximation for the one in the original physical system. Most prominently, the auxiliary selfenergy $\underline{\Sigma_{\text{aux}}}(\omega) = \underline{G}_{0,\text{aux}}^{-1}(\omega) - \underline{G}_{\text{aux}}^{-1}(\omega)$. It is important to note that the mapping to the auxiliary Lindblad system is a purely non-interacting problem concerning only $H_0 + H_E$ and it is independent of H_{int}. The many-body interactions H_{int} are then turned on to calculate properties of H_S coupled to the environment. We note that, if the solution of the auxiliary Lindblad system is performed exactly, the difference $\underline{\Delta}_{\text{aux}}(\omega) \approx \underline{\Delta}_{\text{ph}}(\omega)$ constitutes the only approximation made within AMEA. Further, the mapping can in principle be made arbitrarily accurate by increasing the number of auxiliary bath sites N_B. From now on, we will refer to the auxiliary Lindblad system simply as auxiliary system.

1.2.3 Mapping

To present the details about the mapping procedure to the auxiliary system we will consider the SIAM, where a single interacting site is in contact with an environment of independent particles. Thus, we consider an auxiliary system of size $N = N_B + 1$ where we denote the index of the physical impurity site by f. For technical details, we refer to our work [1] and references there in. The auxiliary non-interacting Green's function of the auxiliary system is given in terms of the three Lindblad matrices $\mathbf{E}, \mathbf{\Gamma}^{(1),(2)}$, here of size NxN, by

$$\begin{aligned} \mathbf{G}^R_{0,\mathrm{aux}}(\omega) &= \left[\omega - \mathbf{E} + i\left(\mathbf{\Gamma}^{(1)} + \mathbf{\Gamma}^{(2)}\right)\right]^{-1}, \\ \mathbf{G}^K_{0,\mathrm{aux}}(\omega) &= 2i\mathbf{G}^R_{0,\mathrm{aux}}(\omega)\left(\mathbf{\Gamma}^{(2)} - \mathbf{\Gamma}^{(1)}\right)\mathbf{G}^A_{0,\mathrm{aux}}(\omega), \end{aligned} \tag{1.31}$$

The hybridization function at the impurity is subsequently obtained as

$$\Delta^R_{\mathrm{aux}}(\omega) = 1/g^R_{0,ff}(\omega) - 1/G^R_{0,\mathrm{aux},ff}(\omega), \tag{1.32}$$

$$\Delta^K_{\mathrm{aux}}(\omega) = G^K_{0,\mathrm{aux},ff}(\omega)/\left|G^R_{0,\mathrm{aux},ff}(\omega)\right|. \tag{1.33}$$

where $g^R_{0,ff}$ is the Green's function of the isolated impurity site. With a suitable chosen cost-function $\chi(\vec{x})$ of the following form,

$$\chi^2(\vec{x}) = \int d\omega \left\| \underline{\Delta}_{\mathrm{aux}}(\omega) - \underline{\Delta}_{\mathrm{ph}}(\omega) \right\|^2, \tag{1.34}$$

where $\vec{x}$ is the collection of all free parameters in the Lindblad matrices, Eq.1.31-1.32 are turned into a (potentially high-dimensional) non-convex optimization problem. Detailed expressions can be found in [1, 2]. In [1] it was found that the value of the cost-function typically reduces quadratically on a logarithmic scale, $\ln \chi \sim -N_B^2$, when the system size is increased. However, this is possibly only true if the global optima are found for a given N_B, which becomes very hard for bigger systems $N_B \gtrsim 6$. For practical purposes it is sufficient to find local minima that maintain a constant exponential decrease of the cost-function, since this equips AMEA overall with an exponential convergence with respect to N_B. We will refer to such minima as good minima.

1.2.3.1 Auxiliary geometries and parameterization

In general[85], the three Lindblad matrices $\mathbf{E}, \mathbf{\Gamma}^{(1),(2)}$ are hermitian matrices where $\mathbf{\Gamma}^{(1),(2)}$ must be PSD and $\Gamma_{if} = \Gamma_{fj} = 0$ such that the impurity is not directly coupled to the Markovian baths. Originally[42, 84], the Lindblad matrices were considered to be real $E_{ij}, \Gamma^{(1)(2)}_{ij} \in \mathbb{R}$. However, due to the freedom to rotate the bath sites, $i \neq f$, which leaves the hybridization, Eq.1.32, unchanged, only one of the three matrices can be chosen tridiagonal, real and symmetric[13], in general. Considering all fitting parameters to be real is a restriction on the parameter space and in [1] we found that better minima are obtained when allowing for imaginary parts as well. A convenient choice is to consider $\mathbf{E}$ of sparse

[13] For instance by the Householder algorithm [86]

form and leave $\mathbf{\Gamma}^{(1),(2)}$ general. $\mathbf{E}$ then has $2N_B$ independent non-zero entries and can be directly parametrized. Here and in the following, we will always consider the general, non particle-hole symmetric case, when quoting the number of fit parameters for a given system size.

The parametrization of the Lindblad couplings turns out to be more involved, due the condition of being PSD and even restrictions have proven to be effective. For notational simplicity, we will omit the superscripts of the Γ-matrices in the following.

Parametrising a Γ-matrix The straight forward way without imposing restrictions is to parametrize $\mathbf{\Gamma}$ as the square of a hermitian matrix $\mathbf{M}$,

$$\mathbf{\Gamma} = \mathbf{M}^\dagger \mathbf{M}\,, \text{with} \quad M_{if} = M_{fj} = 0\,, \tag{1.35}$$

which ensures that $\mathbf{\Gamma}$ is hermitian and PSD. However, this parametrization is not unique, since $\tilde{\mathbf{M}} = \mathbf{U}\mathbf{M}$ with $\mathbf{U}^\dagger\mathbf{U} = \mathbb{1}$ leaves Eq. (1.35) invariant. Thus, this choice introduces redundancies in the fit parameters and, in general, makes optimization algorithms less effective.
Based on the empirical observation that the Γ-matrices of obtained minima usually show a low rank, we have recently employed also a variable-rank parametrization[2] of the form

$$\mathbf{\Gamma} = \gamma\gamma^\dagger\,, \quad \gamma = (\vec{\gamma}_1, ..., \vec{\gamma}_{\text{rank}_\Gamma})\,. \tag{1.36}$$

This has the advantage that the parameter space of the optimization problem is drastically decreased and can be systematically increased by adding vectors to γ.
Another alternative would be to restrict to the case that the $\mathbf{\Gamma}$-matrix has only a single eigenvalue that is zero, stemming from $\Gamma_{if} = \Gamma_{fj} = 0$, and the others are strictly positive. This can be realized with the Cholesky decomposition similar to Eq.(1.35), but with a lower triangular matrix $\mathbf{L}$ instead of $\mathbf{M}$ with real diagonal entries $L_{ii} > 0$, $i \neq f$. This results in an unique parametrization. However, in view of the empirical observation that good or global minima usually have low rank and the Cholesky decomposition excludes exactly these minima from the parameter space, it is probably inferior to the variable-rank approach, Eq.(1.36).

As a general note, a unique parametrization of a PSD matrix, either directly, or via a linear relation such as above, is mathematically impossible due to the non-trivial topology of the space of PSD matrices of rank $r > 1$. A unique parametrization of a PSD matrix can be found using so-called quotient spaces[87, 88]. Since the parametrizations mentioned above have proven to be effective enough for the considered applications and the concept of quotient spaces is mathematically advanced and not straight forwardly implemented numerically, we did not pursue this route.

1.2.3.2 Optimization algorithm

Once, we have parametrized our three Lindblad matrices, we need an optimization algorithm to find good minima. The cost-functions arising within AMEA typically show a

landscape with many local minima and reliably finding the global one or good ones is a formidable task for increasing system size. In the works [16, 17, 42, 89] a PT approach, details presented in[43, 1], was used together with the parametrization, Eq.(1.35), as optimization routine. PT obtains minima by exploring the parameter space in a stochastic manner, it is able to overcome local minima and possibly finds the global optimum. It is thus especially useful in problems with many local minima. Due to its nature, however, the PT approach gets increasingly inefficient with the dimension of the parameter space and does not find good minima anymore for $\dim_{\vec{x}} \gtrsim 100$, even if the program is run for several days[14].

One way, to overcome this so-called curse of dimensionality is to use gradient based optimizations, which follow a certain path in parameter space, until they reach a local minimum. Naturally, these approaches typically do not reach the global optimum and are very starting point dependent. In particular, we tested the Adam algorithm[90] implemented within the python library tensorflow[91], which is an optimization routine from machine-learning tailored to find local minima in very high dimensional problems. With respect to other implementations of gradient based techniques, the gradient does not need to be supplied by hand, but tensorflow internally keeps track of the derivations[15]. Unfortunately, when applied directly with the full parametrization from Eq.(1.35), this approach was not performing well with respect to the obtained minima. It was found that progress can be made by changing the parametrization to the variable-rank parametrization, Eq.(1.36), which has proven to be effective upon increasing the rank and system size in a consecutive manner while straight forwardly trying random starting points at a given system size and rank was found to be inefficient.

In more detail, for a given physical hybridization and corresponding cost-function, we start by finding an optimum of the $N = 3$ system. The latter can be obtained by PT or by running Adam with several random starting points, which usually confirms the minimum found by PT[16]. With the found minima in the variable-rank parametrization, usually featuring Γ-matrices of rank one, we perform the following iterations.

- Increase the system size, $N_B = N_B + 1$, and optimize.
- Increase the rank, $\text{rank}_\Gamma = \text{rank}_\Gamma + 1$, by adding a vector to γ and optimize.
- Iterate increasing the rank until the cost-function does not show a significant decrease. Return to increasing the system size.
- Terminate if target system size is reached or if increasing the system size does not yield a significant decrease in the cost-function.

[14] on a cluster node with sixteen cores

[15] There is no numerical finite difference method involved, it is handled exactly like in symbolic languages.

[16] Although the parametrization in this cases is different, they can be compared by the resulting auxiliary hybridization, and the PT result can be translated to the variable-rank parametrization by solving the eigenvalue problem of Γ obtained by PT and keeping only the dominant eigenvector(s). Generally, there is only one for $N = 3$.

Here, new parameters are always initialized randomly[17] and optimizations are always done with respect to all parameters. With this new optimization approach, we were able to reliably[18] find good minima up to system sizes $N = 10$ with $\dim_{\vec{x}} \approx 100$. In comparison, the full parametrization from Eq.(1.35) would feature $\dim_{\vec{x}} = 180$ parameters.
Thus, also the gradient based approach fails for $\dim_{\vec{x}} \gtrsim 100$ and the key to reach system sizes up to $N_B \approx 10$ is the reduced dimensionality, due to the variable-rank parametrization. This suggests that the variable-rank parametrization would also increase the applicability of PT up to similar system sizes. However, the latter was not tested since the gradient approach in the tensorflow implementation is far superior to the PT approach with respect to the computational resources. This makes the variable-rank parametrization together with the Adam optimization the current method of choice.

1.2.4 Extrapolation to zero cost-function

The accuracy of AMEA can be systematically increased by increasing the auxiliary system size. It is then natural to ask if this systematic can be used to extrapolate results obtained with AMEA to infinite auxiliary system size. In Sec.1.2.3 a cost-function was introduced to optimize the mapping from the physical to the auxiliary system needed within AMEA and formally an infinite system size corresponds to zero cost-function. Within AMEA an extrapolation in system size is thus equivalent to an extrapolation to lower cost-functions. Assuming that the expectation value of an operator, $\langle A\rangle \equiv A$, calculated within the auxiliary system, corresponding to some value of the cost-function χ, is an analytic function of the latter, $A = A(\chi)$, we can expand this function as a Taylor series,

$$A(\tilde{\chi}) = A(\tilde{\chi} = 0) + k_A\tilde{\chi} + O(\tilde{\chi}^2)\,, \quad \tilde{\chi}(\vec{x}) = \chi(\vec{x})/\chi_0\,, \tag{1.37}$$

where we have introduced a normalized cost-function $\tilde{\chi}$ as a meaningful extrapolation parameter. A sensible choice is $\chi_0 = \chi\big|_{\underline{\Delta}_{\text{aux}=0}}$ which turns the normalized cost-function $\tilde{\chi}$ into a measure for the relative deviation from the physical situation.
Since $\tilde{\chi} = 0$ formally represents the physical situation, we have $A(\tilde{\chi} = 0) = A_{\text{ph}}$, where A_{ph} is the value of the desired expectation value in the physical system. Thus, collecting the cost-functions and expectation values for different system sizes yields a series of value pairs $\{\tilde{\chi}_N, A(\tilde{\chi}_N)\}$ and A_{ph} can be obtained by extrapolating these data points linearly to the $\tilde{\chi} = 0$ limit in the $(\tilde{\chi}, A)$-plane.
In [2], we have tested this extrapolation scheme and found that it significantly improves the results. More specifically, the linear fit was performed by minimizing the summed squared error and no error estimation was performed.

1.2.4.1 Error estimation

Here, we want to complement the benchmark in [2] by discussing how error estimates can be obtained and presenting corresponding results. We will assume that an expectation

[17] Initializing them with zeros would lead to zero gradient in the new directions.
[18] Due to the severe starting point dependence of the approach good minima are obtained occasionally.

value of the auxiliary system is affected by some statistical error, like in the SWF algorithm, see Sec.1.2.5, and that higher order terms in the Taylor expansion can be neglected. An individual data point has two sources of errors, a statistical and a systematic one. The systematic error, $\Delta^{\text{sys}}_{A(\chi)}$, is introduced by the AMEA mapping itself and stems from the fact that qualitatively different fits[19] with similar cost-functions can lead to a variety of expectation values. Thus, the corresponding scattering of expectation values does not follow a statistical distribution. To make progress, however, we will assume a Gaussian distribution. Since finding such a collection of qualitatively different minima is troublesome in practice and the corresponding evaluation of expectation values leads to additionally needed many-body solutions, a straight forward determination of the systematic error is impractical.

A very simple approach to obtain an estimate for the systematic error is to use the fact that we can interpret the normalized cost-function as a measure for the relative error from the physical situation and approximate

$$\Delta^{\text{sys}}_{A(\tilde{\chi})} = \tilde{\chi}\left|A(\tilde{\chi})\right|. \tag{1.38}$$

Combining this with the statistical error, $\Delta^{(\text{stat})}_{A(\tilde{\chi})}$ originating from the stochastic solution of the auxiliary system, we can get an estimate for the overall error of the data point by

$$\Delta_{A(\tilde{\chi})} = \sqrt{\left(\Delta^{(\text{sys})}_{A(\tilde{\chi})}\right)^2 + \left(\Delta^{(\text{stat})}_{A(\tilde{\chi})}\right)^2}. \tag{1.39}$$

To get the final estimates for the two free fit parameters of the linear relationship, Eq.(1.37), and the corresponding errors, we employ Bayesian probability theory[92] assuming a Gaussian noise and a flat prior.
In short, a so called posterior distribution is constructed as product over the individual Gaussian distributions of the data points[20] and the parameters as well as error estimates obtained by considering the first and second moment of the posterior distribution with respect to the two parameters. In view of this approach, the results in Ref.[2] are given by the maximum of the posterior distribution, which must not coincide with the average values calculated in the Bayesian approach.

In Fig.1.2.4.1, we present results where the above error estimation scheme is applied to the steady state current in the IRLM. We see that overall the results of Ref.[2] are within one sigma of the new ones, which show a trend to lower values for $J' = 0.5$. Since finite temperature in this model reduces the current, a tentative interpretation of this systematic deviation is that the finite temperature of $T = 0.025$ is more faithfully reproduced in the new results. The data points at small voltages for $J' = 0.2$ constitute exceptions, where the difference of the two approaches yields significantly different results. This is, because these points are very sensitive to uncertainties as discussed in [2].

[19]Fits showing significant deviations in different ω-regions.

[20]To be precise, the product of the individual distributions must be divided by the prior, which is ,however, assumed to be flat and therefore does not influence the result.

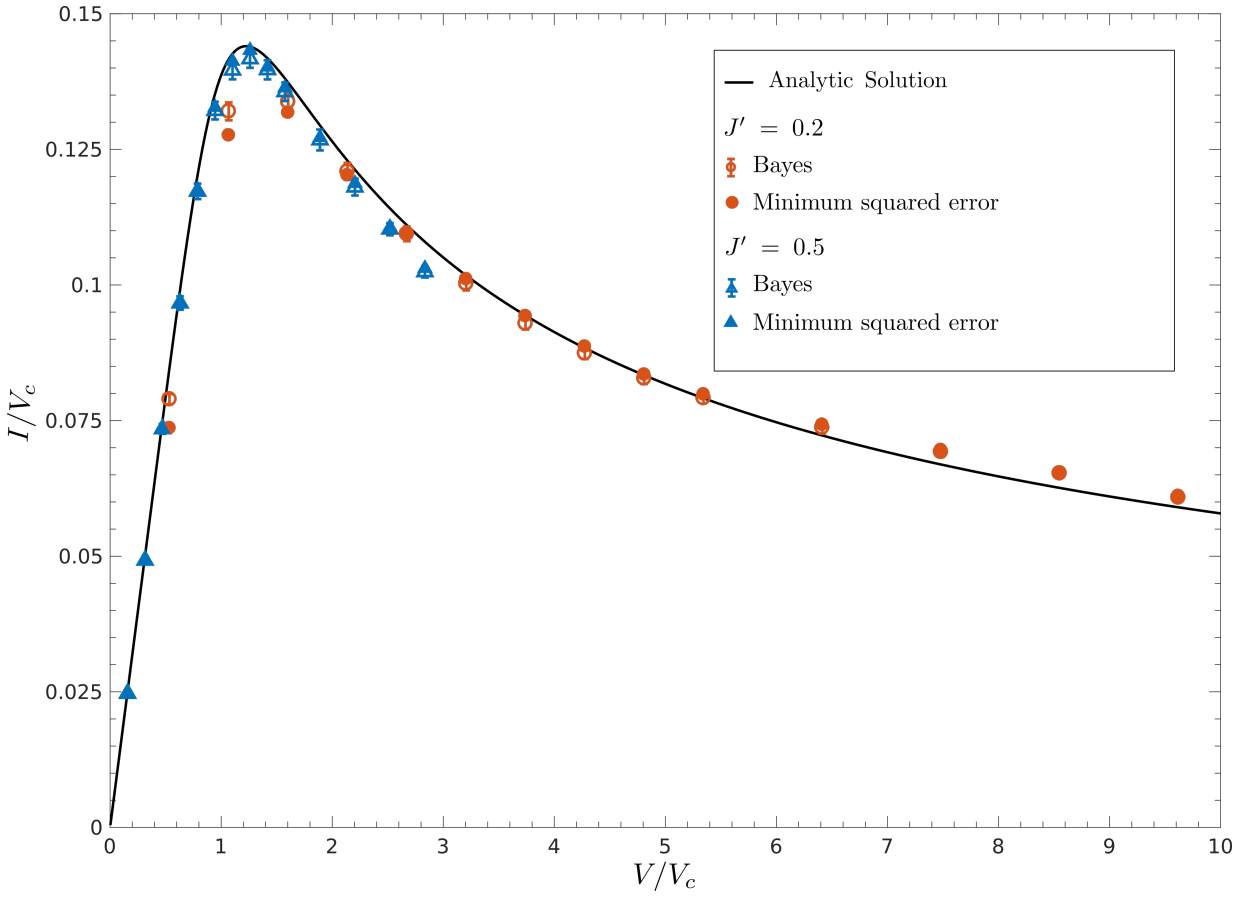

Figure 1.5: The steady state current in the IRLM. Compared are the extrapolated values from AMEA at $T = 0.025$, obtained by minimizing the summed squared error (filled symbols) and by taking the individual errors into account with Bayesian probability theory (open symbols with error bars). The solid black line shows the analytic reference solution at $T = 0$. For further parameters we refer to our work[2].

1.2.5 Stochastic wave-functions

After the mapping to the auxiliary system has been performed, the resulting many-body Lindblad problem has to be solved. Previously, this was done by using SF [93], which maps the super-operator problem for the density matrix to a standard operator problem with twice as many sites, where the density matrix is represented as a state vector. The standard operator problem can be treated by standard numerical many-body approaches such as ED[42] and MPS[16] that where successfully applied. An alternative approach to SF are so-called SWF's[94–96], also referred to as quantum jumps.

In the context of open quantum systems, the SWF algorithm unravels the (classical) stochastics encoded in the density matrix into a probability distribution for the wave-functions. Since this method is formulated entirely in terms of wave-functions, it has the inherent advantage that the Hilbert space of our many-body system does not need to be squared in comparison to SF. For an open quantum system of Lindblad form this probability distribution of wave-functions can be sampled according to the algorithm summarized in [2]. In short, an initial wave-function $|\psi_0\rangle$ is evolved in time by performing a deterministic time-evolution, according to an non-hermitian Hamiltonian H_{eff}, which is interrupted by random jumps.

For a normalized initial state $|\psi_0\rangle$, the survival probability of the deterministic time evolution up to time t, where a jump needs to be performed, is given by its norm,

$$S(t|\psi_0) = \left\| e^{-iH_{\text{eff}}t}\psi_0 \right\|^2, \tag{1.40}$$

which is exponentially decreasing, since the non hermitian part of H_{eff} is given by the Γ-matrices which are PSD. Sampling the corresponding probability distribution by inversion leads to the algorithm used in Ref.[2] where a random number $r_j \in (0.1)$ is drawn from a uniform distribution and the initial state evolved until a time t_j, that fulfills $\|\psi(t_j)\|^2 = r_j$.

1.2.5.1 Fixed time-stepping in the SWF algorithm within ED

In Ref.[2] we presented the SWF algorithm to solve the many-body problem within AMEA. Here, we want to complement this by some further details. Within the current implementation we are working on a fixed time-grid such that measurements are done at multiples of a time interval Δt, as is convenient for the calculation of a GF[21].

Fig.1.2.5.1 shows a sketch of a possible time-evolution of the norm and the fixed time-grid, on which we want to measure. In ED we use the Arnoldi scheme to set up a Krylovspace representation of the Hamiltonian valid up to a certain end time. For more details, we refer to Sec.2.2.2.1 of Ref.[43]. In the following, we will denote the Krylovspace corresponding to a starting vector[22] $|\psi_0\rangle$ and valid up to a time $t_{\max}$ as $\mathcal{K}_{\psi_0}^{t_{\max}}$ and a time evolved state up to time $t < t_{\max}$ with respect to this Krylovspace as $|\psi(t)\rangle_{\mathcal{K}_{\psi_0}^{t_{\max}}}$. Further,

[21] For sampling a steady state expectation value other choices are possible, since all times are equal in the steady state

[22] here $|\psi_0\rangle$ is in general not normalized

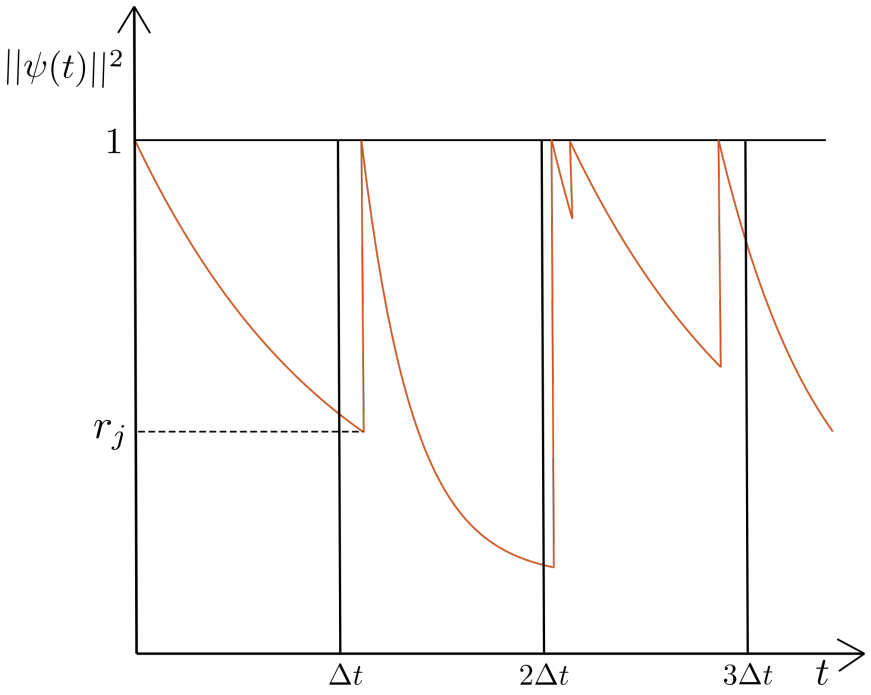

Figure 1.6: Sketch of the norm for a possible realization of the time dependent wavefunction $|\psi(t)\rangle$. Multiple jumps are possible within a time step Δt. The discontinuous jump back to $\|\psi(t_j)\|^2 = 1$ corresponds to a jump in the SWF algorithm, where it is restarted with a normalized state.

the norm at $t_{\max}$ is obtained, without much effort, when setting up the Krylov space $\mathcal{K}_{\psi_0}^{t_{\max}}$. A single time-step of length Δt from $|\psi_0\rangle$ to $|\psi\rangle$ is performed following the pseudo code in Algorithm 1.

Algorithm 1 Perform a time step Δt

$|\psi_0\rangle, r_j, \Delta t \leftarrow$ initial values
$\mathcal{K} = \mathcal{K}_{\psi_0}^{\Delta t}$
if $\|\psi(\Delta t)\|_{\mathcal{K}}^2 \geq r_j$ **then**
    $|\psi\rangle = |\psi(\Delta t)\rangle_{\mathcal{K}}$
else
    ontime = False, $dt = \Delta t$
    while ! ontime **do**
        $t_j^{\text{guess}} = \frac{(\|\psi_0\|^2 - r_j)dt}{\|\psi_0\|^2 - \|\psi(\Delta t)\|^2} \leftarrow$ initial value for Newton
        $t_j =$ find jump time$(\mathcal{K}, t_j^{\text{guess}}) \leftarrow$ perform a root search with the Newton method
        $dt = dt - t_j$
        $|\psi_0\rangle =$ do jump$(|\psi(t_j)\rangle_{\mathcal{K}})$
        $r_j =$ random $\in [0, 1]$
        $\mathcal{K} = \mathcal{K}_{\psi_0}^{dt}$
        if $\|\psi(dt)\|_{\mathcal{K}}^2 \geq r_j$ **then**
            $|\psi\rangle = |\psi(dt)\rangle_{\mathcal{K}}$
            ontime = True
        end if
    end while
end if

1.2.6 AMEA as impurity solver in Floquet DMFT

In Refs.[23, 3, 97, 98] AMEA was used as impurity solver within nonequilibrium steady state DMFT where the solution of a lattice problem is mapped onto solving a self-consistently determined quantum impurity problem. The latter is defined by its hybridization function

$$\underline{\Delta}(\omega) = \underline{g}_{\text{imp}}^{-1}(\omega) - \underline{G}_{loc}^{-1}(\omega) - \underline{\Sigma}(\omega)\,, \tag{1.41}$$

where $\underline{G}_{loc}$ denotes the local GF of the lattice problem and $\underline{g}_{\text{imp}}$ is the GF of the isolated impurity, see also section III D in Ref.[5] which is attached below, Sec.2.2, for a quick overview of the DMFT equations. The resulting impurity problem can be treated straight forward by AMEA as presented above.

Currently used implementation of AMEA as impurity solver, SF+ED: Within DMFT the impurity problem needs to be solved multiple times for an arbitrary hybridization. Currently, only the SF+ED implementation of AMEA is automated enough for

being used as a "black-box" impurity solver. In more detail, the fit is performed by PT, the steady state is obtained by time-evolution with the Arnoldi method and the GF is directly determined in frequency by Bi-Lanczos, see Ref.[43] for details.

The Floquet impurity problem: When studying periodically driven lattice systems, the GF is generalized to the Floquet-Keldysh GF, Eq.(1.21), which encodes the periodic time-dependence in an additional Floquet matrix structure. Naturally, the hybridization function arising from the Floquet DMFT equations shares this structure. In more detail, the hybridization function becomes

$$\underline{\Delta}_{mn}(\omega) = \underline{g}^{-1}_{\mathrm{imp},mn}(\omega) - \underline{G}^{-1}_{loc,mn}(\omega) - \underline{\Sigma}_{mn}(\omega)\,, \tag{1.42}$$

where the indices mn indicate the Floquet structure, and g^{-1}_{mn} denotes the matrix entry of the inverse GF. Thus, the bath of the Floquet impurity problem is perdiocially time-dependent which limits the available impurity solvers. In principle one can employ any impurity solvers developed for time-dependent DMFT since they are able to cope with a general time-dependence of the bath $\underline{\Delta}(t,t')$. However, non-perturbative approaches, such as Continuous-time quantum Monte Carlo[99, 100], are limited in the simulation time and cannot reliably reach the steady state. This limits the available options to impurity solvers of perturbative nature such as IPT[19, 101–105] and the NCA[36, 38, 106], which are naturally applicable only in a certain parameter regime.

1.2.6.1 AMEA in Floquet DMFT

At present, the implemented SF+ED impurity solver as described above is not applicable to the Floquet impurity problem. First, the current form of the Liovillian, Eq.(1.25)-(1.28), is not able to accomodate a time periodic bath. For this, the Lindblad matrices $\mathbf{E}, \mathbf{\Gamma}^{(1),(2)}$ would need to be made time dependent and a periodic bath would be described by

$$\mathbf{E}(t) = \sum_n \mathbf{E}_n e^{-in\Omega t}, \mathbf{\Gamma}^{(1),(2)}(t) = \sum_n \mathbf{\Gamma}^{(1),(2)}_n e^{-in\Omega t}\,, \tag{1.43}$$

where Ω denotes the frequency corresponding to the considered periodicity. Next, the resulting non-interacting Lindblad problem needs to be solved for the Floquet GF of the auxiliary system to obtain the Floquet version of Eq.(1.31), $\underline{G}_{0,\mathrm{aux},mn}$ from which the auxiliary Floquet hybridization $\underline{\Delta}_{\mathrm{aux},mn}$ is obtained straight forward, similar so Eq.(1.32). With a suitable cost-function, respecting also the off-diagonal entries of the Floquet hybridization, the optimization problem for the AMEA mapping is formulated. However, due to Eq.(1.43) the number of fit parameters is multiplied by the number of considered modes and it is questionable, if one is able to obtain good minima, see Sec.1.2.3.2. In contrast to the problems arising in the mapping to the auxiliary system, the many-body solution should be adapted easily calculating the GF by time-evolution with Arnoldi which is already implemented in the search for the steady state.
Due to the complications in the mapping, in our work [5] we followed a different approach

and introduced an approximation within Floquet DMFT which we termed FDSA. The main idea is to exploit the fact that the Floquet formalism can be seen in analog to Bloch theory with a periodicity in time instead of space. We can thus reuse the original DMFT approximation in the time domain and make the selfenergy not only diagonal in spatial indices, which constitutes the orginal DMFT approximation, but also diagonal in Floquet indices. For the technical details, we again refer to section III D in Ref.[5] which is attached below, Sec.2.2. The main point is that the resulting hybridization, like the selfenergy[23], becomes time-translation invariant leading to a standard nonequilibrium steady state impurity problem. From a numerical point of view, the latter is a tremendous simplification, however the convergence of the DMFT self-consistency is generally slower and can become problematic. This is because the impurity problem has no explicit knowledge of the driving frequency Ω, which there only enters through the changing hybridization in the DMFT cycle.

1.2.6.2 FDSA in the Mott regime: AMEA, IPT and NCA

In Ref.[5], we presented a test of the validity of the FDSA in the context of the electric field driven dissipative Hubbard model for intermediate interaction strengths by employing IPT as impurity solver, which allowed a self-consistent comparison of the FDSA versus full Floquet DMFT. Here, we complement this by focusing on the Mott regime and present a comparison of AMEA+FDSA with the NCA[24]. At this point, we want to acknowledge that this method comparison was performed in collaboration with Yuta Murakami from the Group of Phillip Werner, who performed all calculations with the NCA and IPT.
We consider the single-band Hubbard model on a hypercubic lattice in the limit of infinite dimensions. The model is driven by a time-periodic electric field, $E(t) = E\sin(\Omega t)$, which modifies the hopping,

$$v(t) = v_0 e^{-\frac{E}{\Omega}t}, \quad , \tag{1.44}$$

where the bare hopping v_0 serves as unit of energy. The driving is balanced by dissipative bath chains, described by a semi-circular density of states at a fixed inverse temperature β, attached to every lattice site. This leads to a local hybridization,

$$\Gamma^R(\omega) = \frac{g}{W}\sqrt{1-\left(\frac{\omega}{W}\right)^2}, \tag{1.45}$$

parametrized by the half-bandwidth W and the dissipation strength g. For further details of the model we refer to Ref.[37].
For such an AC field, the small parameter controlling the validity of the FDSA is[5] $\alpha = \frac{vE}{\Omega^2}$.

[23] An object which is diagonal in Floquet indices is time-translation invariant and depends only on the time difference. This is most easily seen from Eq.A.13. Thus, $\Sigma(t,t') = \Sigma(t-t')$ as in a steady state situation.

[24] While the NCA, in analogy to IPT, would in principle allow to test the FDSA in a self-consistent manner, we were not able to converge the DMFT self consistency within the FDSA when employing the NCA as impurity solver.

Due to the inverse dependence on the squared driving frequency, we expect the FDSA to work very well around resonant frequencies $\Omega = U$ in the Mott regime[25].

IPT in the Mott regime: Fig.1.7 shows the local and time-averaged density of states, $A(\omega)$, as well as the effective local distribution function[26] $\tilde{f}(\omega)$ obtained by employing IPT as impurity solver with and without the FDSA. We consider two different driving frequencies, $\Omega = \{4, 6\}$ and electric field strengths $E \in [0.4 - 6.0]$ leading to $\alpha_{\Omega=4} \in [0.025, 0.375]$, $\alpha_{\Omega=6} \in [0.0\dot{1}, 0.1\dot{6}]$. We see that the density of states is in perfect agreement up to $\alpha \approx 0.2$, afterwards differences, albeit negligible, become visible. The effective distribution function behaves similarly for frequencies with significant spectral weight and shows differences at higher frequencies. In fig. 1.8, the highly suppressed Floquet-sidebands are plotted. The figure shows that they are also well reproduced within the FDSA. Quantitative differences are observed for the effective distribution function within the Floquet-sidebands. They are insignificant, due to the negligible spectral weight for the considered parameters, but become important for pronounced Floquet-sidebands, which marks the end of the applicability of the FDSA.

The fact that the Floquet-sidebands and their effective occupation are well reproduced within the FDSA is quite noticeable, however their existence even in the FDSA is readily explained by the structure of the Floquet Dyson equation for the lattice GF, which for the present case within the FDSA and for the retarded component reads

$$\begin{aligned} G^{R,-1}_{mn}(\omega, k) &= \omega_n \delta_{mn} - \varepsilon_{m-n}(k) - \left[\Gamma(\omega_n) + \Sigma(\omega_n)\right] \delta_{mn} \,, \\ \omega_n &\equiv \omega + n\Omega \,, \end{aligned} \tag{1.46}$$

where the coupling of the Floquet blocks through the dispersion relation $\varepsilon_{m-n}(k)$ is independent of the omega dependence. Because of this, the Floquet GF does allow a separation in analog to non-interacting electrons[34] as $G^{R,-1}(\omega, k) = \Lambda(k) Q^{-1}(\omega) \Lambda^\dagger(k)$, with unitary $\Lambda(k)$ from Ref.[34] Eq.(15), and $Q^{-1}_{mn}(\omega) = \left[\omega_n - \varepsilon_0(k) - \Gamma(\omega_n) - \Sigma(\omega_n)\right] \delta_{mn}$. Thus, we can write the 00 component of the Floquet GF, analog to Ref.[34] Eq.(33), in the FDSA in the form

$$G^R_{00}(\omega, k) = \sum_n \frac{1}{\omega_n - \varepsilon_0(k) - \Gamma(\omega_n) - \Sigma(\omega_n)} \mathcal{F}_n(k) \,, \tag{1.47}$$

where we have put the multiplicative k dependence in a set of general functions $\mathcal{F}_n(k)$. For no periodic drive the selfenergy, $\Sigma(\omega)$, when plugged into the steady state Dyson equation leads to some steady state density of states. From Eq.(1.47), we see that the time averaged Floquet GF features copies of this steady state density of states with renormalized dispersion relation at integer multiplies of the driving frequencies, i.e. the observed Floquet sidebands in Fig.1.8.

[25] As usual, we denote the Hubbard interaction parameter as U.

[26] defined in equivalence to the fluctuation-dissipation theorem Eq.(1.16).

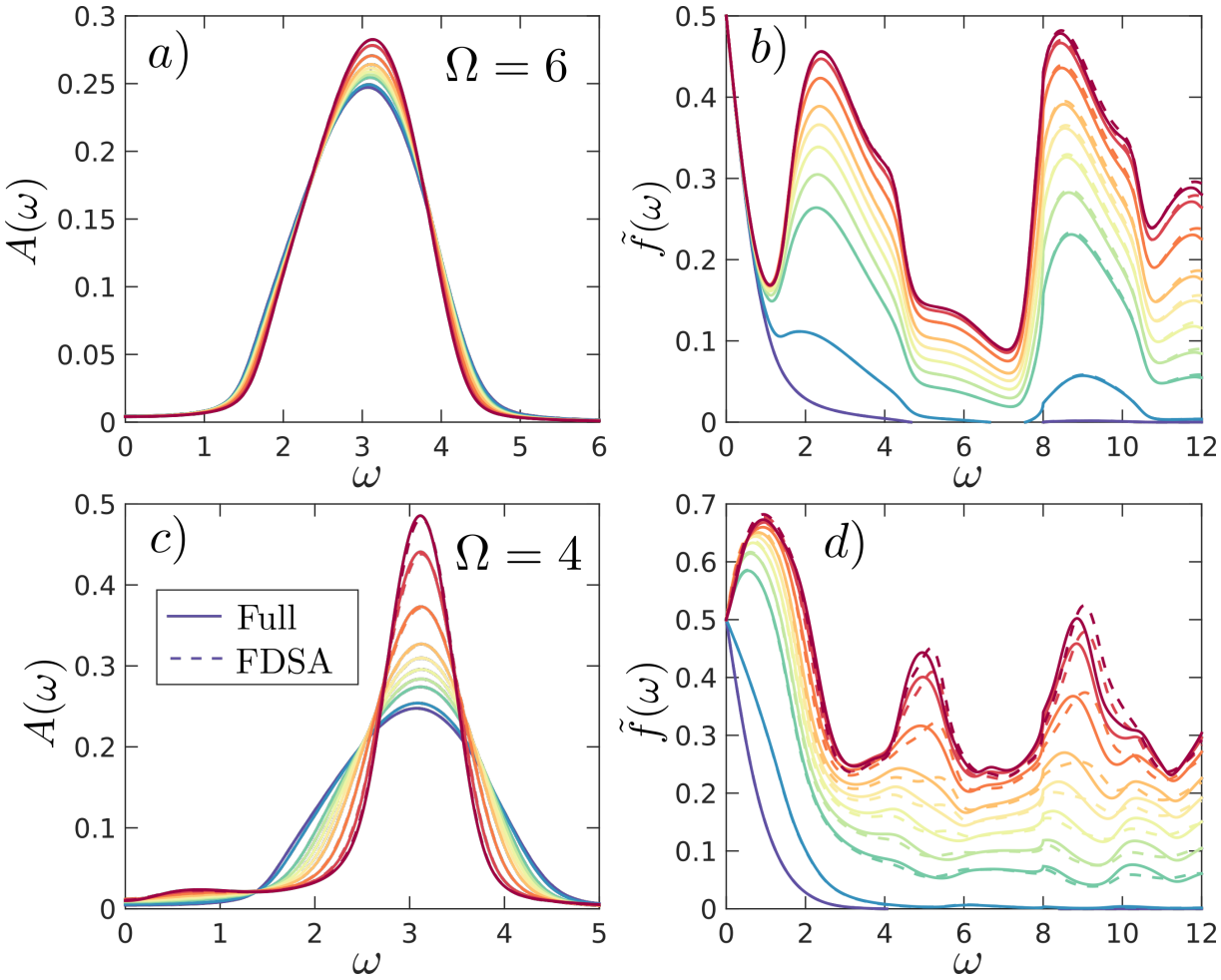

Figure 1.7: Comparison of the local time-averaged density of states, $A(\omega)$, and effective distribution function, $\tilde{f}(\omega)$, obtained by the FDSA (solid lines) and full Floquet DMFT (dashed lines) within IPT. The different colors denote different electric field strengths $E = (0.4, 1.2, 2.4, 3.2, 4.0, 4.8, 6.0)$. Top(Bottom) panels for $\Omega = 6(4)$ corresponding to $\alpha_{\Omega=4} = (0.025, 0.075, 0.15, 0.2, 0.25.0.3, 0.375)$ and $\alpha_{\Omega=6} = (0.0\dot{1}, 0.0\dot{6}, 0.0\dot{7}, 0.1, 0.1\dot{3}, 0.1\dot{6})$. Other parameters are $U = 6$, $\beta = 2$, half-bandwidth of the bath $W = 8$ and the dissipation strength $g = 0.03$. Due to particle-hole symmetry, we show only positive frequencies. Note the different range of the frequency axis for $\tilde{f}(\omega)$ to show the occupation in the Floquet sidebands presented in Fig.1.8.

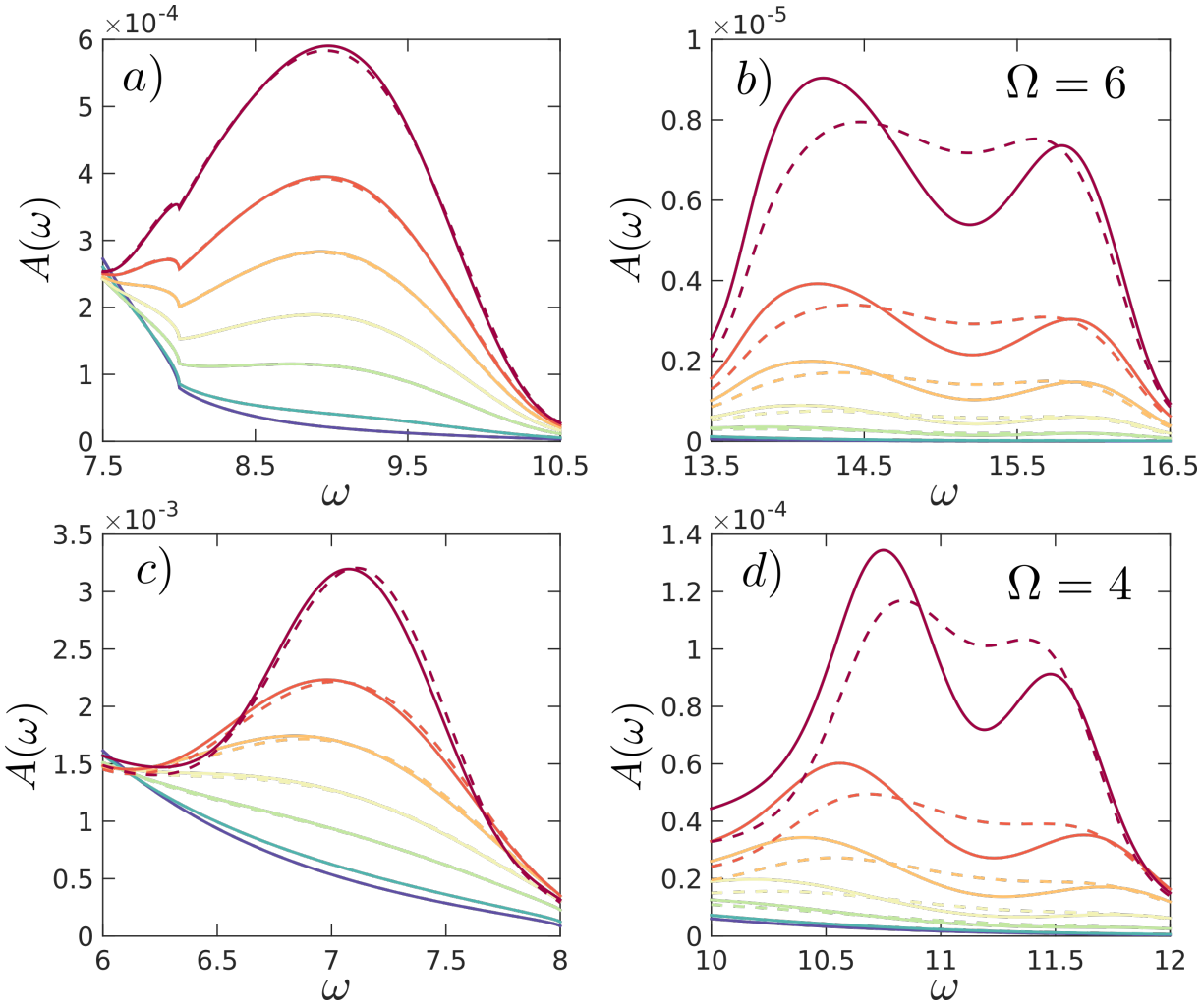

Figure 1.8: The Floquet sidebands corresponding to Fig.1.7. The sharp feature around $\omega = 8$ in panel a) is due to the band-edge of the bath, Eq.(1.45).

AMEA+FDSA vs. NCA: Here, we compare the developed AMEA+FDSA approach against Floquet DMFT within the NCA, which is known to be reliable in the Mott regime of the Hubbard Model[106]. In contrast to the previous test, where any deviation between the results can be ascribed to the FDSA, in the present case, there are multiple sources. First, there is the difference in the impurity solvers, which would lead to deviations even in the standard steady state or equilibrium. For instance, the NCA is known to overestimate the insulating state while AMEA typically underestimates the latter[27]. However it should be noted that both impurity solvers make approximations on the level of the hybridization and not the interaction. In addition, the accuracy of AMEA tends to vary for different electric field strengths depending on the performance of the AMEA fit. Finally, there are again differences induced by the FDSA, which is not used for the NCA results. To keep the latter under control, we consider parameters, where we can expect the errors induced by the FDSA to be negligible to focus on a comparison of the impurity solvers within the context of a periodically driven Mott insulator.
In more detail, we consider the same model and parameters as used above, Fig.1.7, with the restriction to the resonant driving frequency $\Omega = 6$ and all AMEA results are obtained with six auxiliary bath sites. From Fig.1.9a, we see that the Hubbard band agrees well within the two approaches, with the expected trend of a more pronounced gap in the NCA results. More pronounced deviations are visible for the highest two considered electric field strengths and bigger relative differences are observed in the Floquet sideband, Fig.1.9b, which is more pronounced in the NCA. Interestingly, the sharp feature due to the bandedge of the dissipative bath, $\Gamma(\omega)$, at $\omega = 8$ present in the AMEA and IPT results is completely smeared in the NCA.
Looking at the AMEA fits, Fig.1.10, we observe that the sideband in the hybridization is resolved for the highest two electric fields. As a tradeoff for those cases, the hybridization around the Hubbard band and the distribution function is less accurately described by the auxiliary system explaining especially the differences at the top of the Hubbard band in Fig.1.9a. From Fig.1.9c, we observe qualitative agreement in the effective distribution with bigger differences again for the highest two electric fields and artificial oscillations in the AMEA results for smaller electric fields induced by oscillations in the auxiliary effective distribution function[28]. Further, the fact that the occupation in the Floquet sideband, which is poorly represented in the auxiliary system, is in good agreement between NCA and AMEA shows that the latter occupation is dominated by the Floquet contributions from the Hubbard band. This is further supported by the fact that the physical hybridization in the AMEA results, Fig.1.10c, is close to the final result in Fig.1.9c.
Overall, the two approaches show reasonable agreement with larger deviations mainly stemming from the accuracy in the AMEA fit , which can be improved, in principle. Further, we see that AMEA+FDSA is a symbiotic combination, since both are more accurate for small electric fields and/or large driving frequencies. The first one due to the perturba-

[27]This is because a sharp gap in the hybridization is smeared out in the auxiliary system due to the long tails of the involved Lorentzians in the fit.

[28]Here, it is worth to note that the effective distribution function is not directly fitted, but rather the Keldysh component shown in Fig.1.10b is considered in the cost-function.

tive nature of the FDSA and the second one, since the AMEA fit performs worse when Floquet-sidebands have to be resolved.

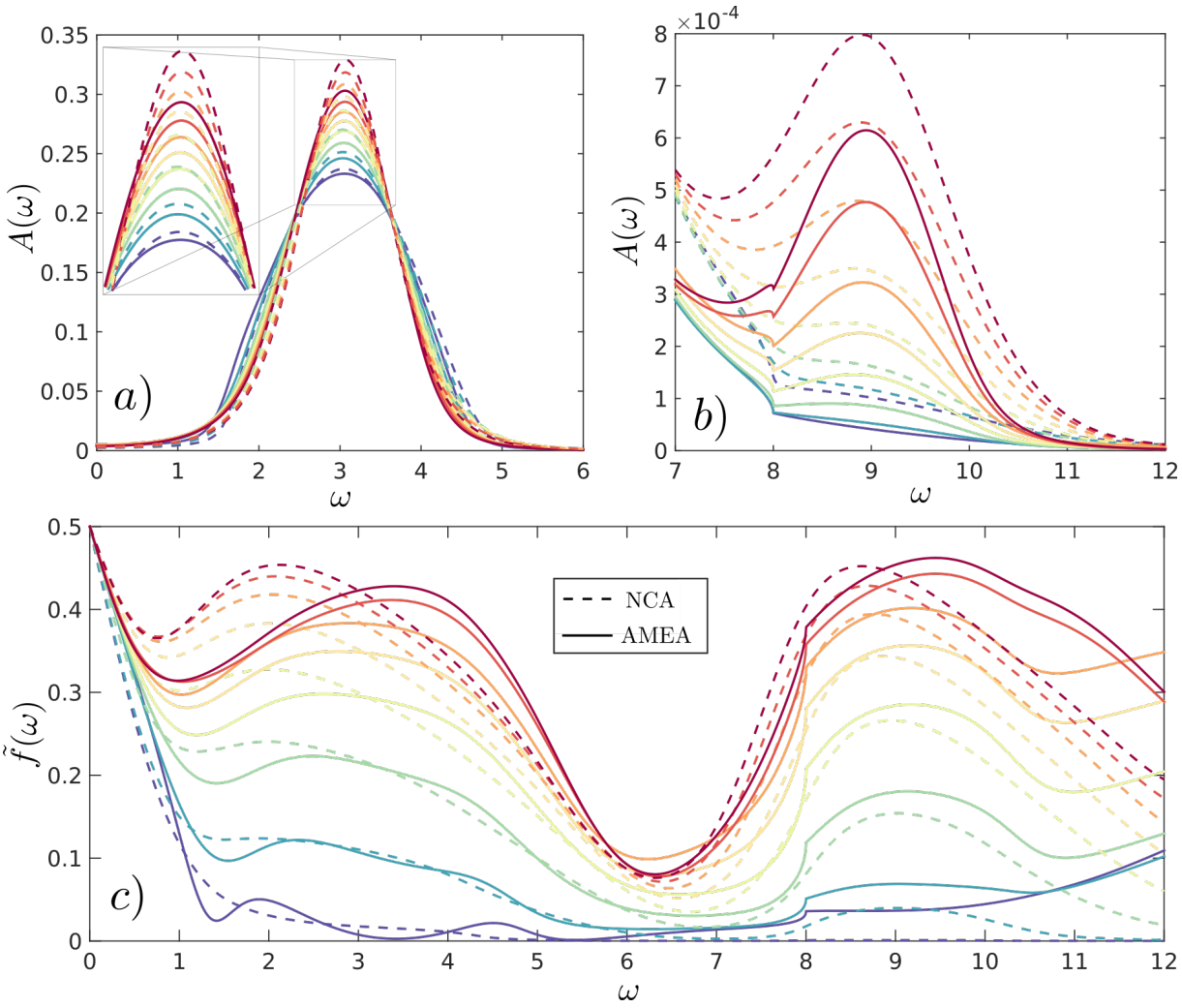

Figure 1.9: Comparison of results obtained by Floquet DMFT with NCA as impurity solver (dashed lines) and AMEA+FDSA within Floquet DMFT (solid lines) for different electric field strengths (colors). The parameters are the same as in Fig.1.7 but only for $\Omega = 6$. Panel *a*) shows the time averaged density of states with the inset representing a zoom onto the indicated region around the top of the peak. Panel *b*) and *c*) show the suppressed Floquet-sideband and the effective distribution function, respectively.

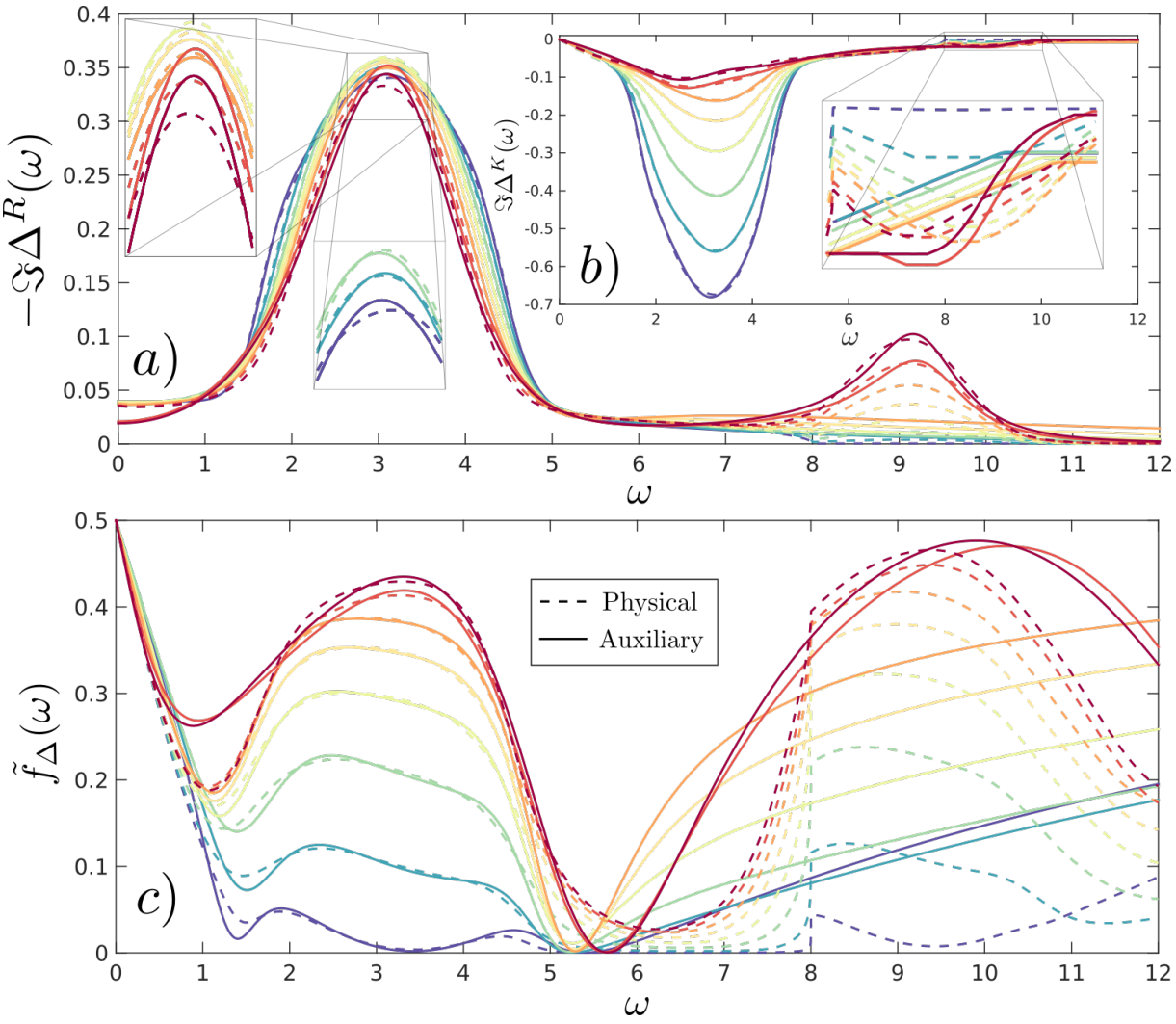

Figure 1.10: The AMEA fit comparing the imaginary part of the last DMFT hybridization (dashed lines) and the corresponding one in the auxiliary system (solid lines) for the results of Fig.1.9. Panel *a*) and *b*) show the retarded and keldysh component, respectively. The latter two are used in the cost-function of the fit. The insets in panel *a*) and *b*) show a zoom on the indicated regions. In panel *c*), we plot the corresponding effective distribution function defined by the relation, $\mathrm{Im}\,\Delta^K(\omega) = 2(1 - 2\tilde{f}_\Delta(\omega))\,\mathrm{Im}\,\Delta^R(\omega)$.

Chapter 2

Publications

This chapter is devoted to the presentation of the manuscripts published in peer reviewed journals. Out of the six publications in which contributions were made during the course of this thesis, we chose to explicitly present only the ones, where parts of the manuscript were written and parts of the presented results were actively obtained by the author of this thesis. The four publications attached below are listed in chronological order and can be grouped in two categories. Ref.[1, 2] are concerned with technical aspects and developments of AMEA while Ref.[5, 6] contain physical applications. In more detail:

The first publication Ref.[1] is concerned with the mapping to the auxiliary system and serves two purposes. First, the technicalities of the mapping are discussed and the previously developed PT optimization algorithm is presented in great detail, thereby complementing earlier works that focused on the many-body aspect of AMEA[16, 42]. Second, different geometries[1] of the auxiliary Lindblad system are considered and their performance in terms of the corresponding cost-functions for different system sizes are investigated as well as their capability to reproduce the Kondo-peak in the equilibrium spectralfunction of the Anderson Impurity Model at the level of six bath sites, $N_B = 6$, in the auxiliary system. Due to the detailed considerations of the technical aspects it was realized that the most general geometry allows for complex Lindblad couplings[2]. The corresponding "full complex" geometry was found to significantly improve the performance of the fit. Especially, $N_B = 4$ allowed us to achieve the same accuracy previously obtained with $N_B = 6$, which is of great importance for the application of AMEA within the SF+ED implementation in DMFT, where maximally six bath sites can be treated.

In the second publication Ref.[5] we apply AMEA as impurity solver in Floquet DMFT considering a Mott-insulating layer which is periodically driven by a time-periodic electric field and coupled to metallic leads with the aim to investigate the effect of impact ionization in the periodic steady state of the system. By neglecting off diagonal entries in the Floquet selfenergy, we could replace the Floquet impurity problem with a steady state one. Testing

[1] restricting the entries in the Lindblad matrices $\mathbf{E}, \mathbf{\Gamma}^{(1),(2)}$,

[2] entries in the $\mathbf{\Gamma}^{(1),(2)}$ matrices

this FDSA in a self-consistent manner by using IPT, we were able to demonstrate its validity for the considered parameters. The achieved simplification on the level of the impurity problem allowed the application of the previously developed AMEA SF+ED steady state impurity solver. It turned out that the increased accuracy, due to the "full complex" geometry introduced in the first paper, was crucial to keep spurious currents in the system under control allowing to obtain reliable results that confirmed the effectiveness of impact ionization in enhancing the photo-current.

In the third publication Ref.[2], further technical developments of AMEA were presented and benchmarked within the IRLM with the focus on an alternative solution strategy for the auxiliary many-body Lindblad problem based on SWF's, which constitutes a very promising approach to make AMEA a feasible choice as future impurity solver within nonequilibrium multi-orbital DMFT. By calculating the equilibrium spectralfunction and the I/V-characteristic of the IRLM we provided a proof of concept and showed that, due to the trivial parallelizability, extremely low wall-times can be reached. The latter results were complemented by studying the effect of finite temperature on the impurity spectralfunction of the IRLM and the presentation of developments regarding the mapping to the auxiliary system utilizing a variable-rank parametrization for the Lindblad $\mathbf{\Gamma}$-matrices as well as optimization routines from machine learning. Additionally, the notion of finite size scaling within AMEA was introduced which was successfully applied to extrapolate the results for the steady state current showing significant improvement.

In the fourth publication Ref.[6], we used the new AMEA SWF+ED implementation to calculate accurate NEGF's of the IRLM in dependence of the bias voltage with the aim to investigate how the prominent NDC of the IRLM manifests itself in the non-perturbative regime. Rewriting the integrand for the steady state current in terms of the local spectral and effective distribution function on the site next to the impurity and comparing to results obtained by the Hartree-Fock method, we were able to confirm the scenario of a renormalized hybridization strength previously found in the literature. Further, the impurity spectralfunction shows the development of a dominant central peak at high voltages, which could be interpreted by considering the many-body steady state density matrix in the central interacting cluster obtained from the numerical simulations and its corresponding single-particle excitations in the atomic limit.

Publication Preambles: In the following, a preamble is included before the presentation of each publication to describe the contributions of the different authors, as needed for the cumulative style of this thesis.

2.1 Publication 1: Geometries of the auxiliary Lindblad system

The article titled *Optimized auxiliary representation of non-Markovian impurity problems by a Lindblad equation* was published in New Journal of Physics **19** 063005, June 2017. The work was conducted by Antonius Dorda (AD) as first author and Max Sorantin (MS) as co-author under the supervision of Wolfgang von der Linden (WL) and Enrico Arrigoni (EA). The work was initialized by EA and AD with the aim to investigate the mapping to the auxiliary system in more detail with respect to different geometries of the latter. The consideration of complex Lindblad couplings was put forward by MS. The optimization calculations were done with the existing PT C++ code, which had been previously developed by AD[43]. AD and MS implemented the different geometries, carried out corresponding optimization calculations and data analysis. The presented spectralfunctions were calculated by MS using the existing SF+ED implementation previously developed by AD[43]. A first version of the manuscript was written by AD, extended and revised by MS with the inclusion of the results for the "full complex" geometry and the section discussing the spectralfunction of the SIAM, further extended and revised by EA adding the Appendix C, and revised by WL. All authors contributed to the discussion of the results.

IOP Publishing New J. Phys. 19 (2017) 063005 https://doi.org/10.1088/1367-2630/aa6ccc

New Journal of Physics
The open access journal at the forefront of physics

Deutsche Physikalische Gesellschaft DPG
IOP Institute of Physics

Published in partnership with: Deutsche Physikalische Gesellschaft and the Institute of Physics

OPEN ACCESS

RECEIVED
13 February 2017

REVISED
6 April 2017

ACCEPTED FOR PUBLICATION
12 April 2017

PUBLISHED
2 June 2017

PAPER

Optimized auxiliary representation of non-Markovian impurity problems by a Lindblad equation

A Dorda, M Sorantin, W von der Linden and E Arrigoni[1]

Institute of Theoretical and Computational Physics, Graz University of Technology, A-8010 Graz, Austria
[1] Author to whom any correspondence should be addressed.

E-mail: arrigoni@tugraz.at

Keywords: strongly correlated systems, quantum systems out of equilibrium, open quantum systems and decoherence, nonequilibrium Green's function, Markovian and non-Markovian systems

Abstract

We present a general scheme to address correlated nonequilibrium quantum impurity problems based on a mapping onto an auxiliary open quantum system of small size. The infinite fermionic reservoirs of the original system are thereby replaced by a small number N_B of noninteracting auxiliary bath sites whose dynamics are described by a Lindblad equation, which can then be exactly solved by numerical methods such as Lanczos or matrix-product states. The mapping becomes exponentially exact with increasing N_B, and is already quite accurate for small N_B. Due to the presence of the intermediate bath sites, the overall dynamics acting on the impurity site is non-Markovian. While in previous work we put the focus on the manybody solution of the associated Lindblad problem, here we discuss the mapping scheme itself, which is an essential part of the overall approach. On the one hand, we provide technical details together with an in-depth discussion of the employed algorithms, and on the other hand, we present a detailed convergence study. The latter clearly demonstrates the above-mentioned exponential convergence of the procedure with increasing N_B. Furthermore, the influence of temperature and an external bias voltage on the reservoirs is investigated. The knowledge of the particular convergence behavior is of great value to assess the applicability of the scheme to certain physical situations. Moreover, we study different geometries for the auxiliary system. On the one hand, this is of importance for advanced manybody solution techniques such as matrix product states which work well for short-ranged couplings, and on the other hand, it allows us to gain more insights into the underlying mechanisms when mapping non-Markovian reservoirs onto Lindblad-type impurity problems. Finally, we present results for the spectral function of the Anderson impurity model in and out of equilibrium and discuss the accuracy obtained with the different geometries of the auxiliary system. In particular, we show that allowing for complex Lindblad couplings produces a drastic improvement in the description of the Kondo resonance.

1. Introduction

Strongly correlated systems out of equilibrium have recently attracted considerable interest due to progress in several experimental fields, such as ultrafast pump-probe spectroscopy [1–5], ultracold quantum gases [6–10], and solid-state nanotechnology [11–13]. These advances have also prompted interest in related theoretical questions concerning thermalization [14–16], dissipation and decoherence [17], and nonequilibrium quantum phase transitions [18–20]. An interesting aspect is the interplay between correlation and dissipation in systems where the latter is not included phenomenologically but is part of the microscopic model. The challenge lies in the fact that one has to treat inhomogenous correlated systems of truly *infinite* size since any finite system would not feature dissipation. When considering purely fermionic correlated systems, dissipation is usually modeled by infinite reservoirs of noninteracting fermions. These reservoirs are in contact with a correlated central region of interest. A paradigmatic example of such a system is the single-site Kondo or Anderson impurity model [21–25]. If there is

just one reservoir with a single chemical potential μ and temperature T, then the whole system (typically) reaches thermodynamic equilibrium, a problem which is nowadays well understood [25–32]. Alternatively, one can consider a nonequilibrium situation [33–55] in which several reservoirs with different μ and T are in contact with the central region. Since the reservoirs are infinite, they act as dissipators and the system in most cases reaches a nonequilibrium steady state in which a particle and/or heat current flows across the central region[2].

There are several approaches to treat such systems numerically [35–51]. Some of them start out from the situation in which the central region and the reservoirs are decoupled, which allows the individual systems to be treated exactly [56–61]. There are different schemes to include the missing coupling between the reservoirs and the central region. First of all, one could carry out a perturbative expansion in terms of the reservoir–central region coupling [56–59]. Low-energy properties are better addressed within a renormalization-group treatment of the perturbation (see, e.g. [62]). Alternatively, one can try and compute the self-energy (most nonequilibrium quantities of interest follow from Dyson's equation) for the correlated sites based on finite clusters consisting of the central region plus a small number N_r of reservoir sites. This is done in nonequilibrium cluster perturbation theory [56, 61], whose accuracy increases with increasing N_r. A generalization of this idea is the nonequilibrium variational cluster approach, [57–60], where single-particle parameters of the model are optimized self-consistently, which allows for the adjustment of the self-energy to the nonequilibrium situation.

1.1. Markovian approximations and beyond

In a different class of approaches, one tries to 'eliminate' the degrees of freedom of the reservoir and take into account its effects on the dynamics of the interacting central region [63–67]. One way to do this is by treating the coupling to the reservoir within a Lindblad equation [63–65]. In this way, the effect of the reservoir is to introduce nonunitary dynamics in the time dependence of the reduced density operator ρ_f of the central region leading to the Lindblad equation, which is a linear, time-local equation for ρ_f preserving its hermiticity, trace, and positivity. One important precondition for the validity of this mapping, however, is the Markovian assumption that the decay of correlations in the reservoir is much faster than typical time scales of the central region. As pointed out, e.g. in [63, 66], the approximations leading to the Markovian Lindblad master equation are justified provided the typical energy scale Ω of the reservoir is much larger than the reservoir–central region coupling. However, for a fermionic system, Ω can be estimated as $\min(W, \max(|\mu - \varepsilon|, T))$, where W is the reservoir's bandwidth, and ε is a typical single-particle energy of the central region. Therefore, even in the wide-band limit $W \to \infty$, the validity of the Markov approximation is limited either to high temperatures or to chemical potentials far away from the characteristic energies of the central region. As a matter of fact, the effect of a noninteracting reservoir with W, $|\mu| \to \infty$ (or $T \to \infty$ with finite μ/T) can be exactly written in terms of a Lindblad equation. This can be easily deduced from the 'singular coupling' derivation of the Lindblad equation [63]. This is valid independently of the strength of the coupling between central region and reservoir. A nontrivial situation is obtained by introducing different reservoirs with different particle densities. The pleasant aspect of this limit is that the Lindblad parameters depend on the properties of the reservoir and of its coupling with the central region only, but not on the ones of the central region.

This is in contrast to the more standard weak-coupling Born–Markov version in which the Lindblad couplings (see, e.g. [63–65]) depend on the central region's properties. To illustrate this, consider a central region consisting of a single site with energy ε_f, i.e. with Hamiltonian

$$H_f = \varepsilon_f \, f^\dagger f \tag{1}$$

(omitting spin) and reduced density matrix ρ_f. The part of the Lindblad operator $\mathcal{L}_b$ describing the coupling to a noninteracting reservoir is given by

$$\mathcal{L}_b \, \rho_f = \Gamma_1 (2 f \rho_f f^\dagger - \{f^\dagger f, \rho_f\}) + \Gamma_2 (2 f^\dagger \rho_f f - \{f f^\dagger, \rho_f\}) \tag{2}$$

with

$$\Gamma_1 = \Gamma (1 - f_F(\varepsilon_f)) \qquad \Gamma_2 = \Gamma \, f_F(\varepsilon_f). \tag{3}$$

Here, Γ is proportional to the reservoir's density of states at the energy ε_f, and f_F is the Fermi function which obviously contains the information on the chemical potential and temperature of the reservoir but also on the onsite energy ε_f in the central region. This could be unsatisfactory since one would like to describe the effect of the reservoir in a form which is independent of the properties of the central region, especially when the latter consists of many coupled sites.

One possible way to eliminate the dependence of the Lindblad couplings on the parameters of the central region is to use an intermediate auxiliary buffer zone (mesoreservoir) between the Lindblad couplings and the

[2] A notable exception is when a bound state is present, i.e. a state with energy outside of the continuum of the reservoir. In this case, there is no unique steady state.

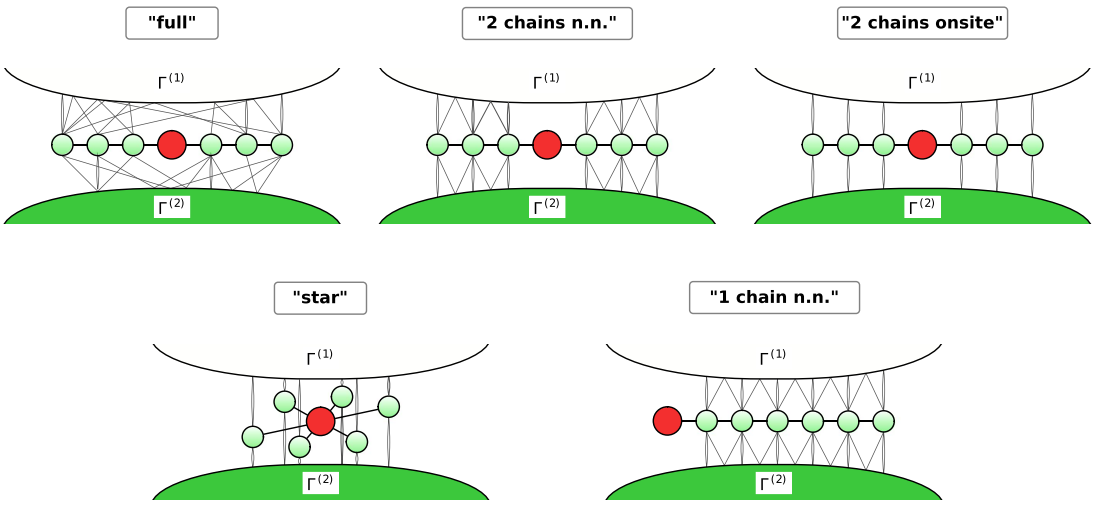

Figure 1. Sketch of the five geometries (setups) for the auxiliary system equation (15). An explicit form of the corresponding matrices for $N_B = 4$ is given in appendix B. The impurity is represented by a red circle while the bath sites are filled green ones. The hoppings described by the matrix $\boldsymbol{E}$ are represented by thick black lines. The couplings to the Markovian environments given by $\boldsymbol{\Gamma}^{(1/2)}$ are expressed by gray lines connected to empty ($\boldsymbol{\Gamma}^{(1)}$) or full ($\boldsymbol{\Gamma}^{(2)}$) reservoirs. On-site terms in the $\boldsymbol{\Gamma}^{(1/2)}$ matrices are illustrated as a double gray line. The setup 'full' represents the most general case with dense $\boldsymbol{\Gamma}^{(1)}$ and $\boldsymbol{\Gamma}^{(2)}$ matrices, which couple each bath site with every other one via the $\Gamma^{(1/2)}_{i,j}$. For simplicity, we don't depict all terms for this 'full' case. For the other (sparse) cases all couplings are drawn, and n.n. denotes nearest neighbor terms in $\boldsymbol{\Gamma}^{(1/2)}$.

central region (see, e.g. [68–71]). The buffer zone consists of isolated discrete sites (levels), each one coupled to a Markovian environment described by Lindblad operators with the same T and μ as given in equations (2) and (3). If the buffer zone is sufficiently large, i.e. if its levels are dense enough, then one can show that the buffer zone including Lindblad operators yields an accurate representation of the reservoir, which becomes exact in the limit of an infinite number of levels. Importantly, the parameters of this buffer zone do not depend on the central region's properties. The disadvantage of this approach is, however, that one needs a quite large number of buffer levels, especially at low temperatures where the Fermi function is sharp. Consequently, the many-body Hilbert space becomes very large, resulting in a challenging problem for the treatment of the correlated situation.

A very effective technique to solve low-dimensional correlated systems are matrix product states (MPS), and great progress has been made in recent years to apply MPS techniques to interacting Lindblad equations [72–85]. With this, rather large systems are within reach even though the numerical effort for Hubbard-type problems is rather high due to an extensive entanglement growth with system size [77, 85].

1.2. This work

In this paper, rather than focusing on solution techniques for the interacting Lindblad equation, we investigate different strategies for the mapping of a general physical ('ph') reservoir onto an auxiliary ('aux') one, consisting of a small number N_B of noninteracting fermionic sites (auxiliary levels) and arbitrary Lindblad terms. This is important since the accuracy of the buffer-zone idea discussed above can be significantly improved by allowing for more general Lindblad couplings, which are determined through an optimization procedure. In this way, the associated interacting impurity solver becomes exponentially accurate with increasing N_B. Moreover, if the appropriate geometry is chosen (figure 1), already a modest value of N_B produces an accurate representation of the physical reservoir. An interesting aspect is that, as in the buffer-zone approach, the combination of intermediate bath levels and couplings to Markovian environments via Lindblad terms allows one to describe a *non-Markovian* bath seen on the impurity site.

We have used these ideas in previous works [85–88] to address nonequilibrium impurity physics in the Kondo regime, with manybody solution techniques based on exact diagonalization (ED) and MPS. Especially in the latter case, we achieved very accurate results for the splitting of the Kondo peak with applied bias. Furthermore, in the equilibrium limit, we found a close agreement with numerical renormalization group (NRG) temperatures well below T_K. The sizes of the auxiliary systems were rather small, $N_B = 16$ for MPS and $N_B = 6$ for ED only,[3] which demonstrates the significant improvement provided by using a Lindblad coupling in the appropriate geometry.

[3] Consider that within the many-body Lindblad equation, we have to deal with the space of density matrices not of state vectors, so that the Hilbert space size is that of an $2(N_B + 1)$ sites Hubbard Hamiltonian.

Here, we want to elaborate in much more detail the advantages of considering long-ranged Lindblad couplings in combination with the optimization strategy. In particular, we investigate five different geometries for the auxiliary Lindblad system, see figure 1.These setups, described in detail in section 2.6, feature different connections between the Markovian bath and the auxiliary levels. The important point is that the accuracy of our approach for fixed N_B crucially depends on the choice of the appropriate geometry. A systematic analysis of the performance of these geometries is, therefore, the main content of this paper. Besides determining the scaling of the accuracy as a function of the number of bath sites N_B, we discuss the importance of the different couplings and relate our results to the commonly used buffer-zone idea. With the applicability of manybody solution techniques in mind, we consider also the case of sparse geometries which are well-suited for MPS. Even with this limitation we find drastic differences between the different geometries. This highlights the huge potential for improvement and furthermore yields important insights into the underlying mechanisms. For ED approaches, any of the discussed geometries can be applied and one is generally interested in finding the best possible mapping for a fixed and low value of N_B. In this case the geometry with long-ranged and complex Lindblad terms outperforms the other choices, as shown below.

Finally, we also discuss results for the interacting spectral function of the Anderson impurity model in and out of equilibrium, obtained with the different geometries. In particular, we show here for the first time to our knowledge that allowing for complex Lindblad couplings produces a drastic improvement in the description of the Kondo resonance.

This paper is organized as follows: in section 2.1, we introduce the models under study and define the basic notation. In section 2.2, we illustrate the most important aspect of this work, namely the mapping of the physical Hamiltonian problem onto an auxiliary open quantum system described by a Lindblad equation. In section 2.3, we present the expressions for the non-interacting Green's function of the auxiliary system, and in section 2.4 we illustrate the fit procedure. In section 2.5, we briefly discuss the relation with the interacting case. In section 3, we present in detail the convergence of the fit as a function of N_B for the different geometries presented in section 2.6 and for different temperatures, as well as a discussion on the advantages and disadvantages of these setups. As an example, we present results for the spectral function of the Anderson impurity model. Finally, in section 4 we summarize our results and discuss possible improvements and open issues. In three appendices we present technical details of the minimization procedure (appendix A), show the explicit form of the matrices for the different geometries (appendix B), and discuss certain redundancies of the auxiliary system (appendix C).

2. Model and method

2.1. Model

We begin with a general discussion, which we eventually apply to the single-site Anderson impurity model. In the general case the central region may represent a small cluster or molecule. The Hamiltonian of the physical system at study is written as

$$H = \sum_{\alpha} (H_{\alpha} + H_{\alpha f}) + H_f \tag{4}$$

where H_f is the Hamiltonian of the central region describing a small cluster of interacting fermions, H_α is the Hamiltonian of the reservoir α describing an infinite lattice of noninteracting particles, and $H_{\alpha f}$ is the coupling between central region and reservoirs.

$$H_f = H_{0f} + H_U \tag{5}$$

consists of a noninteracting part

$$H_{0f} = \sum_{ij} h_{ij} f_i^\dagger f_j \tag{6}$$

and an interaction term H_U. The fermions in the reservoirs can be described by

$$H_\alpha = \sum_{p,p'} \varepsilon_{\alpha p,p'} d_{\alpha p}^\dagger d_{\alpha p'} \tag{7}$$

in usual notation. For simplicity, spin indices are not explicitly mentioned here. Quite generally, a suitable single particle basis can be chosen such that $\varepsilon_{\alpha p,p'} \sim \delta_{p,p'}$. In the context of impurity problems, such a basis is often referred to as 'star representation', see also figure 1. $H_{\alpha f}$ is taken to be quadratic in the fermion operators:

$$H_{\alpha f} = \sum_{p,i} v_{\alpha p i} d_{\alpha p}^\dagger f_i + h.c., \tag{8}$$

and d_i (f_i) are the fermionic destruction operators on the reservoir's (central region's) sites i.

We are interested in a steady-state situation, although the present approach can be easily extended to include time dependence, especially if this comes from a change of the central region's parameters only. In the steady state, the Green's functions depend only on the time difference and we can Fourier transform so that the Green's functions depend on a real frequency ω only, which here is kept implicit. We assume that initially the hybridization $H_{\alpha f}$ is zero and the reservoirs are separately in equilibrium with chemical potentials μ_α and temperatures T_α. Then the $H_{\alpha f}$ are switched on and after a certain time a steady state is reached. We use the non-equilibrium (Keldysh) formalism [89–94] whereby the Green's function can be represented as a 2×2 block matrix

$$\underline{G} = \begin{pmatrix} G^{\mathrm{R}} & G^{\mathrm{K}} \\ 0 & G^{\mathrm{A}} \end{pmatrix}, \tag{9}$$

where the retarded G^{R}, advanced G^{A}, and Keldysh G^{K} components are matrices in the site indices (i, j) of the central region. We will adopt this underline notation in order to denote this 2×2 structure. We use lowercase $\underline{g}$ ($\underline{g}_\alpha$) to denote Green's function of the decoupled central region (reservoir α), while uppercase $\underline{G}$ represent the full noninteracting Green's function of the central region. For simplicity we omit the subscript $_0$, since in this paper we deal mainly with noninteracting Green's functions anyway. We use the subscript $_{\mathrm{int}}$ for interacting ones. $\underline{G}$ is easily obtained from the Dyson equation as

$$\underline{G} = (\underline{g}^{-1} - \underline{\Delta})^{-1}, \tag{10}$$

where

$$\underline{\Delta}_{ij} = \sum_{\alpha,p,p'} v_{\alpha p i}\, v^{*}_{\alpha p' j}\, \underline{g}_{\alpha p,p'} \tag{11}$$

is the reservoir hybridization function (commonly called bath hybridization function) in the Keldysh representation. The retarded Green's functions g^{R}_α for reservoirs with non-interacting fermions in equilibrium can be determined easily by standard tools, and the Keldysh components g^{K}_α can be obtained from the retarded ones by exploiting the fluctuation-dissipation theorem:

$$g^{\mathrm{K}}_\alpha(\omega) = (g^{\mathrm{R}}_\alpha(\omega) - g^{\mathrm{R}}_\alpha(\omega)^\dagger)\, s_\alpha(\omega), \tag{12}$$

which is valid since the uncoupled reservoirs are in equilibrium. Here,

$$s_\alpha(\omega) = 1 - 2\, f_{\mathrm{F}}(\omega, \mu_\alpha, T_\alpha) \tag{13}$$

and $f_{\mathrm{F}}(\omega, \mu_\alpha, T_\alpha)$ is the Fermi function at chemical potential μ_α and temperature T_α.

From now on, for simplicity of presentation, we restrict to the Anderson impurity model (SIAM) in which the central region, described by equation (5), consists of a single site, i.e. there is only one value for the index i, which we drop, and

$$H_U = U n_{f\uparrow} n_{f\downarrow} \qquad n_{f\sigma} = f^\dagger_\sigma f_\sigma. \tag{14}$$

The idea we are going to present in section 2.2 can be immediately extended to the case of a central region consisting of many sites in which each site is connected to separate reservoirs. In the most direct fashion, this can be done with exactly the same approach as formulated here for the SIAM by just mapping each reservoir independently onto auxiliary Lindblad bath sites. An interesting application is, for example, the case of an interacting chain coupled on both sides to reservoirs with different chemical potentials [95]. Also, the extension to the case of arbitrary (quadratic) couplings with the reservoirs that intermix the central region sites relevant, e.g., for cluster dynamical mean-field theory, is conceptually straightforward although more involved.

2.2. Mapping onto an auxiliary master equation

A crucial point in the following considerations is the fact that, even in the interacting case, the influence of the reservoirs upon the central region is completely determined by the bath hybridization function $\underline{\Delta}(\omega)$ only. In other words, *any interacting correlation function of the central region solely depends on the central region Hamiltonian H_f and on $\underline{\Delta}$*. This result is well known at least in equilibrium, and can be easily proven; for example, diagrammatically (see footnote[4]). The argument holds independently on whether one works with equilibrium or nonequilibrium Green's functions. Moreover, it crucially depends on the fact that the reservoir is noninteracting.

[4] Since there are no interactions in the reservoir, external indices of any bare interaction vertex belong to the central region only. Moreover, an interacting correlation function of the central region consists, by definition, of diagrams whose external lines belong to the central region. Consequently, all diagrams consist only of vertices (determined by H_U) and of propagator lines whose endpoints belong to the central region only, i.e. they correspond to noninteracting Green's functions $\underline{G}$ of the central region equation (10). Therefore, all relevant diagrams only depend on H_U and the noninteracting $\underline{G} = (\underline{g}^{-1} - \underline{\Delta})^{-1}$.

This can be exploited to choose different representations for the reservoir. A convenient discretization in *equilibrium* is to represent the reservoir by a finite number of bath sites, as commonly used in the context of NRG [25, 27] or exact-diagonalization-based dynamical-mean-field theory (ED-DMFT) [96–98]. Here, the desired physical hybridization function $\underline{\Delta}_{\rm ph}$ is approximated by an *auxiliary* one $\underline{\Delta}_{\rm aux}$,[5] corresponding to a bath with a finite number of sites. In ED-DMFT, the parameters of these $N_{\rm B}$ bath sites are obtained through fitting the hybridization function in Matsubara space. As can be readily shown, only $2N_{\rm B}$ bath parameters are of relevance per spin degree of freedom, and it is common to choose a 'star' or 'chain' representation.

Clearly, the same fit strategy is inconvenient *out of equilibrium* for several reasons. First of all, the auxiliary system cannot dissipate since it is finite, and a steady state cannot be reached. In [86, 99] we have suggested an auxiliary master equation approach (AMEA), which adopts an auxiliary reservoir consisting of a certain number $N_{\rm B}$ of bath sites which are additionally coupled to Markovian environments described by a Lindblad equation

$$\frac{\mathrm{d}}{\mathrm{d}t}\rho = \mathcal{L}\ \rho = (\mathcal{L}_H + \mathcal{L}_D)\rho. \tag{15}$$

Here, the Hamiltonian for the auxiliary system is given by (we reintroduce spin)

$$H_{\rm aux} = \sum_{ij\sigma} E_{ij} c^\dagger_{i\sigma} c_{j\sigma} + U n_{f\uparrow} n_{f\downarrow}, \tag{16}$$

and enters the unitary part of the Lindblad operator

$$\mathcal{L}_H \rho = -i[H_{\rm aux},\ \rho]. \tag{17}$$

The dissipator $\mathcal{L}_D$ describes the coupling of the auxiliary sites to the Markovian environment and is given by

$$\mathcal{L}_D\rho = 2\sum_{ij\sigma}\Gamma^{(1)}_{ij}\left(c_{j\sigma}\rho c^\dagger_{i\sigma} - \frac{1}{2}\{\rho,\ c^\dagger_{i\sigma}c_{j\sigma}\}\right) + 2\sum_{ij\sigma}\Gamma^{(2)}_{ij}\left(c^\dagger_{i\sigma}\rho c_{j\sigma} - \frac{1}{2}\{\rho,\ c_{j\sigma}c^\dagger_{i\sigma}\}\right). \tag{18}$$

in terms of matrices $\mathbf{\Gamma}^{(1/2)}$ with matrix elements $\Gamma^{(1/2)}_{ij}$ to be determined by an optimization procedure, as discussed below. The indices $i,\ j$ in equations (17) and (18) run over the impurity $i = f$ (we identify $c_{f\sigma} = f_\sigma$) and over the $N_{\rm B}$ bath sites[6]. Similar to the case of the ED-DMFT impurity solver previously mentioned, the idea is to optimize the parameters of the auxiliary reservoir in order to achieve a best fit to the physical bath hybridization function equation (11), i.e., for a given $N_{\rm B}$, $\underline{\Delta}_{\rm aux}(\omega)$ should be as close as possible to $\underline{\Delta}_{\rm ph}(\omega)$:

$$\underline{\Delta}_{\rm aux}(\omega) \approx \underline{\Delta}_{\rm ph}(\omega). \tag{19}$$

As for the ED-DMFT case, one can choose a single-particle basis for the auxiliary bath such that the matrix $\boldsymbol{E}$ is sparse,[7] i.e. it has a 'star' or a 'chain' form and is real valued. However, there is no reason why the matrices $\mathbf{\Gamma}^{(1)}$ and $\mathbf{\Gamma}^{(2)}$ should be sparse and real in the same basis as well, and, in fact, as discussed below, for an ED treatment of the Lindblad problem it is convenient to allow for a general form in order to optimize the fit. This larger number of parameters allows one to fulfill equation (19) to a very good approximation. The introduction of dissipators equation (18) additionally allows us to carry out the fit directly for real ω (see section 2.4) since $\underline{\Delta}_{\rm aux}(\omega)$ is a continuous function. This makes this approach competitive with ED-DMFT for the equilibrium case as well.

Notice that equation (18) is not the most general form of the dissipator, and one could think of including Lindblad terms that contain four or more fermionic operators or also anomalous and spin-flip terms. This would increase the number of parameters available for the fit. However, the latter would violate conserved quantities and the former would describe an *interacting bath*, so that the argument of section 2.2 (see footnote 3) does not apply. As a matter of fact, the exact equivalence to a *noninteracting bath* (see footnote 6) only holds for a quadratic form of the Lindblad operator as in equation (18).

Once the optimal values of the matrices $\boldsymbol{E}$, $\mathbf{\Gamma}^{(1)}$ and $\mathbf{\Gamma}^{(2)}$ for a given physical model are determined for the non-interacting system, one could solve for the dynamics of the correlated auxiliary system defined by equation (15), which amounts to a linear equation for the reduced many-body density matrix. If the number of sites of this system is small, one can solve exactly for the steady state and the dynamics of this interacting system by methods such as Lanczos exact diagonalization or matrix product states (MPS) [81–83, 85].

[5] We shall use suffixes $_{\rm ph}$ and $_{\rm aux}$ to distinguish between the physical bath hybridization function equation (11) and the ones produced by the auxiliary reservoir . Whenever necessary to avoid ambiguities, these suffixes will be used also for other quantities.

[6] It can be easily shown that the dissipative form (equation (18)) exactly corresponds to the coupling of the auxiliary baths to a small number of noninteracting reservoirs with constant density of states and infinite chemical potentials and/or temperatures. This can be easily deduced from the 'singular coupling' derivation of the Lindblad equation [63], see also [115].

[7] We use boldface to denote matrices in the indices $i,\ j$ of the auxiliary system. This should not be confused with $\underline{\ldots}$, which denotes matrices in Keldysh space.

2.3. Computation of the auxiliary bath hybridization function

In order to carry out the fit equation (19), we need to compute the auxiliary reservoir hybridization function $\underline{\Delta}_{\rm aux}(\omega)$ for many values of the bath and Lindblad parameters. This can be done in an efficient manner since only noninteracting Green's functions are needed, see also equation (10) and the preceding discussion. Computing the single-particle Green's function matrix $\underline{\mathbf{Z}}$, obtained from the steady-state solution of equation (15), amounts to solving a noninteracting fermion problem, which scales polynomially with respect to the single-particle Hilbert space . A method to deal with quadratic fermions with linear dissipation based on a so-called 'third quantization' has been introduced in [100]. We adopt the approach of [69] in which the authors recast an open quantum problem like equation (15) into a standard operator problem in an augmented fermion Fock space with twice as many sites and with a non-Hermitian Hamiltonian [69, 101, 102]. This so-called super-fermionic representation is convenient for our purposes, not only to solve for the noninteracting Green's functions but also to treat the many-body problem in an analogous framework to Hermitian problems. An analytic expression for the noninteracting steady-state retarded and Keldysh auxiliary Green's functions was derived in [86]. An alternative derivation, which does not rely on super-fermions, is given in [71]. For the retarded component, we get (see footnote 7)

$$\mathbf{Z}^{\rm R}(\omega) = (\omega - \boldsymbol{E} + i(\boldsymbol{\Gamma}^{(2)} + \boldsymbol{\Gamma}^{(1)}))^{-1}, \tag{20}$$

and the Keldysh component of the inverse Green's function reads

$$(\underline{\mathbf{Z}}^{-1})^{\rm K} = -2i(\boldsymbol{\Gamma}^{(2)} - \boldsymbol{\Gamma}^{(1)}), \tag{21}$$

yielding the Keldysh Green's function

$$\begin{aligned}\mathbf{Z}^{\rm K} &= -\mathbf{Z}^{\rm R}(\underline{\mathbf{Z}}^{-1})^{\rm K}\mathbf{Z}^{\rm A} \\ &= 2i\mathbf{Z}^{\rm R}(\boldsymbol{\Gamma}^{(2)} - \boldsymbol{\Gamma}^{(1)})\mathbf{Z}^{\rm A}.\end{aligned} \tag{22}$$

The *ff* component of $\underline{\mathbf{Z}}$ is the auxiliary impurity Green's function

$$\underline{G}_{\rm aux} = (\underline{\mathbf{Z}})_{ff}. \tag{23}$$

From this, one can determine the retarded component of $\underline{\Delta}_{\rm aux}(\omega)$

$$\Delta^{\rm R}_{\rm aux}(\omega) = 1/g^{\rm R} - 1/G^{\rm R}_{\rm aux}. \tag{24}$$

For the Keldysh component, one has to carry out two inversions of Keldysh matrices (see, e.g. [92]), yielding

$$\Delta^{\rm K}_{\rm aux}(\omega) = -(\underline{G}^{-1}_{\rm aux})^{\rm K} = 1/|G^{\rm R}_{\rm aux}|^2\ G^{\rm K}_{\rm aux}, \tag{25}$$

where the contribution from $g^{\rm K}$ is infinitesimal.

2.4. Fit procedure

From the preceding equations, we can efficiently compute $\underline{\Delta}_{\rm aux}(\omega)$ for a given set of parameters of the auxiliary reservoir. The numerical effort for a single evaluation is low and scales only at most as $\mathcal{O}(N_{\rm B}^3)$. We introduce a vector of parameters $\boldsymbol{x}$ which yields a unique set of matrices $\boldsymbol{E}$, $\boldsymbol{\Gamma}^{(1)}$ and $\boldsymbol{\Gamma}^{(2)}$ within a chosen subset (see, e.g. figure 1 and appendix B) and quantify the deviation from equation (19) through a cost function

$$\begin{aligned}\chi(\boldsymbol{x})^2 &= \frac{1}{\chi_0^2}\int_{-\omega_{\rm c}}^{\omega_{\rm c}} |\underline{\Delta}_{\rm ph} - \underline{\Delta}_{\rm aux}|\ W(\omega){\rm d}\omega, \\ |\underline{\Delta}_{\rm ph} - \underline{\Delta}_{\rm aux}| &= \sum_{\xi\in\{\rm R,K\}} \Im m\ \{\Delta^{\xi}_{\rm ph}(\omega) - \Delta^{\xi}_{\rm aux}(\omega;\boldsymbol{x})\}^2,\end{aligned} \tag{26}$$

and minimize $\chi(\boldsymbol{x})$ with respect to $\boldsymbol{x}$. The normalization χ_0 is hereby chosen such that $\chi(\boldsymbol{x}) = 1$ when $\underline{\Delta}_{\rm aux}(\omega) \equiv 0$. It is important to note that both the retarded and the Keldysh component must be fitted. Due to Kramers–Kronig relations, the real part of $\Delta^{\rm R}_{\rm ph}(\omega)$ is fully determined by its imaginary part, provided the asymptotic behavior is fixed. Therefore, we can restrict to fit its imaginary part, while $\Delta^{\rm K}_{\rm ph}(\omega)$ is purely imaginary. Furthermore, in equation (26) we introduced a cut-off frequency $\omega_{\rm c}$ and a weighting function $W(\omega)$. In this work, we take $W(\omega) = 1$ and $\omega_{\rm c} = 1.5\,D$, with D the half-bandwidth of $\underline{\Delta}_{\rm ph}(\omega)$. Different forms of $W(\omega)$ can be used, for instance in order to increase the accuracy of the fit near the chemical potentials. In general, other definitions for equation (26) are possible such as a piecewise definition with varying interval lengths. By this, one may combine the present approach with NRG ideas such as the logarithmic discretization, and work along these lines is in progress (see also [71]). On the whole, the minimization of equation (26) constitutes a multi-dimensional optimization problem and appropriate numerical methods for it are discussed in appendix A.

As asymptotic limit, we require here $\underline{\Delta}_{\rm aux}(\omega) \to 0$ for $\omega \to \pm\infty$, which is obtained when setting $\Gamma^{(1/2)}_{ff} = 0$. Semipositivity further requires $\Gamma^{(1/2)}_{if} = \Gamma^{(1/2)}_{fi} = 0$. For simplicity, we restrict here to the particle-hole symmetric case. This reduces the number of free parameters in $\boldsymbol{E}$, $\boldsymbol{\Gamma}^{(1)}$ and $\boldsymbol{\Gamma}^{(2)}$. For the case in which the

impurity site f is located in the center and that one has an even number of bath sites N_B, particle-hole symmetry in the auxiliary system is obtained when

$$E_{ij} = (-1)^{i+j+1} E_{N_B+2-j,N_B+2-i},$$
$$\Gamma^{(1)}_{ij} = (-1)^{i+j} \Gamma^{(2)}_{N_B+2-j,N_B+2-i}, \tag{27}$$

for $i, j \in \{1, \ldots, N_B + 1\}$. More details for the particular form of $\boldsymbol{E}$, $\boldsymbol{\Gamma}^{(1)}$, and $\boldsymbol{\Gamma}^{(2)}$ are given in appendix B.

2.5. Interacting case

We now briefly discuss here some relevant issues in connection with the evaluation of particular observables of the physical system from results of the auxiliary system. More details can be found in [85, 86].

As already discussed, by mapping onto an auxiliary *interacting* open quantum system of finite size described by the Lindblad equation (equation (15)), we obtain a manybody problem which can be solved exactly or at least with high numerical precision, provided N_B is not too large. In [86], we presented a solution strategy based on exact diagonalization (ED) with Krylov space methods, and in [85] one based on MPS. In the end, both techniques allow us to determine the interacting impurity Green's function $\underline{G}_{\mathrm{aux,int}}(\omega)$ of the auxiliary system. As discussed previously, in the limit $\underline{\Delta}_{\mathrm{aux}}(\omega) \to \underline{\Delta}_{\mathrm{ph}}(\omega)$ (i.e. for large N_B) this becomes equivalent to the physical one $\underline{G}_{\mathrm{ph,int}}(\omega)$. However, this equivalence only holds for impurity correlation functions, and, for example, it does not apply for the current flowing from a left ($\alpha = l$) to a right ($\alpha = r$) reservoir across the impurity. Therefore, the current evaluated within the auxiliary Lindblad system does not necessarily correspond to the physical current *even for large* N_B,[8] unless one fits the bath hybridization functions $\underline{\Delta}_{\mathrm{ph},\alpha}(\omega)$ for the left and right reservoirs separately. Such a separate fit, however, is not necessary and would simply worsen the overall accuracy for a given N_B. Once the approximate $\underline{G}_{\mathrm{ph,int}}(\omega) \approx \underline{G}_{\mathrm{aux,int}}(\omega)$ is known, the current of the *physical system* can be evaluated by means of the well-known Meir–Wingreen expression [92, 103, 104], albeit by using the Fermi functions and density of states (hybridization functions) of the two *physical* reservoirs separately. Therefore, the knowledge of $\underline{G}_{\mathrm{aux,int}}(\omega)$ enables one to compute most quantities of interest.

An additional step consists in extracting just the self-energy from the solution of the auxiliary impurity system

$$\underline{\Sigma}_{\mathrm{aux}}(\omega) = \underline{G}^{-1}_{\mathrm{aux}}(\omega) - \underline{G}^{-1}_{\mathrm{aux,int}}(\omega).$$

and inserting it into the Dyson equation for the physical system with the exact physical noninteracting Green's function

$$\underline{G}_{\mathrm{ph,int}}(\omega) \approx (\underline{G}_{\mathrm{ph}}(\omega)^{-1} - \underline{\Sigma}_{\mathrm{aux}}(\omega))^{-1}. \tag{28}$$

Clearly, this step is only useful when the relation equation (19) is approximate, since for $\underline{\Delta}_{\mathrm{aux}}(\omega) \to \underline{\Delta}_{\mathrm{ph}}(\omega)$ also the noninteracting Green's functions $\underline{G}_{\mathrm{ph}}(\omega)$ and $\underline{G}_{\mathrm{aux}}(\omega)$ would coincide, i.e. in the hypothetical $N_B \to \infty$ case, and one could just set $\underline{G}_{\mathrm{ph,int}}(\omega) \to \underline{G}_{\mathrm{aux,int}}(\omega)$. For finite N_B, this substitution has the advantage that in equation (28) the noninteracting part $\underline{G}_{\mathrm{ph}}(\omega)$ is exact, and the approximation equation (19) only affects the self energy.

2.6. Different geometries for the auxiliary system

With the goal in mind of providing the best approximation to the full interacting impurity problem described by the Hamiltonian equation (4), we would like to approximate $\underline{\Delta}_{\mathrm{ph}}(\omega)$ by $\underline{\Delta}_{\mathrm{aux}}(\omega)$ as accurately as possible for a given number of bath sites N_B. In principle, one has the freedom to choose different geometries for the auxiliary system, and a generic set of five different setups is depicted in figure 1. (An explicit form of the corresponding matrices for $N_B = 4$ is given in appendix B.) For large N_B all geometries converge to the exact solution $\underline{\Delta}_{\mathrm{aux}}(\omega) \to \underline{\Delta}_{\mathrm{ph}}(\omega)$, and the question is how fast. In section 3, we want to elaborate on this point in detail and present results obtained with those geometries, which we briefly discuss and motivate here.

In all cases one can restrict the geometries to a sparse (e.g. tridiagonal) and real-valued matrix $\boldsymbol{E}$. As is commonly true for impurity problems, the physics on the impurity site is invariant under unitary transformations among bath sites only. For an arbitrary unitary transformation $\boldsymbol{U}$ with $U_{if} = U_{fi} = \delta_{if}$ to new fermionic operators, one obtains an analogous auxiliary system with modified bath parameters $\boldsymbol{E}' = \boldsymbol{U}^\dagger \boldsymbol{E} \boldsymbol{U}$, $\boldsymbol{\Gamma}^{(1)'} = \boldsymbol{U}^\dagger \boldsymbol{\Gamma}^{(1)} \boldsymbol{U}$ and $\boldsymbol{\Gamma}^{(2)'} = \boldsymbol{U}^\dagger \boldsymbol{\Gamma}^{(2)} \boldsymbol{U}$. It is easy to check that the ff-component of the Green's functions equations (20) and (22) is not affected by this transformation. Therefore, we choose without loss of generality $\boldsymbol{E}$ to be sparse as well as real, and for $\boldsymbol{\Gamma}^{(1/2)}$ in the most general case dense matrices with $\mathcal{O}(N_B^2)$ parameters. The

[8] This situation is particularly interesting in equilibrium: with large enough N_B and an appropriate choice of the parameters of the nonequilibrium Lindblad system, one can still produce an auxiliary $\underline{\Delta}_{\mathrm{aux}}(\omega)$ so that the fluctuation dissipation theorem equation (12) is fulfilled to high precision at the impurity, representing an equilibrium physical $\underline{\Delta}_{\mathrm{ph}}(\omega)$. While a finite current may flow in the auxiliary system, the equilibrium properties at the impurity are correctly reproduced.

particular form of $\boldsymbol{E}$ is irrelevant, i.e. whether it is diagonal for bath sites (star) or tridiagonal (chain), as long as the $\boldsymbol{\Gamma}^{(1/2)}$ matrices are transformed accordingly.

Such a general geometry with sparse $\boldsymbol{E}$ and dense $\boldsymbol{\Gamma}^{(1/2)}$ is referred to as 'full' setup in the following. Here, we will further distinguish between the case in which the $\boldsymbol{\Gamma}^{(1/2)}$ are real or they have complex elements ('full complex'). In addition, we consider the four sparse cases '2 chains n.n.', '2 chains onsite', 'star', and '1 chain n. n.', in which also the $\boldsymbol{\Gamma}^{(1/2)}$ are sparse. The meaning of these abbreviations is given in figure 1, see also appendix B. These sparse geometries are, however, not linked to each other by unitary transformations and represent nonequivalent subsets of the 'full' setup. Which one of these is advantageous in practice is not obvious *a priori*, and is discussed in the next section[9].

The 'full' geometry comprises all other ones and thus, obviously, gives the best possible fit for a given N_B. In addition, one can allow for the off-diagonal matrix elements of the $\boldsymbol{\Gamma}^{(1/2)}$ to be complex, thus extending the set of fit parameters. Nevertheless, the sparse setups may be of great value for sophisticated manybody solution strategies for the interacting Lindblad equation, such as MPS. We made use of the 'full' setup (with real parameters) in the ED treatment [86], which is applicable to dense $\boldsymbol{\Gamma}^{(1)}$ and $\boldsymbol{\Gamma}^{(2)}$ matrices and could consider up to $N_B = 6$. Larger systems are prohibitive due to the exponentially increasing Hilbert space (see footnote [2]). On the other hand, within MPS, we can currently consider up to $N_B = 20$ bath sites. However, in favor of the applicability of MPS methods, one should avoid long-ranged hoppings and we thus employed the '2 chains n.n.' geometry. As becomes evident also from the results below, the gain in N_B hereby outweighs the restriction of the fit setup, so that the MPS approach is clearly more accurate. Also, the other sparse setups investigated below are possible candidates for MPS, see also [105]. Besides this, approaches such as the previously mentioned buffer zone scheme and variations of it [68–70], which are often applied concepts in Lindblad-type representation of noninteracting environments, are related to the 'star' geometry; see also our later discussion.

3. Results

As just discussed, while the 'full' geometry is the most efficient one, for the purpose of employing efficient manybody eigenvalue solvers such as MPS, it is of great relevance to consider setups which feature only sparse $\boldsymbol{E}$, $\boldsymbol{\Gamma}^{(1)}$, and $\boldsymbol{\Gamma}^{(2)}$ matrices. Furthermore, it is also of general interest to investigate the importance of long-range terms in the $\boldsymbol{\Gamma}^{(1/2)}$ matrices and why they are crucial to improving the fit. These are the questions that are addressed in this section. Moreover, we will analyze the rate of convergence as a function of N_B for the different setups shown in figure 1, and for different temperatures of the physical system. The detailed knowledge of the convergence properties is important in order to be able to estimate whether or not certain systems can be accurately treated.

We consider a 'physical' SIAM consisting of an impurity site coupled to two reservoirs (leads) at different chemical potentials, corresponding to a bias voltage ϕ across the impurity, and with a flat density of states as plotted in figures (2–4). Typical results for a given ϕ and temperature T are shown in figures (2–4). For the different setups, the quality of the fit is measured by the minimum of the cost function equation (26). As discussed previously, the 'full' setups give the best results. Already for a rather small number of bath sites $N_B \gtrsim 4$, a good agreement between $\underline{\Delta}_{\mathrm{aux}}$ and $\underline{\Delta}_{\mathrm{ph}}$ is achieved, and the convergence is exponential as a function of N_B. Allowing for complex matrix elements produces a drastic improvement. The accuracy obtained with $N_B = 8$ for the real case is essentially achieved already with $N_B = 6$ in the complex case (see also figure 5). In particular, figure 8 shows that this improvement produces a much better description of the Kondo resonance. This is crucial, since $N_B = 6$ is the maximum size that we can currently address by Krylov-space methods. Here, an excellent agreement is evident with minor differences in the Keldysh component. In the retarded component, the largest differences occur at the positions of the jumps in the Keldysh component, i.e. at the chemical potentials. This is a consequence of the simultaneous fit of the retarded and Keldysh components in equation (26), which produces oscillations in the retarded one. These oscillations are strongly reduced in the complex case. By increasing the number of bath sites, the amplitude and the extension of these oscillations in the retarded component decay rapidly.

We now consider the sparse geometries. In contrast to the 'full' setups, no improvement is obtained by allowing the matrix elements to be complex in this case. Among the sparse geometries, the ones with two chains are the most accurate. Both setups perform quite well. Again, a good agreement for small N_B is obtained and a quick improvement shows up with increasing N_B. '2 chains n.n.' has off-diagonal $\boldsymbol{\Gamma}^{(1/2)}$ terms in contrast to '2 chains onsite', which leads to a faster convergence as seen, e.g., for $N_B = 12$. The 'star' and most notably the '1 chain n.n.' geometry are clearly worse. Both exhibit a rather poor convergence as a function of N_B. For the 'star' setup, this is due to the fact that the fitted auxiliary hybridization function consists of a sum of Lorentzian peaks.

[9] The number $C(N_B)$ of fit parameters for each geometry for the particle-hole symmetric case, which we consider here, is presented in appendix B.

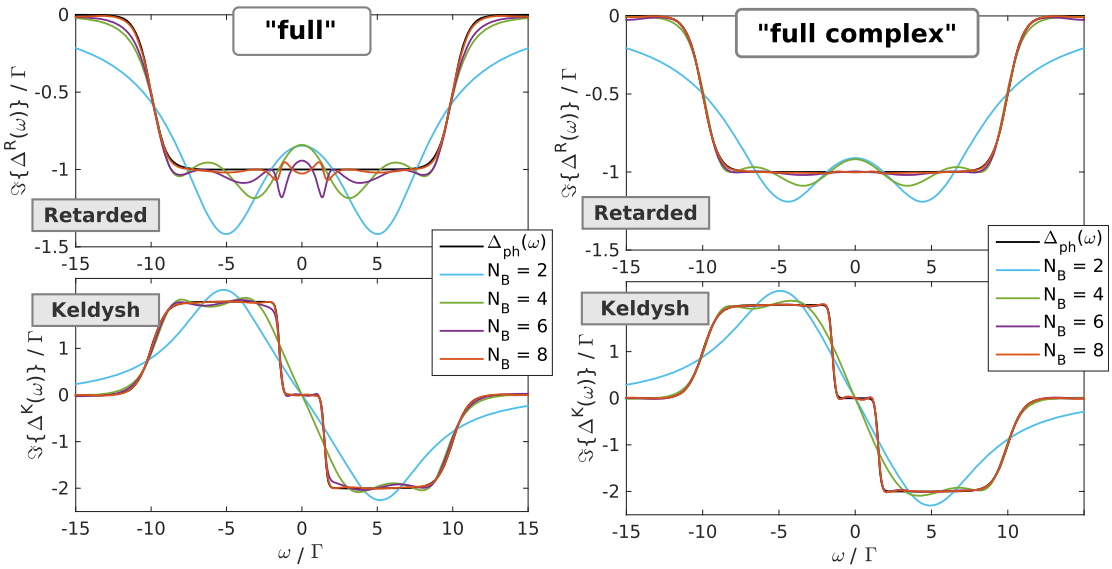

Figure 2. Fit to the bath hybridization functions for the 'full' setups (real and complex) (see figure 1). The physical $\Delta_{ph}(\omega)$ (black lines) describes a reservoir with a flat density of states with hybridization strength Γ and a half bandwidth of $D = 10\,\Gamma$ which is smeared at the edges. An applied bias voltage $\phi = 3\,\Gamma$ shifts the chemical potentials of the two reservoirs (leads) anti-symmetrically and a temperature of $T = 0.1\,\Gamma$ is considered here.

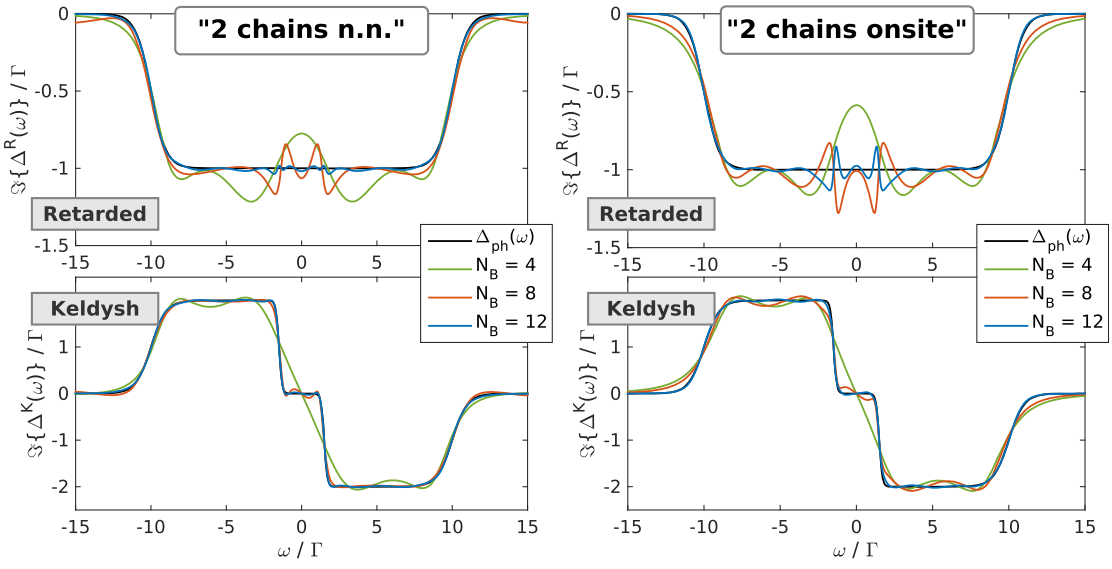

Figure 3. Same as figure 2 for the 'two-chains n.n.' and 'two-chains onsite' setups.

These enter in the Keldysh component with either positive or negative weights and can thus cancel each other. However, the rather broad Lorentzians with long $1/\omega^2$ tails make it apparently difficult to resolve the Fermi edges properly. The problem with slow convergence is most severe for the '1 chain n.n.' geometry. Here, the single chain is clearly inadequate to represent at the same time the desired density of states and the sudden changes in the occupation number, see also the subsequent discussion. While the Keldysh component is roughly reproduced, this comes at the price of large oscillations in the retarded component. In addition, the improvements with increasing N_B are minor and the results for $N_B = 4$ and $N_B = 12$ are very close to each other.

The behavior just discussed is even more visible in the convergence study presented in figures 5 and 6. In figure 5, the minimal values of the cost function χ, equation (26), for various values of N_B and the different setups are shown. Four different temperatures, each of them with $\phi = 0$ and $\phi = 3\,\Gamma$, are considered. As expected, the 'full complex' setup gives the lowest values of χ in all cases, and, moreover, the fastest rate of convergence as a function of N_B. The 'full' setup without complex terms also performs quite well. The sparse geometries '2 chains n.n.' and '2 chains onsite' perform not as well, although still achieving a rather high rate of

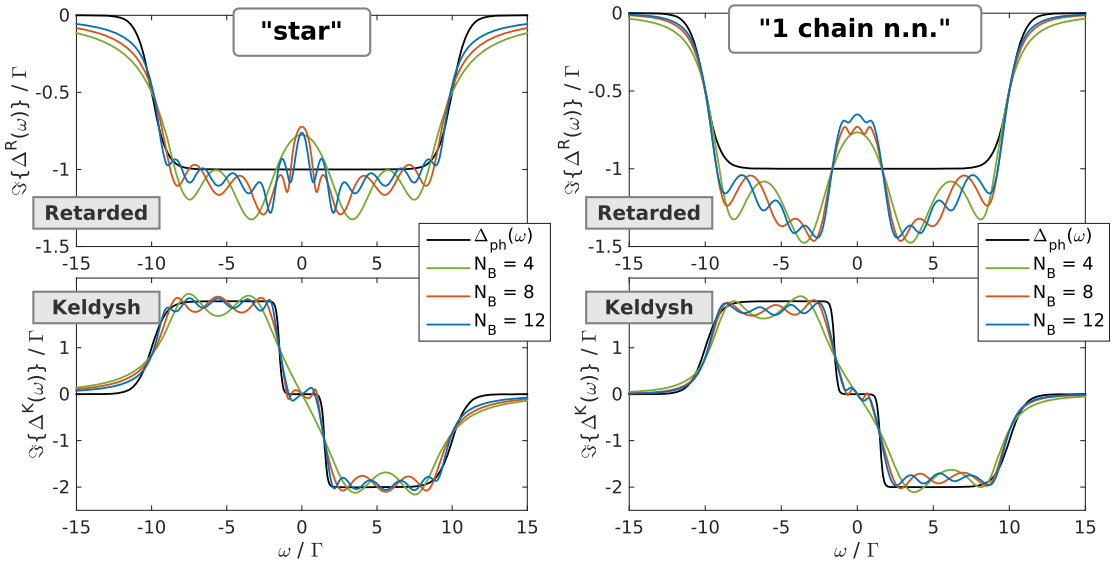

Figure 4. Same as figure 2 for the 'star' and '1-chain n.n.' setups.

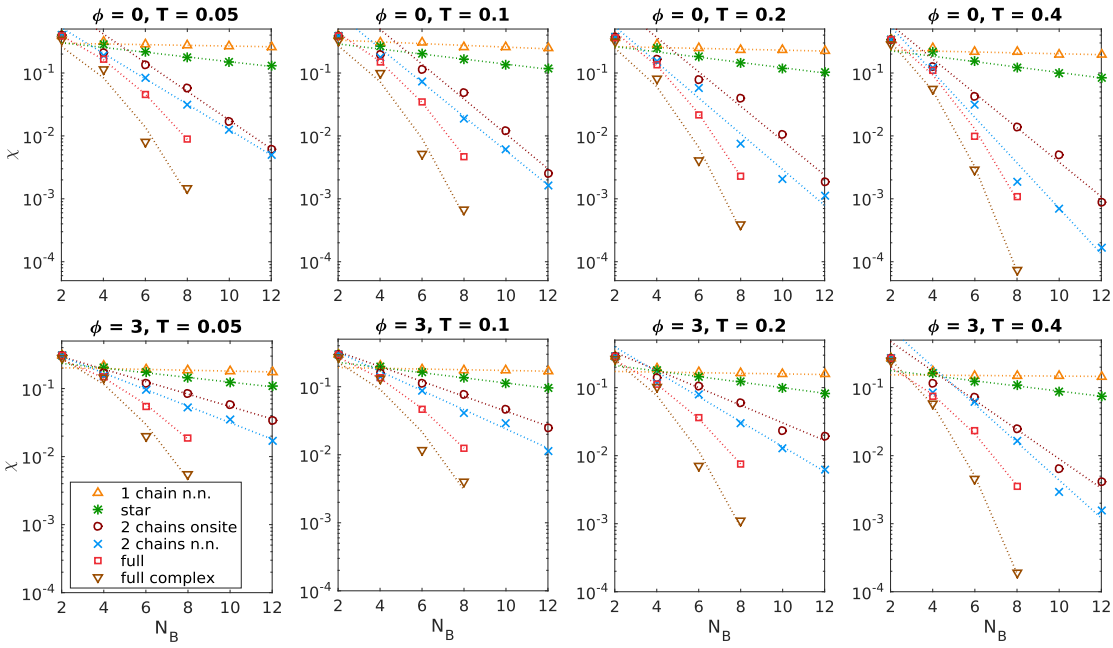

Figure 5. Minimal values of the cost function χ, equation (26), as a function of the number N_B of bath sites for the setups sketched in figure 1 (including 'full complex') for four temperatures $T = \{0.05\,\Gamma,\ 0.1\,\Gamma,\ 0.2\,\Gamma,\ 0.4\,\Gamma\}$ and two bias voltages $\phi = 0$ and $\phi = 3\,\Gamma$. Markers represent the raw data and dotted lines are obtained from the fits of figure 6.

convergence. In most cases studied here, the off-diagonal $\mathbf{\Gamma}^{(1/2)}$ terms in '2 chains n.n.' result in a significant improvement compared to '2 chains onsite', which is the reason why we favored the former in our MPS manybody calculations performed in [85]. In that work, we found that an accuracy of at least $\chi \approx 10^{-2}$ was necessary in order to properly account for Kondo physics. This could be reached already for $N_B \approx 12$.

We now discuss the 'star' setup. One should note that in standard buffer zone approaches [68–70], an equidistant energy spacing $\Delta\epsilon_i \approx 2D/N_B$ with equal onsite $\mathbf{\Gamma}^{(1/2)}$ terms is often assumed for the bath sites. Clearly, such a discretization approach cannot converge exponentially and it is only first-order accurate in the spacing $\Delta\epsilon_i$. On the other hand, in our scheme, we optimize all parameters within a fitting procedure, so the value of the cost function presented here for the 'star' setup can be seen as a lower bound for an improved buffer zone approach. Despite the exponential convergence of the 'star' geometry, it becomes apparent from figure 5 that a very slow rate of convergence is achieved. To reach an accuracy $\chi \approx 10^{-2}$ for the case $T = 0.05\Gamma$ and

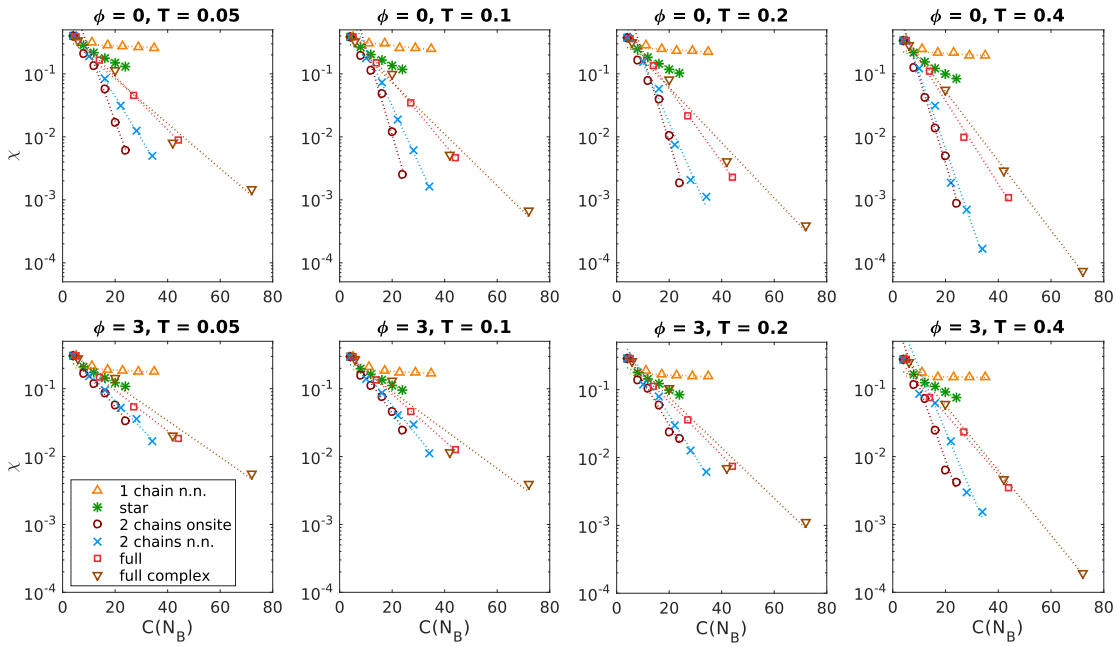

Figure 6. Same as figure 5 but plotted versus the number of fit parameters $C(N_B)$. In order to resolve the scaling with temperature more reliably, we exclude the two data points with the smallest N_B from each of the linear fits, which have not enough structures to resolve low-energy scales. Dotted lines represent results of linear fits in these semi-logarithmic plots. The temperature dependence of the convergence rates (as a function of N_B) obtained in this way are illustrated in figure 7.

$\phi = 0$ for instance, much larger auxiliary systems with $N_B \approx 40$ would be needed. For the MPS-solver used in [85], such large auxiliary systems are out of reach.

Let us now turn to the results for the '1 chain n.n.' setup in figure 5. Despite the poor performance and the strongly limited practical use, the observed behavior is interesting from a fundamental point of view. As becomes evident from the results, a single chain with local dissipators is a particularly bad choice to represent a partially filled bath. The convergence is very slow and an extremely long chain would be needed in order to achieve results comparable to the other geometries. As just shown, a drastic improvement is obtained when using two chains instead. This would be more or less intuitive for the nonequilibrium case in which the physical system also consists of two baths. However, the advantage of the '2 chains' geometry over the '1 chain' case is even more pronounced in the equilibrium case (see $\Phi = 0$). Another important observation to better understand this is the following: in [85], we found nearly identical accuracies when considering the '2 chains' geometry as used here, or a filled/empty restriction of it. In the latter case, one chain has the purpose of representing the filled spectrum and the other chain the empty spectrum of the physical hybridization function[10], and not necessarily the two physical reservoirs. This shows that a single chain of small size is very well suited to reproduce a certain density of states but not simultaneously a Fermi edge or other sharp changes in the occupation number. Furthermore, a '2 chains' filled/empty setup seems to be a rather natural representation where the resolution of sharp features in $\underline{\Delta}_{\mathrm{ph}}(\omega)$, which either correspond to band edges or sudden occupation changes at the Fermi edges, are resolved by appropriate Hermitian couplings $\boldsymbol{E}$ and corresponding broadenings/couplings stemming from $\boldsymbol{\Gamma}^{(1/2)}$. In this way, the filled and empty chain together can well reproduce sharp features in $\Delta^{R}_{\mathrm{ph}}(\omega)$ and $\Delta^{K}_{\mathrm{ph}}(\omega)$[11].

Additionally to the convergence as a function of N_B, we depict in figure 6 the cost function versus the number of available fit parameters $C(N_B)$. As can be seen, the trends in the semi-logarithmic plot are well described by straight lines in all cases, which clearly shows the achieved exponential convergence with respect to $C(N_B)$. For the sparse setups this means that $\chi \propto \exp[-\mathcal{O}(N_B)]$ whereas, for the 'full' setups, even $\chi \propto \exp[-\mathcal{O}(N_B^2)]$. Due to this, the 'full' geometries converge much quicker, as observed in the results just given. With respect to the number of fit parameters, however, the '2 chains' setups perform best. This just means that these setups contain the most relevant subset of all possible fit parameters.

Another important aspect is the dependence of the convergence rate $r(T)$ on temperature. The estimated rates $r(T)$ for each setup are depicted in figure 7. Of course, the superior scaling of the 'full' and the '2 chains' setups is also apparent in the magnitude of $r(T)$. Furthermore, in all cases, one observes the trend that the higher

[10] The filled (empty) spectrum corresponds to the lesser (greater) hybridization function Δ, and furthermore: $\Delta = \Delta^{K}/2 \mp i\, \Im m\, \{\Delta^{R}\}$.

[11] From this point of view, the additional improvement in the 'full' setups can be interpreted in such a way that one achieves an optimal linear combination of filled/empty states with the long-ranged couplings in $\boldsymbol{\Gamma}^{(1/2)}$.

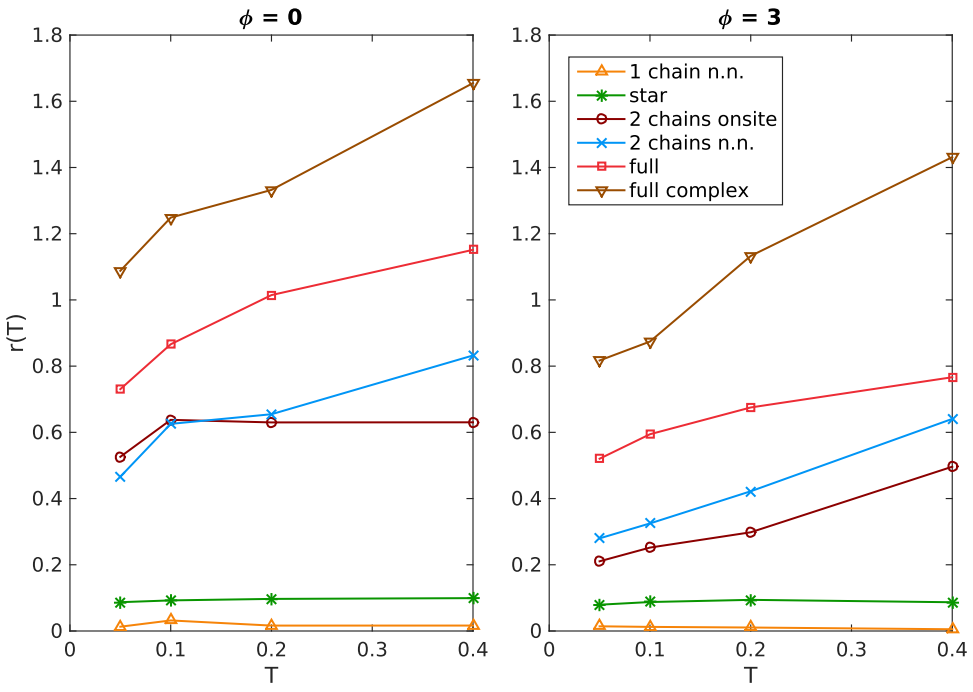

Figure 7. Estimated convergence rates obtained from the data in figure 5 plotted as a function of temperature. The rates for the sparse setups are obtained by assuming $\chi \propto \exp[-r(T)N_B]$. For the 'full' setups, the exponent is quadratic in N_B, and therefore we plotted the differential rate, defined as $-\frac{d\log\chi}{dN_B}$ evaluated at $N_B = 6$.

the temperature the faster the convergence. This can be understood from the fact that, at high T, the Keldysh component $\Delta^K_{ph}(\omega)$ is weakly ω-dependent so that less bath sites are necessary for a reliable fit. Eventually, in the $T \to \infty$ and wide-band limit, the Markov approximation even becomes exact. In the other extreme $T \to 0$ limit, discontinuous functions are present in $\Delta^K_{ph}(\omega)$, produced by the abrupt Fermi edges. However, each of the frequency-dependent functions in the effective set given by equations (20)–(25) is continuous. Therefore, $T \to 0$ can only be reproduced in the limit $N_B \to \infty$. This explains the observed trend that, for a given N_B, the high-temperature regime is generally better represented than the low-temperature one. Furthermore, a nonzero ϕ tends to result in larger values for the cost function, see also figure 5 [12].

In conclusion, the present analysis clearly demonstrates the huge advantage of optimizing the bath parameters of the auxiliary system, and furthermore, of choosing an appropriate geometry when considering only a restricted subset of the 'full' setup.

3.1. Spectral function of the interacting SIAM

We now present and discuss results for the interacting spectral function of the SIAM,

$$A(\omega) = -\frac{1}{\pi}\Im m\, G^R_{ph,int}(\omega) \tag{29}$$

(see equation (28)) in and out of equilibrium and in particular investigate the accuracy obtained by each of the geometries of figure 1 for a fixed N_B. We also discuss the relation with the fidelity in reproducing the physical hybridization function, i.e. the fit just discussed. In figures 8 and 9, we confront the results of the fit on the left with the interacting spectral function on the right. Results for $N_B = 6$ are presented for two values of the bias voltage, $\phi = 0$ (equilibrium case) and $\phi = 3\Gamma$. In particular, we focus on the region around the Kondo peak, which gets split at finite ϕ, since this is the more sensitive to approximations.

Starting with the equilibrium case, we see that all but the two worse geometries are able to resolve the Hubbard side bands. Further improvements of the fit show that, the better an auxiliary system reproduces the Fermi jump in the Keldysh and the plateau in the retarded hybridization function, the sharper is the corresponding Kondo resonance. Only the '2 chains n.n.' setup seems to break this trend as, for $\phi = 0$, its peak is clearly sharper than for the 'full' geometry although the fit is less accurate. However, this peculiarity can be readily explained by looking at the corresponding fit and in particular at the oscillations in the retarded component at low energies. Here, the 'full' geometry shows a substantial dip which in turn leads to a suppression

[12] Note that the difficulty of the fit, i.e. the magnitude of χ, is determined by the degree of variations in Δ_{ph} and the length scale of these variations wrt the half bandwidth D. The coupling strength Γ of the leads enters only trivially. Therefore, ϕ/D and T/D determine χ.

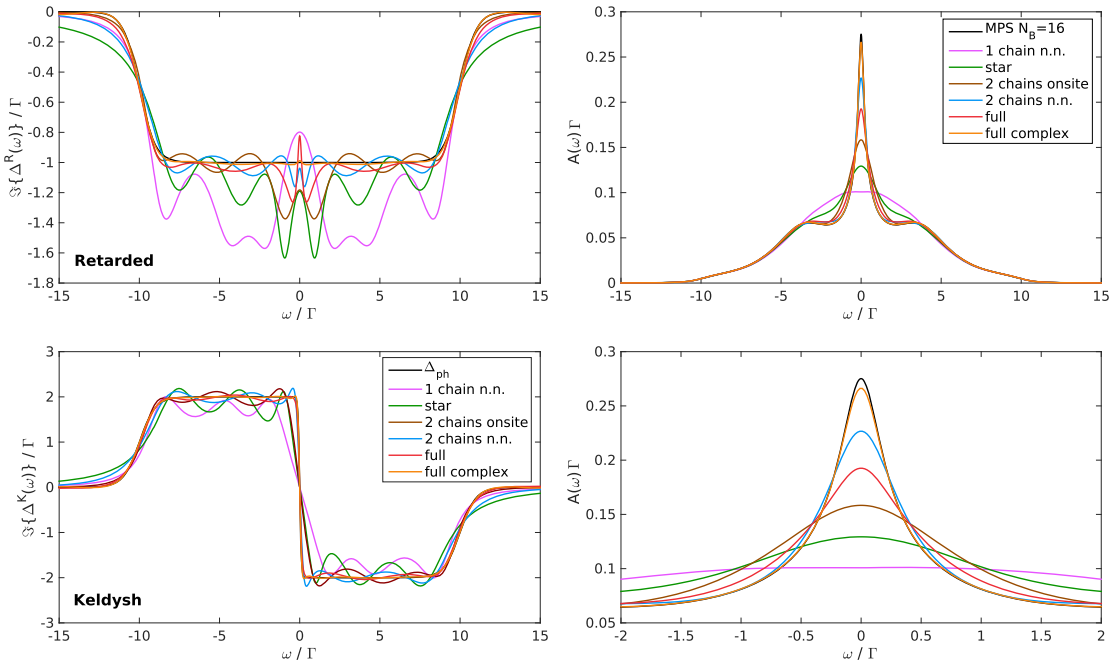

Figure 8. Fits (left) and spectral function (right) in the equilibrium case ($\phi = 0\Gamma$) for the lowest considered temperature $T = 0.05\Gamma$ and with $N_B = 6$. The value of the Hubbard interaction is $U = 6\Gamma$ and, as a reference solution (black curve), we take results for $N_B = 16$ in the '2-chains n.n.' geometry which deviate by at most 1% (at the tip $\omega = 0$) from the numerically exact NRG 85. Geometries in the key are sorted from worst (top) to best fit (bottom).

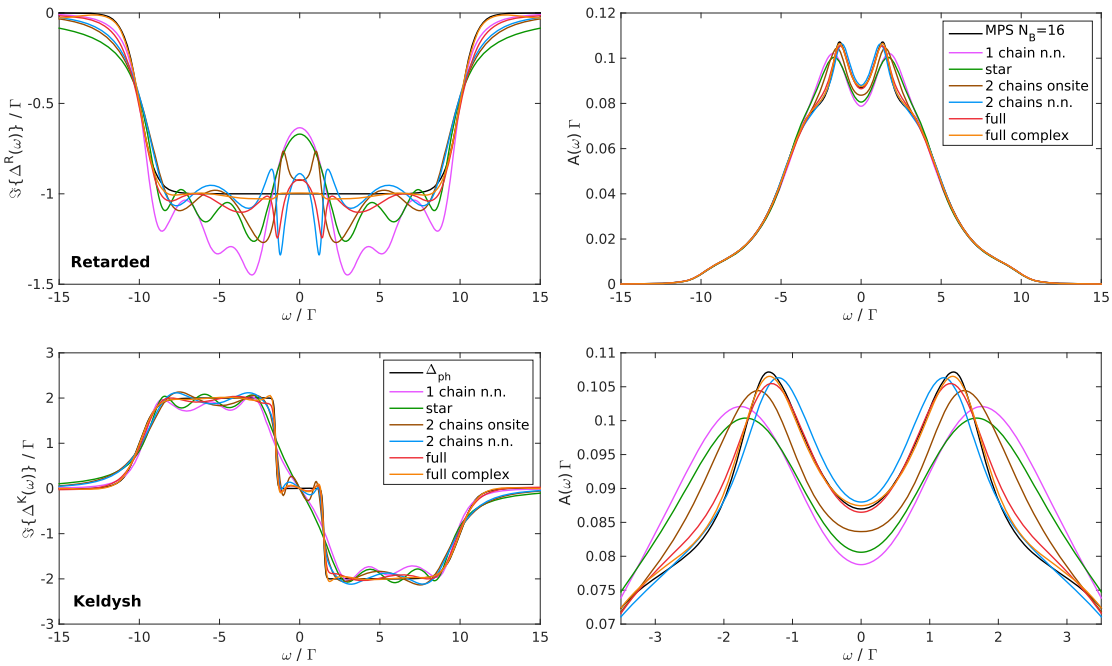

Figure 9. Same as figure 8 out of equilibrium ($\phi = 3\Gamma$).

of the Kondo peak. A way to improve this is to introduce a weight $W(\omega)$ (cf equation (26)) to the fit that emphasizes regions around the chemical potentials. One can also notice the drastic improvement in the description of the Kondo resonance obtained by allowing for complex values of the parameters $\Gamma_{ij}^{(1/2)}$. The same accuracy is expected to be obtained for the real 'full' case for $N_B = 8$, but this is currently beyond the reach of a Krylov-space solution method.

Turning to the nonequilibrium case, we first note that the 'star' and '1 chain' setup are not able to follow the double Fermi step in the Keldysh hybridization function but rather produce a single jump at an elevated

temperature. Thus, assuming for the moment a flat retarded component, one would expect only a single temperature-broadened Kondo resonance. The fact that the spectral function instead shows a two-peak structure is not a genuine effect but rather is connected to corresponding oscillations in the retarded component of the hybridization function. Notice that the two-peak structures occur here at the wrong frequency. In fact, all but the 'full complex' and 'full' setups fail to correctly reproduce the positions of the peaks, despite resolving the double Fermi step, as oscillations in the retarded component interfere with the physical effect. In general, this example shows that one has to be careful with interpretations of structures in the interacting spectral function when the fit does not resolve important features and/or displays unphysical oscillations. On the other hand, if deviations from the physical hybridization function are small, one can be confident that the results are correct. Results suggest this to be the case already with 6 bath sites for the 'full' setups and about 12 bath sites for the '2 chains' geometries.

4. Summary and conclusions

In this work, we presented and developed a general scheme for mapping nonequilibrium correlated quantum impurity problems with infinite non-Markovian fermionic reservoirs onto auxiliary finite open quantum systems. The approach as outlined here can be used to study transport through interacting impurities, Hubbard chains, or small clusters and molecules. For simplicity and clarity we presented results for the single impurity Anderson model (SIAM). The key aspect is to replace the infinite fermionic reservoirs of the original 'physical' problem by an 'auxiliary' one consisting of a combination of a small number N_B of bath levels plus Markovian terms. The auxiliary problem is described by an open quantum system whose dynamics are controlled by a Lindblad equation. Being finite, its manybody problem can be solved with high accuracy by numerical techniques. Despite the fact that the bath levels are directly coupled to a Markovian environment, the dynamics at the impurity site in the auxiliary system correctly describe the *non-Markovian* properties of the physical reservoir.

It is important to note that the overall accuracy can be evaluated by the difference between the bath hybridization functions of the physical and auxiliary system, i.e. the cost function equation (26). While this idea is not new, the key point of our work is the formulation of an optimization procedure in order to determine the parameters of the auxiliary bath levels. This allows us to achieve an exponential convergence of the accuracy of the mapping with increasing N_B. This exponential improvement is probably the reason why a few number of bath sites, such that exact diagonalization can be employed, is sufficient to (at least partially) resolve the exponentially small Kondo scale.

The main scope of this paper was to analyze the mapping procedure itself in detail. One has a certain freedom in the geometry of the auxiliary system. Here, we investigated an exemplary set of possible choices. The most general 'full' geometries achieve the best mapping for a fixed N_B value. In [86] we employed such a real-valued 'full' setup with $N_B = 6$ to analyze the splitting of the Kondo resonance in nonequilibrium. In the present work, we additionally investigated the performance of a complex-valued ('full-complex') geometry and found a drastic improvement for the same N_B. For example, the Kondo resonance turns out to be twice as high and sharp than for the real 'full' case and very close to the one obtained by NRG for $U/\Gamma = 6$, see figure 8.

Depending on the requirements and on the algorithm applied to address the manybody problem, one could prefer one setup or the other. For example, if one uses MPS-like approaches, a chain-like or, more generally, a sparse setup is preferable. In this way, one can address interacting auxiliary systems with larger N_B and improve the accuracy. If long-range hoppings are not a problem, like for Lanczos exact diagonalization, one should use the most general 'full complex' geometry. Krylov-space methods are considerably less time-consuming than MPS. Therefore, they could be more convenient when applying the present AMEA approach in the context of nonequilibrium DMFT where repeated solutions of the impurity problem are required for the DMFT self-consistency. Finally, when combining the approach with NRG, it may be convenient to adopt 'star-like' geometries (see, e.g. [71]).

Concerning sparse setups, we compared the performance of the common 'star' geometry with a '1 chain' and two '2 chains' setups. The results demonstrated clearly that the performance of these individual sparse setups may differ by orders of magnitude. In particular, the widely used 'star' geometry exhibits a very slow rate of convergence with increasing N_B, and a geometry with '1 chain' and local Lindblad drivings performed much worse than the other cases. In contrast, setups with '2 chains' and local Lindblad drivings produced very good results, with an accuracy orders of magnitude better than the other two sparse cases. Together with the results obtained in [85], we can conclude that a so-called filled/empty geometry with '2 chains' is essentially a natural representation of a non-Markovian reservoir by auxiliary Lindblad levels. In this geometry, one chain has the purpose of reproducing the filled spectrum of the original reservoir whereas the other chain reproduces the empty spectrum. This is achieved in each chain separately by an optimal combination of hoppings between the

bath levels and couplings to *one* Markovian environment, which is then either completely filled or empty. By this separation it is possible to resolve sharp features in the original hybridization function in great detail, which may correspond to sharp occupation changes at the Fermi jumps or band edges. A single chain coupled to filled and empty Markovian environments, on the contrary, cannot simultaneously represent a particular density of states and a partially filled spectrum appropriately, as is evident from the '1 chain' setup.

Besides comparing different auxiliary setups, we also analyzed the general convergence properties in detail. As just mentioned, we found an exponential convergence as a function of N_B in all cases, which can be accounted to the optimization strategy for the bath parameters. Furthermore, we analyzed systematically the convergence properties as a function of temperature both in equilibrium as well as in nonequilibrium. This showed the common trend that the high-temperature regime is better represented by the auxiliary system than the low-temperature one, i.e. the rate of convergence of the mapping increases with temperature. Therefore, to achieve a given accuracy it is more challenging to resolve low temperatures, which thus requires larger auxiliary systems. The plain exponential convergence shown here yields a simple tool to extrapolate results for low N_B to higher values, and by this to judge the feasibility of treating certain physical situations.

As a concrete application, we presented results for the spectral function of the interacting SIAM in and out of equilibrium as produced within the different auxiliary setups, and analyzed its relation to a given fit. We found that one has to be careful with interpretations when the fit does not resolve important features and shows sizable oscillations. On the other hand, if deviations from the physical hybridization function are small, one can be confident that the results are correct, which is usually the case already with 6 bath sites for the 'full' setups and about 12 bath sites for the '2 chains' sparse geometries. We also showed that drastic improvements are obtained by allowing for complex-valued parameters.

Besides the technical aspects, the current study contains relevant information to the general question of the representability of *non-Markovian* fermionic reservoirs by open quantum systems, and in particular by Lindblad-type equations. We expect that the insights gained in this work may contribute also to other closely related fields on Markovian and non-Markovian quantum master equations.

Acknowledgments

We would like to thank H G Evertz, M Nuss, F Schwarz, J von Delft, and A Weichselbaum for fruitful discussions. This work was partially supported by the Austrian Science Fund (FWF) within Projects P26508, F04103 (SFB ViCoM), and P24081, as well as NaWi Graz. The calculations were partly performed on the D-Cluster Graz and on the VSC-3 cluster Vienna.

Appendix A. Multi-dimensional minimization

In this section, we provide detailed information for readers interested in an actual implementation. Furthermore, a working code is available on request; to obtain it, simply contact us via e-mail. Much of the information below is contained in standard textbooks and reviews. However, for completeness we outline here the standard algorithm in detail and point out choices we made which turned out to be convenient for the specific problem.

As stated previously, a single evaluation of equations (20)–(25) is numerically cheap since it involves only one matrix inversion and matrix-vector multiplications of size $(N_B + 1)$. Thus, the increase in computation time with N_B is rather moderate. However, the multi-dimensional optimization problem itself is demanding and it strongly depends on the particular behavior of $\chi(\boldsymbol{x})$ when varying the set of parameters $\boldsymbol{x}$. In the worst case scenario, when $\chi(\boldsymbol{x})$ is a rough potential landscape with many local minima and short-scaled variations, one could imagine that it becomes necessary to nearly explore the whole parameter space. However, $\boldsymbol{x}$ is a continuous vector and even when assuming a fixed number of discrete values for each component in $\boldsymbol{x}$, one faces a number of points in parameter space that grows exponentially with $\dim(\boldsymbol{x})$. In the other extreme, for the case in which $\chi(\boldsymbol{x})$ is quadratic in $\boldsymbol{x}$, it is well-known that a conjugate gradient scheme leads to the exact minimum in $\dim(\boldsymbol{x})$ iterations. What we found in practice, when performing the minimization within AMEA [85, 86], is that we have an intermediate situation which exhibits local minima but gradient-based methods still work fine, especially for smaller values of N_B. In the first work on the ED-solver [86], we employed a quasi-Newton line search with many random starting points. This is particularly useful for $N_B < 6$. However, the necessary number of starting points increases rapidly with N_B. Therefore, in the course of the work on the MPS-solver, [85], we looked for more efficient solution strategies. In the end, we implemented a parallel tempering (PT) approach with feedback optimization, which is a Monte Carlo scheme that is able to overcome local minima. We describe it in more detail in the following section. In this way, the minimization problem for the ED-solver with $N_B = 6$ and for the MPS-solver with up to $N_B = 16$ can be solved in reasonable time. This amounts to minimizing

in a space of $\approx 30 - 60$ parameters in both geometries, depending on whether or not one has particle-hole symmetry.[13]

A.1. Markov chain Monte Carlo

The PT algorithm is outlined in detail in the following. For completeness, let us first briefly recap the basic ideas of the underlying Markov chain Monte Carlo (MCMC), and of the related simulated annealing algorithm.

MCMC techniques were originally developed to evaluate thermodynamic properties of classical systems which exhibit a very large phase space where simple sampling strategies fail. For our purposes here, we are interested in minimizing the cost function $\chi(\boldsymbol{x})$ as defined in equation (26) with respect to the parameter vector $\boldsymbol{x}$. For such high-dimensional minimization problems, one can adapt MCMC schemes by viewing $\chi(\boldsymbol{x})$ as an artificial energy and by introducing an artificial inverse temperature β. In the so-called simulated annealing, one samples from the Boltzmann distribution $p(\boldsymbol{x}) = 1/Z \exp(-\chi(\boldsymbol{x})\beta)$ at a certain β, and then successively cools down the artificial temperature. Motivated by the behavior of true physical systems, one expects to end up in the low-energy state when letting the system equilibrate and when cooling sufficiently slowly. Analogous to thermodynamics, one can calculate the specific heat $C_{\mathrm{H}} = \beta^2 \langle \Delta\chi(\boldsymbol{x})^2 \rangle$ and by this locate regions with large changes, i.e. phase transitions, where a slow cooling is critical. However, in practice it may be time consuming to realize the equilibration and sufficiently slow cooling, and for tests within AMEA we often ended up in local minima. In order to obtain a robust algorithm which can also start from previous solutions as needed, for instance, within DMFT, we sought a method which is able to efficiently overcome local minima and still systematically target the low-energy states. For this, a multicanonical and PT algorithm were tested and the latter turned out to be more convenient. In the following, we briefly outline the PT scheme used within AMEA and refer to [106–110] for a thorough introduction to MCMC, simulated annealing, multicanonical sampling, and PT.

As just stated, in a MCMC scheme, one typically samples from the Boltzmann distribution $p(\boldsymbol{x}) = 1/Z \exp(-\chi(\boldsymbol{x})\beta)$ at some chosen inverse temperature β. This is done through an iteratively created chain of states $\{\boldsymbol{x}_l\}$, whereby one avoids the explicit calculation of the partition function Z. An effective and well-known scheme for this is the Metropolis–Hastings algorithm [106, 107]. One starts out with some state $\boldsymbol{x}_l$ and proposes a new configuration $\boldsymbol{x}_k$, whereby it has to be ensured that every state of the system can be reached in order to achieve ergodicity. The proposed state $\boldsymbol{x}_k$ is accepted with probability [106, 107][14]

$$p_{\mathrm{pacc.}}^{l,k} = \min\left\{1, \frac{p(\boldsymbol{x}_k)}{p(\boldsymbol{x}_l)}\right\} = \min\{1, \mathrm{e}^{-(\chi(\boldsymbol{x}_k)-\chi(\boldsymbol{x}_l))\beta}\}. \tag{A.1}$$

If the proposed configuration is accepted, then the next element $\boldsymbol{x}_{l+1}$ in the chain is $\boldsymbol{x}_k$, otherwise $\boldsymbol{x}_l$ again. From equation (A.1) it is obvious that $p_{\mathrm{pacc.}}^{l,k} = 1$ when $p(\boldsymbol{x}_k) > p(\boldsymbol{x}_l)$, so that an importance of sampling towards regions where $p(\boldsymbol{x})$ is large is achieved. One can show that the algorithm fulfills detailed balance and draws a set of samples $\{\boldsymbol{x}_l\}$ that follow the desired distribution $p(\boldsymbol{x})$. However, stemming from the iterative construction, correlations in the chain are present which require a careful analysis for the purpose of statistical physics [106, 107]. For optimization problems, on the other hand, the situation is much simpler and one is just interested in the element in $\{\boldsymbol{x}_l\}$ which minimizes $\chi(\boldsymbol{x})$. Since a proposed step with $\chi(\boldsymbol{x}_k) < \chi(\boldsymbol{x}_l)$ is always accepted, the algorithm targets minima; however, uphill moves in configuration space are also allowed with a probability depending exponentially on the barrier height $\Delta\chi_{k,l} = \chi(\boldsymbol{x}_k) - \chi(\boldsymbol{x}_l)$ and β. Effectively, uphill moves only take place when $\Delta\chi_{k,l}\beta \lesssim \mathcal{O}(1)$. For small values of β, large moves in configuration space with large $\Delta\chi_{k,l}$ are likely to be accepted, whereas for large β the distribution $p(\boldsymbol{x})$ is peaked at minima in $\chi(\boldsymbol{x})$ so that those regions are especially sampled. For the latter case, configurations in the chain $\{\boldsymbol{x}_l\}$ are generally more correlated and once a $\boldsymbol{x}_l$ corresponds to a local minimum, the algorithm may stay there for a very long time.

One has great freedom in defining a proposal distribution from which the new state $\boldsymbol{x}_k$ is drawn given the current configuration $\boldsymbol{x}_l$[15]. Common choices are, for instance, a Gaussian or a Lorentzian distribution with the vector difference $\boldsymbol{x}_k - \boldsymbol{x}_l$ as argument. We favored the former and updated each component i with a probability according to [106]

[13] In order to perform the mapping for even larger systems efficiently, it may be of interest to combine the PT approach with, for instance, gradient-based methods.

[14] In principle, one has to take the proposal probabilities $q_{k,l}$ and $q_{l,k}$ into account. However, since we only consider the case $q_{k,l} = q_{l,k}$ here, the terms drop out of the equations and are neglected everywhere.

[15] Note that, for minimization purposes only, one has in general flexibility in designing the algorithm and the Boltzmann distribution or detailed balance are not compulsory.

$$q^{i}_{l,k} = \frac{1}{\sqrt{2\pi}\,\sigma_i} e^{-\frac{(x_k - x_l)_i^2}{2\sigma_i^2}}. \tag{A.2}$$

Hereby, a different step size σ_i for each component is expedient since the potential landscape $\chi(\boldsymbol{x})$ around $\boldsymbol{x}_l$ is typically highly anisotropic. Ideally, one should make use of the covariance matrix Σ_l of $\chi(\boldsymbol{x}_l)$ and consider as argument for the Gaussian instead $(\boldsymbol{x}_k - \boldsymbol{x}_l)^T \Sigma_l^{-1} (\boldsymbol{x}_k - \boldsymbol{x}_l)$ [106]. However, we encountered a problem in that the estimation of the covariance matrix at run time was strongly affected by noise and thus not feasible. The adjustment of the step sizes σ_i, on the contrary, can be done after a short number of updates by demanding that a value of $p^{l,k}_{\text{pacc.}} \approx 0.5$ is reached on average when modifying the component i. For this, we implemented a check at every single proposal that increases $\sigma_i \to 1.1\sigma_i$ when $p^{l,k}_{\text{pacc.}} > 0.6$ and decreases $\sigma_i \to 0.9\,\sigma_i$ when $p^{l,k}_{\text{pacc.}} < 0.4$. Analogous to the treatment of spin systems, we define one sweep as a single update of all the components of $\boldsymbol{x}$[16].

A.2. Parallel tempering

In a PT algorithm one considers, instead of sampling at one certain temperature, a set of different temperatures β_m^{-1} and corresponding replicas $\boldsymbol{x}_l^m$, each of which is evolved through a Markov chain. The largest β_m thereby target local minima whereas low β_m values allow for large moves in configuration space. The key idea of the PT approach is to let the individual replicas evolve dynamically in the set of β_m. By this, one achieves a situation whereby a replica at high β_m values systematically targets local minima but can overcome potential barriers again when its inverse temperature is changed to lower values. As a result, the time scales to reach an absolute minimum are drastically reduced and an efficient sampling of the low-energy states is achieved. For the purpose of calculating thermodynamic properties, one usually chooses a Metropolis–Hastings probability to swap two replicas with adjacent temperatures [109, 110]

$$p^{m,m+1}_{\text{swap},l} = \min\left\{1, \frac{p^m(\boldsymbol{x}_l^{m+1}) p^{m+1}(\boldsymbol{x}_l^m)}{p^{m+1}(\boldsymbol{x}_l^{m+1}) p^m(\boldsymbol{x}_l^m)}\right\} = \min\left\{1, e^{(\beta_{m+1}-\beta_m)(\chi(\boldsymbol{x}_l^{m+1}) - \chi(\boldsymbol{x}_l^m))}\right\}, \tag{A.3}$$

with the Boltzmann distribution for each β_m given by $p^m(\boldsymbol{x}) = 1/Z_m \exp(-\chi(\boldsymbol{x})\beta_m)$. Such swap moves are conveniently proposed after a certain number of sweeps, which satisfies the sufficient condition of balance for thermodynamics [110]. In practice, we chose 10 sweeps before swapping replicas. For the exchange to effectively take place, the underlying requirement is that the adjacent β_m and β_{m+1} values be close enough to each other, so that the two energy distributions $\Omega[\chi(\boldsymbol{x})] p^m(\boldsymbol{x})$ and $\Omega[\chi(\boldsymbol{x})] p^{m+1}(\boldsymbol{x})$ overlap, with $\Omega[\chi_0] = \int \mathrm{d}\boldsymbol{x}\ \delta(\chi_0 - \chi(\boldsymbol{x}))$ being the density of states of the cost function. This means that a replica at one temperature must represent a likely configuration for the neighboring temperature [110, 111]. In order to achieve this, a crucial point in the PT algorithm is to adjust the distribution of the inverse temperatures properly to the considered situation. Various criteria for this have been devised, see e.g. [110]. A common choice is to demand that the swapping probability equation (A.3) become constant as a function of temperature [112, 113], and in [114] a feedback strategy was presented which optimizes the round trip times of replicas. We tested the latter within AMEA but favored the simpler former criterion in the end, since it allows for a rapid feedback and quick adjustment to large changes in $\chi(\boldsymbol{x}_l^m)$. In the simple situation of a constant specific heat C_{H} with respect to energy χ for instance, an optimal strategy is known since a geometric progression $\beta_m/\beta_{m+1} = \text{const.}$ of temperatures yields a constant swapping probability [110, 111]. For interesting cases, in practice, this is rarely fulfilled, but within AMEA it served as a good starting point. The set of inverse temperatures is then optimized by averaging $p^{m,m+1}_{\text{swap},l}$ over a couple of swappings to obtain the mean probability $\bar{p}^{m,m+1}_{\text{swap}}$ and adjusting the β_m thereafter. For this we chose a fixed lowest and highest β_m value and changed the spacings in between according to

$$\Delta\beta'_m = c\frac{\Delta\beta_m}{\log(\bar{p}^{m,m+1}_{\text{swap}})}, \tag{A.4}$$

with $\Delta\beta_m = \beta_{m+1} - \beta_m$ and c adjusted properly so that $\max(\beta'_m) - \min(\beta'_m) = \max(\beta_m) - \min(\beta_m)$. In [112, 113], it was shown that a constant swapping probability of 20%–23% seems to be optimal. We determined the highest and lowest β_m values by the changes in $\chi(\boldsymbol{x})$ we want to resolve or allow for, and the number of inverse temperatures β_m was then set accordingly in order to roughly obtain $\bar{p}^{m,m+1}_{\text{swap}} \approx 0.25$. Fixing the smallest and largest β_m is, for our purposes, the most convenient choice among the many possibilities.

However, despite the feedback optimization of temperatures as just described, we encountered unwanted behavior in practice, whereby the set of parallel replicas effectively decoupled into several clusters. In suppressing this, we found it advantageous to introduce the following simple modification to equation (A.3)[17]:

[16] Again, different choices are possible. For instance, in cases where $\dim(\boldsymbol{x})$ is very large, random updates of the most relevant components could be more appropriate.

[17] One should note that the modification violates balance conditions and therefore the applicability in statistical physics. However, it is perfectly valid for the purpose of minimization problems.

$$p_{\mathrm{swap},l}^{m,m+1} = \max\{p_{\mathrm{swap},l}^{m,m+1}, p_{\mathrm{swap}}^{\mathrm{th.}}\}, \tag{A.5}$$

with a certain threshold probability $p_{\mathrm{swap}}^{\mathrm{th.}}$, e.g. $p_{\mathrm{swap}}^{\mathrm{th.}} = 0.1$ or 0.05. In this way, one avoids the β_m shifting unnecessarily close to each other and prevents very long time scales in which replicas oscillate only between two neighboring inverse temperatures.

Appendix B. Matrix form and number of independent parameters for the different setups

For the sake of clarity, we present here for the different setups of figure 1 the form of the (Hermitian) matrices $\boldsymbol{E}$ and $\boldsymbol{\Gamma}^{(1)}$ for the case $N_{\mathrm{B}} = 4$ in the particle-hole symmetric case, i.e. under the constraint equation (27) which also fixes $\boldsymbol{\Gamma}^{(2)}$. In addition, we quote the number of available fit parameters $C(N_{\mathrm{B}})$ for each setup. The fit parameters are denoted below as x_i for $i = 1, C(N_{\mathrm{B}})$, with the only constraint being that $\boldsymbol{\Gamma}^{(i)}$ should be semipositive definite. This, together with the requirement that $\underline{\Delta}_{\mathrm{aux}}$ vanish for $\omega \to \infty$, further requires $\Gamma_{ff}^{(1/2)} = \Gamma_{if}^{(1/2)} = \Gamma_{fi}^{(1/2)} = 0$. In the first four setups, the impurity is in the center ($i = 3$). In the '1 chain n.n.', it is on the first site ($i = 1$).

B.1. 'Full' geometry

$$\boldsymbol{E} = \boldsymbol{E}_t \equiv \begin{pmatrix} x_1 & x_3 & 0 & 0 & 0 \\ x_3 & x_2 & x_4 & 0 & 0 \\ 0 & x_4 & 0 & x_4 & 0 \\ 0 & 0 & x_4 & -x_2 & x_3 \\ 0 & 0 & 0 & x_3 & -x_1 \end{pmatrix} \tag{B.1}$$

$$\boldsymbol{\Gamma}^{(1)} = \begin{pmatrix} x_5 & x_9 & 0 & x_{11} & x_{12} \\ x_9^* & x_6 & 0 & x_{13} & x_{14} \\ 0 & 0 & 0 & 0 & 0 \\ x_{11}^* & x_{13}^* & 0 & x_7 & x_{10} \\ x_{12}^* & x_{14}^* & 0 & x_{10}^* & x_8 \end{pmatrix}$$

The parameters x_9 to x_{14} can be complex. Therefore, it is straightforward to see that, for general N_{B} the number of independent (real) parameters is $C(N_{\mathrm{B}}) = \frac{N_{\mathrm{B}}}{2}(N_{\mathrm{B}} + 3)$ for the real case and $C(N_{\mathrm{B}}) = N_{\mathrm{B}}(N_{\mathrm{B}} + 1)$ for the complex case.

B.3. '2-chain n.n.' geometry equation (B.1)

$$\boldsymbol{E} = \boldsymbol{E}_t$$

$$\boldsymbol{\Gamma}^{(1)} = \begin{pmatrix} x_5 & x_9 & 0 & 0 & 0 \\ x_9 & x_6 & 0 & 0 & 0 \\ 0 & 0 & 0 & 0 & 0 \\ 0 & 0 & 0 & x_7 & x_{10} \\ 0 & 0 & 0 & x_{10} & x_8 \end{pmatrix}$$

so in general $C(N_{\mathrm{B}}) = 3N_{\mathrm{B}} - 2$.

B.4. '2-chain onsite' geometry equation (B.1)

$$\boldsymbol{E} = \boldsymbol{E}_t$$

$$\boldsymbol{\Gamma}^{(1)} = \begin{pmatrix} x_5 & 0 & 0 & 0 & 0 \\ 0 & x_6 & 0 & 0 & 0 \\ 0 & 0 & 0 & 0 & 0 \\ 0 & 0 & 0 & x_7 & 0 \\ 0 & 0 & 0 & 0 & x_8 \end{pmatrix}$$

Here, $C(N_{\mathrm{B}}) = 2N_{\mathrm{B}}$.

B.5. 'Star' geometry

$$\boldsymbol{E} = \begin{pmatrix} x_1 & 0 & x_3 & 0 & 0 \\ 0 & x_2 & x_4 & 0 & 0 \\ x_3 & x_4 & 0 & x_4 & x_3 \\ 0 & 0 & x_4 & -x_2 & 0 \\ 0 & 0 & x_3 & 0 & -x_1 \end{pmatrix}$$

$$\mathbf{\Gamma}^{(1)} = \begin{pmatrix} x_5 & 0 & 0 & 0 & 0 \\ 0 & x_6 & 0 & 0 & 0 \\ 0 & 0 & 0 & 0 & 0 \\ 0 & 0 & 0 & x_7 & 0 \\ 0 & 0 & 0 & 0 & x_8 \end{pmatrix}$$

Also here $C(N_B) = 2N_B$.

B.6. '1 chain n.n.' geometry

Remember, here the impurity is on $i = 1$.

$$\boldsymbol{E} = \begin{pmatrix} 0 & x_1 & 0 & 0 & 0 \\ x_1 & 0 & x_2 & 0 & 0 \\ 0 & x_2 & 0 & x_3 & 0 \\ 0 & 0 & x_3 & 0 & x_4 \\ 0 & 0 & 0 & x_4 & 0 \end{pmatrix}$$

$$\mathbf{\Gamma}^{(1)} = \begin{pmatrix} 0 & 0 & 0 & 0 & 0 \\ 0 & x_5 & x_9 & 0 & 0 \\ 0 & x_9 & x_6 & x_{10} & 0 \\ 0 & 0 & x_{10} & x_7 & x_{11} \\ 0 & 0 & 0 & x_{11} & x_8 \end{pmatrix}$$

In this case, $C(N_B) = 3N_B - 1$.

Appendix C. Reduction of bath to a 'star' form

In principle, one can represent a noninteracting dissipative bath consisting of N_B sites $i = 1, \ldots N_B$) coupled to an impurity ($i = f$, we take $f = 0$) by specifying the single-particle parameters E_{ij}, $\Gamma^{(1)}_{ij}$, and $\Gamma^{(2)}_{ij}$ ($i, j = 0,\ldots N_B$), with corresponding Hermitian, and in the case of $\mathbf{\Gamma}^{(1)}$, $\mathbf{\Gamma}^{(2)}$, semipositive definite matrices. We show here that, for the sake of fitting the *retarded* component of a given bath spectral function Δ^R_{aux}, these parameters are redundant.

We rewrite equation (20) in block form

$$\mathbf{Z}^R = \begin{pmatrix} \omega - F_0 & -\widehat{\boldsymbol{T}} \\ -\boldsymbol{T} & \omega - \boldsymbol{F} \end{pmatrix}^{-1} \tag{C.1}$$

where the first 1×1 block contains[18] $F_0 \equiv E_{00} - i\Gamma^{(+)}_{00}$, the $N_B \times N_B$ complex matrix $\boldsymbol{F}$ is given by $F_{ij} \equiv E_{ij} - i\Gamma^{(+)}_{ij}$ for $i, j = 1, \ldots N_B$, the column vectors $T_i \equiv E_{i0} - i\Gamma^{(+)}_{i0}$, $\widehat{T}_i \equiv E_{0i} - i\Gamma^{(+)}_{0i}$, and we have introduced $\mathbf{\Gamma}^{(\pm)} \equiv \mathbf{\Gamma}^{(1)} \pm \mathbf{\Gamma}^{(2)}$.

We are interested in G^R_{aux}, which is the $_{00}$ component of $\mathbf{Z}^R$. By a well known result of matrix inversion, this is given by

$$1/G^R_{aux} = (\omega - F_0 - \widehat{\boldsymbol{T}}(\omega - \boldsymbol{F})^{-1}\boldsymbol{T}), \tag{C.2}$$

which identifies $\Delta^R_{aux} = \boldsymbol{T}^T(\omega - \boldsymbol{F})^{-1}\boldsymbol{T} + \delta F_0$, where $\delta F_0 \equiv F_0 - \varepsilon_f$, which, for simplicity, we set to zero. The first term can be rewritten by introducing the matrix $\boldsymbol{V}$ which diagonalizes $\boldsymbol{F}$,[19] i.e.

$$\boldsymbol{V}^{-1}\boldsymbol{F}\boldsymbol{V} = \boldsymbol{F}_{diag}. \tag{C.3}$$

This gives

$$\begin{aligned} \Delta^R_{aux} &= \widehat{\boldsymbol{T}}\boldsymbol{V}\boldsymbol{V}^{-1}(\omega - \boldsymbol{F})^{-1}\boldsymbol{V}\boldsymbol{V}^{-1}\boldsymbol{T} \\ &= \overline{\widehat{\boldsymbol{T}}}(\omega - \boldsymbol{F}_{diag})^{-1}\overline{\boldsymbol{T}} \\ \overline{\boldsymbol{T}} &\equiv \boldsymbol{V}^{-1}\boldsymbol{T} \qquad \overline{\widehat{\boldsymbol{T}}} \equiv \widehat{\boldsymbol{T}}\boldsymbol{V}. \end{aligned}$$

We can thus replace in equation (C.1) $\boldsymbol{F}$ with a diagonal, complex matrix $\boldsymbol{F}_{diag}$ and $\boldsymbol{T}$ ($\widehat{\boldsymbol{T}}$) with $\overline{\boldsymbol{T}}$ ($\overline{\widehat{\boldsymbol{T}}}$), and we get

$$\begin{aligned} \mathbf{Z}'^R &= (\omega - \boldsymbol{F}')^{-1} \\ \boldsymbol{F}' &\equiv \begin{pmatrix} F_0 & \overline{\widehat{\boldsymbol{T}}} \\ \overline{\boldsymbol{T}} & \boldsymbol{F}_{diag} \end{pmatrix}^{-1}. \end{aligned} \tag{C.4}$$

[18] In order to be more general, we allow for nonzero elements of the $\mathbf{\Gamma}$ matrices on the impurity site as well.

[19] Note that diagonalization of $\boldsymbol{F}$ is not always guaranteed.

Here, $\mathbf{Z}'^{\mathrm{R}}$ has the same $_{00}$ element as $\mathbf{Z}^{\mathrm{R}}$ from equation (C.1), i.e. the same $G^{\mathrm{R}}_{\mathrm{aux}}$ and $\Delta^{\mathrm{R}}_{\mathrm{aux}}$. In this way, by the requirement that $\boldsymbol{E}$ and $\boldsymbol{\Gamma}^{(+)}$ must be Hermitian, we can construct new $\boldsymbol{E}' = (\boldsymbol{F}' + \boldsymbol{F}'^{\dagger})/2$ and $\boldsymbol{\Gamma}'^{(+)} = (\boldsymbol{F}' - \boldsymbol{F}'^{\dagger})/(2i)$, i.e. a new auxiliary system which *yield the same* $\Delta^{\mathrm{R}}_{\mathrm{aux}}$ and have the 'star' geometry (figure 1)[20]. This means that, concerning the *retarded part,* one can restrict to the case of diagonal bath energies and $\boldsymbol{\Gamma}^{(+)}$, i.e., as in the non-dissipative case, $\Delta^{\mathrm{R}}_{\mathrm{aux}}$ is fixed by only $\mathcal{O}(N_{\mathrm{B}})$ independent bath parameters, the rest being redundant. This is also the case when the bath hybridization function is represented by a completely empty and a completely full chain, as discussed in section 3, since in that case one simply fits the *retarded* components of the two chains separately. On the other hand, for the most generic case, $\boldsymbol{\Gamma}^{(1)}$ and $\boldsymbol{\Gamma}^{(2)}$ will not commute and cannot be simultaneously diagonalized, so that the Keldysh component $\Delta^{\mathrm{K}}_{\mathrm{aux}}(\omega)$ appears to still depend on $\mathcal{O}(N_{\mathrm{B}}^2)$ bath parameters (figure 5). Further investigations should be carried out in order to clarify this issue.

References

[1] Giannetti C, Capone M, Fausti D, Fabrizio M, Parmigiani F and Mihailovic D 2016 *Adv. Phys.* **65** 58–238
[2] Orenstein J 2012 *Phys. Today* **65** 44–50
[3] Averitt R D and Taylor A J 2002 *J. Phys.: Condens. Matter* **14** R1357
[4] Iwai S, Ono M, Maeda A, Matsuzaki H, Kishida H, Okamoto H and Tokura Y 2003 *Phys. Rev. Lett.* **91** 057401
[5] Cavalleri A, Dekorsy T, Chong H H W, Kieffer J C and Schoenlein R W 2004 *Phys. Rev.* B **70** 161102
[6] Raizen M, Salomon C and Niu Q 1997 *Phys. Today* **50** 30–4
[7] Jaksch D, Bruder C, Cirac J I, Gardiner C W and Zoller P 1998 *Phys. Rev. Lett.* **81** 3108
[8] Greiner M, Mandel O, Esslinger T, Hänsch T W and Bloch I 2002 *Nature* **415** 39–44
[9] Trotzky S, Cheinet P, Fölling S, Feld M, Schnorrberger U, Rey A M, Polkovnikov A, Demler E A, Lukin M D and Bloch I 2008 *Science* **319** 295–9
[10] Schneider U *et al* 2012 *Nat Phys* **8** 213–8
[11] Bonilla L L and Grahn H T 2005 *Rep. Prog. Phys.* **68** 577
[12] Goldhaber-Gordon D, Göres J, Kastner M A, Shtrikman H, Mahalu D and Meirav U 1998 *Phys. Rev. Lett.* **81** 5225–8
[13] Kretinin A V, Shtrikman H and Mahalu D 2012 *Phys. Rev.* B **85** 201301
[14] Cazalilla M A 2006 *Phys. Rev. Lett.* **97** 156403
[15] Calabrese P and Cardy J 2007 *J. Stat. Mech.* **2007** P06008
[16] Rigol M, Dunjko V and Olshanii M 2008 *Nature* **452** 854–8
[17] Leggett A J, Chakravarty S, Dorsey A T, Fisher M P A, Garg A and Zwerger W 1987 *Rev. Mod. Phys.* **59** 1–85
[18] Mitra A, Takei S, Kim Y B and Millis A J 2006 *Phys. Rev. Lett.* **97** 236808
[19] Diehl S, Tomadin A, Micheli A, Fazio R and Zoller P 2010 *Phys. Rev. Lett.* **105** 015702
[20] Diehl S, Baranov M, Daley A J and Zoller P 2010 *Phys. Rev. Lett.* **104** 165301
[21] Anderson P W 1961 *Phys. Rev.* **124** 41–53
[22] Kondo J 1964 *Prog. Theor. Phys.* **32** 37–49
[23] Schrieffer J R and Wolff P A 1966 *Phys. Rev.* **149** 491–2
[24] Hewson A C 1993 *The Kondo Problem to Heavy Fermions* (Cambridge: Cambridge University Press) (https://doi.org/10.1017/CBO9780511470752)
[25] Bulla R, Costi T A and Pruschke T 2008 *Rev. Mod. Phys.* **80** 395–450
[26] Costi T A, Hewson A C and Zlatic V 1994 *J. Phys.: Condens. Matter* **6** 2519
[27] Wilson K G 1975 *Rev. Mod. Phys.* **47** 773–840
[28] Gull E, Millis A J, Lichtenstein A I, Rubtsov A N, Troyer M and Werner P 2011 *Rev. Mod. Phys.* **83** 349–404
[29] Holzner A, McCulloch I P, Schollwöck U, von Delft J and Heidrich-Meisner F 2009 *Phys. Rev.* B **80** 205114
[30] Nuss M, Ganahl M, Arrigoni E, von der Linden W and Evertz H G 2015 *Phys. Rev.* B **91** 085127
[31] Costi T A and Zlatic V 2010 *Phys. Rev.* B **81** 235127
[32] Zitko R and Pruschke T 2009 *Phys. Rev.* B **79** 085106
[33] Wingreen N S and Meir Y 1994 *Phys. Rev.* B **49** 11040–52
[34] König J, Schmid J, Schoeller H and Schön G 1996 *Phys. Rev.* B **54** 16820–37
[35] Lebanon E and Schiller A 2001 *Phys. Rev.* B **65** 035308
[36] Rosch A, Paaske J, Kroha J and Wölfle P 2003 *Phys. Rev. Lett.* **90** 076804
[37] Kehrein S 2005 *Phys. Rev. Lett.* **95** 056602
[38] Shah N and Rosch A 2006 *Phys. Rev.* B **73** 081309
[39] Han J E and Heary R J 2007 *Phys. Rev. Lett.* **99** 236808
[40] Anders F B 2008 *Phys. Rev. Lett.* **101** 066804
[41] Heidrich-Meisner F, Feiguin A E and Dagotto E 2009 *Phys. Rev.* B **79** 235336
[42] Werner P, Oka T, Eckstein M and Millis A J 2010 *Phys. Rev.* B **81** 035108
[43] Schmitt S and Anders F B 2011 *Phys. Rev. Lett.* **107** 056801
[44] Pletyukhov M and Schoeller H 2012 *Phys. Rev. Lett.* **108** 260601
[45] Reininghaus F, Pletyukhov M and Schoeller H 2014 *Phys. Rev.* B **90** 085121
[46] Smirnov S and Grifoni M 2013 *New J. Phys.* **15** 073047
[47] Nuss M, Ganahl M, Evertz H G, Arrigoni E and von der Linden W 2013 *Phys. Rev.* B **88** 045132
[48] Cohen G, Gull E, Reichman D R and Millis A J 2014 *Phys. Rev. Lett.* **112** 146802
[49] Antipov A E, Dong Q and Gull E 2016 *Phys. Rev. Lett.* **116** 036801
[50] Härtle R, Cohen G, Reichman D R and Millis A J 2015 *Phys. Rev.* B **92** 085430
[51] Wilner E Y, Wang H, Thoss M and Rabani E 2014 *Phys. Rev.* B **90** 115145
[52] Andergassen S, Meden V, Schoeller H, Splettstoesser J and Wegewijs M R 2010 *Nanotechnology* **21** 272001

[20] Interestingly, in many cases the new $\boldsymbol{\Gamma}'^{(+)}$ is no longer positive definite.

2.2 Publication 2: Floquet DMFT

The article titled *Impact ionization processes in the steady state of a driven Mott-insulating layer coupled to metallic leads* was published in Physical Review B. **97** 115113, March 2018. The work was conducted by Max Sorantin (MS) with Antonius Dorda (AD) as co-author supervised by Karsten Held (KH) and Enrico Arrigoni (EA). The work was initiated by KH in collaboration with EA. EA closely guided the project, especially in the early stages, while KH helped with clarifying discussions and guiding directions especially in later stages. MS performed preliminary studies with Matlab implementations by considering a correlated layer sandwiched between two leads in the Hubbard I approximation. EA suggested the step towards DMFT by employing, in some way, the AMEA impurity solver developed previously by AD. MS put forward the idea to solve only the time-averaged impurity problem, which, through further discussions with AD and EA, led to the formulation of the developed FDSA in Floquet-DMFT. MS implemented the "full complex" geometry within the existing SF+ED impurity solver, under guidance of AD, and generalized the C++ real space DMFT+AMEA code existing in the group[3] to Floquet DMFT. AD introduced the idea to use also computationally more lightweight impurity solvers such as IPT (or NCA). A corresponding Floquet DMFT+IPT implementation in Matlab was developed by MS and used to test the validity of the FDSA. The results of a thorough parameter scan of the model, calculations and data analysis performed by MS, were discussed between all authors. The manuscript was written by MS and revised by EA and KH.

[3]Developed by Irakli Titvinidze and AD.

Impact ionization processes in the steady state of a driven Mott-insulating layer coupled to metallic leads

Max E. Sorantin,[1,*] Antonius Dorda,[1] Karsten Held,[2] and Enrico Arrigoni[1,†]
[1]*Institute of Theoretical and Computational Physics, Graz University of Technology, 8010 Graz, Austria*
[2]*Institute of Solid State Physics, TU Wien, 1040 Vienna, Austria*

(Received 18 October 2017; revised manuscript received 22 February 2018; published 8 March 2018)

We study a simple model of photovoltaic energy harvesting across a Mott-insulating gap consisting of a correlated layer connected to two metallic leads held at different chemical potentials. We address, in particular, the issue of impact ionization, whereby a particle photoexcited to the high-energy part of the upper Hubbard band uses its extra energy to produce a second particle-hole excitation. We find a drastic increase of the photocurrent upon entering the frequency regime where impact ionization is possible. At large values of the Mott gap, where impact ionization is energetically not allowed, we observe a suppression of the current and a piling up of charge in the high-energy part of the upper Hubbard band. Our study is based on a Floquet dynamical mean-field theory treatment of the steady state with the so-called auxiliary master equation approach as impurity solver. We verify that an additional approximation, taking the self-energy diagonal in the Floquet indices, is appropriate for the parameter range we are considering.

DOI: 10.1103/PhysRevB.97.115113

I. INTRODUCTION

Strongly correlated materials are known to display intriguing effects and show properties not observed in ordinary systems. Some examples are high-temperature superconductivity [1], half-metallicity [2], spin-charge separation [3], and the Kondo effect [4] just to quote a few. A prototypical class of these materials are so-called Mott insulators where strong electronic interactions are responsible for the spectral gap as realized in transition-metal oxides (TMOs). Recent theoretical works have proposed these materials as candidates for efficient photovoltaics [5–7], exploiting electronic correlations to increase the photovoltaic efficiency.

The key idea is that in a strongly correlated insulator high-energy electrons, created by photoexcitation, are likely to undergo a process called impact ionization thereby exciting another electron across the gap. Although impact ionization is also present in conventional semiconductor devices, the time scales are such that a highly excited electron will generally dissipate its energy to phonons. In contrast, the time scale of electron-electron (e-e) scattering is orders of magnitude shorter in correlated TMOs because of the strong interaction. In this way, the excess energy of photoexcited electrons is substantially less prone to thermal losses and the efficiency of the resulting solar cell is not restricted by the Shockley-Queisser limit [8] any longer. Previous works have studied Mott systems after a photoexcitation with time-dependent dynamical mean-field theory (t-DMFT) investigating the role of impact ionization [9,10] as well as doublon dynamics [11,12] in the subsequent thermalization. This work confirmed the dominant character of impact ionization on short time scales of the order of 10 fs [10] and a high mobility of charge carriers in layered structures [12].

While the aforementioned studies have investigated the short- and medium-time dynamics of these model systems after a short electromagnetic pulse, in the present work we aim at studying a steady-state situation in which the system is under constant illumination and energy is continuously harvested by transferring electrons from a metallic lead at a lower chemical potential into one at a higher chemical potential (see Fig. 1). We consider a purely electronic and highly simplified model for a Mott photovoltaic device consisting of a left/right lead and a correlated layer acting as a photoactive region in between. To study the effect of impact ionization on the photovoltaic efficiency we investigate the photon-frequency-resolved steady-state photocurrent, whereby the illumination is accounted for by coupling the correlated layer to an electric field oscillating with a single frequency. Experimentally this would correspond to studying the photovoltaic effect with a laser in the laboratory.

The energy structure of the system is sketched in Fig. 1. In this special setup, one can distinguish between driving frequencies that support steady-state current without the need of scattering [direct excitations, Fig. 1(a)] and frequencies that require the production of an extra electron-hole excitation by impact ionization [Fig. 1(b)]. While the narrow bandwidth of the leads is certainly rather unconventional, it is ideally suited for the detection of impact ionization, not only for theoretical means but also experimentally. Our main results, Fig. 4 below, show a steep increase of the current in the impact ionization case (by roughly a factor 2 in comparison to the case of direct excitations), accompanied by an increase in the double occupancy.

To corroborate the fact that direct excitations and impact ionization are the dominant processes in this steady-state situation, we investigate the system also in a parameter region

*sorantin@tugraz.at
†arrigoni@tugraz.at

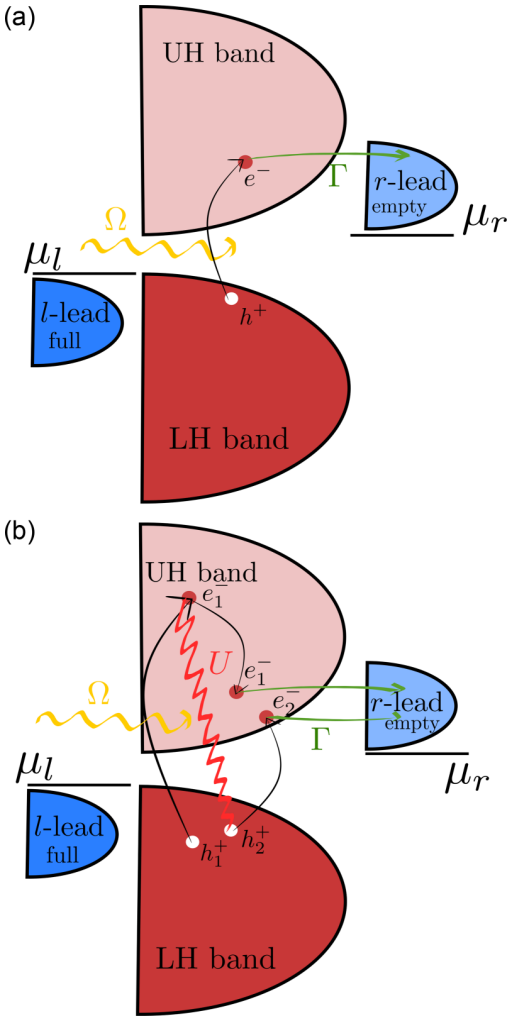

FIG. 1. A sketch of the energy distribution of the system studied and an illustration of the dominant steady-state photoinduced processes. The dark-blue (light-blue) region describes the full (empty) lead, while the lower and upper Hubbard bands of the central layer are marked in dark- and light-red, respectively. Electromagnetic radiation with energy Ω (yellow) initially produces a particle-hole excitation (red wiggly line). For $\Delta_{ss} < \Omega < \Delta_{ss} + 2D$, panel (a) shows an electron coming from the left (full) lead which is photoexcited into the upper Hubbard band at energies such that it can directly escape into the right (empty) lead without further scattering processes. For $\Omega > 2\Delta_{ss}$, panel (b), we have impact ionization: First, an electron-hole pair is created with a high-energy electron via photoabsorption (e_1^-,h_1^+ in the figure). Since the energy of the photoexcited electron is incompatible with states in the right lead, it cannot escape the correlated region. Thus, it can only contribute to the current if it can get rid of its excess energy. The simplest, and therefore dominant process is impact ionization, where e_1^- scatters with a second electron from the lower band, thereby exciting it over the steady-state gap and creating a second e-h pair e_2^-,h_2^+. In the final state, both electrons and holes can now escape into the leads and contribute to the current. Notice that in the present steady-state situation only processes that eventually recover the initial configuration are allowed.

for which impact ionization is prohibited. Here, we find indeed a significant current only in the frequency regime of direct excitations. For strong electric fields, however, we find possible signatures of, what we refer to as, higher order impact ionization processes.

In order to explore properties of the system in a steady state with the period associated with the frequency of the electric field, we employ a Floquet plus DMFT [13–15] approach, whereby the recently introduced auxiliary master equation approach (AMEA) [16–19] is used as an impurity solver. For simplicity, we restrict the self-energy to be diagonal in the Floquet index. We find that this Floquet diagonal self-energy approximation (FDSA) is valid within the parameter range of interest by testing it against a fully time-dependent impurity solver. For this test, i.e., for being able to include the full time dependence, we employ the iterated perturbation theory (IPT).

This work is organized as follows: We introduce the model in Sec. II and outline the technical details related to the Floquet plus DMFT formalism used in this paper in Sec. III. Some additional information and more elaborate discussions on some key points can be found in the Appendix together with a test of the validity of the FDSA. The main results and their discussion are presented in Sec. IV and our conclusions together with an outlook on possible future investigations are presented in Sec. V.

II. MODEL

To make for a first numerical study of the possible increase in photovoltaic efficiency due to impact ionization in the setting of a periodic drive, we work with the most basic model that captures only the key aspects of the physical situation. Since impact ionization is a purely electronic process, we work solely with electrons and neglect any other degrees of freedom. We want to note that, in particular, the coupling to lattice vibrations, including the polaron structure of the electronic quasiparticles, should be included in a more elaborate treatment as the latter are known to play a significant role in photoexcited Mott systems [20–23]. Other extensions of the model are discussed in our conclusions (see Sec. V).

In more detail, we consider a system consisting of a single-band Hubbard layer connected on the two sides with metallic leads described by noninteracting tight-binding models. The central (Hubbard) layer is driven by a time-periodic, monochromatic and homogeneous electric field of frequency Ω. Figure 2 shows a sketch of the lattice system. Its Hamiltonian reads

$$\begin{aligned}
\hat{H} &= \hat{H}_{\text{center}}(t) + \hat{H}_{\text{leads}} + \hat{H}_{\text{coupling}},\\
\hat{H}_{\text{center}}(t) &= -\sum_{\langle ij\rangle,\sigma} t_{ij}(t) c^\dagger_{i,\sigma} c_{j,\sigma} + \frac{U}{2}\sum_{i,\sigma} n_{i,\sigma}(n_{i,\bar{\sigma}} - 1),\\
\hat{H}_{\text{leads}} &= \sum_{\gamma\in\{l,r\}} \left(-t_\gamma \sum_{\langle ij\rangle,\sigma} f^\dagger_{\gamma i,\sigma} f_{\gamma j,\sigma} + \sum_{i,\sigma} \epsilon_\gamma f^\dagger_{\gamma i,\sigma} f_{\gamma i,\sigma} \right),\\
\hat{H}_{\text{coupling}} &= \sum_{\langle i,j\rangle\sigma} \left(V_l f^\dagger_{l_i,\sigma} c_{j,\sigma} + V_r f^\dagger_{r_i,\sigma} c_{i,\sigma} + \text{H.c.} \right). \qquad (1)
\end{aligned}$$

Here, $c^\dagger_{i,\sigma}/c_{i,\sigma}$ denote creation/annihilation operators in the central layer and $n_{i,\sigma} = c^\dagger_{i,\sigma} c_{i,\sigma}$, while $f^\dagger_{\gamma_i,\sigma}/f_{\gamma_i,\sigma}$ refer to operators in the leads. We consider a spatially uniform electric field along the diagonal direction of the central layer. By choosing the temporal gauge, where the scalar potential vanishes,

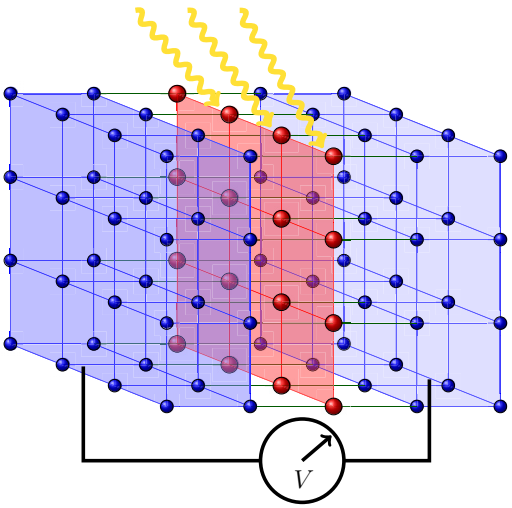

FIG. 2. Sketch of the considered lattice system. The leads, Hubbard layer, monochromatic light, and the coupling between the lead and layer are illustrated in blue, red, yellow, and green, respectively.

the electric field is described by the vector potential $\boldsymbol{A}(t) = \boldsymbol{E}_0 \cos(\Omega t)/\Omega$ resulting, according to the Peierls substitution rule, in a time-dependent hopping

$$t_{ij}(t) = t_c e^{-(ie/\hbar c)\boldsymbol{A}(t)(\boldsymbol{r}_j - \boldsymbol{r}_i)}. \tag{2}$$

The units for the electric field are chosen such that the coefficient $\frac{e}{\hbar c} = 1$. Moreover, we set the lattice spacing to unity and take t_c as the unit of energy throughout this work.

Parameter setup

To study, in particular, the role of impact ionization on the steady-state dynamics, we choose a very special and unconventional parameter setup that allows us to distinguish between regimes in which impact ioniszation can take place or not as the external driving frequency is varied, hence enabling us to isolate the effect under study. To this end, we consider narrow leads with no overlap of their respective density of states and place the lead lower/upper in energy at the top/bottom of the lower/upper Hubbard band. In order to avoid the backflow of carriers into the source, the left (i.e., lower) lead is taken as completely filled, while the right one is empty [24]. Accordingly, the chemical potential μ_l/μ_r lies just above/below the left/right band. Furthermore, we consider large hybridization strengths $\Gamma = 2\pi|V|^2\rho(\omega = 0) = 9.6$, with $V_L = V_R = V$ in Eq. (1) and $\rho(\omega)$ denoting the density of states (DOS) of the leads. A large hybridization guarantees that electrons with the correct energy escape quickly into the right lead [25]. At the same time it must be small enough not to dominate the dynamics in the central layer or to alter its corresponding DOS substantially. As a matter of fact, this is a balancing act and as we will see below the DOS is (somewhat) affected. Finally, we take moderate electric field strengths such that first-order absorption processes dominate. More specifically, we set $E = 2$ for the main results of this work [26] (Fig. 4 with $U = 12$). For the larger value of $U = 30$ we demand that the effective electric field strength α, defined in Sec. III D 1, for resonant driving frequencies, $\Omega = U$, is roughly the same.

The situation is depicted in Fig. 1. In this setup, (particle) current can only flow from the (filled) left lead into the (empty) right one and only when the system is externally driven. In the absence of scattering, the minimal frequency needed to drive a steady-state current is $\Omega \geqslant \Delta_{ss}$, where Δ_{ss} is the energy gap between the leads. Our aim here is not to provide a realistic model for photovoltaic applications, but rather to study and distinguish the different kind of process that can take place in a Mott photovoltaic in a steady-state situation. As we will see below, this setup is ideally suited to identify the existence of impact ionization in a steady state.

III. METHOD

A. Floquet Green's functions

To solve for the (periodic-)steady-state properties of the system we work with the so-called Floquet Green's function (GF) [27–31] formalism, which allows for the evaluation of the steady-state current and spectral properties. Here, every observable of the system, and thus also the single-particle GF, is assumed to be periodic with the external driving frequency. Since a periodically driven system is inevitably out of equilibrium we work with nonequilibrium Keldysh GFs [32–34]. More precisely, one defines the Floquet-Keldysh GF as

$$\underline{G}_{mn}(\omega) = \int dt_{\text{rel}} \frac{1}{\tau} \int_{-\tau/2}^{\tau/2} dt_{\text{avg}} e^{i(\omega+m\Omega)t - i(\omega+n\Omega)t'} \underline{G}(t,t'), \tag{3}$$

where $t_{\text{rel}} = t - t'$, $t_{\text{avg}} = (t + t')/2$, m and n denote the Floquet indices, and the underline indicates the Keldysh matrix structure

$$\underline{G} = \begin{bmatrix} G^R & G^K \\ 0 & G^A \end{bmatrix} \tag{4}$$

with retarded, Keldysh and advanced component. In Appendix A we mention some properties of Floquet GF that are of importance for the current work. Here, we just want to note that the time average (over one driving period) of a matrix in Floquet space $\boldsymbol{X}(\omega)$ is given by

$$\bar{\boldsymbol{X}}(\omega) = \int_{-\tau/2}^{\tau/2} \frac{dt_{\text{avg}}}{\tau} X(\omega, t_{\text{avg}}) = X_{00}(\omega). \tag{5}$$

Here and in the following, we use boldface to indicate matrices in Floquet space (the only other boldface object is the wave vector $\boldsymbol{k}_\parallel$, but there is no ambiguity).

B. Dyson equation

The Dyson equation for the central Floquet lattice GF reads

$$\underline{G}^{-1}_{mn}(\omega, \boldsymbol{k}_\parallel) = \underline{G}^{-1}_{0,mn}(\omega, \boldsymbol{k}_\parallel) - \underline{\Sigma}_{mn}(\omega, \boldsymbol{k}_\parallel), \tag{6}$$

where $\boldsymbol{k}_\parallel = (k_x, k_y)$ is the crystal momentum in the two translational-invariant directions and $\underline{X}^{-1}_{mn}$ denotes the mn element of the inverse Floquet-Keldysh matrix. The GF corresponding to the noninteracting part of the Hamiltonian, Eq. (1), is given by

$$\underline{G}^{-1}_{0,mn}(\omega, \boldsymbol{k}_\parallel) = \underline{g}^{-1}_{0,mn}(\omega, \boldsymbol{k}_\parallel) - \sum_{\gamma \in \{l,r\}} V_\gamma^2 \underline{g}_\gamma(\omega_n, \boldsymbol{k}_\parallel)\delta_{mn} \tag{7}$$

with the shorthand $\omega_n \equiv \omega + n\Omega$ and

$$\left[\underline{g}_0^{-1}(\omega,\boldsymbol{k}_\parallel)\right]^R_{mn} = (\omega_n + i0^+ - \varepsilon_c)\delta_{mn} - \varepsilon_{mn}(\boldsymbol{k}_\parallel),$$
$$\left[\left(\underline{g}_0^{-1}\omega,\boldsymbol{k}_{\parallel|}\right)\right]^K_{mn} = 0. \tag{8}$$

Here, as usual in steady state, we can neglect the Keldysh component of the inverse Green's function of the layer, and $\varepsilon_{mn}(\boldsymbol{k}_\parallel) = \varepsilon_{mn}(k_x) + \varepsilon_{mn}(k_y)$. The Floquet dispersion relation in the presence of the periodic field described by Eq. (2) is readily found to be [15]

$$\varepsilon_{mn}(k) = -t_c(-i)^{m-n} \times \left[e^{ik} J_{m-n}\left(-\frac{E_0}{\Omega}\right) + e^{-ik} J_{m-n}\left(\frac{E_0}{\Omega}\right)\right] \tag{9}$$

with J_n denoting the nth order Bessel function of the first kind. The surface GF of the semi-infinite, decoupled leads are given by

$$g^R_\gamma(\omega,\boldsymbol{k}_\parallel) = \frac{\omega - \varepsilon_\gamma(\boldsymbol{k}_\parallel)}{2t_\gamma^2} - i\frac{\sqrt{4t_\gamma^2 - [\omega - \varepsilon_\gamma(\boldsymbol{k}_\parallel)]^2}}{2t_\gamma^2},$$
$$g^K_\gamma(\omega,\boldsymbol{k}_\parallel) = 2i[1 - 2f_\gamma(\omega)]\mathrm{Im}g^A_\gamma(\omega,\boldsymbol{k}_\parallel), \tag{10}$$

where $f_{l/r}$ is the Fermi function for the l/r lead and $\varepsilon_\gamma(\boldsymbol{k}_\parallel) = \varepsilon_\gamma - 2t_\gamma[\cos(k_x) + \cos(k_y)]$ is the usual dispersion relation for the simple cubic lattice.

C. Time-averaged observables

In this work, we are interested in time-averaged steady-state observables. In particular, we focus on Green's functions, spectral functions, and the current density through the correlated region. By virtue of Eq. (5), the time average of a Floquet GF is readily obtained by picking out the (0,0) component of the corresponding Floquet matrix. It is then natural to define the time-averaged density of states or spectral function as

$$A(\omega) = -\frac{1}{\pi}\mathrm{Im}G^R_{00}(\omega) \tag{11}$$

which obeys the zeroth-order spectral sum rule (normalization to unity) and reduces to the usual definition in the limit of no periodic driving.

To generalize a formula for a quantity that contains the product of GF's to the corresponding time-averaged one in a Floquet system, care has to be taken as objects which commuted in the original formulation might not commute in the Floquet formalism. Thus, one has to be certain about the ordering in a given expression before applying the straightforward substitutions. For the case of the time-averaged current a correctly ordered expression can be found in [16,35] which, according to Appendix A, is readily generalized to

$$j_{L\to R} = v^2 \int_{-\Omega/2}^{\Omega/2}\frac{d\omega}{2\pi}\int_{\mathrm{B.Z.}}\frac{d\boldsymbol{k}_\parallel}{(2\pi)^2}\mathrm{Re}\,\mathrm{Tr}\mathcal{J} \tag{12}$$
$$= v^2 \int_{-\infty}^{+\infty}\frac{d\omega}{2\pi}\int_{\mathrm{B.Z.}}\frac{d\boldsymbol{k}_\parallel}{(2\pi)^2}\mathrm{Re}\mathcal{J}_{00}, \tag{13}$$

where $\mathcal{J}$ is a Floquet matrix given by

$$\mathcal{J} = \left[\boldsymbol{G}^\mathrm{R}\left(\boldsymbol{g}_l^\mathrm{K} - \boldsymbol{g}_r^\mathrm{K}\right) + \boldsymbol{G}^\mathrm{K}\left(\boldsymbol{g}_l^\mathrm{A} - \boldsymbol{g}_r^\mathrm{A}\right)\right] \tag{14}$$

with uppercase $\boldsymbol{G}$ denoting the lattice Floquet GF of the interacting region and lowercase $\boldsymbol{g}_{l/r}$ referring to the two surface GFs of the decoupled leads. The two alternatives in Eq. (12) can be used to check for consistency. They agree for a sufficiently large Floquet matrix cutoff, and the agreement is a sign of convergence with respect to the cutoff.

D. Floquet DMFT

Since the correlated lattice problem cannot be solved exactly, we have to resort to an approximate scheme for calculating the self-energy $\underline{\Sigma}_{mn}(\omega,\boldsymbol{k}_\parallel)$. To this end, we use DMFT [36–38] in its generalization to the periodically driven systems [13–15]. Within DMFT one neglects the $\boldsymbol{k}_\parallel$ dependence of the self-energy, $\underline{\Sigma}_{mn}(\omega,\boldsymbol{k}_\parallel) \approx \underline{\Sigma}_{mn}(\omega)$, which allows one to calculate the approximate self-energy by the solution of a self-consistently determined impurity problem. In the following, we will provide only a very short description of the DMFT scheme and concentrate on the aspects due to the periodic time dependence;, for more details we refer the reader to the recent review on nonequilibrium DMFT [39].

With an initial guess for the self-energy $\underline{\boldsymbol{\Sigma}}(\omega)$, the first step of DMFT is to obtain the local GF from the self-energy via the $\boldsymbol{k}_\parallel$-integrated Dyson equation for the lattice problem

$$\underline{\boldsymbol{G}}_\mathrm{loc}(\omega) = \int_{\mathrm{B.Z.}}\frac{d\boldsymbol{k}_\parallel}{(2\pi)^2}\left[\underline{\boldsymbol{G}}_0^{-1}(\omega,\boldsymbol{k}_\parallel) - \underline{\boldsymbol{\Sigma}}(\omega)\right]^{-1}. \tag{15}$$

The essential step is now the mapping onto an impurity problem. This step is achieved by considering the Dyson equation of the impurity model

$$\underline{\boldsymbol{G}}^{-1}_\mathrm{imp}(\omega) = \underline{\boldsymbol{g}}^{-1}_\mathrm{imp}(\omega) - \underline{\boldsymbol{\Delta}}(\omega) - \underline{\boldsymbol{\Sigma}}(\omega). \tag{16}$$

Here, $\underline{\boldsymbol{g}}^{-1}_\mathrm{imp}(\omega)$ is the noninteraction Floquet-Keldysh GF of the impurity which is defined as in Eq. (8) but without $\varepsilon_{mn}(\boldsymbol{k}_\parallel)$. Demanding equality of the local GF and the impurity GF, $\underline{\boldsymbol{G}}_\mathrm{loc}(\omega) \stackrel{!}{=} \underline{\boldsymbol{G}}_\mathrm{imp}(\omega)$, we get the effective bath hybridization function

$$\underline{\Delta}_{mn}(\omega) = \underline{g}^{-1}_{\mathrm{imp},mn}(\omega) - \left[\underline{G}^{-1}_{\mathrm{loc}\ mn}(\omega) + \underline{\Sigma}_{mn}(\omega)\right], \tag{17}$$

where we have explicitly reintroduced the Floquet indices (instead of the boldface matrices before) to emphasize that the corresponding impurity problem is now subject to a time-periodic driving. At this stage one inputs the obtained hybridization $\underline{\boldsymbol{\Delta}}(\omega)$ from Eq. (17) to an impurity solver, obtains a new self-energy, and iterates the steps above until convergence.

1. *Floquet-diagonal self-energy*

As we have seen above, the Floquet DMFT equations lead to a periodically time-dependent bath for the impurity problem which makes the latter hard to solve. In the literature, the Floquet-DMFT impurity problem is treated with low-order perturbative expansions that work directly in the time domain [13,15,40–45], for example, IPT. While this is numerically possible to carry out quite easily, the drawbacks of such solvers is of course their limitation to certain parameter regimes, in

the interaction and/or hybridization strength. There is also a limited error control when such solvers are applied to new situations where no benchmarks are available. In the present work, we use instead the AMEA, a nonperturbative impurity solver, which is very accurate in addressing steady-state situations in a wide range of parameters [17,18]. When addressing photovoltaic effects, we are in the regime of weak periodic driving where first-order photon absorption processes are dominant. In this case, off-diagonal Floquet terms are suppressed by a factor $\alpha \equiv t_c E_0/\Omega^2$ [46]. Motivated by this, we restrict the self-energies to be diagonal in the Floquet indices. This is in analogy with the original DMFT approximation where one takes the self-energy as being diagonal in lattice indices. It allows the simplification of the Floquet impurity problem to a nonequilibrium steady-state one, albeit with time-translation invariance. Of course, the periodic time dependence of the problem remains via the Floquet-index dependence of the noninteracting Green's function. In more technical terms, instead of solving an impurity problem with the hybridization Eq. (17), we take the time average of the local GF, i.e., $\underline{G}_{\mathrm{loc}\,00}(\omega)$, and calculate from it a time-translation-invariant hybridization function, given by

$$\underline{\Delta}(\omega) = \underline{g}^{-1}_{\mathrm{imp}}(\omega) - [(\underline{G}_{\mathrm{loc},00})^{-1}(\omega) + \underline{\Sigma}(\omega)]. \tag{18}$$

The resulting steady-state impurity problem is then solved to obtain $\underline{\Sigma}(\omega)$, and the Floquet self-energy is reconstructed as

$$\underline{\Sigma}_{mn}(\omega) = \underline{\Sigma}(\omega + n\Omega)\delta_{mn}. \tag{19}$$

This self-energy, plugged into Eq. (6), in turn yields the full Floquet lattice GF. This approximation for the self-energy (FDSA) is of course an *ad hoc* one, since the AMEA solution of a periodic time-dependent problem would have been numerically too time consuming. To check its range of validity, we carry out a numerical test in Appendix C where we use IPT and find that it is very accurate in the parameter region we are interested in.

2. Auxiliary master equation approach impurity solver

For the sake of completeness, we briefly present the DMFT impurity solver used to obtain our results, namely, the so-called AMEA. For details we refer to our recent work [16–19]; for the IPT impurity solver, see Appendix C. The key idea behind the DMFT-AMEA impurity solver, in close analogy with the exact diagonalization (ED) [47] in equilibrium, is to replace the bath of the original impurity problem obtained via the DMFT cycle and defined by the hybridization function [cf. (18)] $\underline{\Delta}(\omega)$, with an auxiliary one described by a corresponding hybridization function $\underline{\Delta}_{\mathrm{aux}}(\omega)$.

In contrast to ED, this auxiliary bath is an open quantum system consisting of a finite number of sites embedded into a Markovian environment. One should, however, point out that the dynamics at the impurity site are non-Markovian. This auxiliary system, being finite, can be solved exactly by conventional Krylov-space methods [17] or matrix-product states [18], and the self-energy at the impurity site can be extracted. The only approximation entering the approach comes from the difference between the $\underline{\Delta}(\omega)$, and the auxiliary one $\underline{\Delta}_{\mathrm{aux}}(\omega)$ provided by the non-Markovian open system. The parameters of the latter are determined by a fit requiring that $\underline{\Delta}(\omega) \approx \underline{\Delta}_{\mathrm{aux}}(\omega)$ as close as possible. This mapping shows an exponential convergence [19] with respect to the number of bath sites in the auxiliary system, allowing quick convergence of results. This has to be, of course, confronted with the exponential growth in the numerical effort to solve the open quantum system.

TABLE I. The parameters for the two considered regimes in accordance with Eq. (1) where t_c serves as the unit of energy. Additionally, we work roughly at room temperature by setting $k_b T = 0.02$ in all calculations. Please recall, $\Gamma = 2\pi|V|^2\rho(\omega = 0)$, D denotes the bandwidth of the leads.

	U	E_0	$t_{l/r}$	$\varepsilon_{l/r}$	D	Δ_{ss}	$V_{l/r}$	$\Gamma_{l/r}$
	H_c			H_{leads}			H_{coupling}	
R_a	30	12	1/6	±12	2	22	0.8	9.6
R_b	12	2	1/6	±3	2	4	0.8	9.6

IV. RESULTS AND DISCUSSION

We investigate our model in two different regimes, R_a and R_b characterized by different values of the Hubbard gap. We show results for time-averaged quantities, namely, the current density, Eq. (12), and (time-averaged-) spectral/Green's functions, Eq. (11), as the driving frequency is varied. For regime R_a, we check our method and implementation by considering the model in a parameter regime incompatible with impact ionization where the result for the current is severely limited by simple arguments as discussed below. The second case, R_b, allows us to directly study the effect of impact ionization. The corresponding parameters are summarized in Table I.

A. General considerations: Direct excitations versus impact ionization

In order to yield impact ionization processes the bandwidth of the upper Hubbard band of the central correlated layer must be larger than twice the gap. Only if this is the case, the photoexcited electron (or hole) in the upper (lower) Hubbard band has enough excess energy to excite an additional electron across the band gap, i.e., to create a second electron-hole pair. Before presenting our actual results, we would like to first discuss the physical processes that we expect upon increasing the photon frequency Ω. For the following discussion, we will assume that only first-order light absorption processes are possible.

First, for $\Omega < \Delta_{ss}$, we have a situation with no current, provided the central DOS has a true gap as in Fig. 1. In the case of a partial gap, as we have in Fig. 4(c), the current should be suppressed, as multiple absorption processes will be needed to overcome the steady-state gap.

For larger frequencies $\Delta_{ss} < \Omega < \Delta_{ss} + 2D$ electrons coming from the left lead are photoexcited to an energy within the bandwidth of the right lead and can directly escape, without the need of further scattering. We refer to such processes, which are illustrated in Fig. 1(a), as direct excitations. In addition, the strong hybridization with the leads ensures that a charge carrier with the right energy quickly leaves the central layer to the other side. Note that in a noninteracting model, say a band

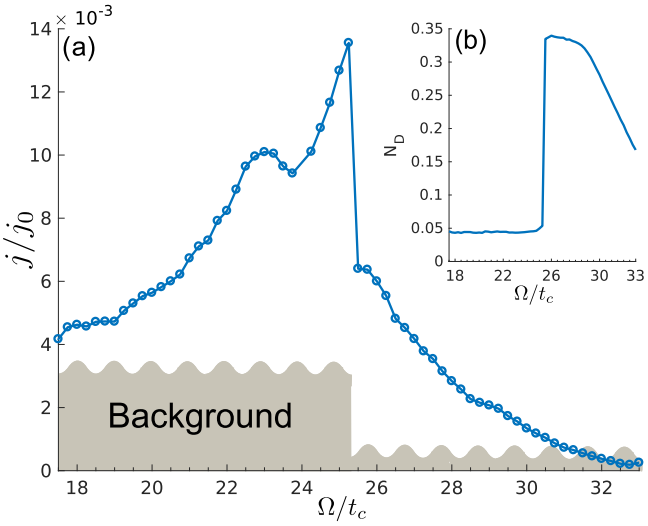

FIG. 3. (a) Time-averaged current density and (b) double occupancy as a function of driving frequency for a situation with a gap larger than the bandwidth so that impact ionization is impossible. Parameters as in R_a in Table I.

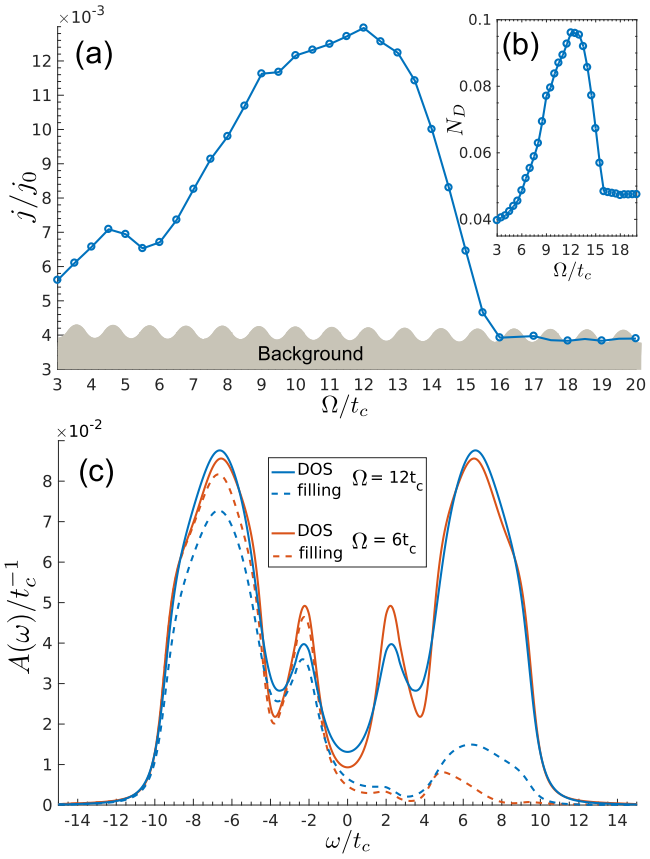

FIG. 4. (a) Time-averaged current density (in units of $j_0 = e\hbar/t_c a^2$) and (b) double occupancy as a function of driving frequency for parameters compatible with impact ionization, R_b in Table I. The current and the double occupancy show the same behavior in the region of the main peak as expected for impact ionization processes. (c) Time-averaged spectral function $A(\omega)$ and corresponding filling $A(\omega)f(\omega)$ [here, $f(\omega)$ denotes the nonequilibrium distribution function] for representative driving frequencies for direct excitations ($\Omega = 6$) and impact ionization ($\Omega = 12$).

insulator for the central layer, this would be the only Ω regime with nonzero current.

Next, we could have, in principle, an intermediate frequency region where the driving frequency is too big for a direct excitation but too low for steady-state impact ionization, $\Delta_{ss} + 2D < \Omega < 2\Delta_{ss}$. However, we will work with parameters such that $\Delta_{ss} = 2D$ and therefore this region is absent.

Finally, for $\Omega > 2\Delta_{ss}$ we enter the regime of impact ionization, illustrated in Fig. 1(b). In this regime each absorbed photon produces two carriers, so that one should expect a current up to twice as large for fixed absorption rate. The abrupt increase of the current at a given frequency hence signals the presence of impact ionization. In our model which neglects phonons and considers the steady state, intraband scattering is not effective in allowing high-energy electrons to dissipate energy in the upper Hubbard band as we argue in Appendix B. For this reason, we can be certain that the current observed for $\Omega > 2\Delta_{ss}$ can only be due to interband scattering from which steady-state impact ionization should be the dominant one.

B. Current and spectral functions

Another aspect that we need to consider before presenting the results for the current density, is that a certain background current is intrinsic within the AMEA approach in the presence of spectral gaps or a band edge. This is due to the fact that the fit to the hybridization function cannot go to zero abruptly when a gap is present, since sharp features are hard to resolve when fitting with smooth functions. We have therefore estimated a "background current" to be removed from the results presented in Figs. 4, 3, and 5(b). For example, for large Ω the current should go to zero in all cases, as there are no final states available for photoexcitation, but instead it settles at a finite value.

This value is the same as the one we get when the external drive is switched off. The background that is estimated by switching off the electric field is indicated by the wiggly lines in Figs. 4 and 3 as well as (5b) and agrees with the residual AMEA current in the region where no current is expected because of large (small) Ω. Unfortunately, the background current is not always independent of frequency, so that it is sometimes hard to identify it. This occurs, for example, when the accuracy of the AMEA fit changes considerably in different frequency regions due to a crossover to different DMFT solutions, as is the case in Fig. 5.

1. *Regime without impact ionization*

We start by considering the system in the large gap regime, R_a in Table I. In this case, for frequencies beyond $\Delta_{ss} + 2D$ (see Sec. IV A), no current should be expected, as high-energy doublons are trapped in the higher Hubbard band and cannot dissipate their energy (see also Appendix B). The corresponding spectral function and filling is shown in Fig. 5. Since impact ionization is not allowed, there should be a substantial current density only in the regime of direct excitations $22 < \Omega < 26$. The corresponding plot in Fig. 3 indeed shows a current above

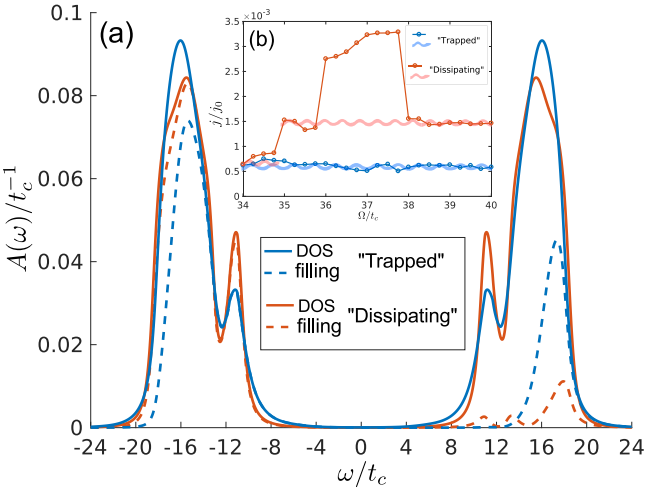

FIG. 5. (a) Time-averaged spectral function and filling at $\Omega = 37$. (b) Time-averaged current density as a function of driving frequency for the two solutions discussed in Sec. IV B 3. Parameter set R_a as in Fig. 3.

the background in this expected frequency region and a clear double peak structure. The latter feature is a simple DOS effect consistent with the picture of direct excitations [48]. The fact that the current shows substantial broadening on the edges of the expected frequency region is due to the above-mentioned limited resolution of the AMEA fitting procedure. Notice that within the FDSA the impurity solver has knowledge about the frequency through the DMFT self-consistency, which, for example, affects the occupation of the upper Hubbard band. Further, we can see that in the region $\Omega > 25$ the background current is much smaller than at lower frequency. This is because the spectral situation changes around that point, since for $\Omega > 24$ electrons can get excited from the lower lead directly in the trapping region above the right lead, leading to an accumulation of high-energy doublons. In Fig. 5 this is reflected in a considerable filling of high-frequency states. The different situation for $\Omega > 25$ in turn allows for a better DMFT fit. This is the reason why also the background level in Fig. 3 changes around $\Omega = 25$ [49]. In summary, the current in Fig. 3 is consistent, within the limited accuracy of the present method, with the physical expectations and we can be confident that our approach captures the relevant physics.

2. Regime with impact ionization

Having established the correctness of our approach in the simple but nontrivial large gap case, we now consider the second set of parameters R_b in Table I. In this case, there is the possibility of impact ionization as sketched in Fig. 1 and discussed in Sec. IV A. The current density as a function of Ω is plotted in Fig. 4 where we can identify three domains separated by smooth transitions: The region around the first maximum at $\Omega \approx 4.5$ corresponds to direct excitations, which are allowed for $4 < \Omega < 8$ (see Sec. IV A). The second domain, hosting the main peak, is consistent with impact ionization, $8 < \Omega < 16$ [50]. The maximum current for these frequencies is roughly twice as large as the one in the region of direct excitations. This corroborates the fact that a single photoabsorption produces two charge carriers in the frequency region for impact ionization. The current for large driving frequencies $\Omega > 16$ is just the background current mentioned above.

From Figs. 4(b) and 4(c), we can see that going from a situation of direct excitations to one with impact ionization the double occupation and, in particular, the occupation of high-energy states (high-energy doublons) compatible with impact ionization increases. This is consistent with our interpretation that the second peak in Fig. 4(a) originates from the latter process. Also in experiment such an abrupt doubling of the current could serve as a clear indication of impact ionization. For example, this can be used to detect impact ionization in semiconductor quantum dots [51] (cf. Ref. [52]).

3. Instability to multiparticle impact ionization processes

Coming back to the large gap case, R_a, an intriguing finding of our analysis is that we actually find two distinct nonequilibrium solutions for large driving frequencies. That is, for $\Omega \gtrsim 35$ there are two DMFT solutions (depending on the initial DMFT self-energy) (see inset of Fig. 5). While this makes the behavior of the current in this region inconclusive, it is instructive to study the spectral properties of these two solutions, which we plot in Fig. 5. In the first solution there is an accumulation of high-energy doublons in the upper Hubbard band and a suppressed current. The second solution is not showing this charge accumulation and supports a substantial steady-state current above the background for $33 \lesssim \Omega \lesssim 38$ hinting at a possible dissipation channel. This second solution gets unstable at lower driving frequencies below $\Omega \approx 35$. On the other hand, this second solution becomes more stable at larger values of the electric field (not shown). We speculate that this behavior may be due to the occurrence of higher-order impact ionization as explained in the following:

Higher-order steady-state impact ionization. As already mentioned, a steady-state process must be such that all the energy going into the system is dissipated again. For the present situation we have one *source* of energy—the driving field characterized by Ω—and one *drain* of energy—namely, the possible energy differences of the leads given by $\phi \equiv \varepsilon_r - \varepsilon_l \pm D$, i.e., for the parameters considered $22 < \phi < 26$. Therefore, we must have

$$m\Omega \stackrel{!}{=} n\phi, \quad \text{with } n \geqslant m \tag{20}$$

in order for a process to be allowed. In view of Eq. (20), direct excitations correspond to $m = n = 1$ while ordinary impact ionization is obtained when $n = 2, m = 1$. The next process is $n = 3, m = 2$. Here two "photons" excite three electrons over the gap. Of course, this process is higher order, so that it will be visible only at large driving intensities. At this point, one can argue that the second metastable DMFT solution mentioned above is related to the latter process as it falls in the corresponding regime with $m = 3, n = 2$, i.e., $33 < \Omega_{2m=3n} < 39$. This interpretation is supported by the fact that the second solution gets more stable at higher light intensities. However, we stress that the interpretation is still very speculative as, due to several reasons connected with our approach, this frequency region is difficult to address.

V. CONCLUSION AND OUTLOOK

We have investigated the effect of impact ionization on the current density through a periodically driven Mott insulator in the (periodic)steady-state using a simplified model for a Mott photovoltaic system. As a function of driving frequency we identify a crossover between a regime of direct excitations into one in which impact ionization takes place and the current is substantially enhanced.

We also consider the deep Mott regime, where the Hubbard gap is larger than the bandwidth such that impact ionization is not possible. Here, we find hints for competing nonequilibrium phases of the system for larger driving frequencies. We give a possible interpretation of this behavior in terms of higher-order impact ionization processes where multiple photoexcitations together with higher-order interband scattering open a dissipation channel supporting a nonvanishing current. The present work addresses a simplified model to study photovoltaic processes in a Mott solar cell but can be generalized in several directions to make for a more realistic modeling of actual solar cells. For instance, realistic metallic leads have typically a wide band and are only partially filled. Instead, we use narrow bands in the leads which are optimally suited to separate impact ionization from other processes. Such narrow lead bands can be realized in organic crystals which have a small hopping amplitude or in materials with strong spin-orbit coupling which splits the band structure into several subbands. The extreme situation of zero bandwidth can be realized by bridging the photoactive region through molecules to the leads. Indeed, this approach is employed for semiconductor quantum dots [53], e.g., with the purpose to extract hot, photoexcited carriers from the quantum dot [54,55]. Moreover, for solar cells based on oxide heterostructures the correlated region should consist of multiple layers making for the possibility to model an electric field gradient which separates electrons and holes. On top of this, one should account for electron-phonon interactions and also long-range Coulomb forces to address bound excitons.

As discussed in Sec. III D 1, in this work we have restricted ourselves to a time-translation-invariant hybridization function. In principle, the solution of the full time-periodic (Floquet) impurity problem can also be obtained within AMEA, and it would therefore be interesting to address the effects of a time-dependent self-energy beyond the FDSA. This would, however, be numerically rather expensive and relevant only in the case of strong driving which is not relevant for solar cell applications.

ACKNOWLEDGMENTS

We would like to thank D. Fugger, I. Titvinidze, W. von der Linden, M. Eckstein, H. G. Evertz, and F. Maislinger for fruitful discussions. This work was partially supported by the Austrian Science Fund (FWF) within Projects P26508 and F41 (SFB ViCoM), as well as NaWi Graz. The calculations were partly performed on the D-Cluster Graz and on the VSC-3 cluster Vienna.

APPENDIX A: PROPERTIES OF FLOQUET GF

First, the Floquet transform, defined through Eq. (3), for a GF that depends only on the time difference $G(t,t') = G(t - t') = G(t_{\rm rel})$ leads to a diagonal Floquet matrix

$$\int dt_{\rm rel} \int_{-\tau/2}^{\tau/2} \frac{dt_{\rm avg}}{\tau} e^{i\omega_m t - i\omega_n t'} G(t_{\rm rel}) = G(\omega_n)\delta_{mn} \tag{A1}$$

with $\omega_n \equiv \omega + n\Omega$. The Floquet matrix entries are then not independent, but we have

$$G_{mn}(\omega) = G_{m-n,0}(\omega + n\Omega). \tag{A2}$$

For the important case of the equal-time correlation function, we get

$$G(t = t') = \sum_{m,n} e^{-i(m-n)\Omega t} \int_{-\Omega/2}^{\Omega/2} \frac{d\omega}{2\pi} G_{mn}(\omega), \tag{A3}$$

and for its time average

$$\begin{aligned} \int_{-\tau/2}^{\tau/2} \frac{d\tau}{\tau} G(t = t') &= \sum_n \int_{-\Omega/2}^{\Omega/2} \frac{d\omega}{2\pi} G_{nn}(\omega) \\ &= \int_{-\infty}^{+\infty} \frac{d\omega}{2\pi} G_{00}(\omega). \end{aligned} \tag{A4}$$

Second, we want to note that the time average of a quantity is always encoded in the diagonal contributions of its corresponding Floquet matrix and thus by virtue of Eq. (A2) contained in the $m = n = 0$ component alone. Finally we want to mention the most appealing aspect of Floquet GFs, namely, that a convolution in time is mapped to the multiplication of the corresponding Floquet GFs which leads to an algebraic Dyson equation in frequency.

APPENDIX B: INTRABAND SCATTERING PROCESSES IN STEADY STATE

It is important to stress that in our steady-state setup and in the absence of other inelastic scattering processes besides electron-electron interaction, high-energy doublons lying above the upper edge of the upper lead cannot easily dissipate their energy via intraband processes so as to be able to exit via the drain lead. Indeed, if a particle (A) loses a certain energy Δ, a second particle (B) must, at the same time, gain that same amount. For the case in which B is in the upper Hubbard band, this would produce an accumulation of particles in the high-energy region of the band, as observed in Fig. 5. However, in a stationary situation the rate of particles flowing into this energy region must be equal to their outflow. For this reason, these high-energy particles must also find a channel to dissipate their energy, but again only electron scattering is available. For the case in which (B) is in the lower Hubbard band, this process would produce an accumulation of particles in the upper part and a depletion in the lower part of the band, and we have the same situation as above.

The only possibility is that the energy Δ is large enough so that particle B is excited across the lead gap, i.e., impact ionization. In the situation of Sec. IV B 1, however, the central bandwidth is smaller than the gap, so that this is possible only within multiscattering and absorption processes. This statement may sound counterintuitive, and in fact in a realistic situation, acoustic phonons will carry away the energy excess.

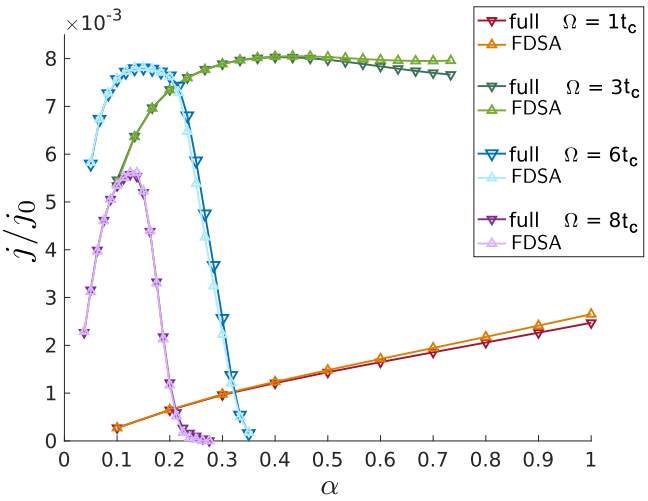

FIG. 6. Test of the FDSA (see Sec. III D 1). Time-averaged current as a function of the effective coupling constant $\alpha \equiv t_c E_0/\Omega^2$ for different driving frequencies obtained with IPT. The lines labeled with "FDSA" correspond to data computed with the FDSA, while the label "full" refers to the solution with the full Floquet impurity problem. For $\alpha \lesssim 1/2$, the FDSA approximation is very reliable.

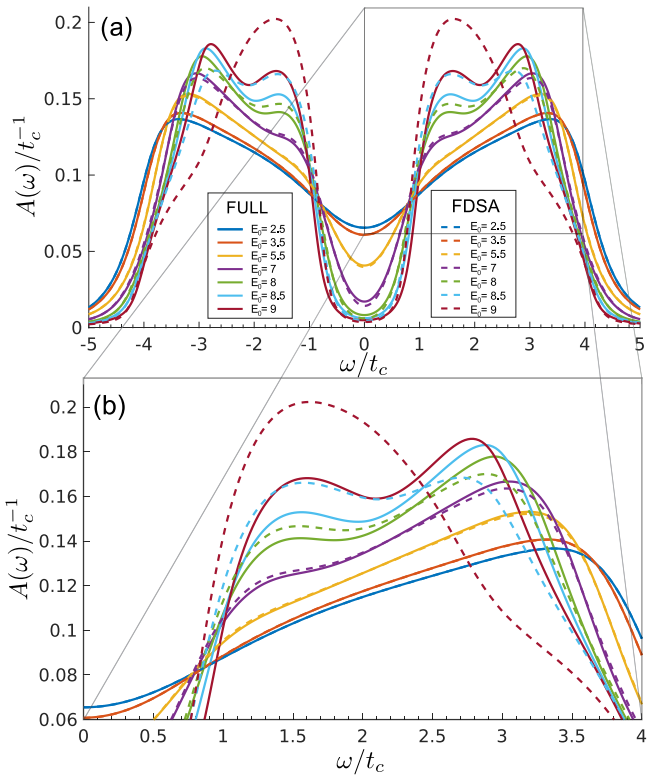

FIG. 7. Test of the FDSA introduced in Sec. III D 1. (a) Time-averaged spectral function for different electric field strengths at constant frequency $\Omega = 5$ obtained with IPT. (b) The lower plot shows a zoom onto the upper Hubbard band as indicated by the box in the upper plot. Numerical parameters are the same as in Fig. 6.

Therefore, the present results are valid for the case that these scattering processes are faster than the electron-phonon dissipation rate. In principle, also magnons are relevant for energy dissipation [12,56]. However, since magnons consist themselves of electronic excitations, electron-magnon scattering is simply another form of electron scattering and the argument above remains valid. In a steady-state situation we are not able to steadily transfer energy and excite magnons in the central Hubbard layer.

APPENDIX C: TEST OF THE VALIDITY OF THE FLOQUET-DIAGONAL SELF-ENERGY

The goal of this Appendix is to test the range of validity for the FDSA. The AMEA impurity solver, while being numerically controlled, is computationally expensive when carrying out a real-time evolution. Hence, for this analysis we employ IPT as an impurity solver, which is much cheaper. Specifically, we compare time-averaged observables from calculations with and without the FDSA.

For the sake of simplicity and because the nature of the approximation does not depend on it, we present here checks where the total system defined by Eq. (1) is two dimensional. That is, the correlated central region is a Hubbard chain instead of a layer. In Figs. 6 and 7 we plot data for $U = 5$, $V_l = V_r = 0.1$, and zero temperature $k_b T = 0$. Figure 6 shows the steady-state current density as a function of the effective driving strength $\alpha = \frac{t_c E_0}{\Omega^2}$ for different driving frequencies Ω. In Fig. 7, we complement this with the results for the local spectral function at $\Omega = 5$ for selected electric field strengths E_0. Together, they confirm that the FDSA is justified for the moderate driving intensities and large frequencies, which we study within AMEA in this paper. The reason why the current approaches zero for the highest two considered Ω's for large electric fields is due to dynamical localization [57] which localizes the spectrum in frequency (see also Fig. 7), and therefore suppresses the current for these higher driving frequencies as "photonic" excitations are no longer possible within the spectrum. A more detailed analysis and benchmark in different parameter regimes with different impurity solvers is beyond the scope of this work and will be presented elsewhere.

For the sake of completeness, let us briefly recapitulate the nonequilibrium IPT equations that have been used for this analysis. In short, IPT is second-order perturbation theory in the Hubbard interaction U. However, in the case of the one-band Hubbard model at particle-hole symmetry it turns out to be exact in the limit of infinite interaction as well. It is hence quite reliable in this case, whereas it fails off particle-hole symmetry. In technical terms, IPT is very simple as the self-energy for a given hybridization $\underline{\Delta}(t,t')$ is given by

$$\Sigma^{\lessgtr}(t,t') = U^2 \mathcal{G}_0^{\lessgtr}(t,t')\mathcal{G}_0^{\lessgtr}(t,t')\mathcal{G}_0^{\gtrless}(t',t), \tag{C1}$$

where $G^{</>}$ refer to the lesser/greater GF in the Keldysh formalism and we introduced the so-called Weiss GF

$$\underline{\mathcal{G}}_0^{-1}(t,t') = \underline{g}_{\text{imp}}^{-1}(t,t') - \underline{\Delta}(t,t'). \tag{C2}$$

[1] B. Keimer, S. A. Kivelson, M. R. Norman, S. Uchida, and J. Zaanen, Nature (London) **518**, 179 (2015).
[2] J. M. D. Coey and M. Venkatesan, J. Appl. Phys. **91**, 8345 (2002).
[3] C. Kim, A. Y. Matsuura, Z.-X. Shen, N. Motoyama, H. Eisaki, S. Uchida, T. Tohyama, and S. Maekawa, Phys. Rev. Lett. **77**, 4054 (1996).
[4] A. C. Hewson, *The Kondo Problem to Heavy Fermions* (Cambridge University Press, Cambridge, 1993).
[5] E. Manousakis, Phys. Rev. B **82**, 125109 (2010).
[6] J. E. Coulter, E. Manousakis, and A. Gali, Phys. Rev. B **90**, 165142 (2014).
[7] E. Assmann, P. Blaha, R. Laskowski, K. Held, S. Okamoto, and G. Sangiovanni, Phys. Rev. Lett. **110**, 078701 (2013).
[8] W. Shockley and H. J. Queisser, J. Appl. Phys. **32**, 510 (1961).
[9] M. Eckstein and P. Werner, Phys. Rev. B **84**, 035122 (2011).
[10] P. Werner, K. Held, and M. Eckstein, Phys. Rev. B **90**, 235102 (2014).
[11] M. Eckstein and P. Werner, Phys. Rev. B **88**, 075135 (2013).
[12] M. Eckstein and P. Werner, Phys. Rev. Lett. **113**, 076405 (2014).
[13] P. Schmidt and H. Monien, arXiv:cond-mat/0202046.
[14] A. V. Joura, J. K. Freericks, and T. Pruschke, Phys. Rev. Lett. **101**, 196401 (2008).
[15] N. Tsuji, T. Oka, and H. Aoki, Phys. Rev. B **78**, 235124 (2008).
[16] E. Arrigoni, M. Knap, and W. von der Linden, Phys. Rev. Lett. **110**, 086403 (2013).
[17] A. Dorda, M. Nuss, W. von der Linden, and E. Arrigoni, Phys. Rev. B **89**, 165105 (2014).
[18] A. Dorda, M. Ganahl, H. G. Evertz, W. von der Linden, and E. Arrigoni, Phys. Rev. B **92**, 125145 (2015).
[19] A. Dorda, M. Sorantin, W. von der Linden, and E. Arrigoni, New J. Phys. **19**, 063005 (2017).
[20] G. De Filippis, V. Cataudella, E. A. Nowadnick, T. P. Devereaux, A. S. Mishchenko, and N. Nagaosa, Phys. Rev. Lett. **109**, 176402 (2012).
[21] H. Okamoto, T. Miyagoe, K. Kobayashi, H. Uemura, H. Nishioka, H. Matsuzaki, A. Sawa, and Y. Tokura, Phys. Rev. B **82**, 060513 (2010).
[22] A. S. Mishchenko, N. Nagaosa, Z.-X. Shen, G. De Filippis, V. Cataudella, T. P. Devereaux, C. Bernhard, K. W. Kim, and J. Zaanen, Phys. Rev. Lett. **100**, 166401 (2008).
[23] While the inclusion of phonons is possible within the present approach, it would take severe method development and numerical effort to treat them nonperturbatively.
[24] In a realistic system, this mechanism is provided by an intrinsic electric field, such as the one of p-n junctions or the polar field present in TMO heterostructures [7].
[25] Strictly speaking this restricts only the right coupling but to stay at particle-hole symmetry we choose a symmetric hybridization.
[26] This ensures that $\alpha < 0.5$ for all calculations which is needed for the validity of the Floquet diagonal self-energy approximation (see Sec. III D 1 and Appendix C).
[27] F. Faisal, Comput. Phys. Rep. **9**, 57 (1989).
[28] S. C. Althorpe, D. J. Kouri, D. K. Hoffman, and N. Moiseyev, Chem. Phys. **217**, 289 (1997).
[29] T. Brandes, Phys. Rev. B **56**, 1213 (1997).
[30] T. Brandes and J. Robinson, Phys. Status Solidi B **234**, 378 (2002).
[31] D. F. Martinez, J. Phys. A: Math. Gen. **36**, 9827 (2003).
[32] L. P. Kadanoff and G. Baym, *Quantum Statistical Mechanics: Green's Function Methods in Equilibrium and Nonequilibrium Problems* (Addison-Wesley, Redwood City, 1962).
[33] J. Schwinger, J. Math. Phys. **2**, 407 (1961).
[34] L. V. Keldysh, Sov. Phys. J. Exp. Theor. Phys. **20**, 1018 (1965).
[35] H. Haug and A.-P. Jauho, *Quantum Kinetics in Transport and Optics of Semiconductors* (Springer, Heidelberg, 1998).
[36] W. Metzner and D. Vollhardt, Phys. Rev. Lett. **62**, 324 (1989).
[37] A. Georges and G. Kotliar, Phys. Rev. B **45**, 6479 (1992).
[38] A. Georges, G. Kotliar, W. Krauth, and M. J. Rozenberg, Rev. Mod. Phys. **68**, 13 (1996).
[39] H. Aoki, N. Tsuji, M. Eckstein, M. Kollar, T. Oka, and P. Werner, Rev. Mod. Phys. **86**, 779 (2014).
[40] A. Lubatsch and J. Kroha, Ann. Phys. (NY) **18**, 863 (2009).
[41] N. Tsuji, T. Oka, and H. Aoki, Phys. Rev. Lett. **103**, 047403 (2009).
[42] R. Frank, New J. Phys. **15**, 123030 (2013).
[43] R. Frank, Appl. Phys. B **113**, 41 (2013).
[44] W.-R. Lee and K. Park, Phys. Rev. B **89**, 205126 (2014).
[45] A. V. Joura, J. K. Freericks, and A. I. Lichtenstein, Phys. Rev. B **91**, 245153 (2015).
[46] The E_0/Ω part is self-evident as it appears explicitly in the Hamiltonian and as an argument of the Bessel functions. The parameter is also proportional to t_c since as the latter goes to zero the explicit time dependence vanishes from the problem as well. The last factor of Ω in the denominator comes from a perturbative argument. Since the diagonal entries in the Floquet matrix are shifted energetically by a factor of Ω, corrections around the diagonal limit, that is, off-diagonal terms, are suppressed by precisely this factor, leaving us overall with the dimensionless quantity $\alpha = t_c E_0/\Omega^2$.
[47] M. Caffarel and W. Krauth, Phys. Rev. Lett. **72**, 1545 (1994).
[48] A double peak structure already appears when considering only the density of states at the initial and final state of the photoexcitation in the lower/upper Hubbard band, i.e., $A(\omega)A(\omega+\Omega)$, where the initial states are restricted to the support of the left lead.
[49] Even if the value of the cost function in the AMEA fit for the two situations would be the same, the background current can still be very different as the resolution of the (lead) band edges might differ substantially.
[50] It should be noted that in the steady-state situation the Ω region where (steady-state) impact ionization is possible, is more restrictive than in the case of an isolated Hubbard system after a photoexcitation (see Sec. IV B 3).
[51] J. J. H. Pijpers, R. Ulbricht, K. J. Tielrooij, A. Osherov, Y. Golan, C. Delerue, G. Allan, and M. Bonn, Nat. Phys. **5**, 811 (2009).
[52] O. E. Semonin, J. M. Luther, S. Choi, H.-Y. Chen, J. Gao, A. J. Nozik, and M. C. Beard, Science **334**, 1530 (2011).
[53] H. Wang, E. R. McNellis, S. Kinge, M. Bonn, and E. Cánovas, Nano Lett. **13**, 5311 (2013).
[54] W. A. Tisdale, K. J. Williams, B. A. Timp, D. J. Norris, E. S. Aydil, and X.-Y. Zhu, Science **328**, 1543 (2010).
[55] E. Cánovas, H. Wang, M. Karakus, and M. Bonn, Chem. Phys. **471**, 54 (2016).
[56] Z. Lenarcic and P. Prelovsek, Phys. Rev. Lett. **111**, 016401 (2013).
[57] D. H. Dunlap and V. M. Kenkre, Phys. Rev. B **34**, 3625 (1986).

2.3 Publication 3: Stochastic Wavefunctions

The article titled *Auxiliary master equation approach within stochastic wave functions: Application to the interacting resonant level model* was published in Physical Review E. **99** 043303, April 2019.
The work was conducted by Max Sorantin (MS) as first author together with Delia Fugger (DF) and Antonius Dorda as co-authors under the supervision of Wolfgang von der Linden (WL) and Enrico Arrigoni (EA). EA initiated this work with the suggestion to test the SWF approach to solve the auxiliary many-body Lindblad system. AD developed and tested a first implementation of the latter in Matlab as well as C++ for the SIAM, which was later optimized and amended to treat the IRLM by MS. MS and DF, under supervision and guidance of WL, worked on possibilities to optimize the calculation of the frequency dependent GF with respect to the needed number of realizations taking the statistical error into account in the Fourier transform (not fruitful). Thereby, MS conducted the analytical calculations within Baysian probability theory while DF performed the numerical tests and data analysis. The idea to utilize a variable-rank parametrization and combining it with a gradient based optimization algorithm was put forward by WL and it was tested within a bachelor thesis by Franz Scherr, supervised and guided by WL and MS. Franz Sherr also provided the first implementation of the new fitting approach in python within the machine learning environment tensorflow, which was later amended to a stepwise increase in system size by MS. The finite size scaling scheme was developed between MS and EA. All calculations and data analysis of presented results were done by MS. The manuscript was mainly written by MS and partly by DF, providing the description of the SWF algorithm, and revised by EA and WL. All authors were involved in the discussion of results.

Auxiliary master equation approach within stochastic wave functions: Application to the interacting resonant level model

Max E. Sorantin,* Delia M. Fugger, Antonius Dorda, Wolfgang von der Linden, and Enrico Arrigoni†
Institute of Theoretical and Computational Physics, Graz University of Technology, 8010 Graz, Austria

(Received 11 December 2018; revised manuscript received 28 February 2019; published 4 April 2019)

We present further developments of the auxiliary master equation approach (AMEA), a numerical method to simulate many-body quantum systems in as well as out of equilibrium and apply it to the interacting resonant level model to benchmark the new developments. In particular, our results are obtained by employing the stochastic wave functions method to solve the auxiliary open quantum system arising within AMEA. This development allows us to reach extremely low wall times for the calculation of correlation functions with respect to previous implementations of AMEA. An additional significant improvement is obtained by extrapolating a series of results obtained by increasing the number of auxiliary bath sites, N_B, used within the auxiliary open quantum system formally to the limit of $N_B \to \infty$. Results for the current-voltage characteristics and for equilibrium correlation functions are compared with the one obtained by exact and matrix-product states–based approaches. Further, we complement this benchmark by the presentation of spectral functions for higher temperatures where we find different behaviors around zero frequency depending on the hybridization strength.

DOI: 10.1103/PhysRevE.99.043303

I. INTRODUCTION

Quantum impurity models have a long history in many-body quantum mechanics. Some prominent examples include the single impurity Anderson model [1] (SIAM), the (Anderson-) Holstein model [2], the Kondo model [3], and the interacting resonant level model [4] (IRLM). They feature interesting, unconventional physics such as the Kondo effect [5] or negative differential conductance [6] and allow for experimental in terms of quantum dots [7]. Besides this, the solution of quantum impurity problems alone constitutes already a crucial task in dynamical mean-field theory [8].

Since the late 2000s, there has been increasing interest in quantum impurities out of equilibrium and the development of numerical methods which are able to accurately simulate such systems poses a great challenge for contemporary condensed matter theory. Existing methods [9] include iterated perturbation theory [10], numerical renormalization group [11], real-time quantum Monte Carlo (QMC) [12,13], noncrossing approximation and beyond [14,15], imaginary-time QMC supplemented by a double analytical continuation [16–19], scattering-states approaches [20,21], perturbative and renormalization group (RG) methods [22–25], time-dependent density-matrix RG and related tensor-network approaches [26–28], numerical RG [29], flow equation [30], functional RG [31,32], and dual fermions [33,34]. A method developed over the past few years is the so-called auxiliary master equation approach [35–37] (AMEA). The advantage of this approach is that, in contrast to approaches which simulate a closed Hamiltonian system, it allows us to directly address the steady state. Also time-dependent correlation functions can be readily evaluated starting from the steady state or any arbitrary initial condition.

AMEA is based on mapping the physical system to an auxiliary open quantum system of Lindblad form. The dynamics of the resulting auxiliary system is described by the density matrix and is solved by numerical means. In previous works the Lindblad system was solved by using the so-called superfermion (SF) representation [38], which formulates the superoperator problem in terms of a standard operator problem with twice as many sites. The operator problem was then solved by standard numerical many-body techniques such as Krylov-space methods [36,39] (ED) or time evolution with matrix product states [40] (MPS). AMEA within SF+MPS was successfully used to calculate highly accurate spectral functions of the SIAM under the influence of a bias voltage [40,41] and the SF+ED implementation was employed as impurity solver within single-site steady-state nonequilibrium dynamical mean-field theory [42–45] (DMFT).

In equilibrium, the combination of density functional theory (DFT) with DMFT (DFT+DMFT) has proven to be very successful in describing materials with strong correlations [46]. However, to address real materials one often has to consider multiorbital correlated regions. Accordingly, on the technical side, for DFT+DMFT one needs a multiorbital impurity solver, which is modeled by an interconnected impurity consisting of multiple interacting sites in contact with individual baths. Within existing implementations of AMEA, SF+MPS, and SF+ED, as well as other nonperturbative nonequilibrium approaches, the treatment of such multiple interacting sites has limitations related either to the memory (SF+ED) or to the CPU time (SF+MPS). For this reason, a different approach to solve the many-body Lindblad problem

*sorantin@tugraz.at
†arrigoni@tugraz.at

is needed in order to employ AMEA as an impurity solver for nonequilibrium DFT+DMFT.

In this work, we make a step in this direction and test an alternative approach which does not rely on the SF representation, namely stochastic wave functions [47–49] (SWF). The new method is statistical in nature and most notably highly parallelizable. This makes it a very promising candidate to exploit the multicore architecture of (future-) cluster facilities. In addition, we introduce the notion of finite-size scaling within AMEA and report on progress regarding the optimization problem arising when mapping to the auxiliary system.

To test and benchmark the new developments, we apply AMEA to the IRLM where we can compare to the existing literature. In addition, we present a short study of the spectral function in dependence of temperature. Our results show the development of a central peak at higher temperatures which rises (lowers) its amplitude for increasing temperature depending on the hybridization strength. This work is structured as follows.

We begin by describing the technical aspects in Secs. II–IV and present the results for the IRLM in Sec. V. In more detail, in Sec. II we outline AMEA for spinless one-dimensional systems and discuss the size limits of existing AMEA approaches with respect to DMFT. Section III and the Appendix are devoted to the description of the SWF algorithm; the finite-size scaling is introduced in Sec. IV. In Sec. V we apply AMEA within SWF to the IRLM and test the finite-size scaling scheme and the capability to compute correlation functions against the literature. We also discuss the temperature dependence of the impurity spectral function. Finally, we present our conclusions together with a summary and outlook in Sec. VI.

II. AUXILIARY MASTER EQUATION APPROACH

We briefly review AMEA to deal with fermionic impurity problems. We consider a generic interacting region of size N_{int} connected to a left and right baths of noninteracting fermions. Accordingly, we write the Hamiltonian as

$$H = H_{\text{int}} + H_{\text{Baths}} + H_{\text{Hyb}}. \tag{1}$$

Here H_{int} describes the interacting region, $H_{\text{Baths}} = \sum_{\alpha=L/R} H_{B_\alpha}$ corresponds to the remaining reservoirs, and H_{Hyb} contains the hopping terms connecting the baths to the interacting region. In the following we will assume that an individual bath is connected only to a single site of the interacting region.

The idea of AMEA is to model the physical situation by an auxiliary open quantum system described by the Lindblad equation. It consists of the interacting region and additional bath sites to approximate the action of the leftover Hamiltonian on the interacting region. In more detail, the Lindblad superoperator (Liouvillian) defining the dynamics of the open quantum system of size $L = N_{\text{int}} + 2N_B$ reads [50]

$$\mathcal{L}\rho = -i[H_{\text{int}}, \rho] + \mathcal{L}_D\rho, \tag{2}$$

$$\mathcal{L}_D\rho = \sum_{\alpha=L/R} \mathcal{L}_\alpha\rho, \tag{3}$$

where ρ is the density matrix of the Lindblad system. The Liouvillian of the dissipative bath sites is given by

$$\begin{aligned}\mathcal{L}_\alpha\rho = &-i\sum_{ij} E_{ij}^{(\alpha)}\left[c_i^\dagger c_j, \rho\right] \\ &+2\sum_{ij}\Gamma_{ij}^{(\alpha),(1)}\left(c_j\rho c_i^\dagger - \frac{1}{2}\left\{\rho, c_i^\dagger c_j\right\}\right) \\ &+2\sum_{ij}\Gamma_{ij}^{(\alpha),(2)}\left(c_i^\dagger\rho c_j - \frac{1}{2}\left\{\rho, c_j c_i^\dagger\right\}\right),\end{aligned} \tag{4}$$

where α denotes the left (right) reservoir [51] and $c_i^{(\dagger)}$ are the creation (annihilation) operators of a fermion on site i of the open quantum system. The time evolution of the system is described by the Lindblad equation,

$$\frac{d}{dt}\rho(t) = \mathcal{L}\rho(t). \tag{5}$$

For the steady state of the original system, Eq. (16), the Dyson equation for the interacting region in the formulation of Keldysh Green's functions reads

$$\underline{\mathbf{G}}_{\text{int}}^{-1}(\omega) = \underline{\mathbf{g}}_{0,\text{int}}^{-1}(\omega) - \underline{\mathbf{\Delta}}_{\text{ph}}(\omega) - \underline{\mathbf{\Sigma}}(\omega), \tag{6}$$

where an underline indicates the 2×2 Keldysh matrix,

$$\underline{\mathbf{X}} \equiv \begin{pmatrix}\mathbf{X}^{\text{Ret}} & \mathbf{X}^{\text{Kel}} \\ \mathbf{0} & \mathbf{X}^{\text{Adv}}\end{pmatrix}, \tag{7}$$

and bold denotes the matrix structure in site indices, $\mathbf{X} = X_{ij}$. In Eq. (6) $\underline{\mathbf{g}}_{0,\text{int}}$ is the Green's function (GF) of the interacting region when isolated from the baths and without interaction, $\underline{\mathbf{\Sigma}}$ is the self-energy, holding all the information about the interaction, and $\underline{\mathbf{\Delta}}$ is the so-called hybridization describing the effect of $H_{\text{Baths}} + H_{\text{Hyb}}$ on the interacting region. For the present case in which the first (last) site of the interacting region couple to the left (right) bath, the hybridization has the spatial structure $\underline{\mathbf{\Delta}} = \text{diag}[\underline{\Delta}_{\text{ph}}^{(L)}, 0, \ldots, 0, \underline{\Delta}_{\text{ph}}^{(R)}]$.

The mapping from the physical to the auxiliary system is performed by fitting the parameters E^α, $\Gamma^{\alpha,(1,2)}$ in Eq. (4) such that the hybridization in the auxiliary system approximates the physical hybridization as close as possible, $\underline{\Delta}_{\text{aux}}^{(\alpha)} \approx \underline{\Delta}_{\text{ph}}^{(\alpha)}$, and this is the only approximation made within AMEA. The accuracy of the mapping can then be systematically improved by increasing the number of auxiliary bath sites N_B and it becomes formally exact in the limit of $N_B \to \infty$. Once the mapping is performed, one can solve the auxiliary system by some appropriate numerical method and evaluate observables belonging to the interacting region. Their accuracy in describing the corresponding exact quantities will be directly related to the difference between $\underline{\Delta}_{\text{aux}}^{(\alpha)}$ and $\underline{\Delta}_{\text{ph}}^{(\alpha)}$.

A. Different AMEA implementations and their applicability to multiorbital DMFT

Here we want to briefly discuss the applicability of the different AMEA implementations as impurity solvers within multiorbital DMFT.

To address the open quantum system problem described by Eq. (4), one can use the SF representation or the SWF approach presented in this paper. These two approaches can

in turn be combined with two different schemes to carry out the time evolution, namely ED or MPS. This makes a total of four different combinations (SF+ED [36], SF+MPS [40], SWF+ED, present paper, and SWF+MPS).

To estimate the number of correlated orbitals that can be treated within DMFT for each one of these methods, we assume that at least four bath sites are needed per correlated orbital to represent accurately a single bath [37,52] leading to a total system size of $L = N_{\mathrm{imp}}(N_B + 1)$. SF+ED is limited in system size to $L \leqslant 7$ due to memory requirements. It is, thus, restricted to the treatment of a single correlated orbital. With the same memory limits, SWF+ED allows for a twice-as-large system, $L \leqslant 14$, which accommodates two correlated orbitals. One should, however, point out that, for the same L, SWF+ED requires more CPU resources. On the other hand, the wall time [53] can be reduced considerably due to the high parallelizability of the SWF approach.

When using MPS as a time-evolution algorithm for AMEA, the situation is more complex. On the one hand, MPS is generically not limited in system size but rather expensive with respect to the wall time. On the other hand, conventional MPS becomes inefficient when the system is not truly one dimensional. This is the case in the SF representation, where the impurity+bath system is mapped into a ladder structure [36,40]. Also the inclusion of additional correlated orbitals makes the problem higher dimensional and thus unsuitable for MPS. Recently, a generalization of MPS suitable to address efficiently a multiorbital impurity problem, the so-called fork tensor product states [54,55] (FTPS) approach, has been introduced. This approach, implemented within the SWF representation, could constitute a promising candidate for a nonequilibrium multiorbital DMFT impurity solver.

B. Mapping to the auxiliary system

Here we briefly want to summarize the mapping procedure and mention key points that we need for the present work. For a thorough discussion of the mapping and technical details we refer to our previous work [37]. The mapping is performed for each individual bath α by minimizing a suitable cost function,

$$\chi^2(\boldsymbol{x}_\alpha) \equiv \chi^2_\alpha = \int \left\| \underline{\Delta}^{(\alpha)}_{\mathrm{ph}} - \underline{\Delta}^{(\alpha)}_{\mathrm{aux}} \right\|^2 d\omega,$$
$$\left\| \underline{\Delta}^{(\alpha)}_{\mathrm{ph}} - \underline{\Delta}^{(\alpha)}_{\mathrm{aux}} \right\|^2 \equiv \sum_{\xi \in \{\mathrm{Ret},\mathrm{Kel}\}} \left[\mathrm{Im}\Delta^{(\alpha),\xi}_{\mathrm{ph}}(\omega) - \mathrm{Im}\Delta^{(\alpha),\xi}_{\mathrm{aux}}(\omega;\boldsymbol{x}_\alpha) \right]^2. \quad (8)$$

Here we have introduced a parameter vector $\boldsymbol{x}_\alpha$ that parametrizes the matrices E^α, $\Gamma^{\alpha,(1,2)}$ in Eq. (4), from which one evaluates the auxiliary hybridization $\Delta^{(\alpha)}_{\mathrm{aux}}$. It is important to note that the precise form of the cost function is very flexible and may be chosen differently for different physical situations. However, proper cost functions should quantify how well the auxiliary system captures some desired physical situation. For instance, the quadratic deviation as used in Eq. (8). One important property of the mapping is that proper cost functions decrease exponentially with the number of fit parameters [37], $-\log \chi_\alpha \propto \dim(\boldsymbol{x}_\alpha)$, which typically leads to a rapid increase of accuracy when the number of bath sites N_B is increased.

In previous works, Eq. (8) was minimized via a parallel tempering (PT) algorithm which is appropriate to find the global minimum. However, it should be noted that within AMEA it is not strictly necessary to find the global optimum [56]. In general, the fit struggles to resolve sharp features such as band edges in the retarded component or the Fermi jumps in the Keldysh component at zero temperature. Therefore, $T = 0$ cannot be reached exactly in practice and the auxiliary system always has some nonzero effective temperature.

Developments of the fit

With increasing dimensionality of the fitting problem, the PT algorithm gets computationally prohibitive and it is not able to find even good local minima anymore for [57] $\dim(\boldsymbol{x}) = 2N_B(N_B + 1) \gtrsim 80$. Good minima should be such that they display an exponential decrease in the cost function when the number of bath sites is increased. To obtain good-enough minima for $N_B = 7, 8$, we use the fact, which we observed empirically, that the Γ matrices of obtained minima typically have very low rank. Utilizing a variable rank parametrization in terms of a corresponding matrix γ,

$$\gamma = (\vec{\gamma}_1, \ldots, \vec{\gamma}_{\mathrm{rank}_\gamma}), \quad \Gamma = \gamma\gamma^\dagger, \quad (9)$$

where $\vec{\gamma}_i$ denote column vectors of length L. Note that the maximal useful rank typically increases with the system size [58]. With this procedure, we have reduced the dimensionality of the parameter vector to $\dim(\boldsymbol{x}) = 2N_B(\mathrm{rank}_\gamma + 1)$, extending the applicability of the PT algorithm to about $N_B = 8$. To achieve an exponential decrease in the cost function for even more bath sites we have adopted an optimization algorithm which makes use of the gradient of the cost function, which can be evaluated directly. This information is not used in the PT algorithm. Suitable gradient-based approaches can be found in the area of machine learning, which provides algorithms tailored to find local minima in very high dimensional problems utilizing variants of steepest descent. Here we employ the ADAM [59] optimizer as implemented in the python library tensorflow [60].

Steepest descent approaches are obviously very sensitive to the starting point. In our case, it has proven to be very effective to first find the solution for a small auxiliary system (small N_B) and, consequently, add bath sites until the required N_B is reached. For a fixed N_B, we start with the result of the previous system size and increase the rank stepwise until no significant decrease in the cost function is observed. In addition to being applicable for larger N_B, the ADAM routine is also faster than PT for a given N_B. This is because the PT algorithm tries to explore the total phase space, whereas ADAM only follows a certain path.

III. SOLUTION OF THE LINDBLAD SYSTEM WITH STOCHASTIC WAVE FUNCTIONS

The auxiliary open system is still correlated but due to its finite size can be addressed by numerical techniques. One route is to make use of the so-called SF representation [38], which maps a superoperator problem to a standard, albeit non-Hermitian, operator problem. The drawback of this approach is that the resulting SF problem is formulated on twice as many effective sites leading to a rapid increase in the

numerical complexity. In previous works employing AMEA we have successfully used the SF representation together with established many-body techniques such as Krylov-space methods [35,36] or MPS [40] to solve for steady-state properties. A completely different route is to use SWF [47–49], also referred to as "quantum jumps," to solve the auxiliary many-body problem. The method is based on the stochastic nature of the Lindblad problem and is formulated in terms of wave functions instead of a density matrix and thus circumvents the need to square the Hilbert space. In the following, we will only give a brief introduction to the SWF method and focus more on a practical prescription to simulate the many-body Lindblad system arising within AMEA. For more details, mathematical definitions and background we refer to the literature [47–49]. In the following we consider a Lindblad system of spinless fermions of size L.

The density operator $\rho(t)$ can be mapped onto a probability distribution $P[\vec{\psi}, t]$ for the quantum mechanical (many-body) wave function [61],

$$|\psi\rangle = \sum_{\lambda=1}^{2^L} \psi_\lambda |\lambda\rangle,$$
$$\vec{\psi} \equiv (\psi_1, \ldots, \psi_{2^L}), \tag{10}$$

where λ indexes a complete set of (many-body) basis states [62]. With the Hilbert space volume element,

$$D\vec{\psi} D\vec{\psi}^* \equiv \prod_{\lambda=1}^{2^L} \frac{i}{2} d\psi_\lambda d\psi_\lambda^*, \tag{11}$$

defining the needed probability measure [63], the expectation value of an observable can then be formally expressed as

$$\langle A(t)\rangle = \int D\vec{\psi} D\vec{\psi}^* \langle\psi|A|\psi\rangle P[\vec{\psi}, t]. \tag{12}$$

In short, instead of dealing with an evolution equation for the density matrix, one formulates a stochastic process on the Hilbert space. For the specific case of a Lindblad system, the process is simulated according to a stochastic differential equation leading to the algorithm presented in Fig. 1.

In this algorithm, a state vector $|\psi\rangle$ is evolved in time according to an effective, but non-Hermitian, Hamiltonian, H_{eff}. H_{eff} comprises the Hamiltonian H_{int} as well as the particle-number-conserving terms from the part describing the L and R baths, i.e., the terms proportional to $E_{ij}^{(\alpha)}$ as well as the terms containing the anticommutators in Eq. (4). This deterministic time evolution is interrupted by stochastic jump processes to different particle sectors, mediated by jump operators $L_k^{(\beta)}$, see Appendix A for details. Observables are determined as the average over expectation values in independent realizations of $|\psi\rangle$. Such a stochastic unraveling of the Lindblad equation into a pure state description, in the form of Eq. (11), only works for quantities which only require the knowledge of the time-dependent density matrix $\rho(t)$, as is the case for expectation values $\langle A\rangle = \text{Tr}A(t)\rho = \text{Tr}A\rho(t)$. When evaluating a Greens function, multiple operators at different times are involved and additional information is required. In order to compute two-time correlation functions,

$$G_{BA}(t, t') = \langle\psi(t_0)|B(t)A(t')|\psi(t_0)\rangle, \tag{13}$$

Stochastic wave function (SWF) algorithm

1. Start with a normalized state $|\psi(t_0)\rangle$ and draw a random number $r_j \in (0, 1)$.
2. Time evolve the state vector with the effective Hamiltonian Eq. A6: $|\psi(t)\rangle = e^{-iH_{\text{eff}}(t-t_0)}|\psi(t_0)\rangle$ up to a time t_j such that $||\psi(t_j)||^2 = r_j$.
3. Perform a quantum jump:
   - Compute the weights for all possible jumps, $w_{\beta k} \propto ||L_k^{(\beta)}\psi(t_j)||^2$.
   - Select one jump process $(\beta' k')$ at random according to the weights.
   - Change $|\psi(t)\rangle = L_{k'}^{(\beta')}|\psi(t_j)\rangle$ and normalize it.
4. Set $t_0 = t_j$ and iterate $1 \to 4$.

Single-time observables

Measure at desired times and average over a sufficient number of realizations $\psi_i(t)$.

$$\langle A(t)\rangle = \frac{1}{n}\sum_{i=1}^{n} \frac{\langle\psi_i(t)|A|\psi_i(t)\rangle}{||\psi_i(t)||^2}$$

FIG. 1. The stochastic wave function algorithm for the time evolution.

we follow the approach outlined in Ref. [48] and consider the stochastic time evolution of a doubled Hilbert space resulting in the algorithm in Fig. 2.

Here a state vector $|\psi\rangle$ is evolved in time together with a corresponding vector $A|\psi\rangle$. A Green's function is then proportional to the stochastic sample of off-diagonal matrix elements of the second operator B, see Eq. (14). Notice that for single-fermion Green's functions, A is a fermionic creation (annihilation) operator. In that case one has to use the negative sign in front of the jump term for the lower part of the doubled Hilbert space, cf. Eq. (A4), see Appendix B in Ref. [64]. Notice that generalizing the doubled Hilbert space to a multiple Hilbert space allows us to sample different correlation functions at once, see Appendix Sec. A 2 b i.

The SWF algorithm requires a routine which is able to time evolve an initial vector with a non-Hermitian generator for some (arbitrarily-) small time dt. In the present work we use the so-called Arnoldi algorithm [39] for the time evolution which is the Lanczos method generalized to the non-Hermitian case. For more details, see the Appendix.

IV. EXTRAPOLATION OF OBSERVABLES TO THE LIMIT OF VANISHING COST FUNCTION

As illustrated above, AMEA is a method which can be systematically improved by increasing the number of bath sites N_B leading to an exponential decrease in the cost function, $\chi = \sum_\alpha \chi_\alpha$, which is a measure of the overall accuracy. Clearly, the best approximation for some quantity of interest

SWF algorithm in the doubled Hilbert space

1. Propagate the state $|\psi(t_0)\rangle$ with the SWF algorithm up to a desired time t' and normalize it.
2. Compute the vector $|\phi(t')\rangle = A\,|\psi(t')\rangle$ and construct a doubled Hilbert space:

$$\mathbf{\Theta}(t') = \begin{pmatrix} \psi(t') \\ \phi(t') \end{pmatrix} \qquad \mathbf{H}_{\text{eff}} = \begin{pmatrix} H_{\text{eff}} & 0 \\ 0 & H_{\text{eff}} \end{pmatrix}$$
$$\mathbf{L}_k^{(\beta)} = \begin{pmatrix} L_k^{(\beta)} & 0 \\ 0 & \pm L_k^{(\beta)} \end{pmatrix}$$

3. Record the norm $||\mathbf{\Theta}(t')||$, normalize the vector and perform the SWF algorithm with the doubled vector $\mathbf{\Theta}$ and operators $\mathbf{H}_{\text{eff}}, \mathbf{L}_k^{(\beta)}$.

Green's functions

Measure at desired times and average over a sufficient number of realizations $\mathbf{\Theta}_i(t)$.

$$G_{BA}(t,t') = \frac{1}{n}\sum_{i=1}^{n} \frac{||\mathbf{\Theta}(t')||^2}{||\mathbf{\Theta}_i(t)||^2} \langle \psi_i(t)|\, B\, |\phi_i(t)\rangle \quad (14)$$

FIG. 2. The stochastic wave function algorithm in the doubled Hilbert space which allows us to calculate correlation functions.

for given N_B is obtained within the auxiliary system with the smallest χ. To improve on these results one can think of numerically extrapolating the results to the $\chi \to 0$ limit. This is equivalent to a scaling to the limit of an infinite number auxiliary bath sites $N_B \to \infty$. However, since the accuracy is directly related to χ rather than N_B, it is more convenient to use χ as an extrapolating parameter. For a given observable A of interest we can assume for its deviation from its exact (physical) value

$$\Delta A(\chi) = A_{\text{ph}} - A_{\text{aux}}(\chi) = k_A \;\; \chi + O(\chi^2) \quad (15)$$

with some constant of proportionality k_A. This suggests that given a series of value pairs $\{\chi_i, A(\chi_i)\}$ one can obtain an approximation to $A_{\text{aux}}(\chi = 0)$ by performing a linear fit in the (χ, A) plane. Within AMEA a series of value pairs $\{\chi(N_B), A\}$ is naturally generated by the different possible auxiliary system sizes. The truncation of the Taylor series, Eq. (15), to first order is only justified for cost functions which are small compared to $\chi_0 \equiv \chi|_{\Delta_{\text{aux}}=0}$ which is χ obtained by Eq. (8) with $\Delta_{\text{aux}} = 0$. The resulting normalized cost function, χ/χ_0, is then a measure for the relative error from the physical situation.

We want to emphasize that the extrapolation scheme presented here is not able to give a consistent error estimate of the extrapolated value as the uncertainty of the individual data points is unknown and not statistically distributed.

Here one has to distinguish between a purely statistical error stemming from the solution of the Lindblad system within stochastic wave functions, which is known and negligible, and the systematic error introduced by the mapping to the auxiliary system, which is unknown. Further, the role of the higher-order terms in Eq. (15) introduces another source of unknown error. To get a grip on the error due to the AMEA mapping, one could perform the extrapolation in some limit where the true value in the physical system is known, for example, at zero interaction strength or for some other parameters where the value is known from the literature. One could then use the deviation from the extrapolation fit as an approximation to the error of a data point. Since there is a lot of freedom in obtaining this error estimates—and it will thus be very situation dependent—we will not pursue this further in the current work where we are interested in an unbiased benchmark of the extrapolation scheme.

Nevertheless, this scheme provides a significant improvement, for example, in the current, as can be seen in Fig. 5.

V. APPLICATION TO THE INTERACTING RESONANT LEVEL MODEL

The IRLM [4] is a commonly used nonequilibrium impurity model of spinless fermions. It features an impurity site connected to two semi-infinite tight-binding chains together with an interaction term coupling the particle densities of the impurity site to the neighboring chain sites, see Fig. 3. The Hamiltonian is defined as

$$\begin{aligned} H_{\text{IRLM}} &= H_L + H_R + H_{\text{dot}}, \\ H_L &= -J\sum_{r=-\infty}^{-2} c_r^\dagger c_{r+1} + \text{H.c.}, \\ H_R &= -J\sum_{r=1}^{+\infty} c_r^\dagger c_{r+1} + \text{H.c.}, \\ H_{\text{dot}} &= -J'\sum_{r=\pm1} c_r^\dagger c_0 + \text{H.c.}, \\ &\quad + U\sum_{r=\pm1}\left(c_r^\dagger c_r - \frac{1}{2}\right)\left(c_0^\dagger c_0 - \frac{1}{2}\right), \end{aligned} \quad (16)$$

where $c_r^\dagger/c_r$ denote the fermionic creation or annihilation operators at site r. Here H_{L-R} describe the semi-infinite tight-binding chains of bandwidth $W = 4J$ and H_{dot} introduces the hopping to the impurity as well as the interaction term. A nonequilibrium steady-state situation is induced in the system via an applied bias voltage V simulated by shifting the chemical potentials of the leads symmetrically, that is, $\mu_l = -\mu_r = \frac{V}{2}$. We use J as unit of energy and work in units where $\hbar = e = k_B = 1$.

The IRLM is known to be integrable [4] and becomes equivalent to the continuum model in the so-called scaling regime where the bandwidth becomes the largest energy scale in the system. Most notably, there is a closed form expression for the steady-state current as a function of the bias voltage [6,65] for the special value of the interaction $U = 2$,

$$I(V) = \frac{V}{2\pi}\,{}_2F_3\left[\left\{\frac{5}{6},\frac{7}{6}\right\},\left\{\frac{1}{4},\frac{3}{4},1\right\};-\left(\frac{V}{V_c}\right)^6\right], \quad (17)$$

with $V_c = r(J')^{\frac{4}{3}}$ and $r \approx 3.2$ [66]. Here ${}_2F_3(a,b;z)$ is the generalized hypergeometric function [67]. The formula

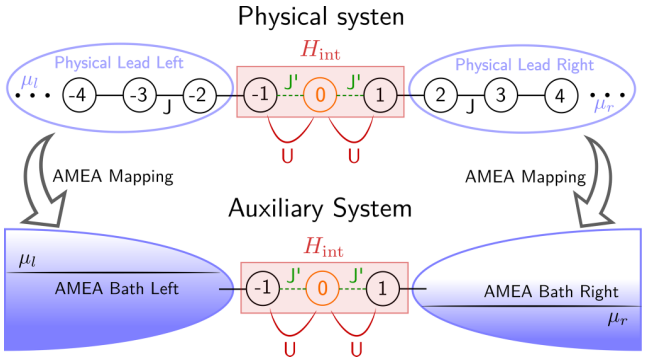

FIG. 3. A sketch of the IRLM as lattice model and its mapping to the auxiliary open quantum system used within AMEA.

Eq. (17) is valid at zero temperature and in the scaling regime. Parameters can be considered to be in the scaling regime [68] if the $I(V)$ function falls onto a single curve in the scaling plot, see Fig. 5. In this way, I/V_c becomes a universal function of the scaled voltage V/V_c alone and in particular does not depend on the hybridization strength J'.

A. AMEA for the IRLM

In the IRLM, the interaction lives on the contact links to the leads and, therefore, the interacting region comprises the sites $r = \{-1, 0, 1\}$ which corresponds to having

$$H_{\rm int} = H_{\rm dot}, \tag{18}$$

$$H_{B_L} = -J \sum_{r=-\infty}^{-3} c_r^\dagger c_{r+1} + \text{H.c.}, \tag{19}$$

$$H_{B_R} = -J \sum_{r=2}^{\infty} c_r^\dagger c_{r+1} + \text{H.c.}, \tag{20}$$

$$H_{\rm Hyb} = -J(c_{-2}^\dagger c_{-1} + c_1^\dagger c_2) + \text{H.c.}, \tag{21}$$

as indicated in Fig. 3. Since $H_{B_{L/R}}$ describe semi-infinite tight-binding chains in equilibrium, $\Delta_{{\rm ph},L/R}$ represent baths with a semicircular density of states with a bandwidth of $W = 4$ and an electronic distribution function given by the Fermi function. Within AMEA, a given parameter set E^α, $\Gamma^{\alpha,(1,2)}$ fixes both the density of states as well as the distribution function of the corresponding bath. Since the Hamiltonian Eq. (16) is particle-hole symmetric, it suffices to perform

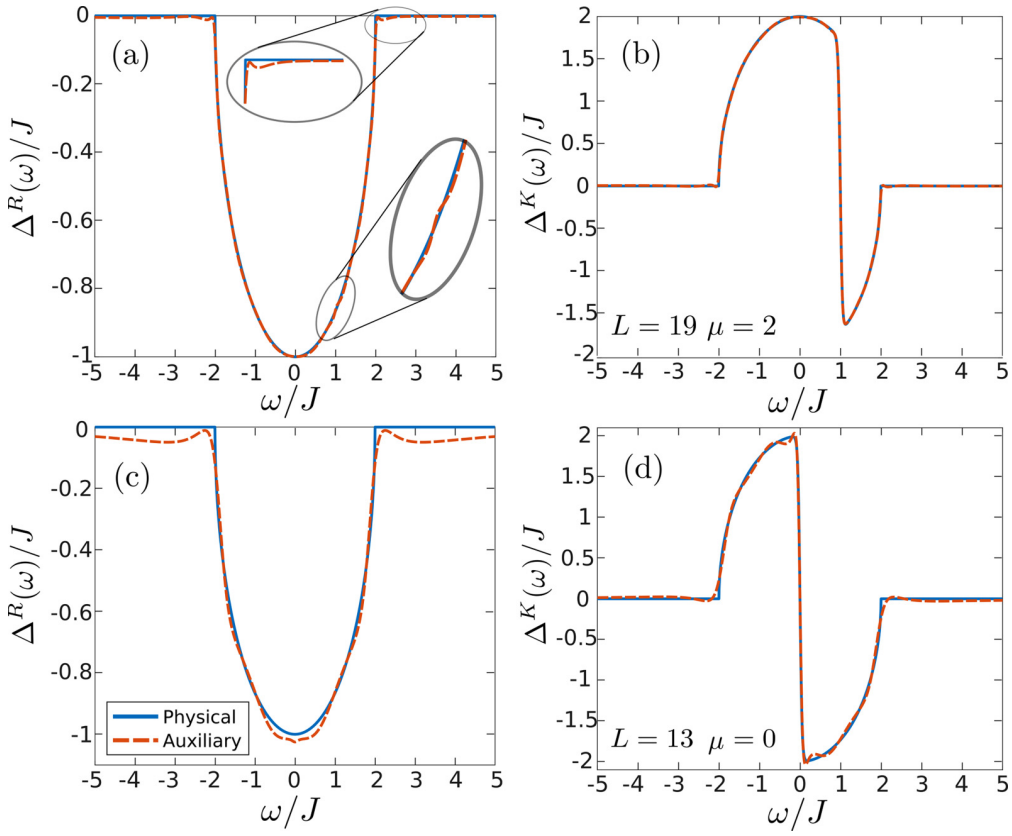

FIG. 4. Comparison of the physical and auxiliary hybridization function at the boundary of the left bath, i.e., $r = -1$, and $T = 0.025$. [(a) and (b)] Retarded-Keldysh part of the hybridization function for $L = 19$, $\mu = 2$. [(c) and (d)] Retarded-Keldysh part of the hybridization for $L = 13$, $\mu = 0$. The $L = 19$ results where obtained with the ADAM routine from Sec. II B 1 while $L = 13$ was optimized with PT. Solid lines represent the hybridization of the physical system, $\Delta_{\rm ph}$, and dashed lines that of the auxiliary system, $\Delta_{\rm aux}$. Panels (a) and (b) show a fit for $\mu \neq 0$ to exemplify the capability of representing a nonequilibrium situation. Panels (c) and (d) illustrate the fit used for the calculation of the equilibrium spectral functions in Fig. 6. The insets in panel (a) show a zoom onto the band edge and the region around the chemical potential, $\mu = 1$, where the sudden occupation change in the Keldysh component typically induces oscillations in the retarded one.

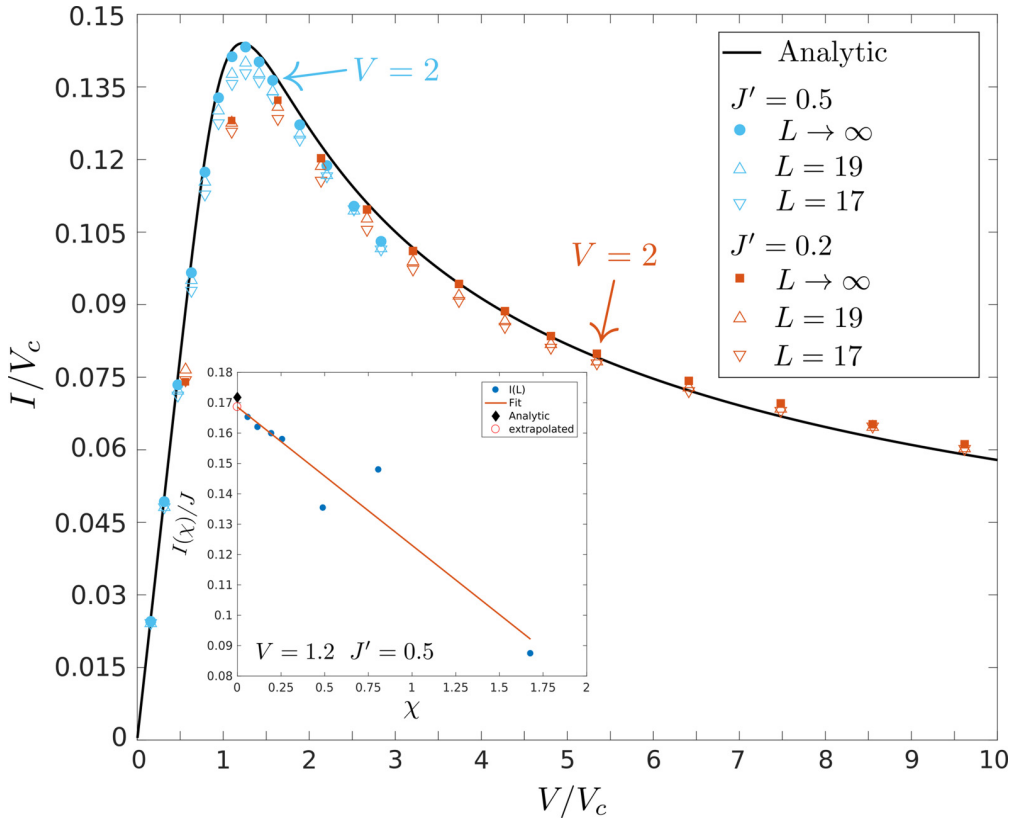

FIG. 5. Scaled steady-state current as function of the scaled bias voltage V/V_c. We plot the analytic solution for $T = 0$ (solid black line), the extrapolated AMEA current (filled circles), and the current for $L = 17$ and $L = 19$ (open symbols). Shown are results for $J' = 0.2$ (red symbols) and $J' = 0.5$ (blue symbols). The arrows indicate the data points which correspond to the voltage $V = 2$ for the two different considered J'. The inset shows an example of the current vs. cost function $I(\chi)$ for $V = 1.2$, $J' = 0.5$ (filled blue circles) and the corresponding linear fit (solid red line) as well as the extrapolated value at zero cost function (open red circle) together with the analytic result (filled black diamond). Other parameters are $T = 0.025$ and $U = 2$.

the fit only for one of the two baths, e.g., the left ones, and obtain the parameters of the right bath by a particle-hole transformation. Thus, also the cost function for the left and right bath will be equal for a given bias voltage, $\chi_L = \chi_R$. To illustrate the mapping, we show in Fig. 4 two examples for such a fit with $L = 13$ ($N_B = 6$) and $L = 19$ ($N_B = 9$). Notice that the same fit can be used for any set of parameters in the interacting region.

B. Extrapolation of the steady-state current

Since there are no free parameters in Eq. (17) we can use this as a benchmark for our numerical approach and test the extrapolation scheme of Sec. IV. However, it should be noted that our results are obtained for $T = 0.025$ while Eq. (17) is the result for zero temperature.

Given an auxiliary system of size L we can evaluate the current over a physical bond i in the auxiliary system [69]

$$\begin{aligned} I_{i,i+1} &= E_{i+1,i}\langle c_{i+1}^\dagger c_i\rangle - E_{i,i+1}\langle c_i^\dagger c_{i+1}\rangle, \\ &= 2E_{i+1,i}\mathrm{Im}\langle c_{i+1}^\dagger c_i\rangle, \end{aligned} \tag{22}$$

where the parameters $E_{i,i+1}$ represent the hopping along the chain in the interacting region. In the following, we consider results obtained with $7 \leqslant L \leqslant 19$. In Fig. 5 we plot the universal steady-state current together with the corresponding data points obtained with AMEA for $J' = 0.5$ and $J' = 0.2$. Shown are the AMEA results for individual system sizes as well as the extrapolated current. We find a linear relationship to normalized cost functions, $\chi/\chi_0 \approx 1$, suggesting that higher-order terms in the Taylor expansion, Eq. (15), are suppressed in the present case.

We see that the current improves significantly toward the analytic solution thanks to the extrapolation scheme. As mentioned above, the analytic solution is only valid for not-too-large bias voltages [70]. Indeed, we see a systematically growing deviation between the analytic solution and the current from AMEA for voltages $V \gtrsim 2$; see the markers in Fig. 5.

For $J' = 0.2$, somewhat larger deviations from the analytic solution are visible around the maximum of the scaled current. These are due to the finite temperature, which introduces a broadening of the Fermi edge and, thus, can be seen as an uncertainty [71] in the chemical potentials or, equivalently, in the voltage $\Delta V \sim T$. The important point is that this uncertainty is symmetric around the correct V value. In the linear regime, this uncertainty is compensated, because to a $\pm\delta V$ corresponds (approximately) a $\pm\delta I$ which essentially

cancels out. This does not occur in the quadratic regime close to the maximum. Therefore, here the error in I is larger. This effect is larger for small J' because any error in the current gets amplified in the scaling plot for $J' = 0.2$ (where $V_c = \approx 0.37$) in contrast to $J' = 0.5$ (where $V_c \approx 1.27$).

The inset in Fig. 5 shows an example extrapolation. As one would expect, the data points with bigger cost functions (smaller system sizes) show a stronger scattering from the linear fit than the more accurate points. While the points with low cost functions make for more confidence in the results, the accuracy of the extrapolated current does not suffer when the biggest system size, $L = 19$, is excluded from the analysis. This suggests that when utilizing the extrapolation to zero cost function, it is probably not necessary to simulate the biggest system sizes within reach. Rather, one can check for a small fraction of points whether the (usually very CPU-time intensive) bigger system size(s) are worth calculating. However, if error estimates are used, then points at lower cost functions will reduce the uncertainty in the final result.

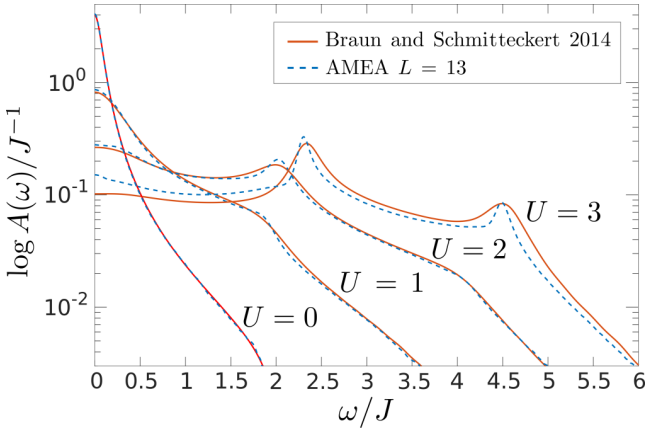

FIG. 6. Equilibrium ($V = 0$) spectral function at the impurity site, $r = 0$, for different interaction strengths. We compare our results with Braun *et al.* [72] (obtained at $T = 0$). Our parameters are $J' = 0.2$, $T = 0.025$.

C. Spectral function of the IRLM

In this section, we evaluate the steady-state single-particle Green's function G at the central impurity site. The calculation is carried out in the real time domain and we use the approach discussed in Sec. III, see also Sec. A 2. We use a step size of $dt = 0.05$ and 10^5 time steps to first reach the steady state at $t_0 = 5\times10^3$. We have verified that expectation values of static observables do not change after this time. Then we sample the Green's function $G(t - t_0)$ for later times beyond t_0 up to $t_{\text{end}} = t_0 + 6000dt$. This is sufficient, since here $G(t_{\text{end}} - t_0) < 10^{-6}$. Finally, we average G over $O(10^5)$ realizations and determine the spectral function by direct Fourier transform. All results presented in this section are obtained with an auxiliary system of size $L = 13$. The corresponding hybridization function is shown in the lower panels of Fig. 4.

Like any nonequilibrium approach, AMEA is also applicable in equilibrium situations which is just the special case when $\mu_l = \mu_r = 0$, allowing us to compare our results against the literature. In Fig. 6, we compare our results to the equilibrium density of states obtained by Braun and Schmitteckert via MPS [72]. For interaction strengths $U < 2$ that are small compared to the bandwidth, we observe a very good agreement with the reference over the whole frequency range. At the self-dual point $U = 2$ we start to see small quantitative deviations of peak heights but still obtain an satisfactory agreement. When the interaction becomes comparable to the bandwidth, $U = 3$, the deviations become significant and continue to grow as the interaction is increased (not shown). The reason for the growing deviations, such as sharper resonances in the AMEA results and a different behavior around zero frequency, is that in the present AMEA mapping to a system of size $L = 13$ the region outside the bandwidth is not well reproduced, see also Fig. 4. While these states do not play a role as long as all energy scales in the system are small compared to the bandwidth, i.e., in the scaling regime, the details of the leads at higher energies become important when the interaction becomes comparable to the bandwidth. However, the latter does not mean that AMEA is not at all applicable in this parameter regime; rather, one has to make sure that the region outside the bandwidth is also faithfully reproduced by the auxiliary system. This can be achieved by using a differently distributed cost function in the fit or by going to larger auxiliary system sizes.

Impurity spectral function at finite temperatures

We complement our benchmark of the spectral function in the limit of low temperatures with a presentation of finite temperature results, where our method has an even better accuracy. In Fig. 7, we plot the impurity spectral function for increasing temperatures and two different hybridization strengths, $J' = 0.2$ and $J' = 0.5$, at the self-dual point $U = 2$.

We observe that with rising temperature the resonances around $\omega \approx 2, 4$ get weakened and the spectral function develops a broad central peak for both considered hybridization strengths. While for $J' = 0.2$ the amplitude of this peak is decreasing with increasing temperature, the trend is reversed for $J' = 0.5$ where the peak is formed around $T = 0.8$ and continues to grow. This different behaviors can be interpreted as the consequence of two competing effects of the increasing temperature. First, there is a shift of spectral weight away from the resonances around $\omega \approx 2, 4$ to small frequencies which leads to an increase of the central peak. Second, in addition to broadening effects due to the hybridization, the central peak gets broadened by temperature which tends to decrease its height due to the overall normalization.

For the smaller hybridization strength, where the initial broadening due to the hybridization is smaller, the increase in broadening initially dominates over the shift of spectral weight, leading to a decreasing central peak as function of temperature, while the two effects balance out for high temperatures, $T \approx 1$. In the case of the larger hybridization, the shift of spectral weight dominates the behavior of the zero-frequency spectral function.

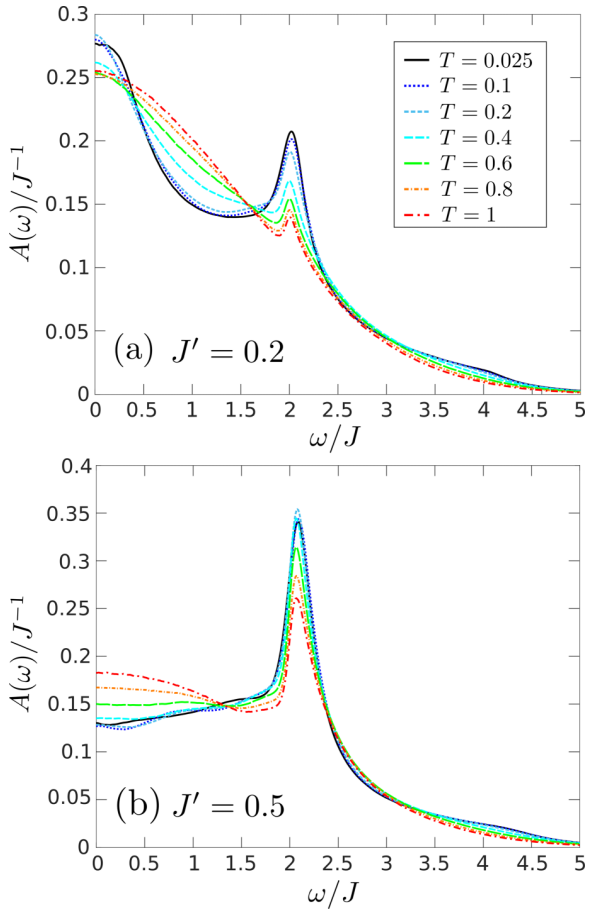

FIG. 7. Equilibrium spectral function at the impurity site, $r = 0$, for different temperatures and two different hybridization strengths. Panel (a) for $J' = 0.2$ and panel (b) for $J' = 0.5$.

D. Performance

From a numerical point of view, the SWF method has two main advantages. First, since one evolves wave functions there is no need to square the Hilbert space as when one deals with the density matrix. For the present case of using Krylov-space methods, this means that one can use a twice as large L and thus achieve a much better accuracy. Second, individual realizations of possible time evolutions are independent, which means that the method is easily parallelizable. This makes SWF very suitable for future cluster facilities which thrive on highly parallel algorithms.

However, the price to pay is a CPU time that is about 20 times longer than solving an auxiliary system with the same value of the cost function by MPS. On the other hand, thanks to parallelization, the wall time can obviously be made almost arbitrarily small. For example, the GF's for $L = 13$ in Fig. 6 where averaged over about half a million realizations where a single one takes around 1 s. For comparison, the solution with the superfermion plus ED approach for $L = 13$ would be on the order of minutes.

VI. SUMMARY, CONCLUSION, AND OUTLOOK

We reported on technical developments within the auxiliary master equation approach and applied it to the IRLM in and out of equilibrium to benchmark the new techniques. We successfully applied the SWF algorithm to determine the steady-state properties of the auxiliary Lindblad system. On the one hand, the SWF algorithm is highly parallelizable allowing to reach very low wall times. On the other hand, we found that in the current implementation of SWF+ED the total CPU time for a spectral function is 20 times higher than in available alternatives for the solution of the auxiliary system introduced by AMEA. Further, we saw that an auxiliary system size of $L = 13$ is enough to obtain reliable spectral information of the IRLM for interactions $U \lesssim W/2$.

We obtained a further significant improvement by extrapolating physical quantities, most notably the current, to the $N_B \to \infty$ limit. In fact, it turns out to be more effective to extrapolate linearly in the cost function χ, which then would correspond to an exponential extrapolation in N_B. Such an extrapolation is able to improve the results significantly and possibly circumvents the need to go to larger system sizes.

In addition, we introduced a variable rank parametrization of the auxiliary Lindblad matrices which typically reduces the number of fitting parameters in the AMEA mapping. Employing the new parametrization together with an optimization routine from machine learning, we were able to maintain an exponential decrease of the cost function also for larger system sizes where the previously used parallel tempering algorithm failed.

In view of the high parallelizability of the SWF algorithm, which we found to hold in practice, the fact that MPS is limited in CPU time rather than system size makes a possible SWF+MPS implementaion of AMEA an ideal combination. Especially the combination of AMEA within SWF and FTPS [54]—a generalization of MPS—together with further optimizations, such as extrapolating the Green's function to larger times with linear prediction, could prove to be very fruitful with respect to nonequilibrium DFT+DMFT.

Besides the technical developments within AMEA and their benchmark within the IRLM, we also investigated the effect of increasing temperature on the impurity spectral function. We find that the competition of temperature induces broadening effects and shift of spectral weight gives rise to different behaviors of the spectrum around zero frequency for different hybridization strengths.

ACKNOWLEDGMENTS

We thank Irakli Titdvinidze, Daniel Bauernfeind, Volker Meden, and Gerhard Dorn for fruitful discussions. A special mention goes to Franz Scherr, who introduced us to the machine-learning environment tensorflow and provided a first implementation for the AMEA mapping. We are grateful to Peter Schmitteckert for providing us with the reference data for the spectral functions. This work was partially supported by the Austrian Science Fund (FWF) within Projects P26508 and F41 (SFB ViCoM), as well as NaWi Graz. The calculations were partly performed on the dCluster and lCluster Graz as well as the VSC-3 cluster Vienna.

APPENDIX: TECHNICAL DETAILS OF THE SWF ALGORITHM

In order to present the SWF algorithm, we consider a general Lindblad system for a generalized "density-matrix" $\tilde{\varrho} = f(\{c^{(\dagger)}\})\rho$, where $f(\{c^{(\dagger)}\})$ denotes some function of fermionic operators,

$$\mathcal{L} = \mathcal{L}_H + \mathcal{L}_D. \tag{A1}$$

It is composed of a central region with Hamiltonian H and the corresponding Liouvillian $\mathcal{L}_H$,

$$\mathcal{L}_H\tilde{\varrho} = -i[H, \tilde{\varrho}], \tag{A2}$$

and a dissipative part described by $\mathcal{L}_D$,

$$\mathcal{L}_D\tilde{\varrho} = 2\sum_{ij}\Gamma^{(1)}_{ij}\left(\pm c_j\tilde{\varrho}c_i^\dagger - \frac{1}{2}\{\tilde{\varrho}, c_i^\dagger c_j\}\right) + 2\sum_{ij}\Gamma^{(2)}_{ij}\left(\pm c_i^\dagger\tilde{\varrho}c_j - \frac{1}{2}\{\tilde{\varrho}, c_j c_i^\dagger\}\right). \tag{A3}$$

Here i and j run over all L sites of the system and $\Gamma^{(1)/(2)}$ are $L \times L$ matrices. The minus sign in Eq. (A3) is valid if $\tilde{\varrho}$ is odd in the number of fermion operators, i.e., $\tilde{\varrho} = c_i^{(\dagger)}\rho$. This is the case with Green's functions, where we need to propagate $c_i^{(\dagger)}\rho$.

In order to obtain the jump operators one has to diagonalize the matrices $\Gamma^{(\beta)}$, $\beta = 1, 2$,

$$2\Gamma^{(\beta)}_{ij} = \sum_k U^{(\beta)}_{ik}\gamma^{(\beta)}_k U^{(\beta)^*}_{jk},$$

and end up with the eigendecomposition of the dissipator,

$$\mathcal{L}_D\rho = \sum_{\beta k}\left(\pm L^{(\beta)}_k\rho L^{(\beta)\dagger}_k - \frac{1}{2}\{\rho, L^{(\beta)\dagger}_k L^{(\beta)}_k\}\right), \tag{A4}$$

$$L^{(1)}_k = \sum_i \sqrt{\gamma^{(1)}_k}U^{(1)*}_{ik}c_i,$$

$$L^{(2)}_k = \sum_i \sqrt{\gamma^{(2)}_k}U^{(2)}_{ik}c_i^\dagger. \tag{A5}$$

The anticommutators in Eq. (A4) are included into the effective, non-Hermitian Hamiltonian [73],

$$H_{\text{eff}} = H - \frac{i}{2}\sum_{\beta k}L^{(\beta)\dagger}_k L^{(\beta)}_k = H - i\sum_{ij}\left[\Gamma^{(1)}_{ij} - \Gamma^{(2)}_{ij}\right]c_i^\dagger c_j - i\sum_i\Gamma^{(2)}_{ii}. \tag{A6}$$

With this Hamiltonian and the jump operators $L^{(\beta)}_k$, Eq. (A5), one formulates the SWF algorithms in Sec. III, Figs. 1 and 2.

1. Jump-time search and Arnoldi

As mentioned in Sec. III we use the so-called Arnoldi algorithm [39] for the time evolution. Arnoldi is a Krylov space method analog to Lanczos but for non-Hermitian Hamiltonians. For a given initial state, $|\psi_0\rangle$, and time interval, dt, a Krylov space, spanned by Q, is generated by iteratively applying H_{eff} to the starting vector until a satisfactory approximation for the time evolution operator $e^{-iH_{\text{eff}}dt} \approx Q^\dagger e^{-iH_K dt}Q$ is found. For any given time t up to the maximal time dt, the state and the corresponding norm needed for the SWF algorithm are given by

$$|\psi(t)\rangle = Q^\dagger e^{-iH_K t}Q|\psi_0\rangle = Q^\dagger e^{-iH_K t}\vec{v}_0, \tag{A7}$$

$$\vec{v}_0 = Q|\psi_0\rangle = (1, 0, 0, \dots)^\top, \tag{A8}$$

$$\|\psi(t)\|^2 = \langle\psi_0|Q^\dagger e^{iH_K^\dagger t}\underbrace{QQ^\dagger}_{\mathbb{1}}e^{-iH_K t}Q|\psi_0\rangle, \tag{A9}$$

$$= \vec{v}_0^\top e^{iH_K^\dagger t}e^{-iH_K t}\vec{v}_0, \tag{A10}$$

where we have used the property that $Q|\psi_0\rangle$ is nothing else than the first Krylov vector and $QQ^\dagger = \mathbb{1}$ is the identity [74]. We want to point out that by virtue of Eq. (A10) the norm can be calculated within the Krylov space representation itself, which is typically of size $\dim_K = O(10)$, without the need to use the transformation matrices Q which are of dimension $\dim_Q = \dim_F \dim_K$, where $\dim_F$ is the dimension of the Hilbert space (many-body Fock space). Differentiating Eq. (A10) yields

$$\frac{d}{dt}\|\psi(t)\|^2 = -2\text{Im}\left(\vec{v}_0^\top e^{iH_K^\dagger t}iH_K e^{-iH_K t}\vec{v}_0\right), \tag{A11}$$

which allows to determine the jump time t_j in the SWF algorithm, satisfying $\|\psi(t_j)\|^2 - r_j = 0$, by applying Newton's method.

2. Practical implementation for the steady-state situation

Here we want comment on the practical implementation for the special case of steady-state quantities.

a. Steady-state observables

We start with the, with respect to the needed numerical simulation protocol, simpler case of sampling a steady-state observable. A steady-state expectation value is obtained like in a MC simulation. We start with a random starting state and time evolve the system until it reaches the steady state, where the system is time-translational invariant (like the thermalization in a MC simulation). Once we are in the steady state, we start measuring the observable generating an autocorrelated time series from which an estimator of the expectation value can be obtained. As usual the time series needs to be long enough to have overcome autocorrelations, which can be checked for example by a Binning plot.

For the present case we typically recorded $N_m = 2^{18}$ measurements separated by a time $\Delta t = N_{t_{\text{skip}}}dt$ with a time step $dt = 0.05$ and $N_{t_{\text{skip}}}dt = 16dt \approx 10\bar{t}_j$, where $\bar{t}_j$ is the average jump time. For thermalization we performed additionally 10% of the total time evolution leading to $O(10^5)$ thermalization time steps. Parallelization can be achieved by computing several individual realizations on a single cluster node, where each realization is bound to one core, for instance.

b. Steady-state single-particle GF's

To obtain steady-state GF's of the Lindblad system we follow Ref. [40]. In short, it is best to calculate the lesser and

greater steady-state GF, defined by

$$G^{<}_{ij}(t) = i\langle c^{\dagger}_i(t)c_j\rangle_\infty, \quad G^{>}_{ij}(t) = -i\langle c_i(t)c^{\dagger}_j\rangle_\infty, \tag{A12}$$

where $\langle\cdot\rangle_\infty = T_r\{\cdot\rho_\infty\}$ denotes the expectation value in the steady state. We sample the GF by first time evolving into the steady state like above. Next, we apply the operator $c_r^{(\dagger)}$, construct the doubled Hilbert space, continue to time evolve in the doubled Hilbert space, and measure according to the SWF algorithm in the doubled Hilbert space.

As stated in the main text, the time steps needed for GF's is of $O(10^3)$ and to reach the accuracy needed for smooth spectral functions, we had to average over $O(10^5)$ realizations. Further, we perform $O(10^5)$ time steps to get into the steady state. For the performance in terms of CPU time, it is crucial that the time steps into the steady state are done only for a small fraction of the realizations; the corresponding final states are saved [75]. Another realization starts from a state obtained by time evolving such a saved state for some time $\Delta t \approx 100\bar{t}_j$, where $\bar{t}_j$ denotes the mean jump time [76], to make sure that individual realizations are independent to a very good approximation. Here we note that only early times will be correlated as the realizations gain in independence through the jumps in the time evolution [77].

i. Multistates. One can sample multiple correlation functions, $G_{B_iA_i}(t,t')$, together when generalizing the doubled Hilbert space to a multiple Hilbert space. For this, generalize

$$\Theta(t) = \begin{pmatrix} \psi(t) \\ \phi_1(t) \\ . \\ . \\ . \\ \phi_n(t) \end{pmatrix} \tag{A13}$$

with the excited states $\phi_i = A_i|\psi\rangle$. For instance, this allows us to sample the lesser and greater GF together in a tripled Hilbert space or multiple components of a cluster GF [78], G_{ij}. The advantage is that $|\psi\rangle$ is only time evolved ones, where as in the individual approach, with only a doubled Hilbert space, $|\psi\rangle$ is time evolved n times.

ii. Destroyed states in the multiple Hilbert space. Here we want to elaborate on the fact that part of the state may be destroyed when applying the SWF algorithm in the multiple Hilbert space. For simplicity, we consider in the following a doubled Hilbert space. Part of the state can get destroyed when the system leaves the physical particle sectors through the application of a jump operator [79]. For instance, a state can get destroyed when the system is in the $N = L$ particle sector and a jump operator $L_k^{(2)}$ gets chosen that increases the particle number.

First, let us note that this cannot happen in the single Hilbert space since the corresponding weight $w_{\beta k} \propto ||L_k^{(2)}\psi(t_j)||^2$ is zero and this jump operator will never be chosen. The situation is different in the doubled Hilbert space when the two components of a state reside in different particle sectors. Too see this, let us consider the case of the greater GF. Here, if $|\psi\rangle$ is in sector N, then $|\phi\rangle$ will always describe a state with $N+1$ particles, since the jump operator applied is the same for both components. If at some time t_{kill}, $|\phi\rangle$ is in the sector L, then the weight for a jump operator that increases the particle number, $w_{\beta k} \propto ||L_k^{(2)}\psi(t_j)||^2 + ||L_k^{(2)}\phi(t_j)||^2$, might be nonzero since the first part can be nonvanishing.

If part of the state is destroyed, then all subsequent measurements in this specific realization of the time series for the GF will all be zero.

It is important to realize that this is the correct behavior. It exemplifies why the doubled Hilbert space is needed when calculating correlation functions and why it would be wrong to simply consider an independent time evolution for the excited state and the initial state separately. In fact, in the independent approach, any correlation between the initial state and the final state would be lost very quickly through the stochastic process and it is key that the two states always jump together, thereby mediating the correlation.

[1] P. W. Anderson, Phys. Rev. **124**, 41 (1961).
[2] T. Holstein, Ann. Phys. **8**, 7325 (1959).
[3] J. Kondo, Prog. Theor. Phys. **32**, 37 (1964).
[4] P. Wiegmann and A. Finkelshtein, J. Exp. Theor. Phys. **48**, 102 (1978).
[5] A. C. Hewson, *The Kondo Problem to Heavy Fermions* (Cambridge University Press, Cambridge, 1993).
[6] E. Boulat, H. Saleur, and P. Schmitteckert, Phys. Rev. Lett. **101**, 140601 (2008).
[7] D. Goldhaber-Gordon, J. Göres, M. A. Kastner, H. Shtrikman, D. Mahalu, and U. Meirav, Phys. Rev. Lett. **81**, 5225 (1998).
[8] W. Metzner and D. Vollhardt, Phys. Rev. Lett. **62**, 324 (1989).
[9] M. Eckstein, A. Hackl, S. Kehrein, M. Kollar, M. Moeckel, P. Werner, and F. Wolf, Eur. Phys. J.: Spec. Top. **180**, 217 (2009).
[10] P. Schmidt and H. Monien (unpublished).
[11] A. V. Joura, J. K. Freericks, and T. Pruschke, Phys. Rev. Lett. **101**, 196401 (2008).
[12] M. Eckstein, M. Kollar, and P. Werner, Phys. Rev. Lett. **103**, 056403 (2009).
[13] M. Eckstein, M. Kollar, and P. Werner, Phys. Rev. B **81**, 115131 (2010).
[14] S. Okamoto, Phys. Rev. Lett. **101**, 116807 (2008).
[15] C. Aron, G. Kotliar, and C. Weber, Phys. Rev. Lett. **108**, 086401 (2012).
[16] J. E. Han, Phys. Rev. B **75**, 125122 (2007).
[17] J. E. Han and R. J. Heary, Phys. Rev. Lett. **99**, 236808 (2007).
[18] A. Dirks, P. Werner, M. Jarrell, and T. Pruschke, Phys. Rev. E **82**, 026701 (2010).
[19] C. Aron, C. Weber, and G. Kotliar, Phys. Rev. B **87**, 125113 (2013).
[20] P. Mehta and N. Andrei, Phys. Rev. Lett. **96**, 216802 (2006).
[21] F. B. Anders, Phys. Rev. Lett. **101**, 066804 (2008).
[22] Y. Meir and N. S. Wingreen, Phys. Rev. Lett. **68**, 2512 (1992).
[23] H. Schoeller and G. Schön, Phys. Rev. B **50**, 18436 (1994).
[24] A. Rosch, J. Paaske, J. Kroha, and P. Wölfle, J. Phys. Soc. Jpn. **74**, 118 (2005).
[25] H. Schoeller, Eur. Phys. J.: Spec. Top. **168**, 179 (2009).
[26] S. R. White and A. E. Feiguin, Phys. Rev. Lett. **93**, 076401 (2004).

[27] A. J. Daley, C. Kollath, U. Schollwöck, and G. Vidal, J. Stat. Mech. (2004) P04005.

[28] T. Prosen and M. Znidaric, J. Stat. Mech. (2009) P02035.

[29] F. B. Anders and A. Schiller, Phys. Rev. Lett. **95**, 196801 (2005).

[30] S. Kehrein, Phys. Rev. Lett. **95**, 056602 (2005).

[31] R. Gezzi, T. Pruschke, and V. Meden, Phys. Rev. B **75**, 045324 (2007).

[32] S. G. Jakobs, V. Meden, and H. Schoeller, Phys. Rev. Lett. **99**, 150603 (2007).

[33] C. Jung, A. Lieder, S. Brener, H. Hafermann, B. Baxevanis, A. Chudnovskiy, A. Rubtsov, M. Katsnelson, and A. Lichtenstein, Ann. Phys. **524**, 49 (2012).

[34] F. Chen, G. Cohen, and M. Galperin, arXiv:1810.10509.

[35] E. Arrigoni, M. Knap, and W. von der Linden, Phys. Rev. Lett. **110**, 086403 (2013).

[36] A. Dorda, M. Nuss, W. von der Linden, and E. Arrigoni, Phys. Rev. B **89**, 165105 (2014).

[37] A. Dorda, M. Sorantin, W. von der Linden, and E. Arrigoni, New J. Phys. **19**, 063005 (2017).

[38] A. A. Dzhioev and D. S. Kosov, J. Chem. Phys. **134**, 044121 (2011).

[39] M. Knap, E. Arrigoni, W. von der Linden, and J. H. Cole, Phys. Rev. A **83**, 023821 (2011).

[40] A. Dorda, M. Ganahl, H. G. Evertz, W. von der Linden, and E. Arrigoni, Phys. Rev. B **92**, 125145 (2015).

[41] D. M. Fugger, A. Dorda, F. Schwarz, J. von Delft, and E. Arrigoni, New J. Phys. **20**, 013030 (2018).

[42] I. Titvinidze, A. Dorda, W. von der Linden, and E. Arrigoni, Phys. Rev. B **92**, 245125 (2015).

[43] A. Dorda, I. Titvinidze, and E. Arrigoni, J. Phys.: Conf. Ser. **696**, 012003 (2016).

[44] I. Titvinidze, A. Dorda, W. von der Linden, and E. Arrigoni, Phys. Rev. B **96**, 115104 (2017).

[45] I. Titvinidze, M. E. Sorantin, A. Dorda, W. von der Linden, and E. Arrigoni, Phys. Rev. B **98**, 035146 (2018).

[46] G. Kotliar, S. Y. Savrasov, K. Haule, V. S. Oudovenko, O. Parcollet, and C. A. Marianetti, Rev. Mod. Phys. **78**, 865 (2006).

[47] J. Dalibard, Y. Castin, and K. Mølmer, Phys. Rev. Lett. **68**, 580 (1992).

[48] H.-P. Breuer, B. Kappler, and F. Petruccione, Phys. Rev. A **56**, 2334 (1997).

[49] H. Breuer, B. Kappler, and F. Petruccione, Eur. Phys. J. D **1**, 9 (1998).

[50] For simplicity we neglect spin.

[51] Here it is worth noting that the matrices $E^{(\alpha)}$, $\Gamma^{(\alpha),1}$, $\Gamma^{(\alpha),2}$ are only nonzero in the part of the system which describes the corresponding bath.

[52] We stress that for fixed total number of bath sites the accuracy of AMEA is comparable to the one of the equilibrium ED solver [80] with more than twice as many bath sites. This is because for fixed N_B AMEA offers more than twice as many fit parameters, E, $\Gamma^{(1)}$, $\Gamma^{(2)}$, than equilibrium ED, which is parametrized by a single matrix, E.

[53] This is the time it takes to obtain a given result. The wall time can be much smaller than the CPU time for a highly parallelized algorithm.

[54] D. Bauernfeind, M. Zingl, R. Triebl, M. Aichhorn, and H. G. Evertz, Phys. Rev. X **7**, 031013 (2017).

[55] D. Bauernfeind, R. Triebl, M. Zingl, M. Aichhorn, and H. G. Evertz, Phys. Rev. B **97**, 115156 (2018).

[56] Although it is desirable, as it gives the best approximation for a given system size.

[57] This corresponds to the case $N_B > 6$ when allowing for the most general Lindblad couplings.

[58] For example, we observed that for a system with $N_B = 9$ bath sites, increasing $\text{rank}_\gamma > 4$ was not fruitful in terms of the cost function.

[59] D. P. Kingma and J. Ba, arXiv:1412.6980.

[60] M. Abadi, A. Agarwal, P. Barham, E. Brevdo, Z. Chen, C. Citro, G. S. Corrado, A. Davis, J. Dean, M. Devin, S. Ghemawat, I. Goodfellow, A. Harp, G. Irving, M. Isard, Y. Jia, R. Jozefowicz, L. Kaiser, M. Kudlur, J. Levenberg, D. Mané, R. Monga, S. Moore, D. Murray, C. Olah, M. Schuster, J. Shlens, B. Steiner, I. Sutskever, K. Talwar, P. Tucker, V. Vanhoucke, V. Vasudevan, F. Viégas, O. Vinyals, P. Warden, M. Wattenberg, M. Wicke, Y. Yu, and X. Zheng, TensorFlow: Large-scale machine learning on heterogeneous systems (2015), available at http://tensorflow.org/.

[61] To be consistent with quantum mechanics, $P[\vec{\psi}, t]$ must not depend on the phase of the wave function and it is only nonvanishing for normalized states.

[62] More generally, λ indexes a complete set of quantum numbers.

[63] $P[\vec{\psi}, t]D\vec{\psi}D\vec{\psi}^*$ can then be interpreted as the probability to find the system within the volume element $D\vec{\psi}D\vec{\psi}^*$ around the state $\vec{\psi}$ at time t.

[64] F. Schwarz, M. Goldstein, A. Dorda, E. Arrigoni, A. Weichselbaum, and J. von Delft, Phys. Rev. B **94**, 155142 (2016).

[65] S. T. Carr, D. A. Bagrets, and P. Schmitteckert, Phys. Rev. Lett. **107**, 206801 (2011).

[66] In more detail, $V_c = \frac{\sqrt{3}}{4^{2/3}} \frac{4\sqrt{\pi}\Gamma(2/3)}{\Gamma(1/6)} T_B$ and $T_B = c(J')^{\frac{4}{3}}$ with $c \approx 2.7$ from [6].

[67] In contrast to previous works [65,81], we use the standard notation of the generalized hypergeometric function, that is, two arguments first than three.

[68] From previous works [70], we know that at $U = 2$ one has to restrict to $J' \lesssim 0.5$ and $V \lesssim 2$ to be in the scaling regime.

[69] In practice, we measure at all physical bonds and average accordingly. There is a tiny breaking of current conservation due to the numerics.

[70] K. Bidzhiev and G. Misguich, Phys. Rev. B **96**, 195117 (2017).

[71] This is a physical effect and not related to our approximation made within AMEA.

[72] A. Braun and P. Schmitteckert, Phys. Rev. B **90**, 165112 (2014).

[73] For this generalize $[H, \rho]$ to $H_{\text{eff}}\rho - \rho H_{\text{eff}}^\dagger$.

[74] Note that for non-Hermitian problems $Q^\dagger Q \neq \mathbb{1}$.

[75] In the present case the time steps into the steady state make for about 10% of the total run time.

[76] The time between consecutive jumps.

[77] One can test for autocorrelations when considering the different realizations for a specific (early-) time step as a time series and apply autocorrelation analysis.

[78] A matrix of GF's corresponding to a cluster of multiple sites.

[79] Naturally, this happens more often in smaller systems.

[80] M. Caffarel and W. Krauth, Phys. Rev. Lett. **72**, 1545 (1994).

[81] C. Schiegg, M. Dzierzawa, and U. Eckern, New J. Phys. **17**, 083060 (2015).

2.4 Publication 4: Steady state NEGF in the IRLM

The article titled *Nonequilibrium Green's functions and their relation to the NDC in the interacting resonant level model* was published in Physical Review B. **99** 075139, February 2019.
The work was conducted by Max Sorantin (MS) with Roman Lucrezi (RL) as co-author and supervised by Wolfgang von der Linden (WL) as well as Enrico Arrigoni (EA). It was initiated by MS and constitutes a follow-up to the third publication using its implementation of AMEA for the IRLM. RL implemented the Hartree-Fock self-consistent equations in Matlab and performed the corresponding computations under supervision of WL. MS used the existing implementation from Ref.[2] to calculate the NEGF's with AMEA. All authors took part in discussing the results and contributed to their interpretation. A first draft of the manuscript was written by MS and revised by EA, RL and WL.

Nonequilibrium Green's functions and their relation to the negative differential conductance in the interacting resonant level model

Max E. Sorantin,* Wolfgang von der Linden, Roman Lucrezi, and Enrico Arrigoni†
Institute of Theoretical and Computational Physics, Graz University of Technology, 8010 Graz, Austria

(Received 20 December 2018; revised manuscript received 6 February 2019; published 20 February 2019)

We evaluate the nonequilibrium single-particle Green's functions in the steady state of the interacting resonant level model (IRLM) under the effect of an applied bias voltage. Employing the so-called auxiliary master equation approach, we present accurate nonperturbative results for the nonequilibrium spectral and effective distribution functions, as well as for the current-voltage characteristics. We find a drastic change of these spectral properties between the regimes of low- and high-bias voltages and discuss the relation of these changes to the negative differential conductance (NDC), a prominent feature in the nonequilibrium IRLM. The anomalous evolution of the effective distribution function next to the impurity shown by our calculations suggests a mechanism whereby the impurity gets effectively decoupled from the leads at voltages where the NDC sets in, in agreement with previous renormalization group approaches. This scenario is qualitatively confirmed by a Hartree-Fock treatment of the model.

DOI: 10.1103/PhysRevB.99.075139

I. INTRODUCTION

Transport through nanodevices such as molecular junctions or quantum dots has become of great interest in the past due to the potential application of these systems as new types of electronic components [1,2]. Generically, the working principle of such components is entailed in their current-voltage (I-V) characteristic. In some situations this can display nonmonotonic behavior, usually referred to as negative differential conductance (NDC), a peculiar effect that is intriguing by itself but also most useful in potential applications [3–7]. Therefore, a thorough understanding of the NDC is highly desirable.

A prototypical model exhibiting a NDC is the so-called interacting resonant level model (IRLM), a simplistic model featuring a two-level quantum dot connected to leads used to study the interplay of quantum fluctuations and electronic correlations in the setting of quantum impurity problems. Introduced by Vigman and Finkelstein [8] in the (equilibrium) context of the Kondo problem, the IRLM in nonequilibrium has received increasing attention over the last decade after the discovery of an analytic expression for the I-V characteristic [9] in the so-called scaling regime and for a special value of the interaction, referred to as the self-dual point of the IRLM.

Previous works on the IRLM in nonequilibrium extended the analytic treatment of the self-dual point [10], considering also higher-order statistics of charge transport [11,12], and provided further validation by numerical treatments of increasing accuracy [13]. Away from the self-dual point, Perfetto *et al.* [14] studied the transport properties of the IRLM employing nonequilibrium Green's functions (NEGFs) focusing on the effect of long-range interactions. In addition, a perturbative treatment within NEGF [15] as well as renormalization group (RG) approaches [16,17], valid for weak interactions, provide further insight for small interactions. In particular, it is found that the NDC within RG arises due to a renormalization of the hopping rate into the leads which gets suppressed for higher voltages [18–20]. In contrast, less is known about the physical mechanism of the NDC at the self-dual point, i.e., for intermediate values of the interaction. Related to the NDC, but also very interesting in itself, is the spectral function of the IRLM which in equilibrium was numerically studied by Braun and Schmitteckert [21] but, to our knowledge, has not been considered so far in a nonequilibrium situation within a nonperturbative treatment.

In this paper, we evaluate NEGF of the IRLM in order to investigate their connection with the NDC and how the spectral and effective distribution functions evolve in terms of the bias voltage. Our results are obtained within the so-called auxiliary master equation approach (AMEA), a numerical method to treat nonequilibrium quantum impurity problems and evaluate their NEGF with considerable accuracy. For simplicity, our calculations refer to the self-dual point, but can be readily carried out for other values of the interaction. Finally, we complement our discussion of the AMEA results with a Hartree-Fock (HF) treatment in order to help with the interpretation.

We find that in the regime of the NDC, the spectral function evolves from a peak at finite frequencies into a dominant central peak and that the NDC can be traced back to the behavior of the effective distribution functions on the first lead sites. We interpret this behavior as an effective decoupling of the impurity from the leads, which is confirmed from the HF calculations.

II. MODEL AND METHOD

A. Model

The IRLM is a well-known impurity model of spinless fermions. It features an impurity site connected to two

*sorantin@tugraz.at
†arrigoni@tugraz.at

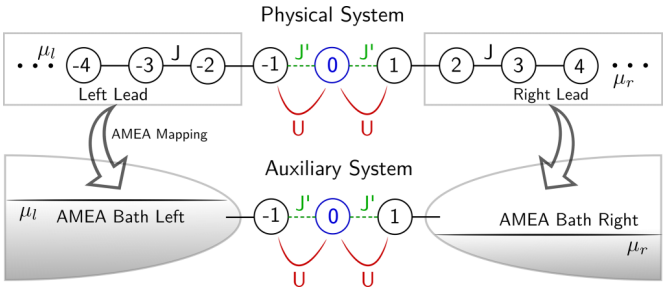

FIG. 1. A sketch of the IRLM as a lattice model and its mapping to the auxiliary open quantum system used within AMEA.

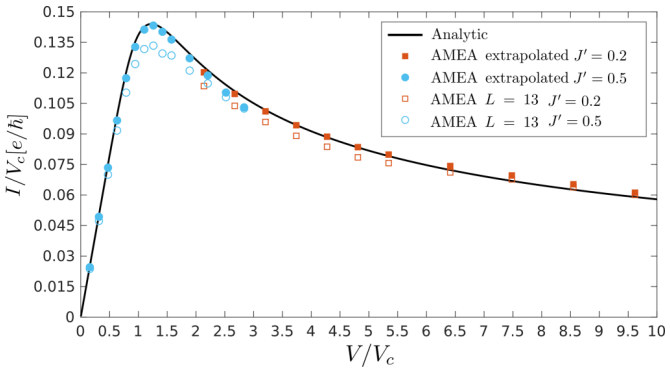

FIG. 2. Current-voltage characteristic of the IRLM for two different hybridization strengths $J' = 0.5$ (blue circles) and $J' = 0.2$ (red squares). We display the analytic solution at $T = 0$ (solid lines), the extrapolated, formally $L \to \infty$, AMEA data from Ref. [31] (solid symbols), and the AMEA current in the $L = 13$ system (open symbols).

semi-infinite tight-binding chains together with a density-density interaction term coupling the impurity site to the neighboring chain sites (see Fig. 1). The Hamiltonian is defined as

$$\begin{aligned} H_{\mathrm{IRLM}} &= H_{\mathrm{L}} + H_{\mathrm{R}} + H_{\mathrm{dot}}, \\ H_{\mathrm{L}} &= -J \sum_{r=-\infty}^{-2} c_r^\dagger c_{r+1} + \mathrm{H.c.}, \\ H_{\mathrm{R}} &= -J \sum_{r=1}^{+\infty} c_r^\dagger c_{r+1} + \mathrm{H.c.}, \\ H_{\mathrm{dot}} &= -J' \sum_{r=-1}^{r=0} c_r^\dagger c_{r+1} + \mathrm{H.c.} \\ &\quad + U \sum_{r=\pm 1} \left(c_r^\dagger c_r - \frac{1}{2}\right)\left(c_0^\dagger c_0 - \frac{1}{2}\right), \end{aligned} \tag{1}$$

where $c_r^\dagger / c_r$ denote the fermionic creation/annihilation operators at site r. Here, $H_{\mathrm{L/R}}$ describe the semi-infinite tight-binding chains and H_{dot} introduces the hopping to the impurity as well as the interaction term. A nonequilibrium steady state situation is induced in the system via an applied bias voltage V simulated by shifting the chemical potentials of the leads symmetrically, that is, $\mu_l = -\mu_r = \frac{V}{2}$. We use J as the unit of energy and work in units where $\hbar = e = k_B = 1$.

The continuum limit and the scaling regime of the IRLM

Here, we want to summarize some well-known facts about the IRLM in the so-called scaling regime, which are important for the present work. A nice overview in the nonequilibrium context can be found in the recent works [8,9,12,13] and references therein.

When the bandwidth of the leads, $W = 4J$, is the dominant energy scale in the system, the lattice model [Eq. (1)] becomes equivalent to its continuum limit [22], allowing for a field theoretic description. In this scaling regime of the IRLM, the physics becomes universal with the emergence of a Kondo energy scale $T_B \sim (J')^{\frac{4}{3}}$. The constant of proportionality is the lattice regularization of the corresponding field theory relating results from the continuum limit to the lattice model.

The continuum model can be solved analytically for the special value of the interaction $U_c^* = \pi$, which corresponds to $U_{\mathrm{lat}}^* \cong 2$ in the lattice model, where the IRLM exhibits a certain self-duality. Most notably, there is a closed form expression for the steady state current at $T = 0$,

$$I(V) = \frac{V}{2\pi}\, {}_2F_3\left[\left\{\frac{5}{6}, \frac{7}{6}\right\}, \left\{\frac{1}{4}, \frac{3}{4}, 1\right\}; -\left(\frac{V}{V_c}\right)^6\right], \tag{2}$$

with $V_c = c(J')^{\frac{4}{3}}$, where $c \approx 3.2$ [23] and ${}_2F_3(a, b; z)$ is the generalized hypergeometric function [24]. From Eq. (2), it immediately follows that $I/V = f(V/V_c)$ depends only on the rescaled voltage and thus has a universal form set by the energy scale T_B. As is best seen by expanding the hypergeometric function up to leading order,

$$I(V \ll V_c) \approx \frac{V}{2\pi}\left[1 - \frac{24}{170}\left(\frac{V}{V_c}\right)^6 + O\left(\frac{V}{V_c}\right)^{12}\right], \tag{3}$$

the current is linear for small voltages $V < V_c$. The most prominent feature of the current arises for $V > V_c$ where the model exhibits a negative differential conductance (see Fig. 2).

B. Method

In this paper, we use the auxiliary master equation approach (AMEA) [25–27] to investigate the IRLM under the influence of an applied bias voltage. AMEA is a method to treat nonequilibrium correlated impurity problems which is particularly efficient to target the steady state. It is based upon mapping the noninteracting bath onto an auxiliary open quantum system whose dynamics is described by the Lindblad equation. This mapping becomes exponentially accurate by increasing the number of sites in this auxiliary system. This open quantum system effectively mimics a system with infinite volume, so that one can reliably reach the steady state. Correlation functions are then obtained by time evolution of the many-body density matrix starting from the steady state.

The dynamics of the auxiliary open quantum system can be solved numerically exact by available approaches. Here, we employ the so-called stochastic wave functions [28–30], whose application to AMEA is presented in Ref. [31]. Within the mapping, the central interacting region $|r| \leqslant 1$ described by H_{dot} (cf. Fig. 1) remains unchanged [32]. In total, the

auxiliary open quantum system thus consists of $L = 3 + 2N_B$ sites, where N_B denotes the number of auxiliary dissipative bath levels used to replace the left (right) semi-infinite leads. For details, we refer to previous publications [25–27,31].

Steady-state current

The current $I_{r,r+1}$ across a bond connecting site r and $r+1$, which is clearly independent of r in the steady state, can be expressed within the Keldysh Green's function (GF) formalism as [33]

$$I_{r,r+1} = t_{r,r+1}^2 \int \frac{d\omega}{2\pi} \mathrm{Re}\, j(\omega),$$
$$j(\omega) = G^R_{rr}(\omega) g^K_{r+1,r+1}(\omega) + G^K_{rr}(\omega) g^A_{r+1,r+1}(\omega), \quad (4)$$

provided the interaction self-energy is zero across the bond. Here, a capital $G_{r,r}(\omega)$ denotes the local GF of the full system, while the lower case $g_{r,r}(\omega)$ is the one when the system is disconnected at the bond connecting the sites r and $r+1$. A convenient choice is the bond from one noninteracting bath to the interacting region, i.e., $r = -2$ to $r = -1$.

In equilibrium, $V = 0$, the Keldysh and retarded GF are not independent and connected by the fluctuation-dissipation theorem, which for the GFs appearing in Eq. (4) reads

$$\mathrm{Im}\, G^K_{rr'}(\omega) = 2[1 - 2f(\omega)]\mathrm{Im}\, G^R_{rr'}(\omega),$$

where $f(\omega)$ denotes the Fermi-Dirac distribution function. In analogy, one can define an effective local nonequilibrium energy distribution function $\tilde{f}_r(\omega)$ via the relation (cf. also, e.g., Refs. [34–38])

$$\mathrm{Im}\, G^K_{rr}(\omega) = 2[1 - 2\tilde{f}_r(\omega)]\mathrm{Im}\, G^R_{rr}(\omega), \quad (5)$$

which by definition reduces back to the Fermi function in an equilibrium situation. With Eq. (5), we can express the current from the left lead into the central region as [39]

$$I_L(V) \equiv I_{-2,-1} = 2\pi(J)^2 \int d\omega A_{-1}(\omega; V) A_{\mathrm{TB}}(\omega) \times [f_L(\omega; V) - \tilde{f}_{-1}(\omega; V)], \quad (6)$$

where $A_r \equiv -\frac{1}{\pi}\mathrm{Im}\, G^R_{rr}$ is the local density of states, $A_{\mathrm{TB}}(\omega)$ denotes the density of states (DOS) of the disconnected left lead, that is, the DOS of a semi-infinite tight-binding chain, and f_L is the Fermi function of the left lead. Here, for convenience, we have indicated any possible dependence on the bias voltage. In Eq. (6), the frequency integrand contains the difference between the effective distribution function at the first correlated site $r = -1$ and the one deep into the left lead weighted with the corresponding DOS.

III. RESULTS

In this section, we present results for the nonequilibrium spectral properties of the IRLM. We are not aware of previous numerically accurate results for the nonequilibrium Green's function of this model from the literature. We consider the self-dual point $U = 2$ and compute results for two different values of the hybridization strength $J' = 0.2$ and $J' = 0.5$ at a finite temperature $T = 0.025$. The size of the auxiliary system, which controls the accuracy of the bath hybridization function (see Refs. [26,27]) is fixed to $L = 13$. Both the steady state as well as the Green's functions are obtained by time evolution by stochastic wave functions (see Ref. [31] for technical details). In order to illustrate the accuracy of the approach, we first plot the steady state current as a function of the bias voltage in Fig. 2. Specifically, we compare data from the present $L = 13$ auxiliary-system calculation with the ones of the more accurate approach of Ref. [31], where the current is obtained via an extrapolation for values of L up to $L = 19$. The analytic solution of the continuum model at $T = 0$ is also shown for comparison. In this paper, we use smaller values of L because a full Green's function calculation for $L = 19$ would be computationally too expensive. These results show that also $L = 13$ provides quite accurate results [40] and, in particular, reproduces the NDC.

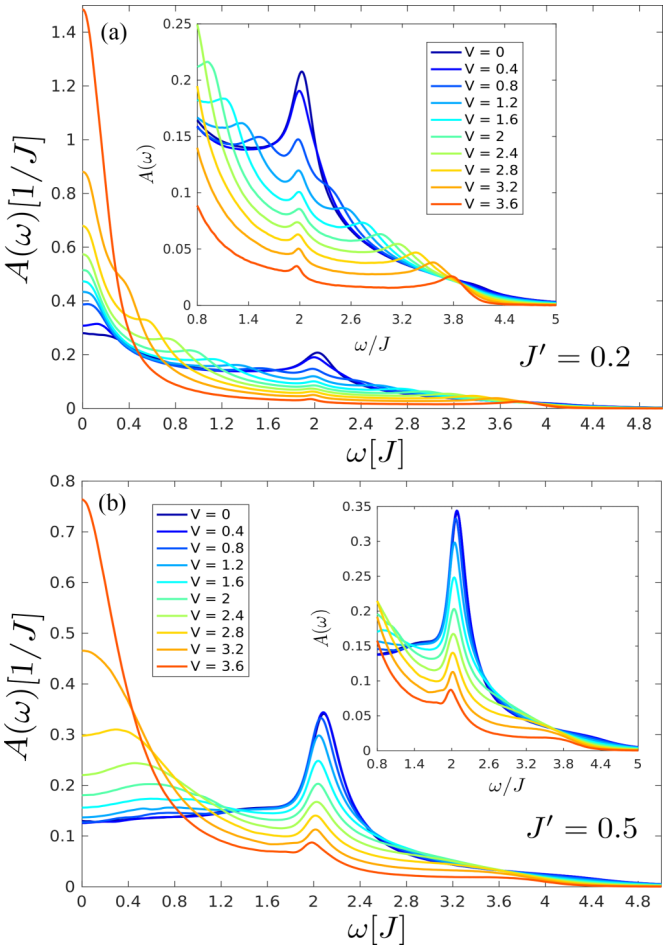

FIG. 3. Local density of states at the impurity site, $r = 0$, for different bias voltages. (a) $J' = 0.2$ and (b) $J' = 0.5$. Other parameters: $T = 0.025$ and $U = 2$. The insets show a zoom around the peak at $\omega = 2$ and its appearing satellite at $\omega = 2 \pm V/2$.

A. Spectral properties at the central impurity site

Figure 3 shows the density of states at the impurity site, $r = 0$, for different bias voltages [41]. The equilibrium ($V = 0$) system is characterized by a pronounced peak at $\omega = 2$. Upon increasing the bias voltage, the spectral weight is removed from the $\omega \approx 2$ in favor of a second peak at zero fre-

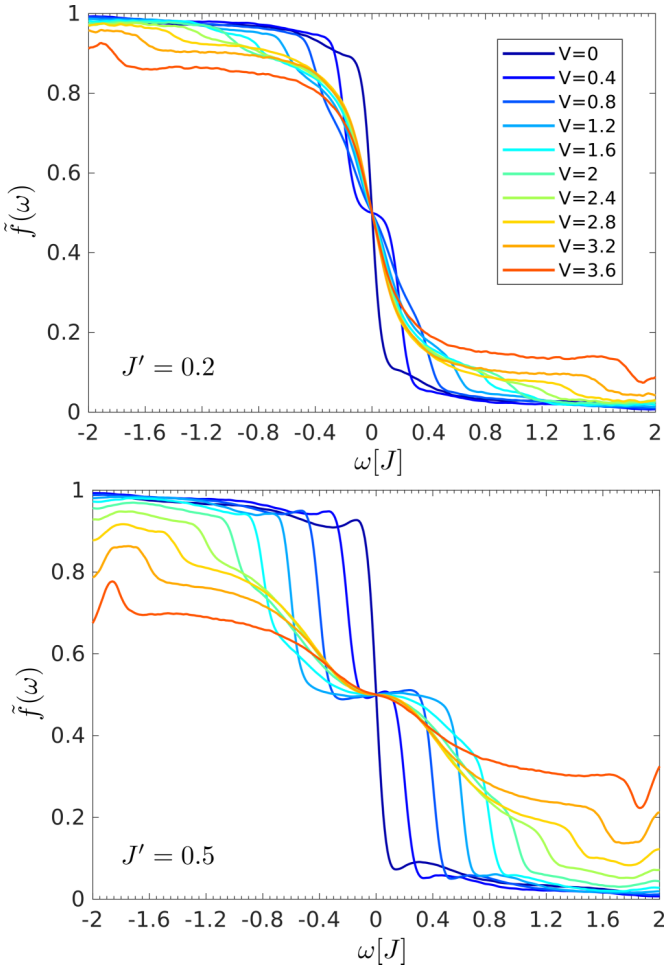

FIG. 4. Distribution function at the central impurity site for different bias voltages. Parameters are as in Fig. 3. The nonsmoothness of the curves is due to the statistical error of the stochastic wave-functions (SWF) approach, which gets amplified for the effective distribution function as this is given by the ratio two Green's functions. For $V = 0$, we observe deviations from the expected Fermi function (see Sec. II B). It is a consequence of the fact that AMEA only reproduces approximately the lead hybridization functions including their occupation. This is improved exponentially upon increasing the size L of the auxiliary system.

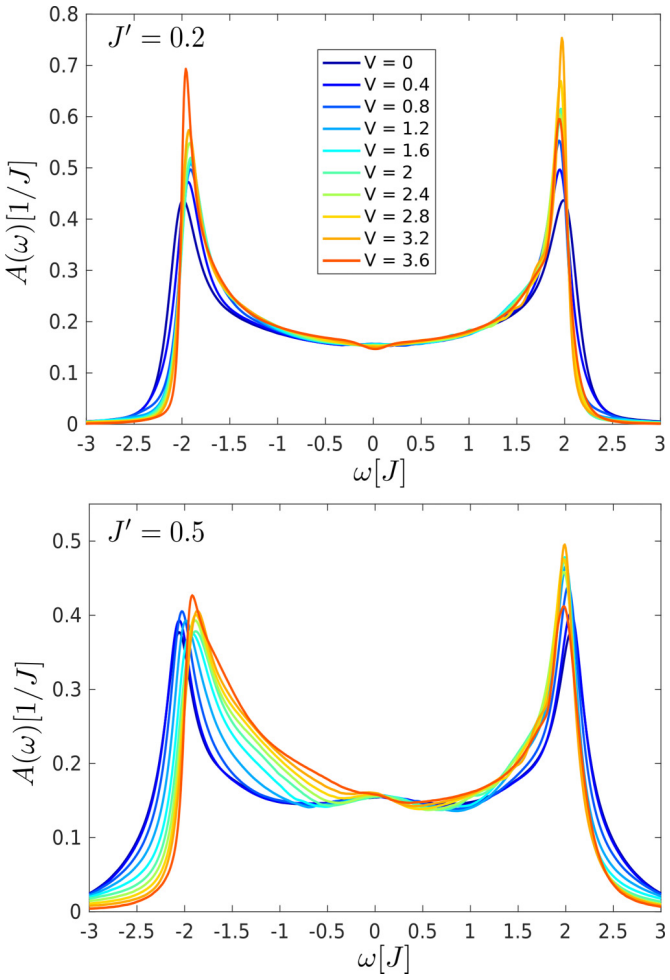

FIG. 5. Local density of states for different bias voltages at site $r = -1$. Parameters are the same as in Fig. 3.

quency, which quickly becomes dominant for large bias voltages. At the same time, the equilibrium resonance develops sidebands at $\omega = 2 \pm V/2$. This effect is more pronounced for the case of low $J' = 0.2$ since a stronger J' broadens all peak features. At large voltages, $V \gtrsim 3.2$ for $J' = 0.2$, the left satellite merges with the central peak.

Out of equilibrium the fermionic effective distribution function obviously deviates from the Fermi-Dirac distribution and acquires an anomalous, position-dependent shape. In Fig. 4, we plot the effective distribution function, $\tilde{f}_r(\omega)$ defined in Eq. (5), at the impurity site, $r = 0$, for different bias voltages. We find that the latter is dominated by a double Fermi step, $2\tilde{f}_{r=0}(\omega) = f_L(\omega) + f_R(\omega)$, for small bias voltages and drastically changes its shape for bias voltages where the NDC sets in.

B. Sites next to the impurity ($r = \pm 1$) and relation with the current integrands

To make contact with the current integrands [Eq. (6)], we now consider the spectral properties on the sites next to the impurity (see also Sec. II B) [42]. Figure 5 displays the local density of states for different bias voltages. It shows two main peaks around $\omega = \pm 2$ [43], and a featureless spectrum in between. For both hybridization strengths, $J' = 0.2$ and $J' = 0.5$, the peaks become sharper and higher with increasing voltage. In addition, for $J' = 0.5$, spectral weight accumulates for negative frequencies up to the lower band edge at $\omega = -2$.

A more interesting behavior can be seen in the corresponding effective distribution function for $r = -1$ presented in Fig. 6. Similarly to the central impurity site, a double Fermi step persists in the linear regime, while for higher-bias voltages the effective distribution function becomes more similar to the effective distribution function of the isolated left lead for which all states for frequencies smaller than its chemical potential μ_l are occupied. More specifically, the plateau in the positive frequency region $0 < \omega < \mu_l$ rises in the regime of the NDC.

To elucidate the effect of the bias-dependent spectral and effective distribution functions on the current [cf. (6)], we display in Fig. 7 for $J' = 0.5$ the difference in the effective

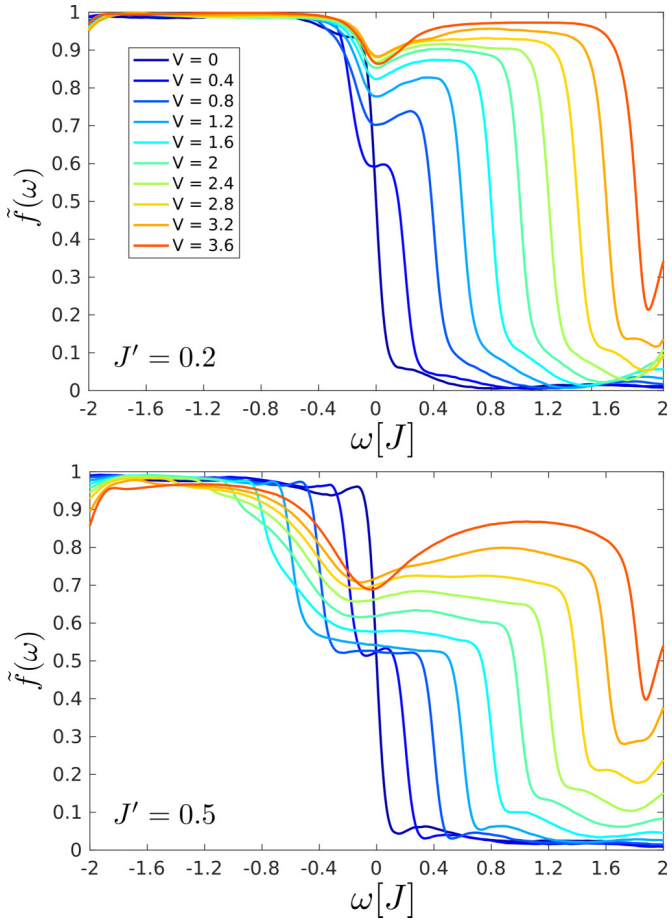

FIG. 6. Same as Fig. 4 but for the site $r = -1$.

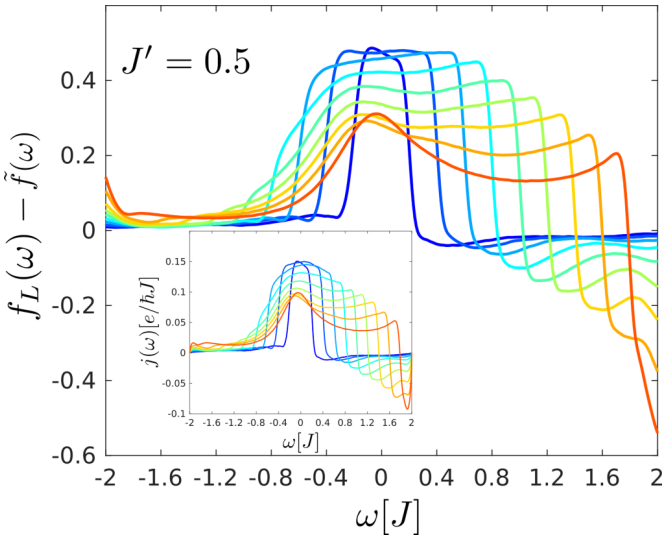

FIG. 7. Difference of the effective distribution functions entering the expression for the current [Eq. (6)] for different bias voltages. The inset shows the overall integrand of Eq. (6), which is dominated by the behavior of the effective distribution functions. We only present the results for $J' = 0.5$. Other parameters and the label as in Fig. 3. Note that the current integrand is identically zero outside the bandwidth, $|\omega| > 2$.

distribution functions entering Eq. (6) as well as the current integrand [44] which can be seen to be dominated by the behavior of the effective distribution function. The difference of the effective distribution functions has a Fermi-window form of amplitude $1/2$ for small voltages which is considerably distorted in the NDC regime. For negative frequencies $\omega \lesssim -1$ the amplitude quickly vanishes due to the corresponding states being filled at larger voltages (see Fig. 6), whereas at positive frequencies, the amplitude gets suppressed with increasing bias voltage which technically leads to the NDC. Outside of the Fermi window the difference of the effective distribution functions becomes slightly negative. One should not overemphasize this negative region, since the negative differential conductance does not depend on this [45].

IV. DISCUSSION AND INTERPRETATION OF THE RESULTS

In order to understand the behavior of the spectral and effective distribution functions presented above, we discuss the probabilities of certain characteristic many-body configuration states on the correlated sites. These are displayed in Fig. 8 and ranked according to their energy for zero voltage. Notice that the configurations in each pair are related to each other by a particle-hole+inversion (PHI) transformation [46] and thus have the same probability. In addition, the states (II_a) and (II_b) have the same probability at zero-bias voltage. The corresponding probability is given by the diagonal terms of the reduced (many-body) steady state density matrix, which is plotted in Fig. 9 as a function of the bias voltage.

One can see that the lowest-energy state, type (I), initially slightly gains weight as the bias voltage is increased. This occurs approximately until the point where the NDC sets in. In the NDC regime, $V > V_{\mathrm{max}}$, the (I) state loses weight and eventually crosses with the state (II_a) which becomes the dominant state at high voltages. Further, the states of type ($\mathrm{II}_{a(b)}$), which are degenerate in equilibrium, get their degeneracy lifted by the bias voltage favoring the (II_a) state since it is the one showing more occupation on the left in accordance with the chemical potentials, $\mu_L > \mu_R$. On the other hand, the weight of the highly suppressed high-energy states (III) stays roughly constant for all bias voltages.

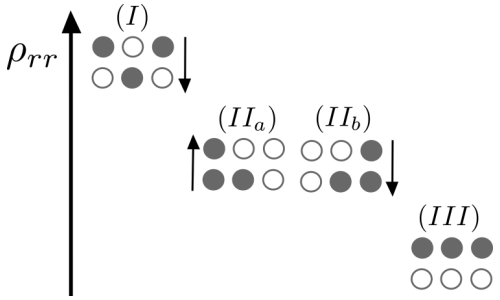

FIG. 8. Sketch of the eight different many-body configurations of the interacting region H_{dot}. The ordering corresponds to their respective weight in the zero-voltage case, where all states of type (II) are equivalent. The arrows indicate the respective behavior for growing bias voltages in the NDC regime. States are displayed in PHI symmetric pairs.

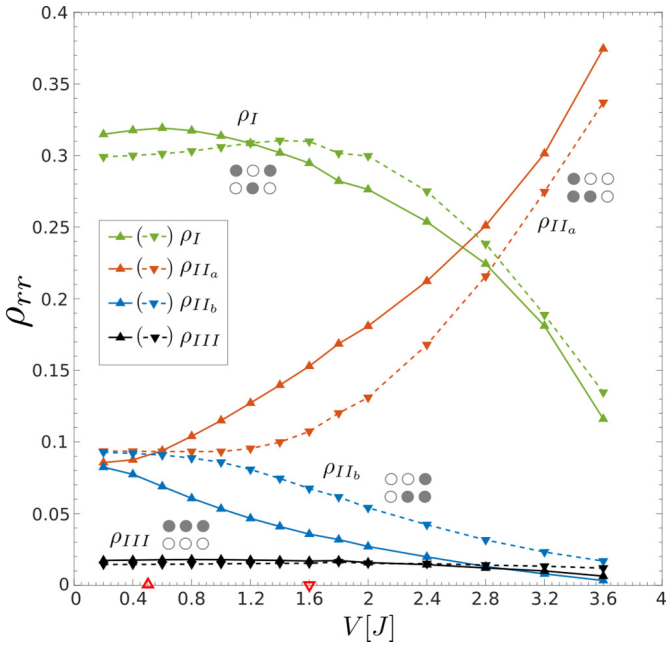

FIG. 9. Probabilities of the many-body configurations displayed in Fig. 8 for $J' = 0.2$ (solid lines) and $J' = 0.5$ (dashed lines). The markers on the x axis mark the voltages corresponding to the maximum of the current, $V_{\max}(J' = 0.2) \approx 0.5$ and $V_{\max}(J' = 0.5) \approx 1.6$.

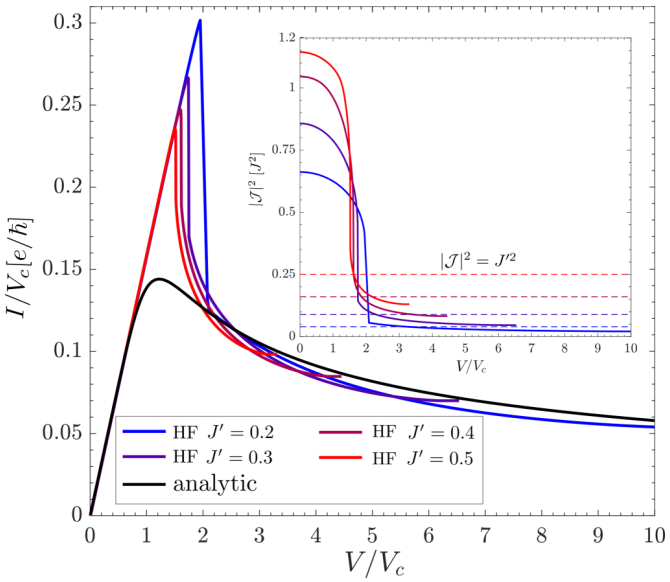

FIG. 10. Scaled current as a function of scaled voltage for different hybridization strengths $0.2 < J' < 0.5$ (colored lines) obtained within Hartree-Fock (HF) and the analytic solution, Eq. (2) (black line). The inset shows the squared effective hopping amplitude $|\mathcal{J}|^2$ obtained within HF as a function of the rescaled bias voltage for $U = 2$, $T = 0$, and different hybridization strengths J'. The dashed lines in the inset mark the squared bare hoppings J'^2.

A. Impurity spectral function

As discussed above, in equilibrium ($V = 0$), the configuration (I) has a large overlap with the ground state. Adding a particle at the impurity site to (I) leads to the state (III). Since the energy difference, in the atomic limit $J' = 0$, between these two states is $\Delta E = 2$, this process can be associated with the $\omega \approx 2$ resonance. The suppression of the $\omega = 2$ resonance for higher voltages immediately follows from the loss of the weight of the (I) state (cf. Fig. 9). It remains to explain the development of the dominant central peak for high voltages. In general, a resonance at zero frequency occurs when two low-lying states differing by one particle, at the corresponding site, are almost degenerate. This is the case for the states of type (II). The development of the central peak is then readily explained by the increased weight of the state (II_a) at high-bias voltages.

B. Negative differential conductance

In Sec. III B, we discussed that on the level of NEGFs the NDC at large voltage in the IRLM arises due to the effective distribution function on the site next to impurity resembling the Fermi function of the corresponding lead. This can be seen as an effective decoupling of the impurity from the leads at large bias voltage.

References [15,47] showed that the NDC in the IRLM is already obtained at the Hartree-Fock (HF) level. Therefore, it is interesting to investigate if the mechanism leading to the NDC obtained from our results is qualitatively similar to the one in the HF approximation.

C. Comparison with Hartree-Fock

We will not present the details of the HF calculations, but we will only underline the connection to the AMEA results. For an alternative discussion of the NDC arising already within HF, we refer to the work of Vinkler-Aviv *et al.* [15]. Within HF for the particle-hole symmetric case, which we are discussing in this paper, the Hamiltonian is the same as the noninteracting one with the only exception that we have a renormalized complex hopping between the central impurity and the $r = \pm 1$ sites,

$$J' \longrightarrow \mathcal{J}_\pm = J' + U\langle c^\dagger_{\pm 1} c_0\rangle_{\mathrm{HF}}. \tag{7}$$

The computation of the GFs can be taken from the $U = 0$ case, keeping in mind that the hopping $\mathcal{J}_\pm$ is complex and has to be determined self-consistently. It occurs that the local NEGFs within HF depend only on $|\mathcal{J}|^2$ and the expression for the distribution function on the site $r = -1$ has the form

$$\tilde{f}_{-1}(\omega; V) = \frac{f_L(\omega; V) + \alpha(\omega, V) f_R(\omega; V)}{1 + \alpha(\omega, V)}, \tag{8}$$

where $\alpha(\omega)$ depends on the bias voltage only through $|\mathcal{J}|^2$ and is proportional to $|\mathcal{J}|^4$ [48].

In Fig. 10, we display the (scaled) current and the squared effective hopping amplitude as a function of the scaled bias voltage within HF. The HF current is qualitatively the same as in the exact solution, but instead of a smooth transition from the linear regime to the NDC, it shows a cusp and a sudden drop [49] at $V/V_c \approx 2$. The drop in the current is accompanied by a drop in the squared effective hopping, which becomes small for voltages outside the linear regime. This behavior of $|\mathcal{J}|^2$ can be interpreted as an effective decoupling of the

impurity from the $r = \pm 1$ sites in the NDC regime, consistent with the interpretation of the AMEA results.

In the regime in which $|\mathcal{J}|^2$ is small, i.e., large V, the impurity is weakly coupled to the reservoirs. Its spectral function thus consists of a single central peak. It follows that the spectral function at site $r = -1$ will be given by the DOS of a semi-infinite tight-binding chain. In addition, from Eq. (8) it is clear that the effective distribution function $\tilde{f}_{-1}(\omega)$ will resemble the one of the left lead since α is strongly suppressed. In the opposite case, when $|\mathcal{J}|^2$ is not small, $\tilde{f}_{-1}(\omega)$ will be close to a double Fermi step and the spectral functions, independent of r, will resemble the DOS of an infinite tight-binding chain. This means that $A_{-1}^{(\mathrm{HF})}(\omega)$ changes between two different shapes in the large and small V regions, in contrast to the AMEA results. Similar to the AMEA results, the NDC within HF is also caused by the change in the effective distribution function since the spectral density $A_{-1}^{(\mathrm{HF})}(\omega)$ in the NDC regime has more spectral weight inside the transport window compared to the solution just before the cusp in the current.

V. SUMMARY AND CONCLUSION

We calculated the nonequilibrium single-particle Green's functions (GFs), as well as the (many-body) steady state density matrix, of the interacting resonant level model (IRLM) in the presence of an applied bias voltage employing the auxiliary master equation approach (AMEA). We find developments of sidebands in the impurity spectral function which transforms into a single peak at zero energy for high-bias voltages in the regime of the negative differential conductance (NDC). Further, on the level of the nonequilibrium spectral and effective distribution functions, the negative differential conductance in the IRLM arises due to the behavior of the effective distribution functions at the sites next to the impurity. In more detail, they feature a double Fermi step which persists in the linear regime of the current and resemble their equilibrium form of one separated lead for high-bias voltages which we interpret as an effective decoupling of the system for voltages in the NDC regime. Supplementing our results with a Hartree-Fock (HF) treatment makes the decoupling explicit and shows that the spectral features resulting in the NDC are shared by both approaches.

In conclusion, our results suggest, in accordance with previous results for small interactions, an effective decoupling of the impurity from the leads as the origin of the NDC in the IRLM also at the self-dual point.

ACKNOWLEDGMENTS

We would like to thank Delia Fugger, Irakli Titvinidze, Gerhard Dorn, and Volker Meden for fruitful discussions. Special mention goes to Antonius Dorda who originally developed most of the code used for the numeric computations. This work was partially supported by the Austrian Science Fund (FWF) within Projects No. P26508 and No. F41 (SFB ViCoM), as well as NaWi Graz. The calculations were partly performed on the D-Cluster and L-cluster Graz and on the VSC-3 cluster Vienna.

[1] M. Ratner, Nat. Nanotechnol. **8**, 378 (2013).
[2] J. Kobak, T. Smolenski, M. Goryca, M. Papaj, K. Gietka, A. Bogucki, M. Koperski, J.-G. Rousset, J. Suffczynski, E. Janik, M. Nawrocki, A. Golnik, P. Kossacki, and W. Pacuski, Nat. Commun. **5**, 3191 (2014).
[3] J. Chen, M. A. Reed, A. M. Rawlett, and J. M. Tour, Science **286**, 1550 (1999).
[4] J. Chen, W. Wang, M. A. Reed, A. M. Rawlett, D. W. Price, and J. M. Tour, Appl. Phys. Lett. **77**, 1224 (2000).
[5] I. Kratochvilova, M. Kocirik, A. Zambova, J. Mbindyo, T. E. Mallouk, and T. S. Mayer, J. Mater. Chem. **12**, 2927 (2002).
[6] Y. Xue, S. Datta, S. Hong, R. Reifenberger, J. I. Henderson, and C. P. Kubiak, Phys. Rev. B **59**, R7852 (1999).
[7] H. Ying, W.-X. Zhou, K.-Q. Chen, and G. Zhou, Comput. Mater. Sci. **82**, 33 (2014).
[8] P. Wiegmann and A. Finkel'shtein, Zh. Eksp. Teor. Fiz. **75**, 204 (1978) [JETP **48**, 102 (1978)].
[9] E. Boulat, H. Saleur, and P. Schmitteckert, Phys. Rev. Lett. **101**, 140601 (2008).
[10] G. Camacho, P. Schmitteckert, and S. T. Carr, arXiv:1810.08246.
[11] A. Branschädel, E. Boulat, H. Saleur, and P. Schmitteckert, Phys. Rev. Lett. **105**, 146805 (2010).
[12] S. T. Carr, D. A. Bagrets, and P. Schmitteckert, Phys. Rev. Lett. **107**, 206801 (2011).
[13] K. Bidzhiev and G. Misguich, Phys. Rev. B **96**, 195117 (2017).
[14] E. Perfetto, G. Stefanucci, and M. Cini, Phys. Rev. B **85**, 165437 (2012).
[15] Y. Vinkler-Aviv, A. Schiller, and F. B. Anders, Phys. Rev. B **90**, 155110 (2014).
[16] S. Andergassen, V. Meden, H. Schoeller, J. Splettstoesser, and M. R. Wegewijs, Nanotechnology **21**, 272001 (2010).
[17] D. M. Kennes and V. Meden, Phys. Rev. B **87**, 075130 (2013).
[18] L. Borda, K. Vladár, and A. Zawadowski, Phys. Rev. B **75**, 125107 (2007).
[19] C. Karrasch, S. Andergassen, M. Pletyukhov, D. Schuricht, L. Borda, V. Meden, and H. Schoeller, Europhys. Lett. **90**, 30003 (2010).
[20] C. Karrasch, M. Pletyukhov, L. Borda, and V. Meden, Phys. Rev. B **81**, 125122 (2010).
[21] A. Braun and P. Schmitteckert, Phys. Rev. B **90**, 165112 (2014).
[22] Also referred to as the wideband limit.
[23] In more detail, $V_c = \frac{\sqrt{3}}{4^{2/3}} \frac{4\sqrt{\pi}\Gamma(2/3)}{\Gamma(1/6)} T_B$ and $T_B = \tilde{c}(J')^{\frac{4}{3}}$ with $\tilde{c} \approx 2.7$ from Ref. [9].
[24] Here, we use the standard notation of the generalized hypergeometric function, two arguments first, then three, in contrast to previous works [12,47].
[25] E. Arrigoni, M. Knap, and W. von der Linden, Phys. Rev. Lett. **110**, 086403 (2013).
[26] A. Dorda, M. Nuss, W. von der Linden, and E. Arrigoni, Phys. Rev. B **89**, 165105 (2014).

[27] A. Dorda, M. Sorantin, W. von der Linden, and E. Arrigoni, New J. Phys. **19**, 063005 (2017).
[28] J. Dalibard, Y. Castin, and K. Mølmer, Phys. Rev. Lett. **68**, 580 (1992).
[29] H.-P. Breuer, B. Kappler, and F. Petruccione, Phys. Rev. A **56**, 2334 (1997).
[30] H. Breuer, B. Kappler, and F. Petruccione, Eur. Phys. J. B **1**, 9 (1998).
[31] M. E. Sorantin, D. M. Fugger, A. Dorda, W. von der Linden, and E. Arrigoni, arXiv:1812.02049.
[32] We note that the mapping needs to be performed for each bias voltage separately but is independent of the parameters in H_{dot}, i.e., J' and U.
[33] H. Haug and A.-P. Jauho, *Quantum Kinetics in Transport and Optics of Semiconductors* (Springer, Heidelberg, 1998).
[34] N. Tsuji, T. Oka, and H. Aoki, Phys. Rev. Lett. **103**, 047403 (2009).
[35] Y. Murakami, N. Tsuji, M. Eckstein, and P. Werner, Phys. Rev. B **96**, 045125 (2017).
[36] J. E. Han and J. Li, Phys. Rev. B **88**, 075113 (2013).
[37] C. Aron, G. Kotliar, and C. Weber, Phys. Rev. Lett. **108**, 086401 (2012).
[38] C. Aron, C. Weber, and G. Kotliar, Phys. Rev. B **87**, 125113 (2013).
[39] Which reduces to the well-known Landauer formula for $U = 0$ involving only the difference of the left/right Fermi functions. To see this, consider Eq. (8).
[40] See also Ref. [31] for a benchmark of the $L = 13$ GF in equilibrium.
[41] We only show the result for positive frequencies since even at finite bias the IRLM is still particle-hole symmetric at the impurity site.
[42] We only show results for the site $r = -1$ as the properties at $r = 1$ are connected by particle-hole symmetry.
[43] We note that for other values of the interaction U, the peaks are not fixed at $\omega = \pm U$ nor do they stay at $\omega \approx 2$ (not shown).
[44] We do not show the corresponding plots for $J' = 0.2$ since they are qualitatively the same and can be readily extracted from Figs. 5 and 6.
[45] That is, the NDC is present even if these negative contributions to the current are ignored.
[46] We note that while at zero bias the model is independently particle-hole and inversion symmetric, at finite voltage the model is symmetric under a simultaneous PHI transformation.
[47] C. Schiegg, M. Dzierzawa, and U. Eckern, New J. Phys. **17**, 083060 (2015).
[48] The precise form is $\alpha(\omega, |\mathcal{J}|^2(V)) = |\mathcal{J}|^4 |\frac{1}{\omega^+ - |\mathcal{J}|^2 \frac{1}{\omega^+ - J^2 g^R_{\mathrm{TB}}}} \frac{1}{\omega^+ - J^2 g^R_{\mathrm{TB}}}|^2$, with $\omega^+ \equiv \omega + i0^+$ and g^R_{TB} denoting the GF of a semi-infinite tight-binding chain.
[49] Reminiscent of a first-order phase transition as is typical within a mean-field treatment.

2.5 Contributions to further publications

In addition to the four publications explicitly presented above, MS contributed as co-author to [3, 4]. In Ref.[3], the interplay between local and long range Coulomb interactions was considered and the charge redistribution in a metal - Mott insulator - metal hetero structure studied. The strong local Coulomb interaction in the Mott insulator was treated within realspace DMFT and the long range Coulomb part on a mean-field level via the Poisson equation. MS helped in the code development and debugging of the C++ program, engaged in the discussions of the results and revised the first version of the manuscript written by Irakli Titvinidze (IT).
The work published in Ref.[4] was a collaboration with the group of Walter Hofstetter in Frankfurt who investigated the charge-density wave state in the dissipative extended Hubbard model as realized in experiments with ultracold fermionic gases. The corresponding first author Jaromir Panas (JP) had implemented his own version of the AMEA SF+ED impurity solver and contacted our group for expertise. MS clarified some technicalities regarding the mapping and provided reference solutions for the impurity model without spin-degeneracy in the bath. In equilibrium test cases JP found that the AMEA SF+ED impurity solver with four bath sites produces the wrong magnetization (even in sign) when compared to a Quantum Monte Carlo (QMC) simulation. To clarify the issue, MS and IT conducted single-shot impurity calculations for the steady state magnetization with the AMEA SWF+ED implementation featuring up to ten bath sites, which proved that the problem is rectified with higher accuracy in AMEA. For this MS adapted the existing SWF+ED implementation and performed the needed fits while IT took care of the many-body computations.

Chapter 3

Summary and Outlook

We have further developed AMEA and applied it to study nonequilibrium many-body effects in the IRLM and the dissipative Hubbard model.

NDC in the IRLM: The NDC in the IRLM (Sec.1.1.2 and Sec.2.4) was investigated by calculating the NEGF'S of the model in the presence of a bias voltage. The corresponding results support the scenario of a renormalized hybridization strength at high voltages leading to the NDC as reported in previous studies based on RG approaches and NEGF evaluated to leading order in the interaction. Since the latter approaches are reliable only in certain parameter regimes (Sec.1.1.2.1), our results complement the existing literature by providing non-perturbative confirmation of the renormalized hybridization, even outside the scaling regime.

The work around the IRLM within this thesis is concentrated on the self-dual point at low temperatures. Since AMEA becomes more efficient with increasing temperature it would be very interesting to study the effect of finite temperatures on the transport properties, which would also allow to consider strong interactions, $U \geq W$. The latter needs an accurate representation of the hybridization also outside the bandwidth, which was not possible to achieve at low temperatures with the limited number of bath sites. Also higher order moments of charge transfer could be considered to study possible charge fractionalization effects, known to be present at the self-dual point, also for other interaction strengths.

Floquet DMFT: The role of impact ionization in the periodic steady state of an electric field driven Mott-insulating layer coupled to metallic leads was studied within Floquet DMFT (Sec.2.2) and its relation to Mott-photovoltaic systems discussed (Sec.1.1.1). We found a significant enhancement of the photo-current in a regime, where impact ionization is possible with respect to its value, when the driving frequency does not support the latter. Our results show that impact ionization plays a dominant role also in the periodic steady state and are thus in line with previous model based calculations, which report the effectiveness of impact ionization on the photovoltaic efficiency of Mott insulators. This has to be confronted with the poor performance of fabricated devices observed in experiments,

which is, however, linked to low carrier mobility, due to imperfections in the samples. Thus, on the level of the simplified toy-model that was considered, this scenario is strengthened by our results in the sense that the periodic drive does not negatively interfere with impact ionization and cannot be the source of the poor efficiency observed in experiments.

To study the effect of impact ionization on the Mott photovoltaic efficiency in a more realistic situation, the model can be generalized in multiple directions. One could consider a heterostructure of Mott insulating layers under light incidence. This would allow to simulate also the internal electric field needed to separate the charge carriers as well as the usage of broad and only partially filled leads, as is more appropriate for the description of metallic reservoirs. Another crucial ingredient for a more realistic description are electron-phonon interactions since they provide a competing dissipation mechanism. For a first study, the electron-phonon interaction could be treated by adding only the leading order diagram to the electronic selfenergy. This could be extended by treating the electron-phonon coupling by the self-consistent Migdal approximation[35], which constitutes a conserving approximation in contrast to the simpler variant. Finally, long ranged Coulomb forces could be introduced to address bound excitons. For instance, this can be done on the level of the Poisson equation as demonstrated within this thesis[3] and would avoid the need to build in the electric field for charge separation by hand, since the latter is build up automatically by the charge redistribution induced by the long-range Coulomb forces.

On the technical side, we have introduced the FDSA within Floquet DMFT (Sec.2.2), which allows to simplify the involved impurity problem to a standard nonequilibrium steady state one. In Sec.1.2.6.2 we extended tests from the original publication[5], performed at intermediate interaction strengths within IPT, to the Mott regime confirming the reliability of the approximation as long as Floquet sidebands are highly suppressed which is the case for low driving amplitudes and or high frequencies. These tests were complemented by a method comparison between the NCA and FDSA+AMEA for the periodically driven dissipative Hubbard model, which cross validates both approaches.

As a final note on Mott photovoltaics we would like to add that the broad application, not restricted to niche markets, as efficient solar-cell is only feasible if the production costs can be made very low. This seems hard to achieve due to the difficulties in the synthesization. However, in view of the high photoresponsivity of the Mott insulating materials, it would be interesting to consider instead of an application as solar-cell also the possibility of a photo-detector which is not so reliant on cheap mass production.

Technical developments of AMEA: AMEA was further developed in various aspects (Sec.1.2.2-1.2.5). Considering a variable-rank parametrization for the $\mathbf{\Gamma}$-matrices in the Lindblad system has proven to substantially reduce the fit parameters in the corresponding optimization problem. This allowed us to reliably find minima, featuring an exponential decrease in the cost-function with respect to increasing system size, for auxiliary systems with up to eight bath sites. Further, we found that a gradient based optimization algorithm from machine learning, in the efficient implementation of a corresponding python library, is an efficient replacement for the previously used PT approach and, in particular, features

drastically lower cpu-times for bigger systems, where the PT algorithm becomes unfeasible. The idea of extrapolating a result obtained with AMEA to zero cost-function by taking into account the information of different auxiliary system sizes was successfully applied to the steady state current in the IRLM showing significant improvement towards the reference solution (Sec.2.3). The latter was complemented in this thesis by the presentation of an error estimation scheme for the extrapolated values (Sec.1.2.4.1). In addition to these developments, an alternative solution strategy for the many-body Lindblad problem based on SWF's was tested. The latter constitutes a completely different approach with respect to the previously considered ones that are based on SF, SF+ED and SF+MPS, where the density matrix is "purified" by considering a system with twice as many sites, thereby squaring the Hilbert space. In contrast to this, the density matrix is unraveled in SWF algorithm by considering stochastic time-evolutions of individual wave-functions, which allows to simulate the system without the need to square the Hilbert space. This allows to treat systems with twice as many bath sites with respect to the SF approach, which, due to the exponential convergence of AMEA with respect to system size, constitutes a drastic improvement in the possible accuracy. This improvement comes at the cost of much higher cpu-times, due to the large number of realizations needed for a sufficiently low statistical error. However, the SWF algorithm, like most stochastic approaches, is trivially parallelizable with respect to the different realizations and therefore allows to reach extremely low wall-times on modern cluster facilities. This paves the way for AMEA to be used as multi-orbital impurity solver within nonequilibrium steady state DMFT, as discussed below.

Outlook on AMEA: Various ways exist to further advance the method. On the level of the mapping and its optimization problem, the current implementations are only able to maintain an exponential decrease of the cost-function for systems with about one hundred fit parameters, $\dim_{\vec{x}} \approx 100$. To effectively find good minima in even higher dimensions, a combination of the stochastic element of the PT algorithm together with a local gradient based optimization is of great potential, whereby the low temperatures in the PT approach are replaced by the deterministic local optimization leading to a more efficient sampling of the parameter space. The efficiency of this approach could be further increased by the consideration of "stretching" techniques[107, 108], where already found minima, and worse ones, are excluded in the further optimization by deforming the cost-function.

The many-body solution within SWF's is presently only implemented in the combination with ED and calls for extensions to other time-evolution schemes such as tensor network techniques. Especially the combination of SWF+MPS is very promising and, in contrast to the already implemented SF+MPS variant, it has the advantage that the system being time-evolved can be chosen truly one-dimensional, which is where the MPS approach is most efficient. In view of multi-orbital nonequilibrium DMFT, the combination of SWF with so-called Fork Tensor Product States (FTPS) is most promising, since the FTPS is tailored to the multi-orbital impurity problem and has already been applied successfully as real-time impurity solver in equilibrium[109, 110].

An interesting development for the many-body solution is the use of Dual Fermions[111–114] (DF) utilizing the auxiliary Lindblad system as reference[115]. The combination is quite natural, since AMEA exactly solves a system with a precisely known auxiliary hybridization. The DF approach then formulates a perturbation expansion in the difference between the physical and auxiliary hybridization around the interacting reference solution. The improved accuracy, boosting a system with two bath sites effectively to six bath sites[115], is paid for by the effort to calculate the two-particle GF of the auxiliary system, needed as input for the first order correction in the DF formalism. The latter becomes a formidable task for system sizes beyond two bath sites, which cannot be fully diagonalized. When applied to bigger auxiliary systems, it is questionable, if the same level of accuracy increase can be maintained, since the reference state is more accurate and thus the first order correction in DF might be less substantial. Further, the combination of DF with many-body solution strategies, which are, as far their implementation is concerned, not strictly limited in system size, like MPS, might not be beneficial. This is, because it could be numerically more efficient to go to bigger system sizes instead of evaluating the two-particle GF. In contrast, when combined with a method like in ED, which, due to memory requirements, is limited in system size, the DF approach constitutes an option to improve the result. A corresponding collaboration with the authors of Ref.[115] is in progress, in order to test the DF scheme in combination with the SF+ED variant of AMEA with the aim to investigate the behavior of DF+AMEA with increasing auxiliary system size. If fruitful, this could be used to enhance the capabilities of the SF+ED impurity solver in DMFT applications. If we assume that two bath sites are enough to represent a single bath, the DF approach also opens the door to use SWF+ED as multi-orbital impurity solver, at least for up to three orbitals, in nonequilibrium steady state DMFT.

One of the strengths of AMEA is that the many-body aspect enters only in the solution of the auxiliary system and is completely decoupled from the foundation of AMEA, which is based on the mapping to the latter. Therefore, any existing or future method to simulate correlated systems, especially time-evolution algorithms which can be applied or generalized to the treatment of a non-hermitian generator, may be adapted and used within AMEA. This endows the method overall with a high flexibility and a great potential for the future.

Appendix A

Details on the Floquet transformation

Here, we present some details about the Floquet transformation, Eq.(1.21).
We consider a function $F(t,t')$ of two time arguments, which is periodic with periodicity τ,

$$F(t,t') = F(t+\tau, t'+\tau)\,. \tag{A.1}$$

First, we transform variables to so-called Wigner coordinates defined by the relative time, $t_{\mathrm{rel}} = t - t'$, and the average time, $t_{\mathrm{avg}} = \frac{t+t'}{2}$. In this new variables, we have

$$F^{(W)}(t_{\mathrm{rel}}, t_{\mathrm{avg}}) = F(t,t') = F(t+\tau, t'+\tau) = F^{(W)}(t_{\mathrm{rel}}, t_{avg}+\tau)\,, \tag{A.2}$$

where the superscript (W) denotes the function after transformation to Wigner coordinates, which we will omit in the following. Performing a Fourier transform in the time-translation invariant coordinate t_{rel}, we obtain

$$F(\omega, t_{\mathrm{avg}}) = \int_{-\infty}^{+\infty} dt_{\mathrm{rel}} e^{i\omega t_{ref}} F(t_{\mathrm{rel}}, t_{\mathrm{avg}})\,. \tag{A.3}$$

Next, we use the periodicity in the average time, Eq. (A.2), to expand the transformed function into a Fourier series

$$F(\omega, t_{\mathrm{avg}}) = \sum_{k=-\infty}^{+\infty} F_k(\omega) e^{-ik\Omega t_{\mathrm{avg}}} \quad \text{with} \quad \Omega = \frac{2\pi}{\tau}\,, \tag{A.4}$$

where the coefficients are given by

$$F_k(\omega) = \frac{1}{\tau}\int_0^{\tau} dt_{\mathrm{avg}} e^{ik\Omega t_{\mathrm{avg}}} F(\omega, t_{\mathrm{avg}})\,. \tag{A.5}$$

Eq(A.5) is referred to as Wigner representation, where all information about the time dependence of the original function is encoded into the frequency dependent expansion

coefficients $F_k(\omega)$. Now, we can define a matrix structure, called Floquet matrix, as

$$F_{mn}(\omega) \equiv F_{m-n}(\omega + \frac{m+n}{2}\Omega) = \int_{-\infty}^{+\infty} dt_{\rm rel} \frac{1}{\tau} \int_0^{\tau} dt_{\rm avg} e^{i(\omega+m\Omega)t - i(\omega+n\Omega)t'} F(t,t') \,, \quad \text{(A.6)}$$

which leads to Eq.(1.21). It has the advantage that a convolution in time variables transforms into a matrix product in Floquet space, i.e. $C(t,t') = A(t,t'') * B(t'',t') \longrightarrow C_{mn}(\omega) = A_{ml}(\omega) B_{ln}(\omega)$.
From now on, F with one subscript denotes the Wigner representation and with two subscripts the Floquet matrix representation. Some useful relations are

$$\begin{aligned} &F_{m\pm k,n}(\omega) = F_{m,n\mp k}(\omega \pm k\Omega) \,, \\ &F_{m,n}(\omega) = F_{m-n,0}(\omega + n\Omega) \,, \\ &F_k(\omega) = F_{n+k,n}(\omega - n\Omega - \frac{k}{2}\Omega) = F_{k,0}(\omega - \frac{k}{2}\Omega)) \,. \end{aligned} \quad \text{(A.7)}$$

Inverse relation: To connect us back to the time variables, we calculate the inverse relation from the Floquet transformation. Using the inverse Fourier transform for Eq.(A.3) and plugging it into Eq.(A.4), we find

$$\begin{aligned} F(t_{\rm rel}, t_{\rm avg}) &= \sum_{k=-\infty}^{+\infty} \int_{-\infty}^{+\infty} \frac{d\omega}{2\pi} e^{-i\omega t_{\rm rel} - ik\Omega t_{\rm avg}} F_k(\omega) \,, \\ &= \sum_{k=-\infty}^{+\infty} \int_{-\infty}^{+\infty} \frac{d\omega}{2\pi} e^{-i\omega t_{\rm rel} - ik\Omega t_{\rm avg}} F_{k,0}(\omega - \frac{k}{2}\Omega) \,, \\ &= \sum_{k=-\infty}^{+\infty} \int_{-\infty}^{+\infty} \frac{d\omega}{2\pi} e^{-i(\omega + \frac{k\Omega}{2})t_{\rm rel} - ik\Omega t_{\rm avg}} F_{k,0}(\omega) \,. \end{aligned} \quad \text{(A.8)}$$

Due to Eq.(A.7), we can rewrite the integration over ω, as

$$\begin{aligned} &\int_{-\infty}^{+\infty} \frac{d\omega}{2\pi} e^{-i\omega t_{\rm rel}} F_{k,0}(\omega) = \sum_{n=-\infty}^{+\infty} \int_{n\Omega}^{(n+1)\Omega} \frac{d\omega}{2\pi} e^{-i\omega t_{\rm rel}} F_{k,0}(\omega) \,, \\ &= \sum_{n=-\infty}^{+\infty} \int_0^{\Omega} \frac{d\omega}{2\pi} e^{-i(\omega+n\Omega)t_{\rm rel}} F_{k,0}(\omega + n\Omega) \,, \\ &= \sum_{n=-\infty}^{+\infty} e^{-in\Omega t_{\rm rel}} \int_0^{\Omega} \frac{d\omega}{2\pi} e^{-i\omega t_{\rm rel}} F_{n+k,n}(\omega) \,. \end{aligned} \quad \text{(A.9)}$$

Plugging it back into Eq.(A.8), we get

$$F(t_{\rm rel}, t_{\rm avg}) = \sum_{n,k=-\infty}^{+\infty} e^{-i(n+\frac{k}{2})\Omega t_{\rm rel}} e^{-ik\Omega t_{\rm avg}} \int_0^\Omega \frac{d\omega}{2\pi} e^{-i\omega t_{\rm rel}} F_{n+k,n}(\omega)\,, \tag{A.10}$$

$$\overset{m\equiv n+k}{=} \sum_{m,n=-\infty}^{+\infty} e^{-i\frac{m+n}{2}\Omega t_{\rm rel}} e^{-i(m-n)\Omega t_{\rm avg}} \int_0^\Omega \frac{d\omega}{2\pi} e^{-i\omega t_{\rm rel}} F_{m,n}(\omega)\,. \tag{A.11}$$

Or in terms of the original time variables (t, t') and for the special case of equal time, we have

$$F(t, t') = \sum_{m,n=-\infty}^{+\infty} e^{-i\Omega(mt-nt')} \int_0^\Omega \frac{d\omega}{2\pi} e^{-i\omega(t-t')} F_{m,n}(\omega)\,, \tag{A.12}$$

$$F(t = t') = \sum_{m,n=-\infty}^{+\infty} e^{-i(m-n)\Omega t} \int_0^\Omega \frac{d\omega}{2\pi} F_{m,n}(\omega)\,. \tag{A.13}$$

As a consequence, for equal times, only the diagonal part of the Floquet matrix contributes to a quantity averaged over one period

$$\begin{aligned}\frac{1}{\tau}\int_0^\tau dt F(t = t') &= \sum_{m,n=-\infty}^{+\infty} \underbrace{\frac{1}{\tau}\int_0^\tau dt e^{-i(m-n)\Omega t}}_{=\delta_{m,n}} \int_0^\Omega \frac{d\omega}{2\pi} F_{m,n}(\omega) \\ &= \sum_{n=-\infty}^{+\infty} \int_0^\Omega \frac{d\omega}{2\pi} F_{n,n}(\omega) = \int_{-\infty}^{+\infty} \frac{d\omega}{2\pi} F_{0,0}(\omega)\end{aligned} \tag{A.14}$$

Publications within this Thesis

[1] A. Dorda, M. Sorantin, W. von der Linden, E. Arrigoni, "Optimized auxiliary representation of non-Markovian impurity problems by a Lindblad equation", *New J. Phys.* **2017**, *19*, 063005.

[2] M. E. Sorantin, D. M. Fugger, A. Dorda, W. von der Linden, E. Arrigoni, "Auxiliary master equation approach within stochastic wave functions: Application to the interacting resonant level model", *Phys. Rev. E* **2019**, *99*, 043303.

[3] I. Titvinidze, M. E. Sorantin, A. Dorda, W. von der Linden, E. Arrigoni, "Charge redistribution in correlated heterostuctures within nonequilibrium real – space dynamical mean – field theory", *Phys. Rev. B* **2018**, *98*, 035146.

[4] J. Panas, M. Pasek, A. Dhar, T. Qin, A. Geißler, M. Hafez-Torbati, M. E. Sorantin, I. Titvinidze, W. Hofstetter, "Density-wave steady-state phase of dissipative ultracold fermions with nearest-neighbor interactions", *Phys. Rev. B* **2019**, *99*, 115125.

[5] M. E. Sorantin, A. Dorda, K. Held, E. Arrigoni, "Impact ionization processes in the steady state of a driven Mott-insulating layer coupled to metallic leads", *Phys. Rev. B* **2018**, *97*, 115113.

[6] M. E. Sorantin, W. von der Linden, R. Lucrezi, E. Arrigoni, "Nonequilibrium Green's functions and their relation to the negative differential conductance in the interacting resonant level model", *Phys. Rev. B* **2019**, *99*, 075139.

References

[7] A. C. Hewson, *The Kondo Problem to Heavy Fermions*, Cambridge Books Online, Cambridge University Press, Cambridge, **1993**.

[8] F. Gebhard, *The Mott Metal-Insulator Transition - Models and Methods*, Springer, Heidelberg, **1997**.

[9] J. Schwinger, "Brownian Motion of a Quantum Oscillator", *J. Math. Phys.* **1961**, *2*, 407.

[10] L. V. Keldysh, "Diagram Technique for Nonequilibrium Processes", *Sov. Phys. JETP* **1965**, *20*, 1018.

[11] J. Robert, S. Niels, G. Kenneth, H. Moritz, E. Tilman, "A Mott insulator of fermionic atoms in an optical lattice", *Nature* **2008**, *455*, 204.

[12] U. Schneider, L. Hackermüller, S. Will, T. Best, I. Bloch, T. A. Costi, R. W. Helmes, D. Rasch, A. Rosch, "Metallic and Insulating Phases of Repulsively Interacting Fermions in a 3D Optical Lattice", *Science* **2008**, *322*, 1520–1525.

[13] D. Goldhaber-Gordon, H. Shtrikman, D. Mahalu, D. Abusch-Magder, U. Meirav, M. A. Kastner, "Kondo effect in a single – electron transistor", *Nature (London)* **1998**, *391*, 156.

[14] F. Simmel, R. H. Blick, J. P. Kotthaus, W. Wegscheider, M. Bichler, "Anomalous Kondo Effect in a Quantum Dot at Nonzero Bias", *Phys. Rev. Lett.* **1999**, *83*, 804–807.

[15] M. Pletyukhov, H. Schoeller, "Nonequilibrium Kondo model: Crossover from weak to strong coupling", *Phys. Rev. Lett.* **2012**, *108*, 260601.

[16] A. Dorda, M. Ganahl, H. G. Evertz, W. von der Linden, E. Arrigoni, "Auxiliary master equation approach within matrix product states: Spectral properties of the nonequilibrium Anderson impurity model", *Phys. Rev. B* **2015**, *92*, 125145.

[17] D. M. Fugger, A. Dorda, F. Schwarz, J. von Delft, E. Arrigoni, "Nonequilibrium Kondo effect in a magnetic field: auxiliary master equation approach", *New Journal of Physics* **2018**, *20*, 013030.

[18] P. Mehta, N. Andrei, "Nonequilibrium Quantum Impurities: From Entropy Production to Information Theory", *Phys. Rev. Lett.* **2008**, *100*, 086804.

[19] P. Schmidt, H. Monien, "Nonequilibrium dynamical mean – field theory of a strongly correlated system", arXiv:cond-mat/0202046, **2002**.

[20] A. Georges, G. Kotliar, W. Krauth, M. J. Rozenberg, "The Local Impurity Self Consistent Approximation (LISA) to Strongly Correlated Fermion Systems and the Limit of Infinite Dimensions", *Rev. Mod. Phys.* **1996**, *68*, 13.

[21] H. Aoki, N. Tsuji, M. Eckstein, M. Kollar, T. Oka, P. Werner, "Nonequilibrium dynamical mean-field theory and its applications", *Rev. Mod. Phys.* **2014**, *86*, 779–837.

[22] H. U. R. Strand, M. Eckstein, P. Werner, "Nonequilibrium Dynamical Mean-Field Theory for Bosonic Lattice Models", *Phys. Rev. X* **2015**, *5*, 011038.

[23] I. Titvinidze, A. Dorda, W. von der Linden, E. Arrigoni, "Transport through a correlated interface: Auxiliary master equation approach", *Phys. Rev. B* **2015**, *92*, 245125.

[24] P. Werner, M. Eckstein, "Field-induced polaron formation in the Holstein-Hubbard model", *EPL (Europhysics Letters)* **2015**, *109*, 37002.

[25] D. Golez, M. Eckstein, P. Werner, "Dynamics of screening in photo – doped Mott insulators", *Phys. Rev. B* **2015**, *92*, 195123.

[26] M. Eckstein, P. Werner, "Ultra-fast photo-carrier relaxation in Mott insulators with short-range spin correlations", *Scientific Reports* **2016**, *6*, Article, 21235.

[27] J. J. Mendoza-Arenas, F. J. Gómez-Ruiz, M. Eckstein, D. Jaksch, S. R. Clark, "Ultra-Fast Control of Magnetic Relaxation in a Periodically Driven Hubbard Model", *Annalen der Physik* **2017**, *529*, 1700024.

[28] H. U. R. Strand, D. Golez, M. Eckstein, P. Werner, "Hund's coupling driven photo-carrier relaxation in the two-band Mott insulator", *Phys. Rev. B* **2017**, *96*, 165104.

[29] L. Du, L. Huang, G. A. Fiete, "Spin-selective thermalization plateau in the mass-imbalanced Hubbard model", *Phys. Rev. B* **2017**, *96*, 165151.

[30] L. Du, G. A. Fiete, "Dynamical recovery of SU(2) symmetry in the mass-quenched Hubbard model", *Phys. Rev. B* **2018**, *97*, 085152.

[31] N. Dasari, M. Eckstein, "Photoexcited states in correlated band insulators", *Phys. Rev. B* **2018**, *98*, 035113.

[32] A. Matthies, J. Li, M. Eckstein, "Control of competing superconductivity and charge order by nonequilibrium currents", *Phys. Rev. B* **2018**, *98*, 180502.

[33] S. Sayyad, R. Žitko, H. U. R. Strand, P. Werner, D. Golež, "Comparative study of nonequilibrium insulator-to-metal transitions in electron-phonon systems", *Phys. Rev. B* **2019**, *99*, 045118.

[34] N. Tsuji, T. Oka, H. Aoki, "Correlated electron systems periodically driven out of equilibrium: $Floquet + DMFT$ formalism", *Phys. Rev. B* **2008**, *78*, 235124.

[35] Y. Murakami, N. Tsuji, M. Eckstein, P. Werner, "Nonequilibrium steady states and transient dynamics of conventional superconductors under phonon driving", *Phys. Rev. B* **2017**, *96*, 045125.

[36] A. Herrmann, Y. Murakami, M. Eckstein, P. Werner, "Floquet prethermalization in the resonantly driven Hubbard model", *EPL* **2018**, *120*, 57001.

[37] Y. Murakami, P. Werner, "Nonequilibrium steady states of electric field driven Mott insulators", *Phys. Rev. B* **2018**, *98*, 075102.

[38] Y. Murakami, M. Eckstein, P. Werner, "High-Harmonic Generation in Mott Insulators", *Phys. Rev. Lett.* **2018**, *121*, 057405.

[39] S. Takayoshi, Y. Murakami, P. Werner, "High-harmonic generation in quantum spin systems", *Phys. Rev. B* **2019**, *99*, 184303.

[40] K. Sandholzer, Y. Murakami, F. Görg, J. Minguzzi, M. Messer, R. Desbuquois, M. Eckstein, P. Werner, T. Esslinger, "Quantum simulation meets nonequilibrium DMFT: Analysis of a periodically driven, strongly correlated Fermi – Hubbard model", arXiv:1811.12826, **2018**.

[41] G. Kotliar, S. Y. Savrasov, K. Haule, V. S. Oudovenko, O. Parcollet, C. A. Marianetti, "Electronic structure calculations with dynamical mean-field theory", *Rev. Mod. Phys.* **2006**, *78*, 865.

[42] A. Dorda, M. Nuss, W. von der Linden, E. Arrigoni, "Auxiliary master equation approach to non – equilibrium correlated impurities", *Phys. Rev. B* **2014**, *89*, 165105.

[43] A. Dorda, PhD thesis, Technical University Graz, **2016**.

[44] O. Inganäs, "Organic Photovoltaics over Three Decades", *Advanced Materials* **2018**, *30*, 1800388.

[45] W. Shockley, H. J. Queisser, "Detailed Balance Limit of Efficiency of p n Junction Solar Cells", *Journal of Applied Physics* **1961**, *32*, 510–519.

[46] P. Werner, K. Held, M. Eckstein, "Role of impact ionization in the thermalization of photoexcited Mott insulators", *Phys. Rev. B* **2014**, *90*, 235102.

[47] J. R. Sites, "Calculation of impact ionization enhanced photovoltaic efficiency", *Solar Cells* **1988**, *25*, 163–168.

[48] R. D. Schaller, V. I. Klimov, "High Efficiency Carrier Multiplication in PbSe Nanocrystals: Implications for Solar Energy Conversion", *Phys. Rev. Lett.* **2004**, *92*, 186601.

[49] M. Aerts, T. Bielewicz, C. Klinke, F. C. Grozema, A. J. Houtepen, J. M. Schins, L. D. A. Siebbeles, "Highly efficient carrier multiplication in PbS nanosheets", *Nature Communications* **2014**, *5*, 3789.

[50] J. Qiu, H.-B. Lu, K.-J. Jin, M. He, J. Xing, "Manganite-layer thickness-dependent photovoltaic effect of $La_{0.9}Sr_{0.1}MnO_3/SrNb_{0.01}Ti_{0.99}O_3$ p–n heterojunction", *Physica B: Condensed Matter* **2007**, *400*, 66–69.

[51] H. Liu, K. Zhao, N. Zhou, H. Lu, M. He, Y. Huang, K.-J. Jin, Y. Zhou, G. Yang, S. Zhao, A. Wang, W. Leng, "Photovoltaic effect in micrometer-thick perovskite-type oxide multilayers on Si substrates", *Applied Physics Letters* **2008**, *93*, 171911.

[52] E. Manousakis, "Photovoltaic effect for narrow-gap Mott insulators", *Phys. Rev. B* **2010**, *82*, 125109.

[53] E. Assmann, P. Blaha, R. Laskowski, K. Held, S. Okamoto, G. Sangiovanni, "Oxide Heterostructures for Efficient Solar Cells", *Phys. Rev. Lett.* **2013**, *110*, 078701.

[54] J. E. Coulter, E. Manousakis, A. Gali, "Optoelectronic excitations and photovoltaic effect in strongly correlated materials", *Phys. Rev. B* **2014**, *90*, 165142.

[55] J. Holleman, M. M. Bishop, C. Garcia, J. S. R. Vellore Winfred, S. Lee, H. N. Lee, C. Beekman, E. Manousakis, S. A. McGill, "Evidence for impact ionization in vanadium dioxide", *Phys. Rev. B* **2016**, *94*, 155129.

[56] L. Wang, Y. Li, A. Bera, C. Ma, F. Jin, K. Yuan, W. Yin, A. David, W. Chen, W. Wu, W. Prellier, S. Wei, T. Wu, "Device Performance of the Mott Insulator $LaVO_3$ as a Photovoltaic Material", *Phys. Rev. Applied* **2015**, *3*, 064015.

[57] H.-T. Zhang, M. Brahlek, X. Ji, S. Lei, J. Lapano, J. W. Freeland, V. Gopalan, R. Engel-Herbert, "High-Quality $LaVO_3$ Films as Solar Energy Conversion Material", *ACS Applied Materials & Interfaces* **2017**, *9*, 12556–12562.

[58] M. Jellite, J.-L. Rehspringer, M. Fazio, D. Muller, G. Schmerber, G. Ferblantier, S. Colis, A. Dinia, M. Sugiyama, A. Slaoui, D. Cavalcoli, T. Fix, "Investigation of $LaVO_3$ based compounds as a photovoltaic absorber", *Solar Energy* **2018**, *162*, 1–7.

[59] M. Eckstein, P. Werner, "Thermalization of a pump-excited Mott insulator", *Phys. Rev. B* **2011**, *84*, 035122.

[60] M. Eckstein, P. Werner, "Nonequilibrium dynamical mean-field simulation of inhomogeneous systems", *Phys. Rev. B* **2013**, *88*, 075135.

[61] M. Eckstein, P. Werner, "Photoinduced States in a Mott Insulator", *Phys. Rev. Lett.* **2013**, *110*, 126401.

[62] M. Eckstein, P. Werner, "Ultrafast Separation of Photodoped Carriers in Mott Antiferromagnets", *Phys. Rev. Lett.* **2014**, *113*, 076405.

[63] A. Branschädel, G. Schneider, P. Schmitteckert, "Conductance of inhomogeneous systems: Real-time dynamics", *Annalen der Physik* **2010**, *522*, 657–678.

[64] E. Canovi, A. Moreno, A. Muramatsu, "Transport through two interacting resonant levels connected by a Fermi sea", *Phys. Rev. B* **2013**, *88*, 245105.

[65] C. CAROLI, R. COMBESCOT, P. NOZIERES, D. SAINT-JAMES, "A direct calculation of the tunnelling current: IV. Electron-phonon interaction effects", *J. Phys. C: Solid State Phys* **1972**, *5*, 21.

[66] M. Cini, "Time-dependent approach to electron transport through junctions: General theory and simple applications", *Phys. Rev. B* **1980**, *22*, 5887–5899.

[67] E. Boulat, H. Saleur, P. Schmitteckert, "Twofold advance in the theoretical understanding of far – from – equilibrium properties of interacting nanostructures", *Phys. Rev. Lett.* **2008**, *101*, 140601.

[68] K. Bidzhiev, G. Misguich, "Out-of-equilibrium dynamics in a quantum impurity model: Numerics for particle transport and entanglement entropy", *Phys. Rev. B* **2017**, *96*, 195117.

[69] C. Karrasch, S. Andergassen, M. Pletyukhov, D. Schuricht, L. Borda, V. Meden, H. Schoeller, "Non-equilibrium current and relaxation dynamics of a charge-fluctuating quantum dot", *EPL (Europhysics Letters)* **2010**, *90*, 30003.

[70] S. Andergassen, V. Meden, H. Schoeller, J. Splettstoesser, M. R. Wegewijs, "Charge transport through single molecules, quantum dots and quantum wires", *Nanotechnology* **2010**, *21*, 272001.

[71] D. M. Kennes, V. Meden, "Interacting resonant-level model in nonequilibrium: Finite-temperature effects", *Phys. Rev. B* **2013**, *87*, 075130.

[72] Y. Vinkler-Aviv, A. Schiller, F. B. Anders, "From thermal equilibrium to nonequilibrium quench dynamics: A conserving approximation for the interacting resonant level", *Phys. Rev. B* **2014**, *90*, 155110.

[73] C. Schiegg, M. Dzierzawa, U. Eckern, "Non-equilibrium transport through a model quantum dot: Hartree–Fock approximation and beyond", *New Journal of Physics* **2015**, *17*, 083060.

[74] J. Rammer, H. Smith, "Quantum field-theoretical methods in transport theory of metals", *Rev. Mod. Phys.* **1986**, *58*, 323–359.

[75] H. Haug, A.-P. Jauho, *Quantum Kinetics in Transport and Optics of Semiconductors*, Springer, Heidelberg, **1998**.

[76] J. Rammer, *Quantum Field Theory of Non-equilibrium States*, Cambridge University Press, **2007**.

[77] M. Gell–Mann, F. Low, "Bound states in Quantum Field Theory", *Phys. Rev.* **1951**, *84*, 350–354.

[78] A. L. Fetter, J. D. Walecka, *Quantum Theory of Many-Particle Systems*, McGraw-Hill, New York, **1971**.

[79] F. Faisal, "Floquet Green's function method for radiative electron scattering and multiphoton ionization in a strong laser field", *Computer Physics Reports* **1989**, *9*, 57–113.

[80] S. C. Althorpe, D. J. Kouri, D. K. Hoffman, N. Moiseyev, "A time-independent wavepacket approach to the (t, t)-method for treating time-dependent Hamiltonian systems", *Chemical Physics* **1997**, *217*, Dynamics of Driven Quantum Systems, 289–296.

[81] T. Brandes, "Truncation method for Green's functions in time-dependent fields", *Phys. Rev. B* **1997**, *56*, 1213–1224.

[82] T. Brandes, J. Robinson, "Transmission through a Quantum Dynamical Delta Barrier", *physica status solidi (b)* **2002**, *234*, 378–384.

[83] D. F. Martinez, "Floquet-Green function formalism for harmonically driven Hamiltonians", *Journal of Physics A: Mathematical and General* **2003**, *36*, 9827.

[84] E. Arrigoni, M. Knap, W. von der Linden, "Nonequilibrium Dynamical Mean Field Theory: an auxiliary Quantum Master Equation approach", *Phys. Rev. Lett.* **2013**, *110*, 086403.

[85] H.-P. Breuer, F. Petruccione, *The Theory of Open Quantum Systems*, Oxford University Press, Oxford, England, **2009**.

[86] R. Martin, R. C, W. J.H., "Householder's tridiagonalization of a symmetric matrix", *J.H. Numer. Math.* **1968**, *11*, 181–195.

[87] M. Journée, F. Bach, P. Absil, R. Sepulchre, "Low-Rank Optimization on the Cone of Positive Semidefinite Matrices", *SIAM Journal on Optimization* **2010**, *20*, 2327–2351.

[88] I. Grubišić, R. Pietersz, "Efficient rank reduction of correlation matrices", *Linear Algebra and its Applications* **2007**, *422*, 629–653.

[89] A. Dorda, M. Ganahl, S. Andergassen, W. von der Linden, E. Arrigoni, "Thermoelectric response of a correlated impurity in the nonequilibrium Kondo regime", *Phys. Rev. B* **2016**, *94*, 245125.

[90] D. P. Kingma, J. Ba, "ADAM: A Method for Stochastic Optimization", arXiv:1412.6980, **2014**.

[91] M. Abadi, A. Agarwal, P. Barham, E. Brevdo, Z. Chen, C. Citro, A. Corrado, Greg S.and Davis, J. Dean, M. Devin, S. Ghemawat, I. Goodfellow, A. Harp, G. Irving, M. Isard, Y. Jia, R. Jozefowicz, L. Kaiser, M. Kudlur, J. Levenberg, D. Mane, R. Monga, S. Moore, D. Murray, C. Olah, M. Schuster, J. Shlens, B. Steiner, I. Sutskever, K. Talwar, P. Tucker, V. Vanhoucke, V. Vasudevan, F. Viegas, O. Vinyals, P. Warden, M. Wattenberg, M. Wicke, Y. Y. Xiaoqiang Zheng, "TensorFlow: Large-Scale Machine Learning on Heterogeneous Distributed Systems", arXiv:1603.04467, **2016**.

[92] W. v. d. Linden, V. Dose, U. v. Toussaint, *Bayesian Probability Theory: Applications in the Physical Sciences*, Cambridge University Press, **2014**.

[93] A. A. Dzhioev, D. S. Kosov, "Super-fermion representation of quantum kinetic equations for the electron transport problem", *J. Chem. Phys.* **2011**, *134*, 044121.

[94] J. Dalibard, Y. Castin, K. Mølmer, "Wave-function approach to dissipative processes in quantum optics", *Phys. Rev. Lett.* **1992**, *68*, 580–583.

[95] H.-P. Breuer, B. Kappler, F. Petruccione, "Stochastic wave-function approach to the calculation of multitime correlation functions of open quantum systems", *Phys. Rev. A* **1997**, *56*, 2334–2351.

[96] H. Breuer, B. Kappler, F. Petruccione, "Heisenberg picture operators in the stochastic wave function approach to open quantum systems", *Eur. Phys. J. B* **1998**, *1*, 9–13.

[97] A. Dorda, I. Titvinidze, E. Arrigoni, "Quasiparticle excitations in steady state transport across a correlated layer", *Journal of Physics: Conference Series* **2016**, *696*, 012003.

[98] I. Titvinidze, A. Dorda, W. von der Linden, E. Arrigoni, "Thermoelectric properties of a strongly correlated layer", *Phys. Rev. B* **2017**, *96*, 115104.

[99] A. N. Rubtsov, V. V. Savkin, A. I. Lichtenstein, "Continuous-time quantum Monte Carlo method for fermions", *Phys. Rev. B* **2005**, *72*, 035122.

[100] P. Werner, A. Comanac, L. de'Medici, M. Troyer, A. J. Millis, "Continuous-Time Solver for Quantum Impurity Models", *Phys. Rev. Lett.* **2006**, *97*, 076405.

[101] A. Lubatsch, J. Kroha, "Optically driven Mott-Hubbard systems out of thermodynamic equilibrium", *Annalen der Physik* **2009**, *18*, 863–867.

[102] R. Frank, "Quantum criticality and population trapping of fermions by non-equilibrium lattice modulations", *New Journal of Physics* **2013**, *15*, 123030.

[103] R. Frank, "Population trapping and inversion in ultracold Fermi gases by excitation of the optical lattice: non-equilibrium Floquet–Keldysh description", *Applied Physics B* **2013**, *113*, 41–47.

[104] W.-R. Lee, K. Park, "Dielectric breakdown via emergent nonequilibrium steady states of the electric-field-driven Mott insulator", *Phys. Rev. B* **2014**, *89*, 205126.

[105] A. V. Joura, J. K. Freericks, A. I. Lichtenstein, "Long-lived nonequilibrium states in the Hubbard model with an electric field", *Phys. Rev. B* **2015**, *91*, 245153.

[106] M. Eckstein, P. Werner, "Nonequilibrium dynamical mean-field calculations based on the noncrossing approximation and its generalizations", *Phys. Rev. B* **2010**, *82*, 115115.

[107] Y.-J. Wang, J.-S. Zhang, "An efficient algorithm for large scale global optimization of continuous functions", *Journal of Computational and Applied Mathematics* **2007**, *206*, 1015–1026.

[108] Y.-J. Wang, J.-S. Zhang, "A new constructing auxiliary function method for global optimization", *Mathematical and Computer Modelling* **2008**, *47*, 1396–1410.

[109] D. Bauernfeind, M. Zingl, R. Triebl, M. Aichhorn, H. G. Evertz, "Fork Tensor-Product States: Efficient Multiorbital Real-Time DMFT Solver", *Phys. Rev. X* **2017**, *7*, 031013.

[110] D. Bauernfeind, R. Triebl, M. Zingl, M. Aichhorn, H. G. Evertz, "Dynamical mean-field theory on the real-frequency axis: $p-d$ hybridization and atomic physics in $SrMnO_3$", *Phys. Rev. B* **2018**, *97*, 115156.

[111] A. N. Rubtsov, M. I. Katsnelson, A. I. Lichtenstein, "Dual fermion approach to nonlocal correlations in the Hubbard model", *Phys. Rev. B* **2008**, *77*, 033101.

[112] H. Hafermann, C. Jung, S. Brener, M. I. Katsnelson, A. N. Rubtsov, A. I. Lichtenstein, "Superperturbation solver for quantum impurity models", *EPL (Europhysics Letters)* **2009**, *85*, 27007.

[113] C. Jung, A. Lieder, S. Brener, H. Hafermann, B. Baxevanis, A. Chudnovskiy, A. Rubtsov, M. Katsnelson, A. Lichtenstein, "Dual-fermion approach to non-equilibrium strongly correlated problems", *Ann. Phys.* **2012**, *524*, 49–61.

[114] A. E. Antipov, J. P. LeBlanc, E. Gull, "Opendf - An Implementation of the Dual Fermion Method for Strongly Correlated Systems", *Physics Procedia* **2015**, *68*, Proceedings of the 28th Workshop on Computer Simulation Studies in Condensed Matter Physics (CSP2015), 43–51.

[115] F. Chen, G. Cohen, M. Galperin, "Auxiliary Master Equation for Nonequilibrium Dual-Fermion Approach", *Phys. Rev. Lett.* **2019**, *122*, 186803.